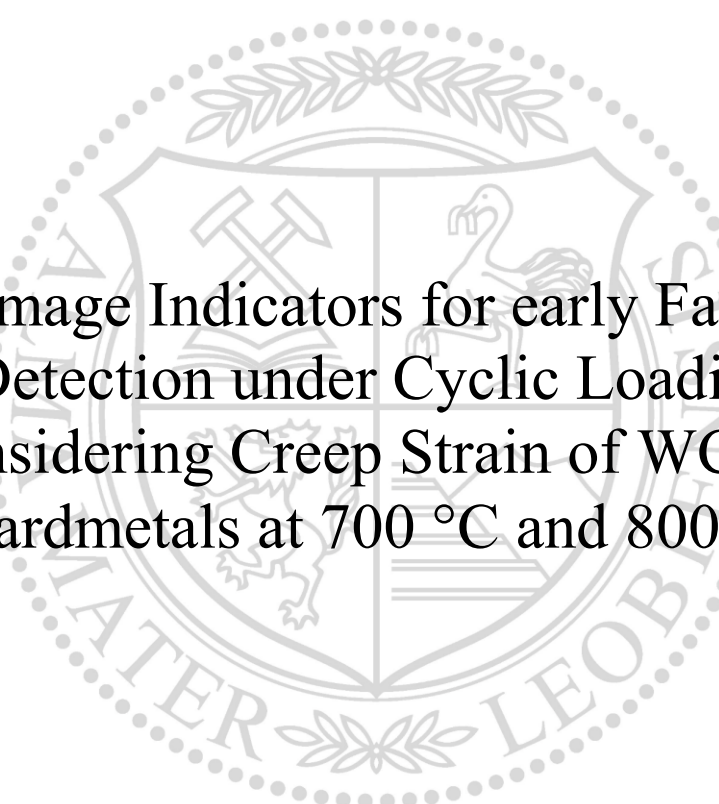




Chair of Physical Metallurgy and Metallic Materials

Doctoral Thesis



Damage Indicators for early Failure  
Detection under Cyclic Loading  
considering Creep Strain of WC-Co  
Hardmetals at 700 °C and 800 °C

Dipl.-Ing. Kathrin Maier, BSc

October 2021





**AFFIDAVIT**

I declare on oath that I wrote this thesis independently, did not use other than the specified sources and aids, and did not otherwise use any unauthorized aids.

I declare that I have read, understood, and complied with the guidelines of the senate of the Montanuniversität Leoben for "Good Scientific Practice".

Furthermore, I declare that the electronic and printed version of the submitted thesis are identical, both, formally and with regard to content.

Date 27.10.2021

A handwritten signature in blue ink that reads 'Maier Kathrin'.

---

Signature Author  
Kathrin Maier

The author gratefully acknowledges the financial support of the Frontrunner-Initiative of the project "Frontrunner: Integrated, data driven development for Cutting Tools" (Project No. 861280). Additionally, the financial support under the scope of the COMET program within the K2 Center "Integrated Computational Material, Process and Product Engineering (IC-MPPE)" (Project No 859480). This program is supported by the Austrian Federal Ministries for Climate Action, Environment, Energy, Mobility, Innovation and Technology (BMK) and for Digital and Economic Affairs (BMDW), represented by the Austrian research funding association (FFG), and the federal states of Styria, Upper Austria and Tyrol.

## Acknowledgements

At this point I would like to thank all of those who supported and motivated me during the preparation of this thesis.

First of all, I would like to express my heartfelt appreciation to Prof. Dr. Reinhold Ebner, for the opportunity to write this thesis at the Materials Center Leoben Forschung GmbH, for his invaluable advice, encouragement and for the trust he has placed in me. I would also like to thank Assoz. Prof. Dr. Daniel Kiener for co-supervising this thesis as my mentor. I thank him for his feedback, input and discussions that helped me a lot keep the red thread.

My sincerest thanks also go to Dr. Thomas Klünsner. I am grateful beyond measure for his patience, his valuable advice, discussions and the countless hours he spent correcting my publication and report drafts. His door was always open to me and without his support I would not be at the point with my thesis where I am today.

Thanks also go to many employees at Ceratizit Austria GmbH; firstly for providing specimens and without their expertise in hard metals this thesis would never have been so successful. My special thanks go to Dr. Christoph Czettel and Dr. Jonathan Schäfer and their teams, they always had a sympathetic ear and a solution ready for me.

Good work can only succeed in a comfortable environment. Therefore, I would like to take this opportunity to thank all of the MCL's staff who have welcomed me so warmly and made it possible for me to research in an inspiring, good working atmosphere. Great thanks also go to all research assistants, PhD students, diploma students and student assistants for inspiring discussions on a wide variety of problems and in helping me to implement my research questions.

Furthermore, I must express my very profound gratitude to my family, my boyfriend and my other friends for providing me with their unfailing support and continuous encouragement throughout my years of studying and the process of researching and writing this thesis. This accomplishment would not have been possible without them.

*Thank you all*



## Abstract

The focus of the present thesis is to provide a sound basis and methodological foundation for the knowledge-based design and optimization of uncoated WC-Co hardmetals for machining processes. Cyclic and step-loading creep tests at 700 °C and 800 °C were used to establish a correlation between experimental data, limit stresses, damage indicators, and early damage formation. Special attention was paid to application-relevant loading conditions occurring in the cutting edge region of milling inserts for steel and titanium work pieces.

Various studies were carried out so far and reported in literature for WC-Co hardmetals under creep, monotonic increasing and cyclic loading conditions at elevated temperatures. However, no study was conducted to identify limits of endurable stresses and diagnose damage development at elevated temperatures.

To fill this gap, six WC-Co hardmetal grades were investigated under uniaxial step-loading creep tests as well as in cyclic tests at stress ratios of  $R = \sigma_{\min}/\sigma_{\max} = -\infty$  and  $R = -1$  up to different stress ranges at 700 °C and 800 °C in vacuum. The investigated hardmetal grades differ in their WC grain size: 0.4  $\mu\text{m}$  to 2.0  $\mu\text{m}$  and Co-content: 6 wt.% to 12 wt.%. Furthermore, microstructural changes were inspected by scanning electron microscopy and by electron backscatter diffraction.

Based on the presence of advancing strain ratcheting above a critical stress range at  $R = -\infty$ , limit stresses were determined associated with microdefect formation, such as nanopores and cavities. Damage indicators were determined from cyclic tests at  $R = -1$  using stress-strain-hysteresis loop parameters. An increasing hysteresis loop area and tension-compression-strain asymmetry with increasing number of load cycles can be associated with the formation of microdefects. Step-loading creep tests also revealed a tension-compression-strain asymmetry as in cyclic tests. Physically, the strain asymmetry can be attributed to faster microdefect formation under tension than under compression. Further, limit stresses and the onset of increase of damage indicators were observed to decrease with increasing temperature. Additionally, strain ratcheting occurred under cyclic loading at  $R = -1$ , as observed at  $R = -\infty$  at 700 °C and 800 °C. Hence, stress-strain-hysteresis loop area, tension-compression-strain asymmetry as well as strain ratcheting are reliable and meaningful damage indicators for bulk material damage.

**Keywords:** WC-Co hardmetal; Uniaxial compression and tension step-loading creep test; Uniaxial cyclic test; Elevated temperature; Damage indicator; Electron microscopy;





## Kurzfassung

Ziel der vorliegenden Arbeit ist es, eine fundierte Basis und methodische Grundlage für die wissensbasierte Auslegung und Optimierung von unbeschichteten WC-Co-Hartmetallen für die spanende Bearbeitung zu schaffen. Durch zyklische Versuche und Kriechversuchen mit stufenweiser Belastung bei 700 °C und 800 °C wurden Zusammenhänge zwischen experimentellen Daten, Grenzspannungen, Schädigungsindikatoren und Vorschädigung hergestellt. Besonderes Augenmerk wurde auf anwendungsrelevante Belastungszustände gelegt, wie sie im Schneidkantenbereich von Fräseinsätzen für Stahl- und Titanwerkstücke auftreten.

In der Literatur wurden über verschiedene Studien zum Verhalten von WC-Co Hartmetallen zu kriechenden, monoton steigenden und zyklischen Belastungsbedingungen bei erhöhten Temperaturen berichtet. Es wurden jedoch keine Studien vorgenommen, um die Grenzen der erträglichen Belastung zu ermitteln und die Schadensentwicklung bei erhöhten Temperaturen zu diagnostizieren.

Um diese Lücke zu schließen wurden in dieser Arbeit sechs WC-Co-Hartmetallsorten in einachsigen Kriechversuchen mit stufenweiser Belastung sowie in zyklischen Versuchen bei Spannungsverhältnissen von  $R = \sigma_{\min}/\sigma_{\max} = -\infty$  und  $R = -1$  bis zu verschiedenen Belastungsspannungen bei 700 °C und 800 °C im Vakuum untersucht. Die untersuchten Hartmetallsorten unterscheiden sich in ihrer WC-Korngröße: 0,4 µm bis 2,0 µm und ihrem Co-Gehalt: 6 Gew.-% bis 12 Gew.-%. Darüber hinaus wurden mikrostrukturelle Veränderungen mittels Rasterelektronenmikroskopie und die Veränderung der WC- und Co-Phase mittels Elektronenrückstreubeugung untersucht.

Basierend auf der fortschreitenden Dehnungszunahme oberhalb eines kritischen Spannungsbereichs bei  $R = -\infty$  wurden Grenzspannungen bestimmt, die mit der Bildung von Mikrodefekten, wie Nanoporen und Hohlräumen, in Zusammenhang stehen. Schadensindikatoren wurden aus zyklischen Versuchen bei  $R = -1$  anhand von Parametern der Spannungs-Dehnungs-Hystereseschleife ermittelt. Eine Zunahme der Hystereseschleifenfläche und der Zug-Druck-Dehnungs-Asymmetrie mit zunehmender Anzahl von Belastungszyklen kann auf die Bildung von Mikrodefekten in Verbindung gebracht werden. Kriechversuche mit schrittweiser Belastung zeigten ebenfalls eine Zug-Druck-Dehnungsasymmetrie wie zyklische Versuche. Physikalisch gesehen kann diese auf eine schnellere Bildung von Mikrodefekten unter Zug als unter

Druckbelastung zurückgeführt werden. Außerdem wurde beobachtet, dass die Grenzspannung und der Beginn des Anstiegs der Schadensindikatoren mit zunehmender Temperatur abnehmen. Außerdem trat bei zyklischer Belastung bei  $R = -1$  eine fortschreitende Dehnungszunahme auf, wie sie bei  $R = -\infty$  bei 700 °C und 800 °C beobachtet wurde. Daher sind die Hystereseschleifenfläche, die Zug-Druck-Dehnungs-Asymmetrie sowie die fortschreitende Dehnungszunahme zuverlässige und aussagekräftige Indikatoren für die Schädigung von Werkstoffen.

**Schlüsselwörter:** WC-Co Hartmetall; Uniaxialer Druck- und Zug-Stufenbelastungs-Kriechversuch; Uniaxialer zyklischer Versuch; Erhöhte Temperatur; Schadensindikator; Elektronenmikroskopie;

# Table of Content

Acknowledgements .....	V
Abstract.....	VII
Kurzfassung .....	IX
1. Introduction .....	1
2. Theoretical Background .....	5
2.1. Fracture Mechanisms .....	5
2.2. Creep Behaviour .....	14
2.3. Cyclic Behaviour at Elevated Temperature .....	22
3. Aims and Main Tasks of the Thesis .....	29
4. Summary and Conclusions .....	37
5. Outlook .....	41
6. References .....	43
7. Publications .....	58
7.1. List of Included Publications .....	58
7.2. Scientific Presentations .....	59
7.3. My Contribution to Included Publications.....	60
Publication I.....	63
Publication II .....	75
Publication III .....	99
Publication IV .....	129
Publication V .....	159



# 1. Introduction

Hardmetals are composed of a hard material phase and a ductile metal matrix phase. Hence, they are classified as metal-matrix composites or dispersion hardened materials due to their brittle hard phase and ductile metal phase. Usually Tungsten carbide (WC), Titanium carbide (TiC) or Tantalum carbide (TaC) are used as a hard phase, which are embedded in the metal phase. The metal phases, also called binder phases, are usually Cobalt (Co), Iron (Fe) or Nickel (Ni) based. The most practical hardmetal composition is WC-Co, due to the good high-temperature properties. This composition is investigated in more detail in the current thesis at 700 °C and 800 °C.

To merge hard- and binder phase into a compact, mainly pore-free material, hardmetals are produced by liquid phase sintering (*Schedler 1988*). During production, the binder phase is molten and encloses the solid hard phase. Additionally to the two phases, additives are added, for instance vanadium- or chromium carbide to inhibit grain growth of the carbides. Due to additives, the WC grain boundaries and molten binder phase contain a certain amount of foreign atoms, which influence the crystal structure due to precipitation or disadvantageous microstresses after sintering at room temperature (*Marshall et al. 2013, 2015, Weidow et al. 2009a*). Further, the hard phase causes high strength and the binder phase results in higher ductility of the hardmetal over a wide temperature range. Hence, the hard- to binder phase ratio influences the hardmetal properties, as the strength and hardness decrease with increasing binder phase content.

Based on the hardmetal properties, they are used in various areas like chipping, wear protection, metal forming, stone-, wood- or plastics machining. Main application is chipping of metals, non-metals and composites as well as wood by various types of tools or as components for chipless forming (*Bose 2011*). Figure 1 shows some hardmetal tools for drilling, turning and milling applications. During chipping, as in metal cutting, hardmetal tools are used for several production steps. They are applied to manufacture products from solid materials to the finished product with high quality (*Ferreira et al. 2009*). Due to diverse hardmetal tools for chipping, they are intensively investigated in scientific research to understand and improve them as well as to increase their service life.



Figure 1: Various hardmetal tools for drilling, turning and milling applications. Source: By courtesy of the company Ceratizit Austria GmbH (*Ceratizit Austria GmbH 2021*).

Hardmetal components have to withstand different mechanical and thermal loads depending on their application. Loads acting on tools depend on various parameters: tool geometry, material being machined, cutting parameters, duration of use, temperature variations, machine tool vibrations, chip sticking and loosening, chip breaking during the cutting process, cutting interruptions, hardmetal composition and tool coating (*Adjam et al. 2019, Ferreira et al. 2009, Schleinkofer et al. 1995*). Due to load and temperature variations in the binder phase, a phase transformation from the face-centered cubic (fcc) to the hexagonal close-packed (hcp) crystal structure is possible at room temperature as well as elevated temperatures (*Schleinkofer et al. 1996a, Kindermann et al. 1999, Miyake et al. 1968*).

Cyclically and monotonically increasing thermomechanical loads act simultaneously at the cutting tool edges (*Komanduri 1993, Ferreira et al. 2009*). Hence, knowledge about static and cyclic properties of hardmetals is necessary to optimize tools. Since elevated temperatures occur in tools during service, high-temperature investigations are necessary next to room temperature investigations to understand thermal activated processes in WC-Co hardmetals (*Schedler 1988*).

Three complementary investigation directions can be used to enable diagnostics of practical service life and further development of hardmetal tools (*Ferreira et al. 2009*): 1.) Determination of mechanical and thermal loads acting on tools, 2.) Numerical calculations of stress, strain and heat fields, 3.) In-operando investigations of the hardmetal behaviour. To perform all directions of investigation is time-consuming. Based on experiment and finite element simulations of tools during cutting in literature, very high stresses up to 1000 MPa (*Nemetz et al. 2019, Kagnaya et al. 2009*) and at elevated temperatures up to 1200 °C (*Kagnaya et al. 2011*) were observed or predicted at tool cutting edges.

In the current thesis, investigation into the material behaviour under application-relevant stresses and temperatures occurring on the cutting tool edges during chipping of steel and titanium work pieces is considered. For this purpose, different uncoated WC-Co hardmetal tool substrates are analysed under uniaxial cyclic loading at elevated temperatures and uniaxial step-loading creep tests. The results are summarized in five publications, which are linked by similar results from step-loading creep and cyclic tests regarding material behaviour, endurable limit stresses as well as damage development diagnosis in WC-Co hardmetals at 700 °C and 800 °C. The selected temperatures are below the usual temperature range in literature, but are typical for many hardmetal application areas. Results and data from the current thesis are important contributions to further development of simulations and better understanding of damage development in WC-Co hardmetal tools.





## 2. Theoretical Background

WC-Co hardmetals have good high-temperature properties which allow them to be used in various areas of material processing to withstand different mechanical and thermal loads. However, their material properties and response to mechanical loading are influenced by their chemical composition and microstructure. Additionally, precise knowledge about operating conditions and behaviour are required to understand the material- and failure behaviour of WC-Co hardmetal tools. Hence, various studies are carried out in literature under creep, monotonic increasing and cyclic loading conditions at room temperature and elevated temperatures. From these studies, a knowledge base for WC-Co hardmetals has been established. In the following sections, the fundamentals of fracture, creep and cyclic behaviour at elevated temperature are discussed in more detail. At the same time, gaps in the state of the art are pointed out and related to the available publications in this thesis.

### 2.1. Fracture Mechanisms

Various defect types are formed during processing or operation in hardmetals (*Jonke et al. 2017, Roebuck et al. 1988, Suzuki et al. 1975, Casas et al. 2001, Pugsley et al. 2001, Góez et al. 2012*). They act as failure origin in components and cause defect-controlled fracture behaviour (*Rice et al. 1978, Jonke et al. 2017*). The various defects of different size and shape were identified by fracture surface studies (*Jonke et al. 2017, Klümsner et al. 2010a, Obrtlík et al. 1992, Kotas et al. 2017, Krobath et al. 2018*): pores, large carbide grains above the average carbide grain size, microcracks, carbide or binder phase accumulations, foreign phase inclusion accumulations and surface treatment damage. Figure 2 shows two examples of internal defects as fracture origin on fracture surfaces: WC-grain- and foreign phase inclusion accumulations. The largest defects in the hardmetal volume often serve as starting points for cracks, because they reduce stress and/or strain required for cracking (*Munz et al. 1989*). Due to defect-controlled fracture behaviour of hardmetals, specimens made of the same type of compound exhibit different mechanical behaviour (*Danzer et al. 2008, González et al. 2020*), e.g. different number of load cycles to failure during cyclic tests (*Obrtlík et al. 1992, Li et al. 2013*).

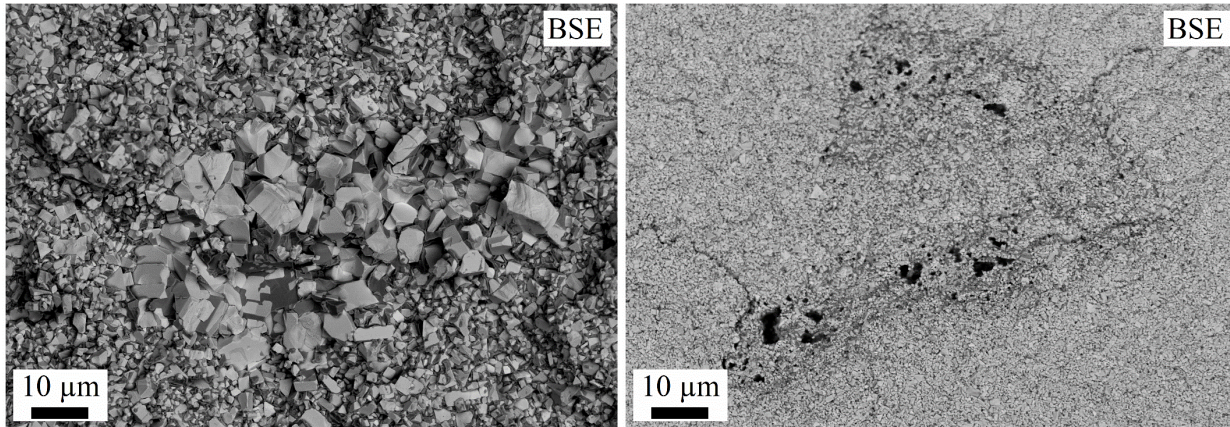


Figure 2: Scanning electron microscope micrograph showing fracture origin on fracture surfaces due to internal defects like (a.) WC-grain-accumulations, and (b.) foreign phase inclusion accumulations (black) in the microstructure of cyclic loaded WC-Co hardmetals in backscatter electron (BSE) contrast mode. Source: Micrograph originates from own results.

Particularly important for the fracture behaviour of WC-Co hardmetals are the hard WC carbide phase and the ductile Co-phase, which behave differently under mechanical load. Hence, deformation and damage mechanisms have been identified in WC-Co hardmetals: elastic deformation, plasticity due to dislocation movements, transgranular fracture of binder- and/or carbide phase, stress-assisted mass transport of binder phase, cracking or sliding of WC/Co phase boundaries or WC/WC grains boundaries, cavity formation at interfaces as well as within the binder phase (*Yousfi et al. 2015, Sigl et al. 1987, Östberg et al. 2006a*).

Due to local stress concentrations at internal defects and reaching of a critical stress, cracks form at weak spots in the microstructure. Weak spots could be the Co-phase, WC phase or interfaces between the phases. With increasing crack length material resistance rises due to the formation of a process zone near the crack tip, which is attributed to intrinsic and extrinsic mechanisms (*Suresh 1991, Fett et al. 1992, Ritchie 1988*). Intrinsic mechanisms are defined as processes that occur in front of the crack tip, see Figure 3: microcrack formation, plastic zone formation and phase transformations. Extrinsic mechanisms are processes that occur behind the crack tip: crack flank wedging, ligaments and fibre bridges formation.

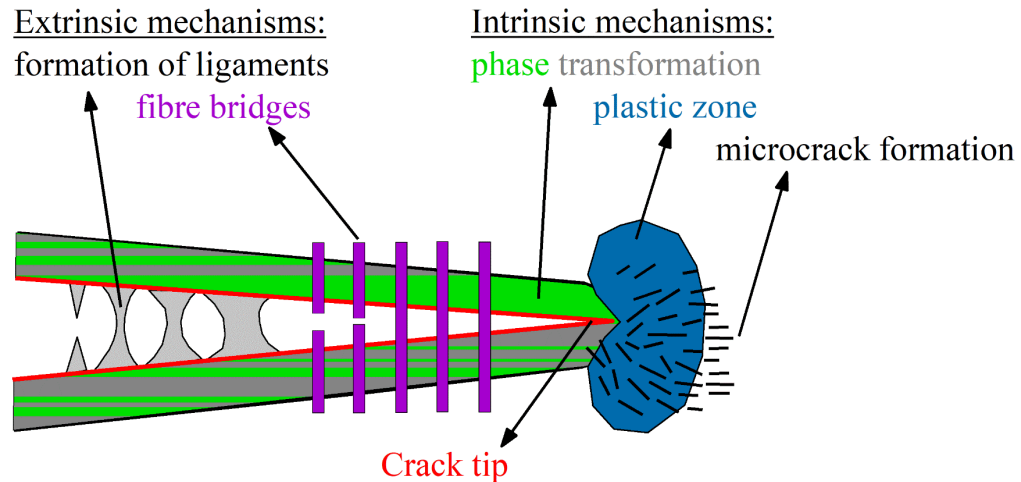


Figure 3: Illustration of the crack tip (red) with intrinsic and extrinsic mechanisms. Intrinsic mechanisms are processes occurring in the vicinity of the growing crack tip, like phase transformation (green-dark grey), the formation of a plastic zone (blue) or microcrack formation (small black lines). Extrinsic mechanisms are processes behind the crack tip, such as the ligament formation (light grey) or fiber bridges (violet). Source: Own representation based on (Suresh 1991, Ritchie 1988).

Additionally to deformation mechanisms in WC-Co hardmetals described above, fracture paths and damage formation were investigated in literature (Sigl *et al.* 1984, Fischmeister *et al.* 1988, Sigl *et al.* 1987). Brittle fracture was observed on the macro scale and on the micro scale, ductile fracture of the binder phase was noticed next to brittle fracture of carbide grains (Fischmeister 1983, Gurland 1988, Johannesson *et al.* 1988, Mari *et al.* 1999, Sigl *et al.* 1987). Further, an increasing number of internal interfaces is present due to the two phases, in contrast to single-phase materials. Hence, four possible fracture paths are identified (Sigl *et al.* 1987, 1984, Fischmeister 1983, Chermant *et al.* 1976, Hong *et al.* 1983, Lea *et al.* 1981, Nabarro *et al.* 1968):

- 1.) Transgranular fracture through the Co-phase („B“),
- 2.) Transgranular fracture through the WC-phase („C“),
- 3.) Cracking/sliding/fracture of WC/WC grain boundaries („C/C“),
- 4.) Cracking/sliding/fracture of WC/Co phase boundaries („C/B“).

In general, there are three steps that ultimately lead to the fracture of the material: 1.) crack initiation; 2.) subcritical crack growth, and 3.) catastrophic crack propagation. A crack is termed critical if a critical stress intensity in front of the tip causes catastrophic propagation and ultimate failure of the material. For hardmetals no subcritical crack growth was observed at room temperature tests. Hence, at room temperature conditions, they exhibit brittle fracture at the macro scale with only two fracture steps: crack initiation at internal defects or microstructure and catastrophic crack propagation (*Johannesson et al. 1988, Sigl et al. 1987, Roebuck et al. 1988, Exner et al. 2001, Osterstock et al. 1983*). In case of purely elastic deformation, the WC-phase carries a higher proportion of external stresses, due to the higher volume fraction as well as due to the higher Young's modulus compared to the Co-phase, "elastic zone" in Figure 4 (*Sigl et al. 1984*). After elastic deformation, crack formation and growth occur at internal defects or at weak spots in the hard phase. Weak spots can be, for example, WC/WC contact regions with reduced cohesive strength due to misorientation angles between contacting carbide grains (*Csanádi et al. 2020, Deshmukh et al. 1982, Exner 1983, Östberg et al. 2006b, Weidow et al. 2009b*), the negative influence of various chemical elements at the carbide interfaces (*Christensen et al. 2003, Henjered et al. 1986, Östberg et al. 2006a, Vicens et al. 1994, Weidow et al. 2011*), or large carbide grains (*Almond 1983, Fischmeister 1983, Kursawe et al. 2001, Roebuck et al. 1988, Suzuki et al. 1975, Almond et al. 1977*). The propagation of cracks in the hard phase is primarily trans- or intercrystalline on the fracture paths "C" and "C/C".

After the hard phase has fractured, stresses are redistributed into the Co-phase in front of the crack tip. Exceeding the yield strength of the Co-phase during stress redistribution, the Co-phase starts to flow plastically. At the crack tip and in the hard phase, a plane strain state exists. Further, adhesion forces between WC grains and Co-phase are strong (*Schedler 1988*), which help in combination with the plane strain state to prevent failure of the Co-phase by detachment from the hard phase and simultaneous necking in front of the crack tip (*Sigl et al. 1984*). Considering the volume constancy, plastic deformation of Co leads to pore formation, pore growth and pore coalescence (*Spiegler et al. 1992*). Consequently, binder phase bridges form behind the crack tip, holding the crack flanks together, causing a reduced stress concentration at the crack tip. This type of crack tip zone is characteristic for crack propagation in hardmetals and is defined as "multiligament zone", see Figure 4, (*Sigl et al. 1984, Sigl 1986*). Formation of binder ligaments is estimated to dissipate between 80-95% of the total energy required to fracture WC-Co hardmetals,

depending on their composition (*Schmauder et al. 1989*). Note that the carbide accounts for about 96% to 70% of the total mass, which is significantly higher than the proportion of Co-phase. Consequently, a significant part of the hardmetal toughness is due to the plastic deformation of the binder phase.

With continued loading, ligaments behind the crack tip in the Co-phase rupture and open crack flanks are formed, see "fracture zone" in Figure 4 (*Fischmeister 1983, Fischmeister et al. 1988, Gurland 1988, Sigl et al. 1984, 1987, Fischmeister et al. 1989, Spiegler et al. 1992*). Multiligament fracture of the Co-phase shifts the stress concentration in the material, leading to repeated crack initiation at weak spots in front of the crack tip until ultimate specimen failure.

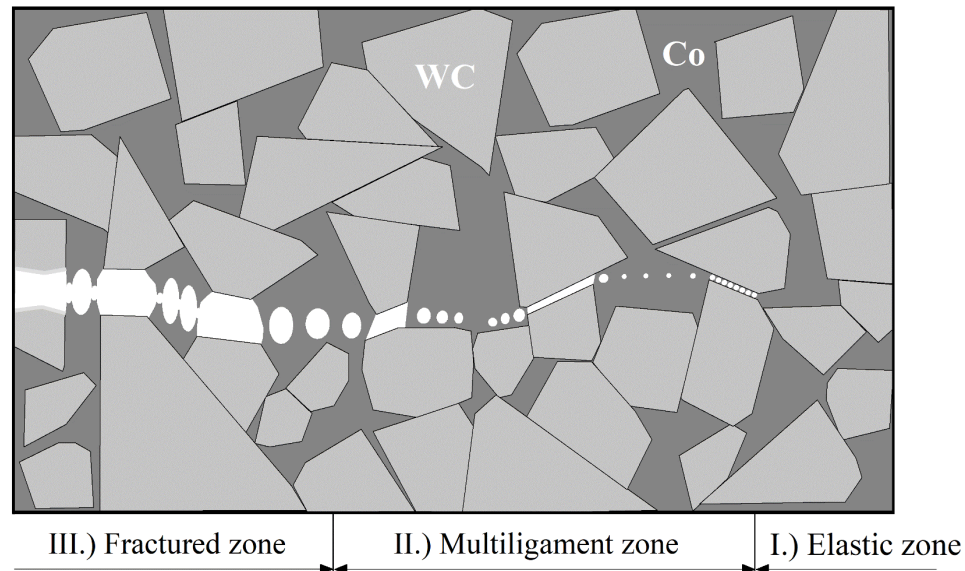


Figure 4: Classification of the crack tip region in WC-Co hardmetals under static loading: I.) Elastic zone without pore formation in the Co-binder phase. II.) Multiligament zone with nucleation and growth of pores within the Co-binder phase. III.) Fractured zone with coalescence of pores and growth of microcavities within the Co-phase. The WC-phase is visible in light grey, the Co-phase in dark grey and microcracks as well as pores in white. Source: Own representation based on (*Fischmeister et al. 1988, Sigl et al. 1988*).

As mentioned above, milling causes monotonous and cyclic loads with development of elevated temperatures in WC-Co hardmetals. Due to the thermal influence, in addition to mechanical processes, creep processes occur in the Co-phase (*Mingard et al. 2021, Yousfi et al. 2015, Smith et al. 1968*). Fatigue tests at room temperature and at elevated temperature as well as creep tests of WC-Co hardmetals exhibit subcritical crack growth after crack initiation in

contrast to static tests (*Johannesson et al. 1988, Roebuck et al. 1988, Schmid et al. 1988, Almond et al. 1980, Suresh 1991, Schleinkofer et al. 1995, 1996a, 1996b*). During subcritical crack growth, a crack with a certain initial crack length grows stepwise due to continuous energy supply. When the crack opens, Co-phase bridges deform plastically behind the crack tip (*Sigl 1986*), while crack closure leads to compression of these bridges. Therefore, the crack can propagate piecewise if the binder phase bridges fail, see Figure 4. After reaching a critical crack length unstable crack growth follows and ultimate specimen failure occurs.

Fatigue tests at room temperature (*Kindermann et al. 1999, Schleinkofer et al. 1996b, Obrtlík et al. 1992, Fry et al. 1988, Llanes et al. 2002, Sailer et al. 2001, Li et al. 2013*) and above 600 °C (*Kindermann et al. 1999, Tritremmel et al. 2017*), as well as creep tests above 800 °C (*Yousfi et al. 2015, Mingard et al. 2021, Lay et al. 1987, Ueda et al. 1975*) have revealed defects and crack paths occurring mainly intergranular and in the Co-phase volume. Additionally, examining fracture surfaces at room temperature of cyclically loaded specimens have exhibited less smooth surfaces, which is attributed to multiple fracture origins under cyclic loading (*Li et al. 2013*). Further, subcritical crack growth has been identified to result in different crack paths than without subcritical crack growth. In case of the former, the crack grows through the Co-phase, while failure without subcritical crack growth results in crack growth through the Co-phase and carbide phase.

Failure behaviour of hardmetals at room temperature (*Spiegler et al. 1992, Schleinkofer et al. 1995, Sigl et al. 1987*) and partly for elevated temperatures has been widely studied (*Kindermann et al. 1999, Tritremmel et al. 2017, Mingard et al. 2021, Yousfi et al. 2015*). Knowledge of damage mechanisms under cyclic or creep loading is based on fracture surfaces, microstructural changes near the fracture surface and by examining the crack path. Only a few investigations examined pre-failure damage mechanisms and their appearance in WC-Co hardmetals. Therefore, the current thesis focuses on investigations of the early stages of damage in WC-Co hardmetal specimens prior to specimen failure and critical crack growth for step-loading creep tests (see Publication II and Publication III) and for cyclic loading at stress ratios of  $R = \sigma_{\min}/\sigma_{\max} = -\infty$  and  $R = -1$  (see Publication IV and Publication V) at 700 °C and 800 °C.

### Co-Phase Transformation in WC-Co hardmetals

Fracture surfaces of WC-Co hardmetal specimens subjected to cyclic loading indicate a failure at low plastic strain with brittle character (*Almond et al. 1980, Schleinkofer et al. 1995, Erling et al. 2000*). The low plastic strain at fracture was also attributed, among other factors, to binder phase embrittlement, since a diffusionless phase transformation was observed in the Co-phase during the deformation process under cyclic as well as under creep (*Mingard et al. 2021, Almond et al. 1980, Roebuck et al. 1984, Schleinkofer et al. 1995*).

At room temperature, pure Co exhibits a hcp crystal structure, which is stable up to 417 °C. Above 417 °C, the hcp crystal structure transforms into the fcc crystal structure due to Shockley partial dislocations (*Seeger et al. 1958*). Due to the dislocation movement on every other close packed (111)-plane, the stacking sequence of the close packed plane of the fcc crystal structure changes to the hcp crystal structure (*Seeger et al. 1958*). By transforming the crystal structure of pure Co from hcp to fcc, a volume expansion of about 0.27 to 0.36 was observed (*Davis 2000*).

In various WC-Co hardmetal grades at room temperature, only the fcc crystal structure was detected after liquid phase sintering (*Schaller et al. 1988, Miyake et al. 2004*). The fcc crystal structure forms during liquid phase sintering due to the formation of a solid solution with tungsten, carbon or other additives, which stabilize the fcc crystal structure in the Co-phase. Another reason for the presence of the fcc crystal structure is the shape change limitation during phase transformation due to the WC grain boundaries (*Vasel et al. 1985*). However, at room temperature, WC-Co hardmetals can simultaneously contain the fcc and hcp crystal structures in the Co-phase (*Mingard et al. 2013, Marshall et al. 2013, Mingard et al. 2011*). If both crystal structures are present, the hcp Co-phase can be identified as twinning structure in the fcc crystal structure, see Figure 5. The Co-phase crystal structure depends on various factors: dissolved elements due to manufacturing processes (*Roebuck et al. 1984, Marshall et al. 2015, 2013, Weidow et al. 2009a, Eizadjou et al. 2020*), WC grain size (*Marshall et al. 2013*) and stresses resulting from differences in the thermal expansion coefficients of WC and Co-phase (*Adjam et al. 2020*). Also, the transformation of the fcc to the hcp crystal structure in hardmetals was not observed below 417 °C as in the case of pure Co. Due to the high dissolved element concentration in the Co-phase, the fcc-hcp transformation transition temperature shifts to 750 °C (*Jia et al. 1998*).

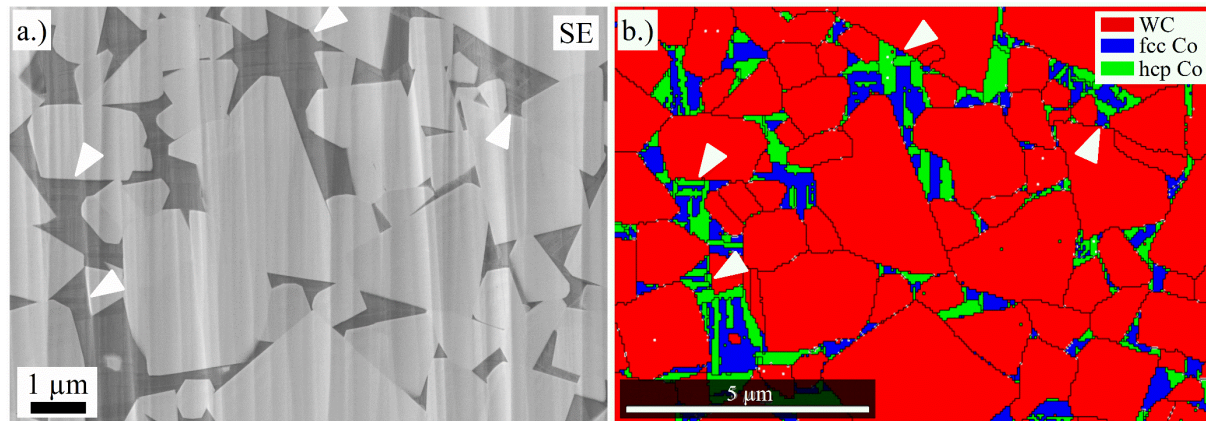


Figure 5: (a.) Scanning electron microscope (SEM) micrograph showing the microstructure of a virgin WC-10 wt.% Co hardmetal grade with an average WC grain size of  $2.0\ \mu\text{m}$  in secondary electron (SE) contrast mode. The WC-phase is visible in light grey, the Co-phase in dark grey and hcp-Co twins in the fcc Co-phase are marked by white triangles. (b.) EBSD phase distribution map: WC grains in red, fcc Co-phase in blue, and hcp Co-phase in green for the same image section as in (a.). White triangles in the EBSD map are at the same positions as in the SEM micrograph. Source: Micrograph and EBSD phase distribution maps originates from own results.

Experiments at room temperature under monotonic increasing (*Schleinkofer et al. 1996b*, *Kindermann et al. 1999*, *Sarin et al. 1975*, *Roebuck et al. 1988*) and cyclic loading (*Schleinkofer et al. 1996b*, *Kindermann et al. 1999*, *Miyake et al. 1968*, *Otsuka et al. 1989*) revealed that the phase transformation of Co is a stress and/or strain controlled process (*Almond et al. 1980*). In addition, influences on mechanical properties have been observed due to the Co-phase transformation (*Roebuck et al. 1988*, *Kursawe et al. 2001*, *Sarin et al. 1975*) leading to decreasing fatigue strength (*Roebuck et al. 1984*) and decreasing fracture toughness (*Schleinkofer et al. 1996b*) and increasing magnetic coercivity (*Beste et al. 2001*). Experiments under cyclic loading conditions at room temperature revealed that phase transformation is also an important damage mechanism (*Schleinkofer et al. 1996b*, *Sarin et al. 1975*, *Otsuka et al. 1989*), and that the amount of hcp Co-phase is directly proportional to the number of load cycles (*Miyake et al. 1968*). The hcp crystal structure has a lower ductility compared to the fcc crystal structure thus ductility of the Co-phase decrease with increasing number of load cycles. The lower ductility is associated with a reduction of possible slip systems from twelve for fcc to three for the hcp crystal structure (*Jackson 1991*). A slip system change due to crystal structure change causes a reduction in plastic strain up to the fracture of the Co-phase. The phase transformation was detected during cyclic loading at room temperature (*Kindermann et al. 1999*) as well as during creep tests above  $800\ ^\circ\text{C}$



based on microstructure studies (*Mingard et al. 2021, Yousfi et al. 2015*). However, the role of the fcc to hcp Co-phase transformation at elevated temperatures is unclear.

As mentioned above, volume expansion occurs in pure Co due to the crystal structure transformation from hcp to fcc. A volume change has also been observed in WC-Co hardmetals, although different opinions exist in literature in terms of a volume increase or decrease (*Roebuck et al. 1984, Vasel et al. 1985, Kindermann et al. 1999*). As mentioned above, additional elements are present in the Co-phase, which have to be rearranged during phase transformation affecting the unit cell volume per atom (*Roebuck et al. 1984*).

Phase transformation of Co from fcc to hcp crystal structure has been studied in various research works in cyclic and creep tests revealing an influence on the mechanical properties of hardmetals (*Roebuck et al. 1988, Kursawe et al. 2001, Sarin et al. 1975*). However, no investigations focused on phase transformations in Co prior to the failure of the WC-Co hardmetal specimens and its influence on the damage evolution.

Therefore, the current thesis investigates into the change in phase transformation in Publication II for step-loading creep tests as well as in Publication IV and Publication V for cyclic loading at stress ratios of  $R = -\infty$  and  $R = -1$  at different stages of deformation before specimen failure and critical crack growth.

## 2.2. Creep Behaviour

The following section covers the basics of creep of WC-Co hardmetals and relevant topics. The description of the behaviour in WC-Co hardmetals during creep is essentially based on Publication I, Publication II and Publication III, which are included at the end of the current thesis. The thesis deals with uniaxial compression and tension step-loading creep tests at 700 °C and 800 °C. Therefore, the state of the art for creep investigations of WC-Co hardmetals below 1000 °C and for uniaxial loading conditions is highlighted in more detail in the current section.

Applications of hardmetals, as chipping of various materials, include stresses above 1000 MPa and temperatures between 600 °C and 1000 °C (*Nemetz et al. 2019, 2020, Kagnaya et al. 2011, Schedler 1988*). At room temperature, WC-Co hardmetals exhibit high strength and ductility. However, at increased temperatures, the strength decreases and thermally activated processes have to be considered, which cause time dependent effects. Hence, an engineering based understanding of the creep properties of WC-Co hardmetals is necessary next to an understanding of time-independent properties.

Literature defines creep as time-dependent plastic deformation at constant stress and temperature (*Roesler et al. 2007*). Usually the temperature influence on creep is expressed as ratio of applied temperature  $T$  to melting temperature  $T_m$ , which is used to calculate the temperature where creep processes are expected to be active. For metals, it is well known that creep processes are active at temperatures above 30% to 50% of absolute  $T_m$  (*Bürgel et al. 2011*). In case of ceramics and two-phase composites, they are activated at temperatures greater than or equal to 50% of absolute  $T_m$  (*Bürgel et al. 2011, Sherby et al. 1968*). According to section "Fracture Mechanisms", creep-loaded specimens exhibit subcritical crack growth and deformation is mainly carried by the Co-phase. Hence, the point at which creep processes are active in WC-Co hardmetals is estimated based on the  $T_m$  of the Co-phase. However, the Co-phase contains additional elements, primarily tungsten and carbon atoms. Hence, the  $T_m$  is used from the composition of W-C-Co with  $T_m = 1280$  °C (1553.1 K) (*Schedler 1988*). The critical temperature, above which creep processes must be considered in WC-Co hardmetals, is 500 °C (773.15 K), corresponding to a  $T/T_m$  ratio of about 0.5.

In literature, creep has been studied in WC-Co hardmetals starting at 500 °C up to over 1000 °C. Investigations were performed under bending (*Lay et al. 1987, Schmid et al. 1988, Lay et al. 1984, Han et al. 2009, Östberg et al. 2006a, Buchegger et al. 2013, Ueda et al. 1977*), uniaxial compression (*Smith et al. 1968, Useldinger et al. 2017, Roebuck et al. 1982, Sakuma et al. 1992, Yousfi et al. 2015, Lay et al. 1987*) and tensile loading (*Ueda et al. 1975, Mingard et al. 2021, Doi et al. 1984, Wirmark et al. 1986, Lee et al. 1997, Roebuck et al. 2015*) as well as indentation (*Zunega 2013, Roebuck et al. 1988, 1982*). Tests were mostly performed as standard creep tests, where the specimens are loaded under constant stress and temperature for a period of time.

To consider the effect of load or temperature variations during creep experiments, tests with gradually increasing loads, cyclic mechanical loading or temperature gradients were performed for metallic and ceramic materials (*Dowling 2012, Giannopoulos et al. 2011, Miller 2000, Goti et al. 2012, Kim et al. 2017, Mingard et al. 2021, Roebuck et al. 2015*). To observe the creep behaviour of WC-Co hardmetals, step-loading creep tests, which are performed by incrementally increasing the mechanical stress and holding it constant for a specified time at each stress step, were used (*Mingard et al. 2021, Roebuck et al. 2015*). Individual stress steps from creep experiments are similarly examined in standard creep tests. A detailed description of creep test with stepwise loading is presented in Publication I. This test procedure is used to investigate the creep behaviour of WC-Co hardmetals in Publication II and Publication III. Step-loading creep tests allow to analyse the creep behaviour of materials under different applied stresses in a time-efficient single measurement.

Standard creep tests measure length changes of the specimen over time at constant stress and temperature. Recorded creep curves can be classified into three regions, as shown in Figure 6(a.). The first region corresponds to primary creep, where the creep rate  $\dot{\epsilon}$  decreases continuously, see region I in Figure 6(b.). During primary creep, the predominant mechanism is assumed to be the generation of numerous dislocations that cannot be degraded by recovery processes. Due to increasing dislocation density, the dislocation movements are hindered, which leads to material hardening. Hence, the  $\dot{\epsilon}$  decrease during primary creep are caused by strain hardening effects due to the setup of a stationary dislocation structure (*Bürgel et al. 2011*). The second region is called secondary creep, where the  $\dot{\epsilon}$  stabilizes with increasing test time and remains constant, see region II in Figure 6(b.). Dislocation density and strain hardening of the

material increase to a maximum until an equilibrium is reached between externally applied load and internal stresses due to dislocations. The dislocation density reaches a dynamic equilibrium and stays constant over time. With increasing strain, pores and cracks form in the material (Granacher 1991).  $\dot{\epsilon}_S$  is determined by the region of constant slope (secondary creep stage), see Figure 6(a.), and is used to determine further creep parameters: stress exponent  $n$  and activation energy  $Q$ . Also,  $\dot{\epsilon}_S$  is a measure of the materials creep strength (Kassner 2015). The  $\dot{\epsilon}_S$  and the creep strength are inverse proportional to each other. The last region in the creep curve is called tertiary creep. In this region, the strain and  $\dot{\epsilon}$  increase again, which is attributed to microcrack formation starting from pores and cavities, weakening structural integrity of the material (Bürigel et al. 2011). Due to crack formation and increasing crack growth, the creep test ends with fracture of the specimen, see the cross in region III in Figure 6(a.) and Figure 6(b.) (Kassner 2015). The creep curve shape at one temperature and stress value depends on the test parameters: temperature, stress and material. To investigate time-dependent processes, using creep tests for one temperature, one stress level and one material, hours to years are often required as testing time.

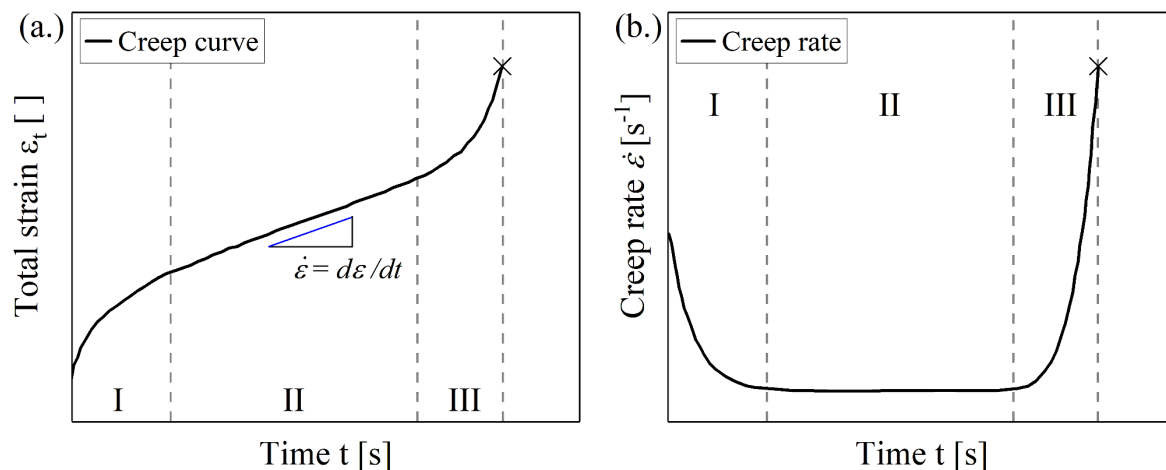


Figure 6: (a.) Creep curve defined as plot of the total strain  $\epsilon_t$  over time  $t$  with three stages of creep for constant temperature and stress condition: I.) primary creep, II.) secondary or steady-state creep, and III.) tertiary creep. The linear slope of the creep curve defines the secondary creep rate  $\dot{\epsilon}_S = d\epsilon/dt$  at the stage of secondary creep. With increasing time and within the tertiary creep stage, strain increases rapidly followed by specimen failure, marked with a cross. (b.) Displaying the creep rate  $\dot{\epsilon}$  as a function of time  $t$  with the three stages of creep. Source: Own representation based on (Roesler et al. 2007).

Investigations of the mechanical behaviour below 1000 °C and uniaxial loading conditions for WC-Co hardmetals are limited in literature (*Smith et al. 1968, Ueda et al. 1975, Mingard et al. 2021, Doi et al. 1984, Roebuck et al. 2015, Useldinger et al. 2017, Wirmark et al. 1986*). Compression (*Smith et al. 1968, Useldinger et al. 2017*) and tension (*Ueda et al. 1975, Doi et al. 1984, Mingard et al. 2021*) creep tests were performed up to maximum 750 MPa. Comparing maximum creep stresses investigated in literature with occurring operating stresses, these from literature are far below operational stresses, for example, about 1000 MPa occur during milling (*Nemetz et al. 2019*). Further, WC-Co hardmetals of different compositions, hard phase to binder phase ratio, react differently to external loads, hence not all types of WC-Co hardmetals are suitable for certain practical applications (*Schmid 1987*). In literature, various WC-Co hardmetal grades have been investigated with respect to creep behaviour: grades with WC grain sizes from submicron to coarse (0.5 µm to 5.0 µm) with Co-contents up to 20 wt.% (*Smith et al. 1968, Roebuck et al. 1982, Useldinger et al. 2017, Ueda et al. 1975, Doi et al. 1984, Wirmark et al. 1986, Mingard et al. 2021*). Figure 7(a.) and Figure 7(b.) show WC-Co hardmetal grades for uniaxial compression and tensile creep tests up to 1000 °C from literature in comparison to investigated grades of the current thesis. Grades with 12 wt.% Co and WC grain sizes smaller than medium are still lacking in literature. Further ultrafine WC-Co hardmetal grades were hardly studied under creep. Thus, the current thesis investigates into the tension and compression creep behaviour of WC-12 wt.% Co hardmetals with an average WC grain size of 0.4 µm, 0.7 µm and 2.0 µm.

Creep deformation and mechanisms occurring for metals as well as for hardmetals are related to the steady-state (secondary) creep rate  $\dot{\epsilon}_S$ . The following Equation (1) is often used to describe the creep behaviour of different materials at steady-state  $\dot{\epsilon}_S$  (*Kassner 2015*):

$$\dot{\epsilon}_S = A \sigma^n e^{-Q/RT} \quad (1)$$

with the material constant  $A$ ,  $\sigma$  the applied stress, the stress exponent  $n$ ,  $Q$  the activation energy,  $R$  the gas constant and  $T$  the test temperature.

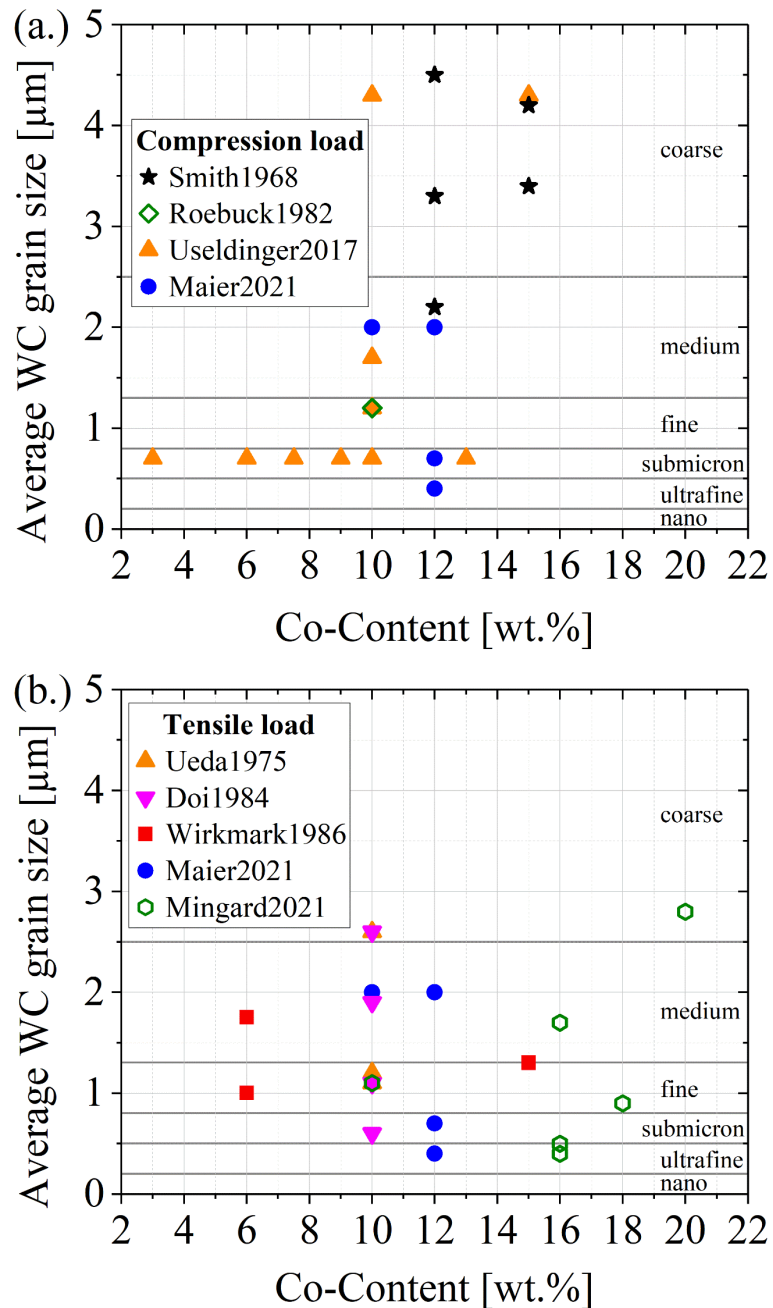


Figure 7: Investigated WC-Co hardmetal grades in literature under uniaxial (a.) compression- and (b.) tension creep tests between 600 °C and 1000 °C compared to investigated grades in Publication II and Publication III at 700 °C and 800 °C in the current thesis (blue - circle). Uniaxial compression creep tests were performed by Smith1968 (*Smith et al. 1968*) between 800 °C to 1000 °C, by Roebuck1982 (*Roebuck et al. 1982*) at 600 °C and by Useldinger2017 (*Useldinger et al. 2017*) between 800 °C to 950 °C. Uniaxial tensile creep tests were performed by Ueda1975 (*Ueda et al. 1975*) between 750 °C to 950 °C, by Doi1984 (*Doi et al. 1984*) between 750 °C to 900 °C, by Wirkmark1986 (*Wirkmark et al. 1986*) and by Mingard2021 (*Mingard et al. 2021*) between 800 °C to 900 °C.

Stress exponent  $n$  and activation energy  $Q$  are used to estimate which creep mechanism is dominant at which stress  $\sigma$  and temperature  $T$ . To determine  $n$  and  $Q$ ,  $\dot{\epsilon}$  is plotted over  $\sigma$  or  $1/T$  in double logarithmic manner. However, the dominant creep mechanism depends on the applied  $\sigma$ ,  $T$  and material composition (*Kassner 2015*).

Creep mechanisms of WC-Co hardmetals have been identified based on studies on hardmetal microstructure, creep rates, stress exponents and activation energy. The following presents the state of the art on understanding creep mechanisms of WC-Co hardmetals for maximum uniaxial compression and tension stresses up to 750 MPa (*Ueda et al. 1975, Doi et al. 1984, Wirmark et al. 1986, Smith et al. 1968*) between 750 °C to 1000 °C. Below 1000 °C, in the case of uniaxial creep tests, a distinction is made between low-stress creep (load stresses below 400 MPa) and high-stress creep (load stresses above 400 MPa) (*Ansell et al. 1959*).

At low-stress creep, a stress exponent value of  $n = 1$  has been observed, which has been associated with diffusion processes in the Co-phase around WC grains (*Ueda et al. 1975, Smith et al. 1968, Lay et al. 1987*). At low stresses only a low dislocation density develops, hence creep deformation due to dislocations can be neglected (*Bürgel et al. 2011*). Diffusion creep is based on vacancy migration where grain boundaries serve as sources and sinks for vacancies. Diffusion creep can be classified as Coble- and Nabarro-Herring creep. The former refers to diffusion of vacancies and atoms along grain boundaries, while Nabarro-Herring creep refers to lattice diffusion in the grain volume. Both depend on temperature and grain size of the material. At low temperatures, Coble-creep dominates in materials because lower activation energy is required for grain boundary diffusion. In contrast, at high temperatures Nabarro-Herring creep dominates (*Bürgel et al. 2011*).

$n$ -values from 2 to 6 were observed at high stress creep, which are associated with WC grain boundary sliding at  $n = 2-3$  and dislocation creep with looping as well as dislocations climbing around WC grains for  $n \geq 3$  (*Ueda et al. 1975, Smith et al. 1968, Useldinger et al. 2017, Doi et al. 1984, Wirmark et al. 1986, Lay et al. 1987, Bürgel et al. 2011*). Diffusion creep and grain boundary sliding depend on the WC grain size of the investigated WC-Co hardmetal grade. The coarser the grains, the lower the proportion of grain boundary creep.

WC grain size and Co-content have been noticed to influence the  $\dot{\epsilon}_S$  of WC-Co hardmetals (Lay et al. 1987, Lee 1995, Sakuma et al. 1992, Lay et al. 1984, Smith et al. 1968, Doi et al. 1984, Osterstock 1983, Wirmark et al. 1986). The  $\dot{\epsilon}_S$  directly relates to the amount of Co-content in WC-Co hardmetals (Smith et al. 1968, Osterstock 1983, Wirmark et al. 1986). The Co-phase creeps faster than the WC grains (Lay et al. 1984). As mentioned above, the material's grain size influences diffusion creep and grain boundary sliding. Hence, with decreasing WC grain size the amount of grain boundary areas per unit volume increases, which is favourable for diffusion processes at WC grain boundaries. However, the influence of the WC grain size on  $\dot{\epsilon}_S$  is related to applied temperature and applied stress (Smith et al. 1968, Lay et al. 1987, Roebuck et al. 1988, Doi et al. 1984, Useldinger et al. 2017, Wirmark et al. 1986).  $\dot{\epsilon}_S$  increases with increasing WC grain size up to 400 MPa and below 900 °C (Osterstock 1983, Wirmark et al. 1986, Doi et al. 1984, Ueda et al. 1975, Abe et al. 2008). Above 900 °C and stresses up to 400 MPa,  $\dot{\epsilon}_S$  increases with decreasing WC grain sizes (Osterstock 1983, Wirmark et al. 1986, Doi et al. 1984, Smith et al. 1968).

The creep mechanisms, as described above, were identified by standard creep tests for WC-Co hardmetal grades with different average WC grain size and varying Co-content at temperatures up to 1000 °C under compressive or tensile stresses up to 750 MPa. Different  $n$ -values were observed at different applied stresses, which indicates a change in the creep mechanism when varying the load stress. In literature, differences between tensile and compressive creep tests below 1000 °C are not discussed. Deviations between stress-strain creep behaviour in tension compared to compression loading of WC-Co hardmetals has only been investigated by Roebuck et al. (Roebuck et al. 2015) in alternating uniaxial tension and compression tests on WC-Co hardmetals at 1000 °C. An asymmetric behaviour was observed by Roebuck et al., where  $\dot{\epsilon}$  under tension was significantly higher than under compression for the same load. However, no microstructural studies were performed (Roebuck et al. 2015). Hence, responsible mechanisms for the strain asymmetry in the WC-Co hardmetal microstructure are not known. However, cavities are reported to form at WC/Co phase boundaries during tension and compression creep tests above 800 °C (Mingard et al. 2021, Ueda et al. 1975, Yousfi et al. 2015). Also, formation of Co-phase lamellae at WC/WC grain boundaries was observed (Yousfi et al. 2015). Further, strain asymmetry was noticed in ceramics and attributed to accelerated specimens failure under tension (Hoffmann et al. 1994, Morrell et al. 1973, Wiederhorn et al. 1991, 1988, Birch et al. 1978). For WC-Co hardmetals,



except at 1000 °C, no publications have been found that compare compression and tension creep. However, such investigations are necessary to understand the existence of varying  $n$ -values at different applied stresses below 1000 °C. Hence, Publication II of the current thesis investigates the tension-compression strain asymmetry at 700 °C and 800 °C for a WC-10 wt.% Co hardmetal grade. Temperatures of 700 °C and 800 °C were selected to mimic realistic temperatures during applications in milling operations. Besides compression and tension creep tests, Publication II, the microstructure at the onset of strain asymmetry was investigated using scanning electron microscope and electron backscatter diffraction.

As described above, creep behaviour of WC-Co hardmetal grades between 500 °C and elevated temperatures was investigated in literature, but only low stresses, far below the range of tool application, were considered. Also, only a few results from uniaxial tests above 750 MPa under compression or tension are available. Figure 7(a.) and Figure 7(b.) show investigations on WC-Co hardmetal grades with 12 wt.% Co and WC grain sizes smaller than medium are still lacking. Further ultrafine WC-Co hardmetal grades were hardly studied under creep. Thus, Publication III in the current thesis investigates into the creep behaviour of WC-12 wt.% Co hardmetals with an average WC grain size of 0.4  $\mu\text{m}$ , 0.7  $\mu\text{m}$  and 2.0  $\mu\text{m}$ . Tests were performed at 700 °C as well as 800 °C under uniaxial tension and compression step-loading creep tests in vacuum. Further, the ultrafine-grained WC-Co hardmetal grade microstructure was analysed under compression creep tests at 800 °C after defined stress levels with respect to creep mechanism and damage development prior to failure.

### 2.3. Cyclic Behaviour at Elevated Temperature

The following section deals with relevant topics on cyclic tests, hysteresis loops and damage indicators, which are necessary to understand the results of the current thesis. Description of fatigue, characteristics of cyclic stress-strain-hysteresis loops and damage indicators used for diagnose damage development is based on explanations in Publication IV and Publication V included in the current thesis.

New materials and faster processing push WC-Co hardmetal tools to their property limits. Hence, several research groups studied their mechanical properties (*Östberg et al. 2006a, Novikov et al. 2007, Teppernegg et al. 2016*), deformation mechanisms (*Buss 2004, Ueda et al. 1975, Han et al. 2009, Lay et al. 1987*), microstructure changes (*Ueda et al. 1977, Gottschall et al. 1980, Lay et al. 1987*) and performance characteristics (*Nemetz et al. 2018, Amin et al. 2007*) at elevated temperatures under various test conditions. Hence, material behaviour of WC-Co hardmetals and damage development via monotonically increasing or cyclic loading at room temperature has been extensively studied. At elevated temperature, cyclic tests were carried out via bending at  $R = -1$  up to 900 °C in air (*Kindermann et al. 1999*) and uniaxial loading under  $R = -\infty$  at 600 °C and 700 °C in vacuum (*Tritremmel et al. 2017*). Cyclic tests were carried out to investigate into fatigue material behaviour and fatigue material strength (*Gee et al. 2014, Roebuck et al. 1988, Schleinkofer et al. 1996a, Llanes et al. 2014, Klünsner et al. 2010b, Kindermann et al. 1999*).

Fatigue is defined as progressive and localized damage in materials which occurs during cyclic loading (*Bürgel et al. 2011*), these cracks originate and grow at small loads, which are below monotone failure loads. Fatigue behaviour of WC-Co hardmetals is evaluated by plotting the cyclic stress over the number of load cycles to failure, which is known as Wöhler curve. This characteristic is used to determine the fatigue material strength, which is the maximum stress a material withstands fatigue failure for a given number of load cycles.

However, no study analysed early stage of damage in WC-Co hardmetals, like nanopore or cavity formation, during cyclic loading. To evaluate early stages of damage under cyclic loading, parameters are required that allow to diagnose fatigue processes in materials. Following parameters are often mentioned for this purpose in literature: stiffness, hysteresis loop area, plastic strain amplitude or strain asymmetry over cyclic loading duration. These parameters are also referred to as damage indicators, for diagnose damage in materials at an early stage, as they are regarded as

driving forces for damage (Chowdhury *et al.* 2018, Orth *et al.* 1993, Tan *et al.* 2010, Lemaitre 1984). Therefore, technical terms and phenomenological considerations on the behaviour of material response under cyclic loading are presented in the following.

During cyclic tests, specimens are cyclically loaded: strain-controlled or stress-controlled. Closed cyclic stress-strain-hysteresis loops are recorded until specimen failure, see Figure 8, from which certain characteristic parameters can be measured, calculated and related to common material behaviour. Measured parameters are for example maximum and minimum applied test stress ( $\sigma_{\max}$  and  $\sigma_{\min}$ ) or strain ( $\varepsilon_{\max}$  and  $\varepsilon_{\min}$ ), while calculated characteristics are mean stress  $\sigma_m = (\sigma_{\max} + \sigma_{\min})/2$ , stress range  $\Delta\sigma = \sigma_{\max} - \sigma_{\min}$ , stress amplitude  $\sigma_a = \Delta\sigma/2$ , mean strain  $\varepsilon_m = (\varepsilon_{\max} + \varepsilon_{\min})/2$ , total strain range  $\Delta\varepsilon = \varepsilon_{\max} - \varepsilon_{\min}$ , strain amplitude  $\varepsilon_a = \Delta\varepsilon/2$  or Young's modulus  $E$ .

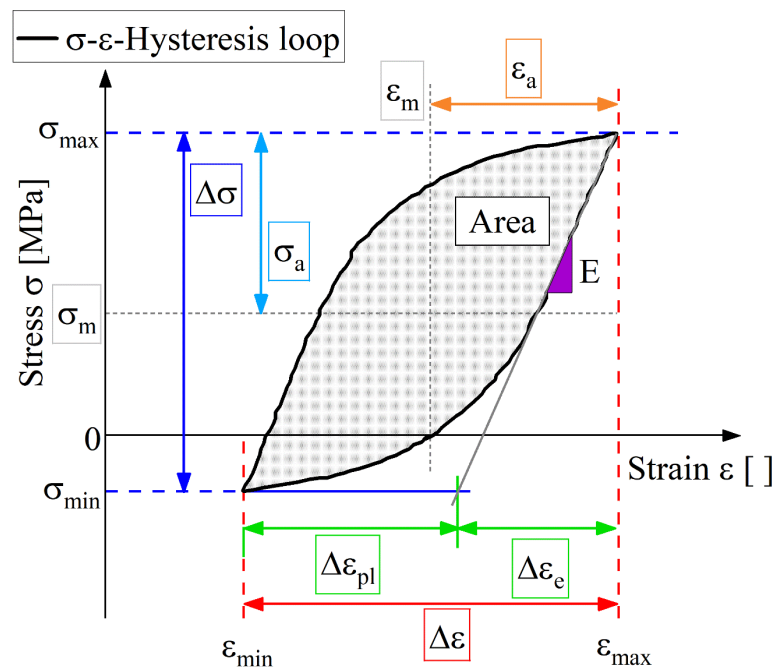


Figure 8: Closed cyclic stress-strain-hysteresis loop with certain parameters: maximum and minimum applied test stress ( $\sigma_{\max}$  and  $\sigma_{\min}$ ) or strain ( $\varepsilon_{\max}$  and  $\varepsilon_{\min}$ ), mean stress  $\sigma_m$  or mean strain  $\varepsilon_m$ , stress range  $\Delta\sigma$  or total strain range  $\Delta\varepsilon$ , stress amplitude  $\sigma_a$  or strain amplitude  $\varepsilon_a$  and Young's modulus  $E$ . Source: Own representation based on (Bürgel *et al.* 2011, Christ 1991).

By applying symmetric loading, a well-known material response is hardening or softening. Which one of the two effects is observed depends on the mechanical history of the material.

Materials that are annealed or soft prior to cyclic loading exhibit tendencies of hardening, which is caused by formation and accumulation of mobile dislocations, at immobile dislocations and large-angle grain boundaries. Higher stresses are required to further move dislocations and thus deform the material, due to hindered dislocation mobility, pinning effect. In contrast, massively pre-formed material tend to soften due to cyclic testing (*Merkel et al. 2008*).

Figure 9(a.) to Figure 9(f.) show the two different materials responses for stress-controlled and strain-controlled experiments based on the time histories of stress and strain, influence on the stress-strain-hysteresis loop and cyclic deformation curves. In case of a stress-controlled test and material softening (hardening), an increase (decrease) of the plastic strain amplitude  $\Delta\varepsilon_p$  (width of the hysteresis loop at  $\sigma = 0$ ) with increasing number of load cycles can be recognized. In strain-controlled tests, decreasing (increasing) elastic strains are a result of softening (hardening) processes causing a decrease (increase) in stress amplitude (*Fancher 1968, Reik et al. 1979, Schmiedt-Kalenborn 2020*).

In addition to changes in the plastic strain amplitude, also the hysteresis loop area changes, see Figure 9(b.) and Figure 9(e.). According to Fancher et al. and Kliman et al., the area of the stress-strain-hysteresis loop is defined as: "*Specific damping energy is the amount of energy dissipated in a unit volume of material per cycle and is simply the area inside the stress-strain hysteresis loop (Fancher 1968)*" and "*A cyclically loaded material absorbs a certain amount of energy  $\Delta W$  in every cycle, which is usually characterized by a hysteresis loop area (Kliman et al. 1984)*". From a physical point of view, the energy dissipation occurs mainly by diffusion of point defects and the movement of dislocations (*Roesler et al. 2007*).

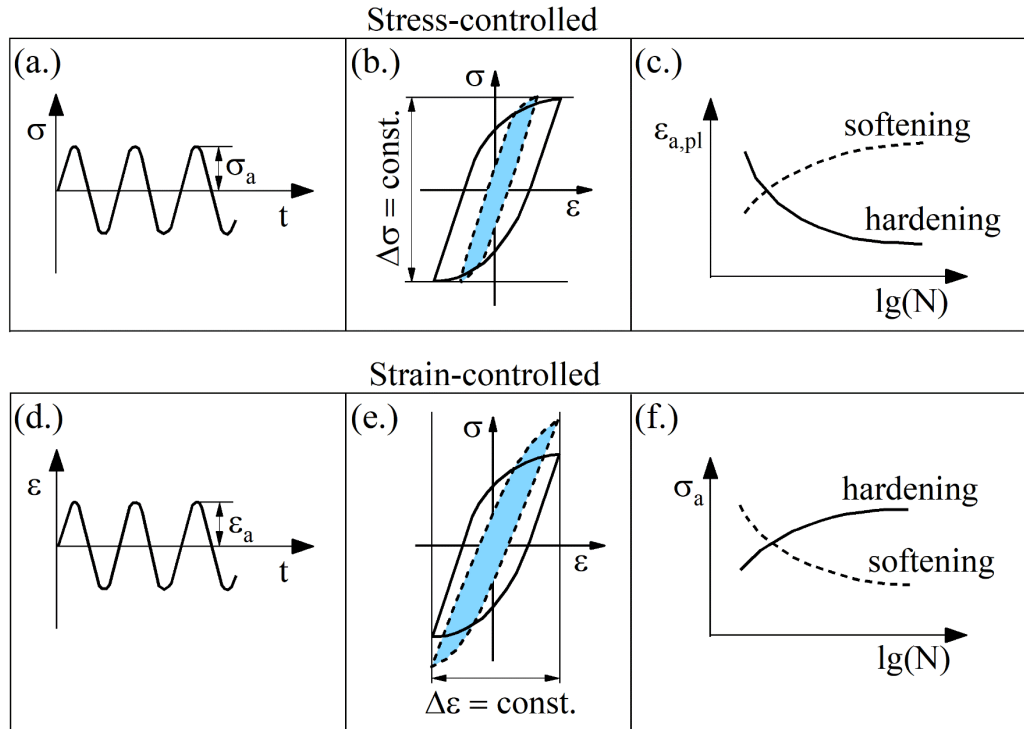


Figure 9: (a.) to (c.) is a stress-controlled and (d.) to (f.) strain-controlled experimental setup for cyclic testing. (a.) and (d.) represent the time evolution of strain and stress. (b.) and (e.) show the influence on the hysteresis loop in a stress-strain-diagram. Blue coloured hysteresis loop after higher number of cycles compared to the white coloured hysteresis loop indicates cyclic hardening. (c.) and (f.) summarize the changes of stress and strain amplitudes due to cyclic loading in case of material hardening and softening. Source: Own representation based on (Reik *et al.* 1979).

Another effect is cyclic creep, called ratcheting, by asymmetric cyclic loading under stress-controlled experimental conditions (Christ 1991, Bürgel *et al.* 2011). In this context, asymmetric means the experimental procedure is carried out with a mean stress greater than zero. Generally, cyclic creep is defined as gradual accumulation of inelastic strain, cycle by cycle, which is attributed to time-independent and time-dependent plasticity mechanisms during the loading and unloading process (Chaboche *et al.* 1989, Lin *et al.* 1969). When cyclic creep occurs under cyclic loading, the hysteresis loops between the stress limits shift along the strain axis with increasing number of load cycles. Hence, the strain increases without stabilization at a certain strain value (Weiß *et al.* 2004). Figure 10 shows cyclic creep, based on the time histories of strain and stress, and the influence on the stress-strain-hysteresis loop. In literature, the occurrence of cyclic creep is considered to be a significant factor in material failure (Chaboche 2008, Kang *et al.* 2006), which is associated with pores and cavities formation (Rider *et al.* 1995, Weiß *et al.* 2004).

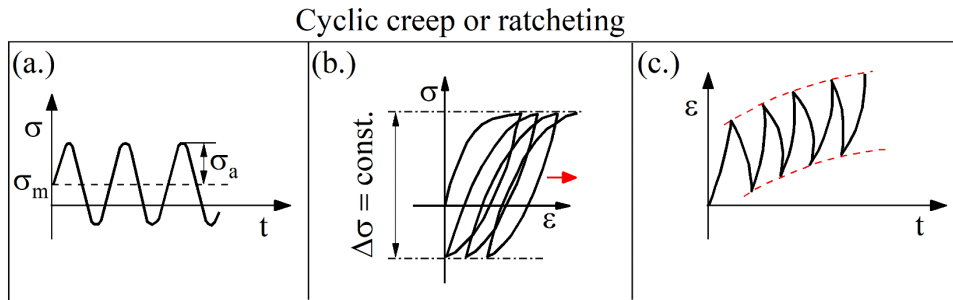


Figure 10: (a.) to (c.) stress-controlled experiment with mean stress greater than zero under cyclic testing and occurrence of cyclic creep. (a.) and (c.) represent the time evolution of stress  $\sigma$  and strain  $\varepsilon$  respectively. (b.) shows the influence on the hysteresis loop in a stress-strain-diagram. Source: Own representation based on (*Christ 1991*).

Another effect on strain with increasing number of load cycles during cyclic loading is the tension-compression-strain asymmetry, as mentioned in the section “Creep Behaviour”. With increasing number of load cycles, higher strains are reached faster under tension than under compression within one load cycle. Due to the fast increase of tensile strain, a stress-strain-hysteresis loop tilting occurs under tensile loading, see Figure 11, which is linked to a Young's modulus  $E$  change with increasing number of load cycles (*Lemaitre et al. 2005*). Thereby, the decreasing in stiffness with increasing number of load cycles is caused by microdefects, such as pores and cavities. Further, strain asymmetries are attributed to accelerated microdefect formation under tension compared to compression, as reported for ceramic materials in (*Hoffmann et al. 1994, Morrell et al. 1973, Wiederhorn et al. 1991, 1988, Birch et al. 1978*).

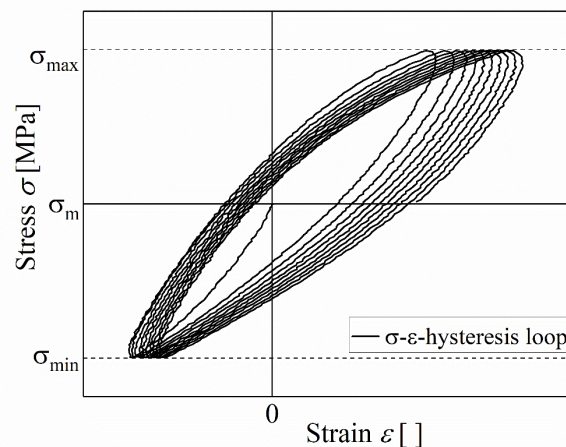


Figure 11: Tension-compression strain asymmetry evolution within 10 load cycles under stress-controlled cyclic loading with mean stress  $\sigma_m = 0$  MPa and test temperature at 800 °C. Source: Stress-strain hysteresis curve originates from own results.

In literature, the aim of the cyclic loading tests and the understanding of fatigue in WC-Co hardmetals was on the one hand to improve the performance of components and on the other hand to predict their lifetime. However, less cyclic tests at elevated temperature under uniaxial conditions have been performed in literature to analyse the cyclic stress-strain behaviour of hardmetals. The stress-strain response for one hardmetal grade for only three load cycles at  $R = -1$  at 1100 °C were investigated in (Roebuck *et al.* 2015). During the three load cycles a small maximum stress of 110 MPa was applied. Additionally, at 600 °C and 700 °C, stress-strain hysteresis was investigated for one WC-Co hardmetal grade up to 5000 load cycles at  $R = -\infty$  up to high applied stress ranges of 2900 MPa and 3500 MPa (Tritremmel *et al.* 2017). Cyclic stress-strain hysteresis loop changes over testing time are only reported in (Klünsner *et al.* 2010b, Tritremmel *et al.* 2017). Both research works performed cyclic tests at  $R = -\infty$ , but at different temperatures. Investigations at room temperature were performed in (Klünsner *et al.* 2010b) and at elevated temperatures in vacuum in (Tritremmel *et al.* 2017). Based on cyclic stress-strain hysteresis loops, strain ratcheting was observed and additionally, in (Tritremmel *et al.* 2017), the damage behaviour after cyclic tests was examined.

Besides various studies on fatigue strength, only a few studies on cyclic stress-strain hysteresis loop changes, such as strain ratcheting, are available in literature for WC-Co hardmetals. In addition, there are no data available on limit stresses beyond which changes in the characteristic features of the stress-strain hysteresis loop occur, such as loop area, amplitude of plastic strain, or strain asymmetry. Further, no investigations were performed on damage development under cyclic loading, including creep at elevated temperature. Hence, Publication IV and Publication V of the current thesis focus on damage development before specimen failure under cyclic loading for two stress ratios at  $R = -\infty$  and  $-1$  at 700 °C and 800 °C. To diagnose damage development before specimen failure, the damage development which may lead to failure of the component was associated with different measurement data, as loop area or plastic strain amplitude.





### **3. Aims and Main Tasks of the Thesis**

The aim of the thesis was to experimentally investigate the mechanical response and damage behaviour of six WC-Co hardmetal grades during subcritical crack growth before specimen failure. Tests were performed under uniaxial cyclic loading conditions at  $R = -\infty$  and  $R = -1$  and at 700 °C as well as at 800 °C in vacuum. Additionally, step-loading creep tests were used to test the WC-Co hardmetal specimens at the same temperatures in vacuum. Special attention was paid to application-relevant loading and temperature conditions occurring at the cutting edge of milling inserts for steel and titanium work pieces. The thesis is composed of five own publications. Goals, challenges, methodological approaches and results for each publication are explained in more detail below.

#### **Publication I - Uniaxial step-loading test setup for determination of creep curves of oxidation-sensitive high strength materials in vacuum under tensile and compressive load**

Publication I focused on a test setup for high strength materials to apply monotonic increasing or cyclic loads as well as to perform uniaxial step-loading creep tests at elevated temperatures. Special attention was paid to uniaxial tension and compression step-loading creep tests for one WC-Co hardmetal grade, which were performed using a specific specimen geometry.

A detailed understanding of the creep behaviour under high load and elevated temperature is required for evaluating materials in case of long-term applications. Different test types are used in literature to perform creep experiments: bending, tension, compression or indentation at constant stress and temperature conditions. However, WC-Co hardmetal tools are repeatedly loaded and unloaded as well as exposed to load and temperature fluctuations during applications. Additionally, special test setups are required for high-temperature testing due to the high oxidation tendency of WC-Co hardmetals in ambient atmospheres and high strength.

Uniaxial tension and compression step-loading creep tests were performed via a servo-hydraulic testing machine under isothermal conditions at 700 °C in vacuum for a WC-12 wt.% Co hardmetal grade with an average WC grain size of 0.7 µm. Induced eddy currents and thermocouples were used for heating and temperature control within the specimen gauge length. Compared to conventional creep tests, mechanical stress is increased stepwise and the stress is kept

constant for 500 s at each stress step. Strain gauge length was contactless measured with a laser extensometer.

A specific geometry with a non-constant specimen diameter was used to avoid buckling under compression. Hence, the specimen cross-section changes over the test range, the experimentally determined strain values were corrected using finite element simulations. Under tensile and compressive loading, creep rates were determined at each stress level. Creep rate minima were observed under tension above a stress of 500 MPa and under compression above -700 MPa, which were interpreted as secondary creep rate. Step-loading creep tests allow to investigate creep behaviour of high-strength materials in a time-efficient single measurement.

### **Publication II - A physical reason for asymmetric creep deformation behaviour of WC-Co hardmetal under tension and compression loading at 700 °C and 800 °C**

Aim of Publication II was the experimental determination of strain asymmetry in uniaxial step-loading creep test according to Publication I, which leads to different stress-strain response of WC-Co hardmetal grades under tension and compression loading at elevated temperature. At stresses above the limit stress, tensile strain values were observed to be higher than compressive strain values with increasing stress, resulting in a tension-compression strain asymmetry. Special attention was paid to microstructural changes just prior and above the onset of the strain asymmetry and the associated physical reasons for the strain asymmetry at the microstructural scale.

WC-Co hardmetals are used as tool material for chipping different kinds of materials, whereby high temperatures occur during the machining process. A few studies available in literature have investigated strain asymmetry at temperatures below 1000 °C for WC-Co hardmetals under uniaxial loads. Unfortunately, they did not consider the microstructural changes that are believed to be the cause of strain asymmetry in the WC-Co hardmetals.

Hence, Publication II focused on investigating the strain asymmetry of a WC-10 wt.% Co hardmetal grade with an average WC grain size of 2.0 µm after tension and compression uniaxial step-loading creep tests at 700 °C and 800 °C. Two test series were performed, where specimens were loaded to defined strain limits for both investigated temperatures and specimens were loaded in steps up to 300 MPa under tension and compression at 800 °C, respectively. To investigate the physical reasons of the strain asymmetry, the specimen microstructure for the latter test series was analysed by scanning electron microscopy (SEM) and electron backscatter diffraction (EBSD).

Strain asymmetry for tensile and compressive stresses was observed when exceeding a limit stress of 600 MPa at 700 °C and above 250 MPa at 800 °C. From microstructural analyses it can be concluded, that the physical reason for strain asymmetry was a larger number of cavities formed at WC/WC interfaces and at WC/Co phase boundaries under tension than under compression. Additionally, step-loading creep tests revealed that parts of the fcc Co-phase have transformed into hcp Co-phase. Next to phase transformation of the Co-phase, plastic straining were observed to be mainly carried by the Co-phase. However, no indications for plastic strains or changes in the crystal orientation of the WC phase were observed.

### **Publication III - Creep behaviour of WC 12 wt.% Co hardmetals with different WC grain sizes tested in uniaxial tensile and compression step-loading tests at 700 °C and 800 °C**

In Publication III, the creep mechanisms and creep resistance under tension and compression were experimentally investigated by performing uniaxial step-loading creep tests, according to Publication I for three different WC-12 wt.% Co hardmetal grades at 700 °C and 800 °C. For all investigated hardmetal grades a time-dependent creep behaviour with stationary secondary creep was observed for stresses above  $\approx 150$  MPa at both temperatures. Special attention was paid to the WC grain size influence on creep resistance with increasing temperature and the damage evolution with increasing stress levels. Creep strength of WC-Co hardmetal grades strongly depends on the WC grain size, as mechanism changes were noticed at low stresses with increasing temperature.

Depending on the WC grain size and the Co-content and due to differences in the chemical composition and microstructure of hardmetals, different material properties such as strength or creep resistance are observed. Creep studies under uniaxial conditions and temperatures below 1000 °C, have been performed on grades with WC grain sizes ranging from 0.5  $\mu\text{m}$  to 4.5  $\mu\text{m}$  with Co-contents ranging from 3 wt.% to 20 wt.%. However, there are only sparse concerning creep behaviour of WC-Co hardmetals under 900 °C and uniaxial loading conditions above 750 MPa. Literature also lacks on results at grades with 12 wt.% Co and an average WC grain size smaller than 2.5  $\mu\text{m}$ .

Hence, in Publication III uniaxial tension and compression step-loading creep tests were performed for three WC-12 wt.% Co hardmetal grades with an average WC grain size of 0.4  $\mu\text{m}$ , 0.7  $\mu\text{m}$ , and 2.0  $\mu\text{m}$  at 700 °C and 800 °C in vacuum. Further, the ultrafine-grained

WC-12 wt.% Co hardmetal was investigated under compression at 800 °C up to different maximum stress levels of -350 MPa, -950 MPa and -1350 MPa using three single specimens in order to investigate the microstructure changes in detail.

During creep tests at 700 °C and 800 °C, two stress exponent intervals were observed, where a value of  $\approx 1$  was determined at low stresses and values between 4 and 6 above a critical stress level. A stress exponent of 1 was associated with diffusion processes in the Co-phase around WC grains and above 4 with dislocation creep in the Co-phase. At 700 °C and 800 °C, the medium-grained grade exhibit the highest creep rates  $\dot{\epsilon}_s$  compared to submicron- and ultrafine-grained grades. Additionally, a shift of the  $\dot{\epsilon}_s$  values to higher values was observed for the ultrafine-grained grade at low stresses at 800 °C, resulting that the submicron-grained grade has the highest creep resistance at 800 °C. The increase in  $\dot{\epsilon}_s$  of the ultrafine-grained grade was attributed to the large number of grain boundary area per unit volume compared to the submicron-grained grade, promoting vacancy diffusion at grain boundaries. Further, under tensile loading, all specimens creep faster than under compressive loading, since cavities are preferentially formed, as reported in Publication II. Microstructural analyses of the ultrafine-grained grade revealed that above the investigated stress levels of -950 MPa and -1350 MPa, damage occurs in the form of nanopores as well as cavities, and these are larger and numerous when loaded up to the latter level.

#### **Publication IV - Strain ratcheting limit stresses as a function of microstructure of WC-Co hardmetals under uniaxial cyclic loads under a stress ratio of $R = -\infty$ at elevated temperatures**

The goal of Publication IV was the experimental determination of limit stresses for different WC-Co hardmetal grades, above which advancing strain ratcheting is observed during uniaxial cyclic compression tests at 700 °C and 800 °C. Special attention was paid to microstructural changes which are connected with the onset of advancing ratcheting and on the resulting development of damage at the microstructure scale. At stresses below the limit stress, plastic strain per cycle decreases and plastic strain accumulation (strain ratcheting) stops after a characteristic number of load cycles. Above the limit stresses, advancing strain ratchetting was observed where strain stabilization does not occur and promotes the formation of cavities and nanopores at phase triple points, WC/WC grain boundaries and WC/Co interfaces.

To study mechanical properties of WC-Co hardmetals, monotonically increasing and cyclic loads at room temperature and elevated temperatures were carried out in literature. The fatigue behaviour of hardmetals was reported in literature for various stress ratios  $R = \sigma_{\min}/\sigma_{\max}$ . However, no detail results are available regarding the limit stresses above which strain ratcheting occurs under cyclic compressive loading at elevated temperature.

Hence Publication IV investigated the influence of increasing stresses, the WC grain size and the Co-content on the strain evolution. For this purpose, six WC-Co hardmetal grades were tested under uniaxial cyclic compression at a stress ratio of  $R = -\infty$  and varying stress ranges  $\Delta\sigma$  at 700 °C as well as 800 °C in vacuum. The investigated grades differ in their WC grain size (0.4  $\mu\text{m}$  to 2.0  $\mu\text{m}$ ) and Co-content (6 wt.% to 12 wt.%). SEM was used to investigate the microstructural changes of the WC-10 wt.% Co (WC size 2.0  $\mu\text{m}$ ) hardmetal grade and the response of the WC- and Co-phase by EBSD at loading stresses below and above the limit stresses for advancing ratcheting at 700 °C.

Strain stabilization was observed in low stress ranges, whereas advancing strain ratcheting, without strain stabilization, occurred with increasing number of loading cycles above a critical stress range  $\Delta\sigma_c$ . In this way, lower and upper cut-off values of limit stresses were determined for all investigated WC-Co hardmetal grades. At 700 °C, the highest limit stress,  $\Delta\sigma = 2500$  MPa, was reached for the grade with the lowest Co-content and submicron-sized WC grains. While at 800 °C the limit stress drops to about  $\Delta\sigma = 1000$  MPa for the three investigated submicron-grained hardmetals with Co-contents between 6 wt.% and 12 wt.%. Specimens with the lowest limit stress range at 700 °C and 800 °C are WC-Co hardmetal grade with highest Co-content and medium-grained WC grain size. Beside nanopores and cavity formation, Co-phase transformation from fcc to hcp was observed at stress ranges exceeding the limit stress range, but no plastic deformation occurs in WC grains.

Additionally, a continuously advancing strain ratcheting was observed for the ultrafine-grained WC-12 wt.% Co grade at smaller  $\Delta\sigma$  than for the submicron-grained grade at 800 °C. The smaller limit stress was attributed to a mechanism change due to the smaller WC grain size than in the submicron-grained grade. A mechanism change was also observed in Publication III for creep experiments for the same WC-Co hardmetal grades below 1000 MPa at 700 °C and 800 °C, see comparison between cyclic and creep tests in Figure 12(a.) to Figure 12(d.).

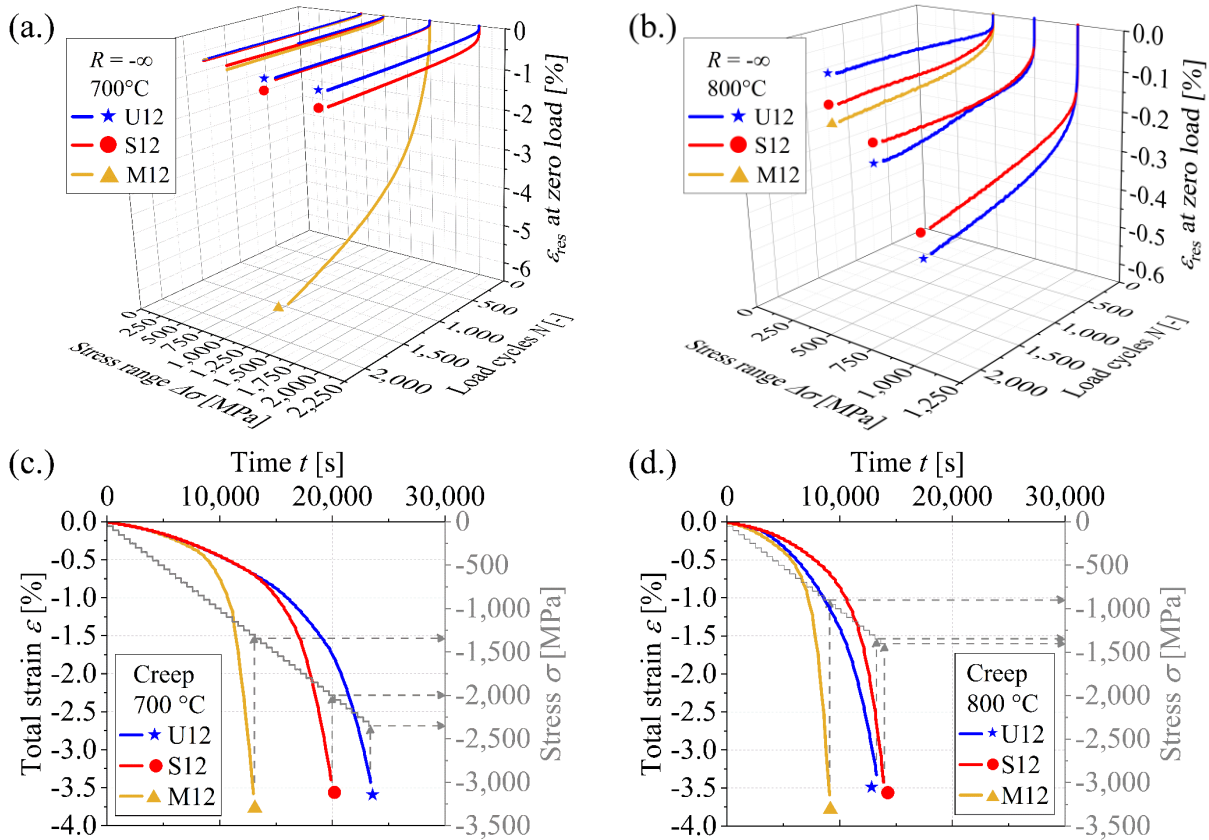


Figure 12: (a.) and (b.) Residual strain  $\epsilon_{res}$  at zero stress after loading with  $R = -\infty$  for three WC-Co hardmetal grades at 700 °C and 800 °C over load cycles  $N$ , respectively. The specimens were loaded at stress ranges  $\Delta\sigma = 750$  MPa, 1000 MPa, 1500 MPa and 2000 MPa at 700 °C and at  $\Delta\sigma = 500$  MPa, 750 MPa, 1000 MPa at 800 °C. (c.) and (d.) show compression step-loading creep curves at 700 °C and 800 °C of the same three WC-Co hardmetal grades as for the cyclic test, respectively. In addition to the step-loading creep curves in (c.) and (d.), the corresponding applied stress levels (grey lines) are shown; grey dotted arrows indicate the final stress level.

The letters in the material abbreviations refer to the average WC grain size: U = ultrafine (blue - star), S = submicron (red - circle) and M = medium (dark yellow - triangle), according to the ISO standard (ISO 4499-2 2008), and the numbers after the letters indicate the Co-content: 12 wt.%. Source: The images originates from own results. Similar representations of (a.) and (b.) are published in Publication III as Figure 3(a.) and Figure 3(b.). (c.) and (d.) are published in Publication IV as Figure 2(a.) and Figure 2(b.).

**Publication V - Damage indicators for early fatigue damage assessment in WC-Co hardmetals under uniaxial cyclic loads at a stress ratio of  $R = -1$  at elevated temperatures**

Publication V focused on experimental development of stress-strain-hysteresis loops for determining damage indicators for uniaxial symmetric cyclic tests, using the test setup described in Publication I. Special attention was paid to microstructural changes with increasing number of load cycles in correlation with stress-strain-hysteresis loop parameters and the resulting damage development at the microstructure scale. From observed results, the hysteresis loop area as well as the tension-compression-strain asymmetry increased with increasing stress amplitudes, temperature and number of load cycles. Further, the increase of both parameters with increasing number of load cycles could be related to the nanopore and cavity formation at WC/WC interfaces as well as at WC/Co phase boundaries. Hence, the hysteresis loop area and the strain asymmetry are reliable and meaningful damage indicators for bulk material damage.

A better understanding of the failure mechanisms of WC-Co hardmetals under chipping application conditions and the ability to diagnose damage development are key factors to understand the limits of endurable cyclic loads at a certain temperature. However, studies in literature are missing about examination of stress-strain hysteresis loops and damage indicators under cyclic loading at elevated temperature.

Publication V discusses the damage formation with increasing number of load cycles and the effect on stress-strain-hysteresis loops for two WC-10 wt.% Co hardmetal grades with an average WC grain size of 0.7  $\mu\text{m}$  and 2.0  $\mu\text{m}$ . For this purpose, specimens were loaded under uniaxial cyclic tests at  $R = -1$  at 700 °C and 800 °C in vacuum. The microstructure of the grade with an average WC grain size of 2.0  $\mu\text{m}$  was analysed by SEM and EBSD after cyclic testing up to defined numbers of load cycles at a stress amplitude of 1000 MPa at 800 °C in order to study damage evolution at microstructure level.

Based on stress-strain hysteresis loops, increasing loop areas and tension-compression-strain asymmetries with increasing number of load cycles were observed for specimens which failed during cyclic testing at 700 °C and 800 °C. Further, at 800 °C specimen failure occurred earlier than at 700 °C. Besides increasing in hysteresis-loop area and strain asymmetry, cyclic creep was also clearly observed at 800 °C. In addition to the correlation of microdefect formation with increasing hysteresis-loop area and strain asymmetry with increasing load cycles, EBSD data revealed that the fcc Co-phase transformed into hcp Co-phase under cyclic loading.





## 4. Summary and Conclusions

The focus of the present thesis is to provide a sound basis and methodological foundation for the knowledge-based design and optimization of WC-Co hardmetals for machining processes.

Cyclic and step-loading creep tests were used to establish a correlation between experimental data, limit stresses, damage indicators, and early damage formation. Table 1 lists the damage indicators determined and their relationship to the experimental data and material response during loading. Figure 13 shows the determined limit stresses, above which strain ratchetting occurs, at  $R = -\infty$  for both investigated temperatures 700 °C and 800 °C. These values are selected, because they are below the usual investigated temperature range in literature, but are typical for many WC-Co hardmetal application areas. Damage development at the microstructure scale during cyclic- and step-loading creep tests showed evidence of early damage at phase triple points, WC/WC grain boundaries and WC/Co interfaces. Based on defined limit stresses, limit stress maps of damage initiation in the bulk material were developed in order to optimize WC-Co hardmetal for chipping processes. Additionally, the similar material behaviour under creep and cyclic loading of the ultrafine WC-12 wt.% Co hardmetal grade between 700 °C and 800 °C was particularly noteworthy.

Table 1: Summary of observed damage indicators from cyclic as well as creep tests at 700 °C and 800 °C to diagnose damage development without microstructure analysis.

Damage indicator	Load condition	Effects	Material behaviour
<b>Tension-compression strain asymmetry</b>	Cyclic at $R = -1$ , Creep	Faster increase of strain and creep rate under tension than under compression	Reduction of stiffness under tension compared to compression due to microcracks and micro- or nanocavities.
<b>Stress-strain-hysteresis loop area</b>	Cyclic at $R = -1$	Plastic strain amplitude and loop area increase	Material hardening or softening due to cyclic plastic straining
<b>Strain ratcheting / Cyclic creep</b>	Cyclic at $R = -1$ and $R = -\infty$	Hysteresis loops shift between stress limits along mean stress	Continuous accumulation of ratcheting strain; crack initiation and propagation without stabilization at a certain strain value.

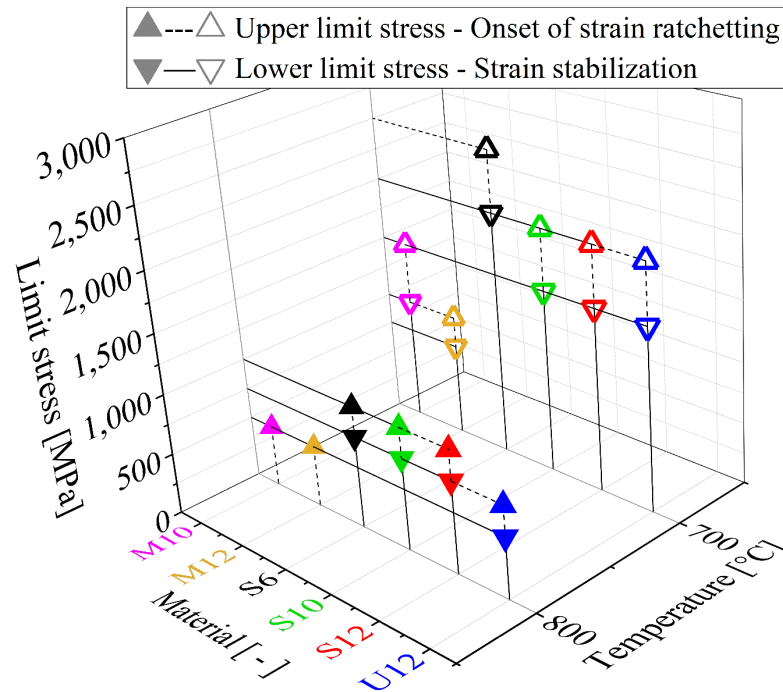


Figure 13: Determined limit stresses, above which strain ratchetting occurs, for six investigated WC-Co hardmetal grades studied at  $R = -\infty$  and 700 °C as well as 800 °C. The letters in the material abbreviations refer to the average WC grain size: U = ultrafine, S = submicron and M = medium, according to the ISO standard (*ISO 4499-2 2008*), and the numbers after the letters indicate the Co-content: 6 wt.%, 10 wt.% and 12 wt.%. The lower limit stress (triangle facing downwards) and upper limit stress (triangle facing upwards) for a certain loading situation are defined by the maximum and minimum stress range values at which strain stabilization or start of strain ratchetting were observed, respectively. However, it should be considered that the true limit stress ranges are close to experimentally determined limit stress ranges, since stress steps of 250 MPa below 1000 MPa and stress steps of 500 MPa above 1000 MPa were used. Source: This image originates from own results and is published in Publication IV as Figure 4(a.).

Highlights of the results from each publication are summarized briefly hereafter:

**Publication I** presented a uniaxial test setup for high strength materials, to perform step-loading creep, monotonic or cyclic loading tests under tension or compression at elevated temperatures and vacuum conditions. A hourglass shaped specimen geometry ensured that under compressive loading specimen buckling was avoided. The application of a non-constant specimen diameter resulted in local variation of the actual strain along the specimen length, so that simulations have to be performed to correct the measured strains. Additionally, special attention was paid to uniaxial tension and compression step-loading creep tests for WC-Co hardmetal grades

at 700 °C. Performing step-loading creep tests via the uniaxial test setup, creep behaviour for operation relevant conditions up to 3000 MPa can be investigated in a time-efficient single measurement. The test setup was used in up-following publications to study creep and cyclic behaviour of various WC-Co hardmetal grades.

In **Publication II**, uniaxial tension and compression step-loading creep tests were performed for WC-10 wt.% Co hardmetal grade with an average WC-grain size of 2.0 µm at 700 °C and 800 °C to experimentally determine strain asymmetry. The onset-stresses above which strain asymmetry occurs at a given temperature were determined. In addition, the stresses under compression were twice as high to achieve a similar value of creep rate as under tension at 800 °C, which was attributed to the faster formation of microdefects under tension.

Besides strain asymmetry studies, creep mechanism and creep strength studies were performed in **Publication III**. Investigations were performed under tension and compression step-loading creep tests for three WC-12 wt% Co hardmetal grades with WC grain sizes ranging from ultrafine to medium size at 700 °C and 800 °C. These investigations revealed stress exponents  $n$  of  $n \approx 1$  at low stresses and between  $n \approx 4$  and 6 above a critical stress level. Thereby, low  $n$ -values are associated with vacancy diffusion and high  $n$ -values with grain boundary sliding and dislocation creep. Also, the creep rate of WC-Co hardmetals with medium and submicron WC grain size was less affected by increasing temperature than of the ultrafine grade creep rate. Further, microstructure analysis of the ultrafine-grained grade showed that the number of microdefects and microdefect size increased at high stresses.

In **Publication IV**, cyclic tests were performed for six WC-Co hardmetal grades at a stress ratio of  $R = -\infty$  at 700 °C and 800 °C to experimentally investigate the limit stresses for advancing ratcheting. From microstructural analysis, it can be concluded that applied stresses above the limit stress for the onset of advanced strain ratcheting result into nanopores and cavities formation as well as Co-phase transformation from fcc to hcp crystal structure. Therefore, it was deduced that advancing strain ratchetting can be considered as an important indicator for the detection of early damage. Further, limit stresses for the onset of advanced strain ratcheting for all investigated WC-Co hardmetal grades decreased with increasing temperature. In connection with Publication III, also a mechanism change was assumed to occur depending on the WC grain size with increasing temperature for the ultrafine and submicron-grained WC-12 wt.% Co hardmetal grades.

In **Publication V**, the feasibility of using the evolution of stress-strain hysteresis loops as an indicator of damage evolution was investigated for two WC-Co hardmetals at a stress ratio of  $R = -1$  at 700 °C and 800 °C. Microstructural analysis revealed that increasing stress-strain-hysteresis loop areas and tension-compression-strain asymmetries correlate with the formation of nanopores and cavities in the Co-phase and between WC/WC grain boundaries as well as with the fcc to hcp Co-phase transformation. A strain asymmetry was also found in Publication II by step-loading creep tests, caused by faster microdefect formation under tension. The results suggest that the area of the stress-strain hysteresis loop and the tension-compression-strain asymmetry can be considered as important damage indicators. Further, ratcheting, also called cyclic creep, was observed with increasing temperature, which also contributed to damage formation, as reported in Publication IV.

## 5. Outlook

In the current thesis, the creep as well as the cyclic material behaviour of different WC-Co hardmetal grades were examined at 700 °C and 800 °C. However, not all six hardmetal grades were studied via creep, cyclic test or microstructural analysis. Hence, some research is still required to more accurately interpret the material behaviour of the missing grades under creep and cyclic loading.

Investigations at 700 °C and 800 °C showed that the ultrafine-grained WC-Co hardmetal grade exhibited a significant material behaviour change at 800 °C compared to 700 °C during creep, which was associated with vacancy diffusion due to the ultrafine WC grain size. Further investigations for the ultrafine-grained grade, as well as for other grades, would be cyclic tests at  $R = -1$  and  $R = -\infty$  to determine whether there is a different material behaviour compared to creep. Additionally, in-situ tests would be useful to investigate directly the processes taking place in the Co-binder and at WC/Co phase boundaries. To understand better the temperature influence on the material behaviour of WC-Co hardmetals, experiments at other temperatures, such as 600 °C, 750 °C or above 800 °C, would be interesting.

To verify the identified damage indicators and the microstructure influence, further cyclic tests at  $R = -1$  would be useful, including other WC-Co hardmetal grades with different average WC grain size and Co-content.

Based on the identified damage indicators, investigations regarding the residual strength of loaded and thus pre-damaged specimens compared to virgin specimens are also of interest, as the Co deformation behaviour has also been altered, e.g. by increasing the dislocation density, in addition to damage such as formation of nanopores and cavities between WC/Co phase boundaries. To this end, residual strength studies using in-situ micromechanical tensile tests would be useful.

In the WC-10 wt.% Co hardmetal grade with an average WC grain size of 2.0  $\mu\text{m}$ , in addition to the occurrence of damage at the microstructure level, an increase in hcp Co-phase at the expense of fcc Co-phase was also observed. Thus, further studies of hardmetal grades with a pure fcc Co crystal structure (and thus a more stable fcc crystal structure) before loading would be interesting to determine material behaviour and the differences of the damage behaviour. Since no consistent studies of Co phase transformation due to different loading conditions were performed

in the present work, it would be useful in the future to investigate dependencies of temperature, composition of WC-Co hardmetal grades or loading conditions on phase transformation. One way to investigate the temperature influence is for example in-situ high temperature testing, which provide direct insight into temperature-dependent microstructure changes of the Co-phase and influences by the surrounding WC grains during testing.

## 6. References

- (Abe et al. 2008) - F. Abe, T.-U. Kern, R. Viswanathan, *Creep-Resistant Steels* 2008.
- (Adjam et al. 2019) - S. Adjam, D. Mari, *A Link between Durability of WC-Co Coated Cutting Tools and Mechanical Damping Spectra*, Int. J. Refract. Met. Hard Mater., 85, (2019), p. 105068, <https://doi.org/10.1016/j.ijrmhm.2019.105068>.
- (Adjam et al. 2020) - S. Adjam, D. Mari, T. LaGrange, *Strain Glass Transition of Cobalt Phase in a Cemented Carbide*, Int. J. Refract. Met. Hard Mater., 87, (2020), p. 105161, <https://doi.org/10.1016/j.ijrmhm.2019.105161>.
- (Almond 1983) - E. A. Almond, “*Deformation Characteristics and Mechanical Properties of Hardmetals*,” in *Science of Hard Materials* 1983, pp. 517–561.
- (Almond et al. 1977) - E. A. Almond, B. Roebuck, *Defect-Initiated Fracture and the Bend Strength of WC-Co Hardmetals*, Met. Sci., 11, 10, (1977), pp. 458–461, <https://doi.org/10.1179/msc.1977.11.10.458>.
- (Almond et al. 1980) - E. A. Almond, B. Roebuck, *Fatigue-Crack Growth in WC-Co Hardmetals*, Met. Technol., 7, 1, (1980), pp. 83–85, <https://doi.org/10.1179/030716980803287080>.
- (AMETEK Inc. n.d.) - AMETEK Inc., *EDAX Smart Insight* (<https://www.edax.com/>, accessed le 20 September 2020).
- (Amin et al. 2007) - A. K.M.Nurul Amin, Ahmad F. Ismail, M. K. Nor Khairusshima, *Effectiveness of Uncoated WC-Co and PCD Inserts in End Milling of Titanium Alloy—Ti-6Al-4V*, J. Mater. Process. Technol., 192–193, (2007), pp. 147–158, <https://doi.org/10.1016/J.JMATPROTEC.2007.04.095>.
- (Ansell et al. 1959) - G.S. Ansell, J. Weertman, *Creep of a Dispersion-Hardened Aluminum Alloy*, Trans. Met. Soc. AIME, 215, (1959), pp. 838–843.
- (Bachmann et al. 2010) - F. Bachmann, Ralf Hielscher, Helmut Schaeben, “*Texture Analysis with MTEX- Free and Open Source Software Toolbox*,” in *Solid State Phenomena* 2010, vol. 160, pp. 63–68.
- (Beste et al. 2001) - Ulrik Beste, Hakan Engqvist, Staffan Jacobson, “*Pressure Cycling Induced Modification of a Cemented Carbide*,” in *15th International Plansee Seminar, Reutte/Austria, 2001*, pp. 685–697.
- (Birch et al. 1978) - J.M. Birch, B. Wilshires, D.J. Godfrey, *Deformation and Fracture*

*Processes during Creep of Reaction Bonded and Pressed Silicon Nitride*, Proc. Brit. Ceram. Soc., 26, (1978), pp. 141–154.

(Bose 2011) - Animesh Bose, *A Perspective on the Earliest Commercial PM Metal-Ceramic Composite: Cemented Tungsten Carbide*, Int. J. Powder Metall. (Princeton, New Jersey), 47, 2, (2011), pp. 31–50.

(Buchegger et al. 2013) - C. Buchegger, W. Lengauer, “*Creep Behaviour of Hardmetals with Alternative Binder Alloys at Elevated Temperatures*,” in *Proceedings of the 18th Plansee Seminar 2013*, Reutte; Austria, 2013, p. HM85.

(Bürgel et al. 2011) - Ralf Bürgel, Hans Jürgen Maier, Thomas Niendorf, *Handbuch Hochtemperatur- Werkstofftechnik 2011*.

(Buss 2004) - Katharina Buss, *High Temperature Deformation Mechanisms of Cemented Carbides and Cermets*, 3095, (2004), p. 156.

(Casas et al. 2001) - B. Casas, X. Ramis, M. Anglada, J. M. Salla, L. Llanes, “*Oxidation-Induced Strength Degradation of WC-Co Hardmetals*,” in *International Journal of Refractory Metals and Hard Materials 2001*, vol. 19, pp. 303–309.

(Cerazit Austria GmbH 2021) - Cerazit Austria GmbH, *CERATIZIT | Cutting Tool Solutions* (<https://www.cerazit.com/int/en/offerings/cutting-tool-solutions.html>, accessed 1e 4 August 2021).

(Chaboche 2008) - J. L. Chaboche, *A Review of Some Plasticity and Viscoplasticity Constitutive Theories*, Int. J. Plast., 24, 10, (2008), pp. 1642–1693, <https://doi.org/10.1016/j.ijplas.2008.03.009>.

(Chaboche et al. 1989) - J. L. Chaboche, D. Nouailhas, *A Unified Constitutive Model for Cyclic Viscoplasticity and Its Applications to Various Stainless Steels*, J. Eng. Mater. Technol. Trans. ASME, 111, 4, (1989), pp. 424–430, <https://doi.org/10.1115/1.3226490>.

(Chermant et al. 1976) - J. L. Chermant, F. Osterstock, *Fracture Toughness and Fracture of WC-Co Composites*, J. Mater. Sci., 11, 10, (1976), pp. 1939–1951, <https://doi.org/10.1007/BF00708272>.

(Chowdhury et al. 2018) - Md Mahmudur Chowdhury, Mohd Aminul Hoque, Nianjun Fu, Jeffrey C. Suhling, Sa’D Hamasha, Pradeep Lall, “*Characterization of Material Damage and Microstructural Evolution Occurring in Lead Free Solders Subjected to Cyclic Loading*,” in *Proceedings - Electronic Components and Technology Conference 2018*, vol. 2018-May,



pp. 865–874.

(Christ 1991) - Hans-Jürgen Christ, *Wechselverformung von Metallen: Zyklisches Spannungs-Dehnungs-Verhalten Und Mikrostruktur*, 1st ed.1991.

(Christensen et al. 2003) - Mikael Christensen, Göran Wahnström, *Co-Phase Penetration of (Formula Presented) Grain Boundaries from First Principles*, Phys. Rev. B - Condens. Matter Mater. Phys., 67, 11, (2003), p. 11, <https://doi.org/10.1103/PhysRevB.67.115415>.

(Csanádi et al. 2020) - Tamás Csanádi, Marek Vojtko, Ján Dusza, *Deformation and Fracture of WC Grains and Grain Boundaries in a WC-Co Hardmetal during Microcantilever Bending Tests*, Int. J. Refract. Met. Hard Mater., 87, (2020), p. 105163, <https://doi.org/10.1016/j.ijrmhm.2019.105163>.

(Danzer et al. 2008) - Robert Danzer, Tanja Lube, Peter Supancic, Rajiv Damani, *Fracture of Ceramics*, Adv. Eng. Mater., 10, 4, (2008), pp. 275–298, <https://doi.org/10.1002/adem.200700347>.

(Davis 2000) - Joseph R Davis, *Nickel, Cobalt, and Their Alloys 2000*.

(Deshmukh et al. 1982) - R. Deshmukh, J. Gurland, *Orientation of Contiguous Tungsten Carbide Crystals in Sintered WC-Co as Determined from Slip Line Traces*, Metallography, 15, 4, (1982), pp. 383–390, [https://doi.org/10.1016/0026-0800\(82\)90029-5](https://doi.org/10.1016/0026-0800(82)90029-5).

(Doi et al. 1984) - H Doi, F; Ueda, Y; Fujiwara, H Masatomi, *Influence of Carbide Grain Size on Elevated Temperature Tensile Creep of WC-10%Co Alloy*, Int. J. Refract. hard Met., 3, 3, (1984), pp. 146–148.

(Dowling 2012) - Norman E Dowling, *Mechanical Behavior of Materials: Engineering Methods for Deformation, Fracture, and Fatigue*, 4th ed., Boston, MA, 2012.

(Eizadjou et al. 2020) - Mehdi Eizadjou, Hansheng Chen, Christoph Czettel, Julia Pachthofer, Sophie Primig, Simon P. Ringer, *An Observation of the Binder Microstructure in WC-(Co+Ru) Cemented Carbides Using Transmission Kikuchi Diffraction*, Scr. Mater., 183, (2020), pp. 55–60, <https://doi.org/10.1016/j.scriptamat.2020.03.010>.

(Erling et al. 2000) - G. Erling, S. Kursawe, S. Luyckx, H. G. Sockel, *Stable and Unstable Fracture Surface Features in WC-Co*, J. Mater. Sci. Lett., 19, 5, (2000), pp. 437–438, <https://doi.org/10.1023/A:1006755208450>.

(Exner et al. 2001) - H. E. Exner, L. Sigl, M. Fripan, O. Pompe, “*Fractography of Critical and Subcritical Cracks in Hard Materials*,” in *International Journal of Refractory Metals and*

*Hard Materials* 2001, vol. 19, pp. 329–334.

(Exner 1983) - Hans Eckart Exner, “*Qualitative and Quantitative Interpretation of Microstructures in Cemented Carbides*,” in 1983, pp. 233–262.

(Fancher 1968) - Douglas Roscoe Fancher, *Stress-Strain Hysteresis Loops and Rheological Epicycles Item Type Text; Thesis-Reproduction (Electronic)*, soutenue à l'University of Arizona., 1968.

(Ferreira et al. 2009) - J. A.M. Ferreira, M. A.Pina Amaral, F. V. Antunes, J. D.M. Costa, *A Study on the Mechanical Behaviour of WC/Co Hardmetals*, Int. J. Refract. Met. Hard Mater., 27, 1, (2009), pp. 1–8, <https://doi.org/10.1016/j.ijrmhm.2008.01.013>.

(Fett et al. 1992) - Theo Fett, Dietrich Munz, *Subcritical Crack Growth of Macrocracks in Alumina with R-Curve Behavior*, J. Am. Ceram. Soc., 75, 4, (1992), pp. 958–963, <https://doi.org/10.1111/j.1151-2916.1992.tb04166.x>.

(Fischmeister et al. 1988) - H. F. Fischmeister, S. Schmauder, L. S. Sigl, *Finite Element Modelling of Crack Propagation in WC-Co Hard Metals*, Mater. Sci. Eng., 105–106, PART 2, (1988), pp. 305–311, [https://doi.org/10.1016/0025-5416\(88\)90711-2](https://doi.org/10.1016/0025-5416(88)90711-2).

(Fischmeister 1983) - H.F. Fischmeister, “*Conference Key Note Paper Development and Present Status of the Science and Technology of Hard Materials*,” in R. Viswanadham (ed.), *Science of Hard Materials* 1983, pp. 1–45.

(Fischmeister et al. 1989) - Hellmut F. Fischmeister, Hans Eckart Exner, Max-Hermann Poeh, Stephan Kohlhoff, Peter Gumbsch, Siegfried Schmauder, Lorenz S. Sigl, Roland Spiegler, *Modelling Fracture Processes in Metals and Composite Materials / Modellieren von Bruchvorgängen in Metallen Und Verbundwerkstoffen*, Int. J. Mater. Res., 80, 12, (1989), pp. 839–846, <https://doi.org/10.1515/ijmr-1989-801201>.

(Fry et al. 1988) - P. R. Fry, G. G. Garrett, *Fatigue Crack Growth Behaviour of Tungsten Carbide-Cobalt Hardmetals*, J. Mater. Sci., 23, 7, (1988), pp. 2325–2338, <https://doi.org/10.1007/BF01111884>.

(Gee et al. 2014) - Mark G. Gee, A. J. Gant, B. Roebuck, K. P. Mingard, “*Wear of Hardmetals*,” in *Comprehensive Hard Materials* 2014, vol. 1, pp. 363–383.

(Giannopoulos et al. 2011) - Ioannis P. Giannopoulos, Chris J. Burgoyne, *Prediction of the Long-Term Behaviour of High Modulus Fibres Using the Stepped Isostress Method (SSM)*, J. Mater. Sci., 46, 24, (2011), pp. 7660–7671, <https://doi.org/10.1007/s10853-011-5743-x>.

(Góez *et al.* 2012) - A. Góez, D. Coureaux, A. Ingebrand, B. Reig, E. Tarrés, A. Mestra, A. Mateo, E. Jiménez-Piqué, L. Llanes, *Contact Damage and Residual Strength in Hardmetals*, Int. J. Refract. Met. Hard Mater., 30, 1, (2012), pp. 121–127, <https://doi.org/10.1016/j.ijrmhm.2011.07.013>.

(González *et al.* 2020) - Luis M. González, Ernesto Chicardi, Francisco J. Gotor, Raul Bermejo, Luis L. Pitarch, Yadir Torres, *Influence of the Test Configuration and Temperature on the Mechanical Behaviour of WC-Co*, Metals (Basel), 10, 322, (2020), pp. 1–12, <https://doi.org/10.3390/met10030322>.

(Goti *et al.* 2012) - R. Goti, B. Viguier, F. Crabos, *Effect of Thermal Cycling on High Temperature Creep of Coated CMSX-4*, Superalloys 2012, (2012), pp. 411–419, <https://doi.org/10.1002/9781118516430.ch45>.

(Gottschall *et al.* 1980) - R. J. Gottschall, Wendell S. Williams, I. D. Ward, I. D. Ward, *Microstructural Study of Hot-Deformed Cemented Carbides*, Philos. Mag. A Phys. Condens. Matter, Struct. Defects Mech. Prop., 41, 1, (1980), pp. 1–7, <https://doi.org/10.1080/01418618008241826>.

(Granacher 1991) - J. Granacher, *Zur Übertragung von Hochtemperaturkennwerten Auf Bauteile*, VDI-Berichte Nr. 852., (1991), pp. 325–352.

(Gurland 1988) - J. Gurland, *New Scientific Approaches to Development of Tool Materials*, Int. Mater. Rev., 33, 1, (1988), pp. 151–166, <https://doi.org/10.1179/imr.1988.33.1.151>.

(Han *et al.* 2009) - X. Han, N. Sacks, Y. V. Milman, S. Luyckx, *On Plastic Deformation Mechanisms of WC-15 Wt% Co Alloys at 1000 °C*, Int. J. Refract. Met. Hard Mater., 27, 2, (2009), pp. 274–281, <https://doi.org/10.1016/j.ijrmhm.2008.09.021>.

(Henjered *et al.* 1986) - A. Henjered, M. Hellsing, H. D. Andrén, H. Nordén, *Quantitative Microanalysis of Carbide/Carbide Interfaces in WC-Co-Base Cemented Carbides*, Mater. Sci. Technol. (United Kingdom), 2, 8, (1986), pp. 847–855, <https://doi.org/10.1179/mst.1986.2.8.847>.

(Hoffmann *et al.* 1994) - M. J. Hoffmann, G. Petzow, *Tailoring of Mechanical Properties of Si<sub>3</sub>N<sub>4</sub> Ceramics*, 1st ed. 1994.

(Hong *et al.* 1983) - Joonpyo Hong, Joseph Gurland, “A Study of the Fracture Process of WC-Co Alloys,” in *Science of Hard Materials 1983*, pp. 649–669.

(ISO 4499-2 2008) - ISO 4499-2, *ISO 4499-2:2008 Hardmetals-Metallographic Determination of Microstructure-Part 2: Measurement of WC Grain Size*, (2008).

(Jackson 1991) - A.G. Jackson, "Slip Systems," in *Handbook of Crystallography* 1991, pp. 83–88.

(Jia et al. 1998) - K. Jia, T. E. Fischer, B. Gallois, *Microstructure, Hardness and Toughness of Nanostructured and Conventional WC-Co Composites*, *Nanostructured Mater.*, 10, 5, (1998), pp. 875–891, [https://doi.org/10.1016/S0965-9773\(98\)00123-8](https://doi.org/10.1016/S0965-9773(98)00123-8).

(Johannesson et al. 1988) - Bengt Johannesson, Richard Warren, *Subcritical Crack Growth and Plastic Deformation in the Fracture of Hard Metals*, *Mater. Sci. Eng.*, 105–106, PART 2, (1988), pp. 353–361, [https://doi.org/10.1016/0025-5416\(88\)90717-3](https://doi.org/10.1016/0025-5416(88)90717-3).

(Jonke et al. 2017) - M. Jonke, T. Klünsner, P. Supancic, W. Harrer, J. Glätzle, R. Barbist, R. Ebner, *Strength of WC-Co Hard Metals as a Function of the Effectively Loaded Volume*, *Int. J. Refract. Met. Hard Mater.*, 64, (2017), pp. 219–224, <https://doi.org/10.1016/j.ijrmhm.2016.11.003>.

(Kagnaya et al. 2009) - T. Kagnaya, C. Boher, L. Lambert, M. Lazard, T. Cutard, *Wear Mechanisms of WC-Co Cutting Tools from High-Speed Tribological Tests*, *Wear*, 267, 5–8, (2009), pp. 890–897, <https://doi.org/10.1016/j.wear.2008.12.035>.

(Kagnaya et al. 2011) - T. Kagnaya, M. Lazard, L. Lambert, C. Boher, T. Cutard, *Temperature Evolution in a WC-6%Co Cutting Tool during Turning Machining: Experiment and Finite Element Simulations*, *WSEAS Trans. Heat Mass Transf.*, 6, 3, (2011), pp. 71–80.

(Kang et al. 2006) - Guozheng Kang, Yujie Liu, Zhao Li, *Experimental Study on Ratchetting-Fatigue Interaction of SS304 Stainless Steel in Uniaxial Cyclic Stressing*, *Mater. Sci. Eng. A*, 435–436, (2006), pp. 396–404, <https://doi.org/10.1016/j.msea.2006.07.006>.

(Kassner 2015) - M. E. Kassner, *Fundamentals of Creep in Metals and Alloys*, 3rd ed. 2015.

(Kim et al. 2017) - Woo-Gon Kim, Jae-Young Park, I Made Wicaksana Ekaputra, Seon-Jin Kim, Jinsung Jang, *Influence of Hold Time and Stress Ratio on Cyclic Creep Properties Under Controlled Tension Loading Cycles of Grade 91 Steel*, *Nucl. Eng. Technol.*, 49, 3, (2017), pp. 581–591, <https://doi.org/10.1016/J.NET.2016.11.007>.

(Kindermann et al. 1999) - P. Kindermann, P. Schlund, H. G. Sockel, M. Herr, W. Heinrich, K. Görting, U. Schleinkofer, *High-Temperature Fatigue of Cemented Carbides under Cyclic Loads*, *Int. J. Refract. Met. Hard Mater.*, 17, 1, (1999), pp. 55–68, [https://doi.org/10.1016/S0263-4368\(99\)00014-1](https://doi.org/10.1016/S0263-4368(99)00014-1).

(Kliman et al. 1984) - V. Kliman, M. Bílý, *Hysteresis Energy of Cyclic Loading*, *Mater. Sci. Eng.*, 68, 1, (1984), pp. 11–18, [https://doi.org/10.1016/0025-5416\(84\)90239-8](https://doi.org/10.1016/0025-5416(84)90239-8).

(Klünsner et al. 2010a) - T Klünsner, S Wurster, R Pippan, M Jenko, R Ebner, P Supancic, J Glätzle, A Püschel, “*Comparison of Bending Strength of Wc-Co Hard Metal in Millimeter and Micrometer Sized Specimens*,” in *18th European Conference on Fracture: Fracture of Materials and Structures from Micro to Macro Scale 2010*.

(Klünsner et al. 2010b) - Thomas Klünsner, Stefan Marsoner, Reinhold Ebner, Reinhard Pippan, Johannes Glätzle, Arndt Püschel, “*Effect of Microstructure on Fatigue Properties of WC-Co Hard Metals*,” in *Procedia Engineering 2010*, vol. 2, pp. 2001–2010.

(Komanduri 1993) - Ranga Komanduri, *Machining and Grinding: A Historical Review of the Classical Papers*, Appl. Mech. Rev., 46, 3, (1993), pp. 80–132, <https://doi.org/10.1115/1.3121404>.

(Kotas et al. 2017) - Agnieszka Betzwar Kotas, Herbert Danninger, Brigitte Weiss, Ken Mingard, Jose Sanchez, Luis Llanes, *Fatigue Testing and Properties of Hardmetals in the Gigacycle Range*, Int. J. Refract. Met. Hard Mater., 62, (2017), pp. 183–191, <https://doi.org/10.1016/j.ijrmhm.2016.07.004>.

(Krobath et al. 2018) - M. Krobath, T. Klünsner, W. Ecker, M. Deller, N. Leitner, S. Marsoner, *Tensile Stresses in Fine Blanking Tools and Their Relevance to Tool Fracture Behavior*, Int. J. Mach. Tools Manuf., 126, (2018), pp. 44–50, <https://doi.org/10.1016/j.ijmachtools.2017.12.005>.

(Kursawe et al. 2001) - S. Kursawe, Ph. Pott, H.G. Sockel, W. Heinrich, M. Wolf, *On the Influence of Binder Content and Binder Composition on the Mechanical Properties of Hardmetals*, Int. J. Refract. Met. Hard Mater., 19, 4–6, (2001), pp. 335–340, [https://doi.org/10.1016/S0263-4368\(01\)00026-9](https://doi.org/10.1016/S0263-4368(01)00026-9).

(Lay et al. 1987) - S. Lay, J. Vicens, F. Osterstock, *High Temperature Creep of WC-Co Alloys*, J. Mater. Sci., 22, 4, (1987), pp. 1310–1322, <https://doi.org/10.1007/BF01233127>.

(Lay et al. 1984) - Sabine Lay, Frederic Osterstock, “*High Temperature Creep of Pure Tungsten Carbide and WC-Co Alloys with Low Cobalt Volumic Ratios*,” in *Deformation of Ceramic Materials III 1984*, vol. 18, pp. 463–471.

(Lea et al. 1981) - C. Lea, B. Roebuck, *Fracture Topography of WC-Co Hardmetals*, Met. Sci., 15, 6, (1981), pp. 262–266, <https://doi.org/10.1179/msc.1981.15.6.262>.

(Lee et al. 1997) - I. C. Lee, T. Sakuma, *High-Temperature Tensile Ductility in WC-Co Cemented Carbides*, Metall. Mater. Trans. A Phys. Metall. Mater. Sci., 28A, 9, (1997), pp. 1843–

1847, <https://doi.org/10.1007/s11661-997-0114-6>.

(Lee 1995) - In Chul Lee, *A Threshold Stress for High-Temperature Plastic Flow in WC-Co Cemented Carbides*, *Met. Mater.*, 1, 2, (1995), pp. 125–132, <https://doi.org/10.1007/BF03025923>.

(Lemaitre 1984) - Jean Lemaitre, *How to Use Damage Mechanics*, *Nucl. Eng. Des.*, 80, 2, (1984), pp. 233–245, [https://doi.org/10.1016/0029-5493\(84\)90169-9](https://doi.org/10.1016/0029-5493(84)90169-9).

(Lemaitre et al. 2005) - Jean Lemaitre, Rodrigue Desmorat, *Engineering Damage Mechanics: Ductile, Creep, Fatigue and Brittle Failures* 2005.

(Li et al. 2013) - Anhai Li, Jun Zhao, Dong Wang, Xinliang Gao, Hongwei Tang, *Three-Point Bending Fatigue Behavior of WC-Co Cemented Carbides*, *Mater. Des.*, 45, (2013), pp. 271–278, <https://doi.org/10.1016/j.matdes.2012.08.075>.

(Lin et al. 1969) - T. H. Lin, Y. M. Ito, *Mechanics of a Fatigue Crack Nucleation Mechanism*, *J. Mech. Phys. Solids*, 17, 6, (1969), pp. 511–523, [https://doi.org/10.1016/0022-5096\(69\)90006-4](https://doi.org/10.1016/0022-5096(69)90006-4).

(Llanes et al. 2002) - L. Llanes, Y. Torres, M. Anglada, “*On the Fatigue Crack Growth Behavior of WC-Co Cemented Carbides: Kinetics Description, Microstructural Effects and Fatigue Sensitivity*,” in *Acta Materialia* 2002, vol. 50, pp. 2381–2393.

(Llanes et al. 2014) - Luis Llanes, Marc Anglada, Yadir Torres, “*Fatigue of Cemented Carbides*,” in *Comprehensive Hard Materials* 2014, vol. 1, pp. 345–362.

(Mari et al. 1999) - D. Mari, S. Bolognini, G. Feusier, T. Viatte, W. Benoit, *Experimental Strategy to Study the Mechanical Behaviour of Hardmetals for Cutting Tools*, *Int. J. Refract. Met. Hard Mater.*, 17, 1, (1999), pp. 209–225, [https://doi.org/10.1016/S0263-4368\(98\)00078-X](https://doi.org/10.1016/S0263-4368(98)00078-X).

(Marshall et al. 2015) - Jessica M. Marshall, Mathilde Giraudel, *The Role of Tungsten in the Co Binder: Effects On WC Grain Size and Hcp-Fcc Co in the Binder Phase*, *Int. J. Refract. Met. Hard Mater.*, 49, 1, (2015), pp. 57–66, <https://doi.org/10.1016/j.ijrmhm.2014.09.028>.

(Marshall et al. 2013) - Jessica M. Marshall, Alexandra Kusoffsky, “*Binder Phase Structure in Fine and Coarse WC-Co Hard Metals with Cr and v Carbide Additions*,” in *International Journal of Refractory Metals and Hard Materials* 2013, vol. 40, pp. 27–35.

(Merkel et al. 2008) - Manfred Merkel, Karl-Heinz Thomas, *Taschenbuch Der Werkstoffe*, 7th ed., München, 2008.

(Miller 2000) - R.J. Miller, *Design Approaches for High Temperature Composite*

*Aeroengine Components*, Compr. Compos. Mater., (2000), pp. 181–207, <https://doi.org/10.1016/B0-08-042993-9/00138-8>.

(Mingard et al. 2013) - K. P. Mingard, H. G. Jones, M. G. Gee, B. Roebuck, J. W. Nunn, *In Situ Observation of Crack Growth in a WC-Co Hardmetal and Characterisation of Crack Growth Morphologies by EBSD*, Int. J. Refract. Met. Hard Mater., 36, (2013), pp. 136–142, <https://doi.org/10.1016/j.ijrmhm.2012.08.006>.

(Mingard et al. 2011) - K. P. Mingard, B. Roebuck, J. Marshall, G. Sweetman, *Some Aspects of the Structure of Cobalt and Nickel Binder Phases in Hardmetals*, Acta Mater., 59, 6, (2011), pp. 2277–2290, <https://doi.org/10.1016/j.actamat.2010.12.004>.

(Mingard et al. 2021) - K Mingard, S Moseley, S Norgren, H Zakaria, D Jones, B Roebuck, *Microstructural Observations of High Temperature Creep Processes in Hardmetals*, Powder Metall., (2021), pp. 1–11, <https://doi.org/10.1080/00325899.2021.1877866>.

(Miyake et al. 1968) - Kazuo Miyake, Yoshio Fujiwara, Kenichi Nishigaki, *On the Fatigue of WC-Co Alloys*, J. Japan Inst. Met., 32, 11, (1968), pp. 1128–1131, [https://doi.org/10.2320/jinstmet1952.32.11\\_1128](https://doi.org/10.2320/jinstmet1952.32.11_1128).

(Miyake et al. 2004) - Koji Miyake, Satoru Fujisawa, Atsushi Korenaga, Takao Ishida, Shinya Sasaki, “*The Effect of Pile-up and Contact Area on Hardness Test by Nanoindentation*,” in *Japanese Journal of Applied Physics, Part 1: Regular Papers and Short Notes and Review Papers 2004*, vol. 43, pp. 4602–4605.

(Morrell et al. 1973) - R. Morrell, K.H.G. Ashbee, *High Temperature Creep of Lithium Zinc Silicate Glass-Ceramics*, J Mater Sci , 8, (1973), pp. 1253–1270, <https://doi.org/10.1007/BF00549340>.

(Munz et al. 1989) - Dietrich Munz, Theo Fett, *Mechanisches Verhalten Keramischer Werkstoffe 1989*.

(Nabarro et al. 1968) - F R N Nabarro, S. Bartolucci Luyckx, *The Theory of the Strength of Tungsten Carbide-Cobalt Compacts*, Suppl. to Trans. Japan Inst. Met., 9, (1968), pp. 610–615.

(Nemetz et al. 2020) - A W Nemetz, W Daves, T Klünsner, C Praetzas, W Liu, T Tepperneegg, C Czettel, F Haas, C Bölling, J Schäfer, *Experimentally Validated Calculation of the Cutting Edge Temperature during Dry Milling of Ti6Al4V*, J. Mater. Process. Technol., 278, (2020), p. 116544, <https://doi.org/https://doi.org/10.1016/j.jmatprotec.2019.116544>.

(Nemetz et al. 2018) - Andreas W. Nemetz, Werner Daves, Thomas Klünsner, Werner

Ecker, Tamara Tepperneegg, Christoph Czettl, Ivan Krajinović, *FE Temperature- and Residual Stress Prediction in Milling Inserts and Correlation with Experimentally Observed Damage Mechanisms*, J. Mater. Process. Technol., 256, (2018), pp. 98–108, <https://doi.org/10.1016/j.jmatprotec.2018.01.039>.

(Nemetz et al. 2019) - Andreas W Nemetz, Werner Daves, Thomas Klünsner, Werner Ecker, Jonathan Schäfer, Christoph Czettl, Thomas Antretter, *Cyclic Heat-up and Damage-Relevant Substrate Plastification of Single- and Bilayer Coated Milling Inserts Evaluated Numerically*, Surf. Coatings Technol., 360, (2019), pp. 39–49, <https://doi.org/https://doi.org/10.1016/j.surfcoat.2019.01.008>.

(Novikov et al. 2007) - N. V. Novikov, V. P. Bondarenko, V. T. Golovchan, *High-Temperature Mechanical Properties of WC-Co Hard Metals (Review)*, J. Superhard Mater., 29, 5, (2007), pp. 261–280, <https://doi.org/10.3103/s1063457607050012>.

(Obtlik et al. 1992) - Karel Obtlik, Jaroslav Polák, Michal Hájek, Jan Vrbka, “*Low Cycle Fatigue in WC-Co Cemented Carbides*,” in *Low Cycle Fatigue and Elasto-Plastic Behaviour of Materials—31992*, pp. 43–48.

(Orth et al. 1993) - F. Orth, L. Hoffmann, H. Zilch-Bremer, G. W. Ehrenstein, *Evaluation of Composites under Dynamic Load*, Compos. Struct., 24, 3, (1993), pp. 265–272, [https://doi.org/10.1016/0263-8223\(93\)90220-K](https://doi.org/10.1016/0263-8223(93)90220-K).

(Östberg et al. 2006a) - Gustaf Östberg, Katharina Buss, Mikael Christensen, Susanne Norgren, Hans-Olof Andrén, Daniele Mari, Göran Wahnström, Ingrid Reineck, *Mechanisms of Plastic Deformation of WC–Co and Ti(C, N)–WC–Co*, Int. J. Refract. Met. Hard Mater., 24, 1, (2006), pp. 135–144, <https://doi.org/https://doi.org/10.1016/j.ijrmhm.2005.04.009>.

(Östberg et al. 2006b) - Gusto Östberg, M. U. Farooq, M. Christensen, H. O. Andrén, U. Klement, G. Wahnström, *Effect of  $\Sigma 2$  Grain Boundaries on Plastic Deformation of WC-Co Cemented Carbides*, Mater. Sci. Eng. A, 416, 1–2, (2006), pp. 119–125, <https://doi.org/10.1016/j.msea.2005.09.095>.

(Osterstock 1983) - Frederic Osterstock, “*High Temperature Creep of Some WC-Co Alloys*,” in *Science of Hard Materials 1983*, pp. 671–687.

(Osterstock et al. 1983) - Frederic Osterstock, Jean Louis Chermant, “*SOME ASPECTS OF THE FRACTURE OF WC-Co COMPOSITES*,” in 1983, pp. 615–629.

(Otsuka et al. 1989) - A. Otsuka, K. Tohgo, H. Sugawara, F. Ueda, H. Hohjo, “*Fatigue of*



*WC–Co Hardmetals Under Tension-Compression Loading — the Effects of Co Content and WC Grain Size,*” in *Proceedings of The 7th International Conference On Fracture (ICF7)1989*, pp. 1289–1296.

(Pugsley et al. 2001) - V. A. Pugsley, G. Korn, S. Luyckx, H. G. Sockel, W. Heinrich, M. Wolf, H. Feld, R. Schulte, “*The Influence of a Corrosive Wood-Cutting Environment on the Mechanical Properties of Hardmetal Tools,*” in *International Journal of Refractory Metals and Hard Materials*2001, vol. 19, pp. 311–318.

(Reik et al. 1979) - Wolfgang Reik, Peter Mayr, Eckard Macherauch, • *Vergleich Der Woehler-Kurven Aus Spannungsgesteuerten, Gesamtdehnungsgesteuerten Und Plastischdehnungsgesteuerten Versuchen.*, Arch. fur das Eisenhüttenwes., 50, 9, (1979), pp. 407–411, <https://doi.org/10.1002/srin.197904765>.

(Rice et al. 1978) - R W Rice, J J Mecholsky, S W Freiman, S M Morey, *Failure Causing Defects in Ceramics : What NDE Should Find Failure Causing Defects in Ceramics : What NDE Should Find*, Proc. Rev. Prog. Quant. NDE, September 1976, (1978), pp. 257–272.

(Rider et al. 1995) - R. J. Rider, S. J. Harvey, H. D. Chandler, *Fatigue and Ratcheting Interactions*, Int. J. Fatigue, 17, 7, (1995), pp. 507–511, [https://doi.org/10.1016/0142-1123\(95\)00046-V](https://doi.org/10.1016/0142-1123(95)00046-V).

(Ritchie 1988) - R. O. Ritchie, *Mechanisms of Fatigue Crack Propagation in Metals, Ceramics and Composites: Role of Crack Tip Shielding*, Mater. Sci. Eng., 103, 1, (1988), pp. 15–28, [https://doi.org/10.1016/0025-5416\(88\)90547-2](https://doi.org/10.1016/0025-5416(88)90547-2).

(Roebuck et al. 1982) - B. Roebuck, E. A. Almond, *Equivalence of Indentation and Compressive Creep Tests on a WC/Co Hardmetal*, J. Mater. Sci. Lett., 1, 12, (1982), pp. 519–521, <https://doi.org/10.1007/BF00724735>.

(Roebuck et al. 1988) - B. Roebuck, E. A. Almond, *Deformation and Fracture Processes and the Physical Metallurgy of WC–Co Hardmetals*, Int. Mater. Rev., 33, 1, (1988), pp. 90–112, <https://doi.org/10.1179/imr.1988.33.1.90>.

(Roebuck et al. 1984) - B. Roebuck, E. A. Almond, A. M. Cottenden, *The Influence of Composition, Phase Transformation and Varying the Relative F.C.C. and H.C.P. Phase Contents on the Properties of Dilute CoWC Alloys*, Mater. Sci. Eng., 66, 2, (1984), pp. 179–194, [https://doi.org/10.1016/0025-5416\(84\)90179-4](https://doi.org/10.1016/0025-5416(84)90179-4).

(Roebuck et al. 2015) - B. Roebuck, S. Moseley, *Tensile and Compressive Asymmetry in*

*Creep and Monotonic Deformation of WC/Co Hardmetals at High Temperature*, Int. J. Refract. Met. Hard Mater., 48, (2015), pp. 126–133, <https://doi.org/10.1016/j.ijrmhm.2014.08.007>.

(Roesler et al. 2007) - J. Roesler, H. Harders, M. Baeker, *Mechanical Behaviour of Engineering Materials*, 1st ed.2007.

(Sailer et al. 2001) - T. Sailer, M. Herr, H. G. Sockel, R. Schulte, H. Feld, L. J. Prakash, “*Microstructure and Mechanical Properties of Ultrafine-Grained Hardmetals*,” in *International Journal of Refractory Metals and Hard Materials*2001, vol. 19, pp. 553–559.

(Sakuma et al. 1992) - T. Sakuma, H. Hondo, *Plastic Flow in WC-13wt.%Co at High Temperatures*, Mater. Sci. Eng. A, A156, 2, (1992), pp. 125–130, [https://doi.org/10.1016/0921-5093\(92\)90144-P](https://doi.org/10.1016/0921-5093(92)90144-P).

(Sarin et al. 1975) - V. K. Sarin, T. Johannesson, *On the Deformation of WC–Co Cemented Carbides*, Met. Sci., 9, 1, (1975), pp. 472–476, <https://doi.org/10.1179/030634575790444531>.

(Schaller et al. 1988) - R. Schaller, J. J. Ammann, C. Bonjour, *Internal Friction in WC-Co Hard Metals*, Mater. Sci. Eng., 105–106, PART 2, (1988), pp. 313–321, [https://doi.org/10.1016/0025-5416\(88\)90712-4](https://doi.org/10.1016/0025-5416(88)90712-4).

(Schedler 1988) - Wolfgang Schedler, *Hartmetall Für Den Praktiker. Aufbau, Herstellung, Eigenschaften Und Industrielle Anwendung Einer Modernen Werkstoffgruppe*, Düsseldorf, 1988.

(Schleinkofer et al. 1996a) - U. Schleinkofer, H. G. Sockel, K. Görting, W. Heinrich, *Fatigue of Hard Metals and Cermets*, Mater. Sci. Eng. A, 209, 1–2, (1996), pp. 313–317, [https://doi.org/10.1016/0921-5093\(95\)10106-3](https://doi.org/10.1016/0921-5093(95)10106-3).

(Schleinkofer et al. 1996b) - U. Schleinkofer, H. G. Sockel, K. Görting, W. Heinrich, *Microstructural Processes during Subcritical Crack Growth in Hard Metals and Cermets under Cyclic Loads*, Mater. Sci. Eng. A, 209, 1–2, (1996), pp. 103–110, [https://doi.org/10.1016/0921-5093\(95\)10098-9](https://doi.org/10.1016/0921-5093(95)10098-9).

(Schleinkofer et al. 1995) - U. Schleinkofer, H.G. Sockel, P. Schlund, K. Görting, W. Heinrich, *Behaviour of Hard Metals and Cermets under Cyclic Mechanical Loads*, Mater. Sci. Eng. A, 194, 1, (1995), pp. 1–8, [https://doi.org/10.1016/0921-5093\(94\)09660-0](https://doi.org/10.1016/0921-5093(94)09660-0).

(Schmauder et al. 1989) - S Schmauder, H.F. Fischmeister, R. Spiegelner, M.H. Poech, “*Modellierung von Risswachstumsvorgängen in Zweiphasenwerkstoffen*,” in *Metallkundliche Probleme Der Werkstoffentwicklung*1989, p. 16.

(Schmid 1987) - H. G. Schmid, *The Mechanisms of Fracture of WC-11 Wt% Co between*

20° C and 1000° C, Mater. forum, 10, 3, (1987), pp. 184–197.

(Schmid et al. 1988) - H. G. Schmid, D. Mari, W. Benoit, C. Bonjour, *The Mechanical Behaviour of Cemented Carbides at High Temperatures*, Mater. Sci. Eng., 105–106, PART 2, (1988), pp. 343–351, [https://doi.org/10.1016/0025-5416\(88\)90716-1](https://doi.org/10.1016/0025-5416(88)90716-1).

(Schmiedt-Kalenborn 2020) - Anke Schmiedt-Kalenborn, *Mikrostrukturbasierte Charakterisierung Des Ermüdungs- Und Korrosionsermüdungsverhaltens von Lötverbindungen Des Austenits X2CrNi18-9 Mit Nickel- Und Goldbasislot*, 1st ed., Wiesbaden, 2020 (Werkstofftechnische Berichte | Reports of Materials Science and Engineering).

(Seeger et al. 1958) - A. Seeger, U. Dehlinger, *Kristallphysik II / Crystal Physics II*, 1st ed., Berlin, Heidelberg, 1958 (Handbuch der Physik / Encyclopedia of Physics).

(Sherby et al. 1968) - Oleg D. Sherby, Peter M. Burke, *Mechanical Behavior of Crystalline Solids at Elevated Temperature*, Prog. Mater. Sci., 13, C, (1968), pp. 325–390, [https://doi.org/10.1016/0079-6425\(68\)90024-8](https://doi.org/10.1016/0079-6425(68)90024-8).

(Sigl et al. 1987) - L. S. Sigl, H. E. Exner, *Experimental Study of the Mechanics of Fracture in WC-Co Alloys*, Metall. Trans. A, Phys. Metall. Mater. Sci., 18 A, 7, (1987), pp. 1299–1308, <https://doi.org/10.1007/BF02647199>.

(Sigl et al. 1988) - L.S. Sigl, H.F. Fischmeister, *On the Fracture Toughness of Cemented Carbides*, Acta Metall., 36, 4, (1988), pp. 887–897, [https://doi.org/10.1016/0001-6160\(88\)90143-5](https://doi.org/10.1016/0001-6160(88)90143-5).

(Sigl 1986) - Lorenz Sigl, *Das Zähigkeitsverhalten von WC-Co Legierungen*, Düsseldorf, 1986.

(Sigl et al. 1984) - Lorenz S Sigl, H.E. Exner, H.F. Fischmeister, “Characterization of Fracture Processes and Fracture Relevant Parameters in WC-Co Hardmetals,” in , Rhodos, Greece, 1984, pp. 631–644.

(Smith et al. 1968) - J. T. Smith, J. D. Wood, *Elevated Temperature Compressive Creep Behavior of Tungsten Carbide-Cobalt Alloys*, Acta Metall., 16, 10, (1968), pp. 1219–1226, [https://doi.org/10.1016/0001-6160\(68\)90003-5](https://doi.org/10.1016/0001-6160(68)90003-5).

(Spiegler et al. 1992) - R. Spiegler, H. F. Fischmeister, *Prediction of Crack Paths in WCCo Alloys*, Acta Metall. Mater., 40, 7, (1992), pp. 1653–1661, [https://doi.org/10.1016/0956-7151\(92\)90108-Q](https://doi.org/10.1016/0956-7151(92)90108-Q).

(Suresh 1991) - S Suresh, *Fatigue of Materials, Cambridge Solid State Science Series*, Press

Synd. Univ. Cambridge, Cambridge, (1991).

(Suzuki et al. 1975) - Hisashi Suzuki, Kozi Hayashi, *The Strength of WC–Co Cemented Carbide in Relation to Structural Defects*, Trans Jap Inst Met, 16, 6, (1975), pp. 353–360, <https://doi.org/10.2320/matertrans1960.16.353>.

(Tan et al. 2010) - T. F. Tan, C. K.H. Dharan, *Cyclic Hysteresis Evolution as a Damage Parameter for Notched Composite Laminates*, J. Compos. Mater., 44, 16, (2010), pp. 1977–1990, <https://doi.org/10.1177/0021998309360942>.

(Tepperneegg et al. 2016) - T. Tepperneegg, T. Klünsner, C. Kremsner, C. Tritremmel, C. Czettl, S. Puchegger, S. Marsoner, R. Pippan, R. Ebner, *High Temperature Mechanical Properties of WC-Co Hard Metals*, Int. J. Refract. Met. Hard Mater., 56, (2016), pp. 139–144, <https://doi.org/10.1016/j.ijrmhm.2016.01.002>.

(Tritremmel et al. 2017) - C. Tritremmel, T. Klünsner, B. Sartory, C. Czettl, S. Marsoner, “*Cyclic Plastic Deformation Behaviour of WC-Co Hard Metals at Elevated Temperatures*,” in *19th Plansee Seminar - International Conference on Refractory Metals and Hard Materials*, Reutte/Austria, 2017, pp. 1–9.

(Ueda et al. 1977) - F. Ueda, H. Doi, F. Fujiwara, H. Masatomi, *Bend Deformation And Fracture Of WC-Co Alloys At Elevated Temperatures*, Trans Jpn Inst Met, 18, 3, (1977), pp. 247–256, <https://doi.org/10.2320/matertrans1960.18.247>.

(Ueda et al. 1975) - F. Ueda, H. Doi, F. Fujiwara, H. Masatomi, Y. Oosawav, *Tensile Creep of WC-10%Co and WC-10%TaC-10%Co Alloys at Elevated Temperatures*, Trans. Japan Inst. Met., 16, 9, (1975), pp. 591–600, <https://doi.org/10.2320/matertrans1960.16.591>.

(Useldinger et al. 2017) - R. Useldinger, U. Schleinkofer, *Creep Behaviour of Cemented Carbides — Influence of Binder Content, Binder Composition and WC Grain Size*, Int. J. Refract. Met. Hard Mater., 62, (2017), pp. 170–175, <https://doi.org/10.1016/j.ijrmhm.2016.06.013>.

(Vasel et al. 1985) - C. H. Vasel, A. D. Krawitz, E. F. Drake, E. A. Kenik, *Binder Deformation in WC-(Co, Ni) Cemented Carbide Composites*, Metall. Trans. A, 16, 12, (1985), pp. 2309–2317, <https://doi.org/10.1007/BF02670431>.

(Vicens et al. 1994) - J. Vicens, M. Benjdir, G. Nouet, A. Dubon, J. Y. Laval, *Cobalt Intergranular Segregation in WC-Co Composites*, J. Mater. Sci., 29, 4, (1994), pp. 987–994, <https://doi.org/10.1007/BF00351421>.

(Weidow et al. 2011) - Jonathan Weidow, Hans Olof Andrén, *APT Analysis of WC-Co*

*Based Cemented Carbides*, *Ultramicroscopy*, 111, 6, (2011), pp. 595–599, <https://doi.org/10.1016/j.ultramic.2011.01.033>.

(Weidow et al. 2009a) - Jonathan Weidow, Susanne Norgren, Hans Olof Andrén, *Effect of V, Cr and Mn Additions on the Microstructure of WC-Co*, *Int. J. Refract. Met. Hard Mater.*, 27, 5, (2009), pp. 817–822, <https://doi.org/10.1016/j.ijrmhm.2009.02.002>.

(Weidow et al. 2009b) - Jonathan Weidow, Jenni Zackrisson, Bo Jansson, Hans Olof Andrén, *Characterisation of WC-Co with Cubic Carbide Additions*, *Int. J. Refract. Met. Hard Mater.*, 27, 2, (2009), pp. 244–248, <https://doi.org/10.1016/j.ijrmhm.2008.11.007>.

(Weiß et al. 2004) - E. Weiß, B. Postberg, T. Nicak, J. Rudolph, *Simulation of Ratcheting and Low Cycle Fatigue*, *Int. J. Press. Vessel. Pip.*, 81, 3, (2004), pp. 235–242, <https://doi.org/10.1016/j.ijpvp.2004.01.002>.

(Wiederhorn et al. 1991) - S.M. Wiederhorn, B.J. Hockey, *High Temperature Degradation of Structural Composites*, *Ceram. Int.*, 17, 4, (1991), pp. 243–252, [https://doi.org/10.1016/0272-8842\(91\)90018-U](https://doi.org/10.1016/0272-8842(91)90018-U).

(Wiederhorn et al. 1988) - S.M. Wiederhorn, D.E. Roberts, T.-J. Chuang, L. Chuck, *Damage-enhanced Creep in a Siliconized Silicon Carbide: Phenomenology*, *J. Am. Ceram. Soc.*, 71, (1988), pp. 602–608, <https://doi.org/10.1111/j.1151-2916.1988.tb05926.x>.

(Wirmark et al. 1986) - G. Wirmark, G. L. Dunlop, C. Chatfield, *Tensile Creep of WC-Co Cemented Carbides at 800 - 900 C*, *Int. J. Refract. hard Met.*, 5, 3, (1986), pp. 153–157.

(Yousfi et al. 2015) - M. A. Yousfi, J. Weidow, A. Nordgren, L. K.L. Falk, H. O. Andrén, *Deformation Mechanisms in a WC-Co Based Cemented Carbide during Creep*, *Int. J. Refract. Met. Hard Mater.*, 49, 1, (2015), pp. 81–87, <https://doi.org/10.1016/j.ijrmhm.2014.07.016>.

(Zunega 2013) - Jonee Christine Zunega, *High Temperature Indentation of WC/Co Hardmetals, soutenue à l'University of Southampton, 2013*.

## 7. Publications

### 7.1. List of Included Publications

1. Kathrin Maier, Thomas Klünsner, Martin Krobath, Christian Tritremmel, Stefan Marsoner, Christoph Czettl  
**Uniaxial step loading test setup for determination of creep curves of oxidation-sensitive high strength materials in vacuum under tensile and compressive load**  
*International Journal of Refractory Metals & Hard Materials*, 92 (2020) 105327  
Current Status & Status Date: Published – July 06, 2020
2. Kathrin Maier, Thomas Klünsner, Werner Ecker, Philip Pichler, Stefan Marsoner, Christoph Czettl, Jonathan Schäfer, Reinhold Ebner  
**A physical reason for asymmetric creep deformation behaviour of WC-Co hard metal under tension and compression loading at 700 °C and 800 °C**  
*International Journal of Refractory Metals & Hard Materials*, 97 (2021) 105526  
Current Status & Status Date: Published – March 12, 2021
3. Kathrin Maier, Thomas Klünsner, Martin Krobath, Philip Pichler, Stefan Marsoner, Werner Ecker, Christoph Czettl, Jonathan Schäfer, Reinhold Ebner  
**Creep behaviour of WC 12 wt.% Co hardmetals with different WC grain sizes tested in uniaxial tensile and compression step-loading tests at 700 °C and 800 °C**  
*International Journal of Refractory Metals & Hard Materials*, 100 (2021) 105633  
Current Status & Status Date: Published – July 12, 2021
4. Kathrin Maier, Thomas Klünsner, Philip Pichler, Stefan Marsoner, Werner Ecker, Christoph Czettl, Jonathan Schäfer, Reinhold Ebner  
**Strain ratcheting limit stresses as a function of microstructure of WC-Co hardmetals under uniaxial cyclic loads under a stress ratio of  $R = -\infty$  at elevated temperatures**  
*International Journal of Refractory Metals & Hard Materials*, 102 (2021) 105699  
Current Status & Status Date: Published – September 22, 2021

5. Kathrin Maier, Thomas Klünsner, Philip Pichler, Stefan Marsoner, Werner Ecker, Christoph Czettl, Jonathan Schäfer, Reinhold Ebner  
**Damage indicators for early fatigue damage assessment of WC-Co hardmetals under uniaxial cyclic loads under a stress ratio of  $R = -1$  at elevated temperatures**  
*International Journal of Refractory Metals & Hard Materials, XX (2021) XXX*  
Current Status & Status Date:  
“Submitted - Manuscript Number: IJRMHM-D-21-00682” – September 27, 2021

## 7.2. Scientific Presentations

1. Kathrin Maier, Thomas Klünsner, Christian Tritremmel, Stefan Marsoner, Christoph Czettl, **Stress-strain behaviour and microstructural changes of WC-Co hard metals under cyclic loading at elevated temperature**, *Conference: 15th. Int. Metallography Conference 2018, Leoben, Austria, September 2018*, Contribution Type: Oral Presentation
2. Kathrin Maier, Thomas Klünsner, Christian Tritremmel, Stefan Marsoner, Philip Pichler, Christoph Czettl, **Asymmetry in creep kinetics of WC-10wt.% Co under tensile and compression loading at 700°C**, *Conference: European Congress and Exhibition on Advanced Materials and Processes - EUROMAT2019, Stockholm, Sweden, September 2019*, Contribution Type: Poster Presentation
3. Kathrin Maier, Thomas Klünsner, Werner Ecker, Philip Pichler, Stefan Marsoner, Christoph Czettl, Reinhold Ebner, **Microstructural defect evolution in WC-Co hard metals during cyclic loading at elevated temperature and its connection with stress-strain hysteresis loop shape**, *Conference: European Congress and Exhibition on Advanced Materials and Processes - EUROMAT 2021, Virtual - Graz, Austria, September 2021*, Contribution Type: Oral Presentation

### 7.3. My Contribution to Included Publications

#### Publication I

My contribution to the first Publication included here was concept preparation as well as selection of the investigated WC-Co hardmetal grade. The hardmetal specimen in its special hourglass geometry was manufactured by the project partner *Ceratizit Group GmbH*. *Christian Tritremmel* and I performed uniaxial tensile and compressive step-loading creep tests at 700 °C by a servo-hydraulic testing machine at *MCL Leoben* according to parameters which were defined by myself. Test data was evaluated by myself and prepared as diagrams for the publication. Due to the hourglass geometry, the experimentally determined strain values are underestimated and a strain correction via finite element simulation was performed. The strain correction was carried out by *Martin Krobath*, who also wrote about this topic in the manuscript. Therefore, the manuscript was written to 15% by *Martin Krobath* and to 85% by myself.

#### Publication II

My contributions to the second Publication were conceptualization and the selection of the investigated WC-Co hardmetal grades. The hourglass-shaped hardmetal specimens were manufactured by the project partner *Ceratizit Group GmbH*. The performance of the uniaxial tensile and compression step-loading creep tests at 700 °C and 800 °C with a servo-hydraulic testing machine at *MCL Leoben* was carried out by *Philip Pichler* and myself. Used parameters for the experimental investigations were predefined by myself. Experimental data was evaluated by myself and prepared as diagrams for the publication. According to my specifications, the microstructure was investigated by *Bernhard Sartory* and *Jaroslav Wosik* via scanning electron microscopy (SEM) and electron backscatter diffraction (EBSD). EBSD analysis was done with the software package "Orientation Imaging Microscopy" (OIM) version 7 from EDAX (*AMETEK Inc. n.d.*) and with "MTEX Toolbox" version 5.3 (*Bachmann et al. 2010*) in Matlab version R2019b by myself. Data visualisation and text writing for the manuscript was done 100% by myself.



**Publication III**

The third Publication concept was created by myself. I selected the investigated WC-Co hardmetal grades, which were produced by the project partner *Ceratizit Group GmbH*. Testing of the hourglass-shaped hardmetal specimens under uniaxial tensile and compressive step-loading creep tests at 700 °C and 800 °C was performed by *Philip Pichler* and myself. Used test parameters were determined by myself in advance. Due to the non-constant specimen cross-section and the resulting underestimated strain values, a strain correction was performed via finite element simulation by *Martin Krobath*. *Martin Krobath* also wrote and reviewed the passages about strain correction in the manuscript. Microstructural damage was documented by SEM micrographs performed by *Bernhard Sartory* and *Jaroslav Wosik*. Experimental data and SEM images were analysed by myself and prepared as graphs for the manuscript, which was written to 90% by myself and 10% by *Martin Krobath*, who wrote the passages about the strain correction as well as the Appendix.

**Publication IV**

I prepared the concept of the fourth publication and selected the investigated WC-Co hardmetal grades, which were produced by the project partner *Ceratizit Group GmbH*. Testing of the hardmetal specimens under uniaxial cyclic loading under a stress ratio of  $R = \sigma_{\min}/\sigma_{\max} = -\infty$  at 700 °C and 800 °C was performed by *Philip Pichler* and myself. Used test parameters were defined by myself in advance. Formed cavities or cracks and the deformation of the WC and Co-phase were documented by SEM and EBSD images by *Bernhard Sartory* and *Jaroslav Wosik*. Experimental data as well as SEM and EBSD images were analysed by myself and prepared as graphs for the manuscript, which was 100% written by myself.

**Publication V**

I also prepared the manuscript concept for the last, fifth, publication. The WC-Co hardmetal grades used for the publication were selected by myself and manufactured by the project partner *Ceratizit Group GmbH*. Testing of the hardmetal specimens under uniaxial cyclic loading under a stress ratio of  $R = -1$  at 700 °C and 800 °C was performed by *Philip Pichler*, while used test parameters were defined by myself. Microdefects as well as cracks in the microstructure and deformations of individual WC-Co phases were investigated by SEM and EBSD measurements by

*Bernhard Sartory* and *Jaroslav Wosik*. Experimental data as well as SEM and EBSD images were analysed by myself and prepared as graphs for the manuscript, which was 100% written by me.

The following table summarizes the percentage of my contribution for the preparation of the publications.

	<b>Conception and planning<sup>1</sup></b>	<b>Experiments</b>	<b>Analysis and interpretation</b>	<b>Manuscript preparation<sup>1</sup></b>
<b>Publication I</b>	100	50	80	85
<b>Publication II</b>	100	50	90	100
<b>Publication III</b>	100	50	90	90
<b>Publication IV</b>	100	25	90	100
<b>Publication V</b>	100	25	90	100

*Kathrin Maier*

---

<sup>1</sup> Supervision not included

# **Publication I**

**Uniaxial step loading test setup for determination of creep curves of oxidation-sensitive high strength materials in vacuum under tensile and compressive load**

**Kathrin Maier, Thomas Klünsner, Martin Krobath, Christian Tritremmel, Stefan Marsoner, Christoph Czettl**

**Published in**

**International Journal of Refractory Metals & Hard Materials,**

**92 (2020) 105327**

## Uniaxial step loading test setup for determination of creep curves of oxidation-sensitive high strength materials in vacuum under tensile and compressive load

Kathrin Maier<sup>1\*</sup>, Thomas Klünsner<sup>1</sup>, Martin Krobath<sup>1</sup>, Christian Tritremmel<sup>1</sup>, Stefan Marsoner<sup>1</sup>,  
Christoph Czettel<sup>2</sup>

<sup>1</sup> Materials Center Leoben Forschung GmbH, Roseggerstraße 12, 8700 Leoben, Austria

<sup>2</sup> CERATIZIT Austria GmbH, Metallwerk-Plansee Straße 71, 6600 Reutte, Austria

\*Corresponding author: kathrin.maier@mcl.at

**Keywords:** Tensile and compression creep behavior, Uniaxial step loading creep test, WC-Co hard metal, Vacuum, Eddy current heating, Strain correction

### Abstract

For long-term applications of components, such as in turbomachinery or automotive engineering, knowledge of creep behavior under increased load and temperature is of interest. Creep tests are commonly used to investigate the creep behavior of materials at a constant test temperature above room temperature under a constant force. The present work describes a so-called uniaxial step loading creep test setup and first results for a WC-Co hard metal under isothermal conditions at 700 °C in vacuum. Heating and temperature control within the tested specimen's gauge length were performed by induced eddy currents and a thermocouple, respectively. In contrast to conventional creep tests, the mechanical load is increased stepwise and the stress at each level is kept constant for 500 s. Displacement of the strain gauge markings was measured contactless with a laser extensometer. First tests were carried out for a WC-Co hard metal under compression and tensile loading. In order to avoid buckling of the high-strength material under compression, a special specimen geometry with non-constant specimen diameter was used. The minimum creep rate was determined for each applied tensile and compressive stress level. Under tensile load, minima of the creep rate were observed above a stress of 500 MPa that are interpreted as the secondary creep rates. Under compressive load, the respective creep rate minima were observed above a stress of -700 MPa.

## 1. Introduction

Thermally activated processes such as creep become relevant at temperatures above 30 to 50% of the absolute melting temperature. Creep is defined as a time-dependent plastic deformation of a material at constant load and temperature [1]. During a conventional creep test under uniaxial loading, the length change of the specimen is recorded over time. The typical creep curve is separated into three regions, shown in Figure 1: the curve starts with primary creep, during which the creep rate gradually decreases. As the test time increases, the creep rate stabilizes and remains constant, this phase is referred to as secondary creep. In the stable curve range, the creep rate is evaluated, which is used to determine further creep parameters such as stress exponent and activation energy [2]. By passing through the primary and secondary creep, time- and temperature-dependent changes occur in the microstructure, such as dislocation movements and formation of precipitates, up to pore formation [3]. In the tertiary stage the creep rate increases significantly and the tested material accumulates damage, i.e. based on cavities, micro cracks are formed which weaken the material's structural integrity. The test ends with the fracture of the specimen [2].

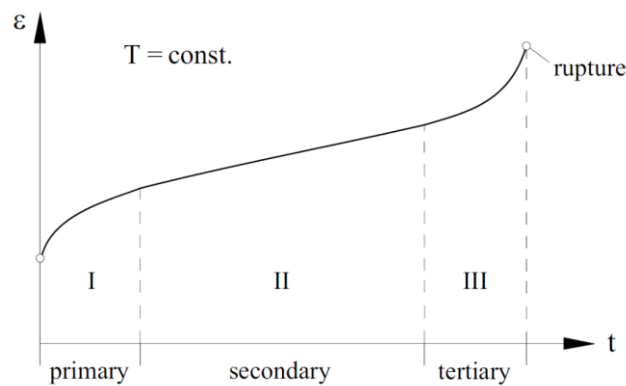


Figure 1: Typical creep curve with plastic strain  $\epsilon_{cr}$  over time  $t$  with the three typical stages of creep: primary, secondary and tertiary [4].

The shape of the typical creep curves for a single temperature and a single stress value depends on the test parameters used: temperature, stress and material. The creep test, to determine one creep curve, may take hours to years.

In the past, creep tests have been performed using various types of experiments applying various loading conditions. Established techniques are for example tensile [5], compression [6,7], bending [8], indentation [9] or electro-thermomechanical [10] tests at constant load and temperature conditions. During the service life of materials and tools, they are progressively loaded and unloaded under variations in load and temperature. In order to include the variations of load or temperature in creep tests, experiments are performed with stepwise increasing loads, cyclic mechanical loading or thermal cycling [11–15]. In metal cutting tools, temperatures above 1,000 °C can be reached [16]. Such high temperatures and the changing

mechanical properties with increasing temperature [17,18] caused a preference to investigate the creep behavior above 800 °C.

High temperature material testing of many high-strength materials, such as hard metals, requires special test setups as a result of their high tendency for oxidation at elevated temperatures in ambient atmosphere. At 600 °C and above, the oxidation kinetics of hard metals increase exponentially with temperature [19], therefore vacuum conditions are necessary. In addition, the materials exhibit high strength even at elevated temperatures, so that the applied high compressive loads bring the risk of specimen buckling. In addition to compression tests [7], this is also a limiting factor in electro-thermomechanical tests [10]. In creep experiments with stepwise increasing loads or thermal cycling, viscoelastic and other ductile materials have been investigated to date [11–14, 20]. In the case of I. P. Giannopoulos et al. [12] a graded stepped isostatic method (SSM) is used to minimize necessary testing efforts to determine the creep behavior of Kevlar fibers. The applied test method is applicable only under tensile loading conditions and up to 200 °C in ambient atmosphere. For the investigation of the thermally activated creep properties of high-strength materials, this kind of technique is not appropriate since the possible temperature range is too low. Uniaxial cyclic creep tests were documented for higher temperatures carried out for steels under tensile-tensile loading at 600 °C [15]. Different stress ratios  $R = \sigma_{\min}/\sigma_{\max}$  in the range from 0.50 to 0.95 with a fixed mean stress are applied to the specimens. At the minimum and maximum load, the load is not relieved immediately, but held constant for a certain time to characterize creep influence in the material. This experiment simulates cyclic creep / fatigue interactions by testing under load control mode and cyclic frequencies. In some of the documented testing techniques, e.g. in [6] the creep strain is determined via the testing machine's cross head displacement and not directly at the specimen which limits the accuracy of the strain measurement. Other techniques apply temperature by direct conduction of electrical current through the specimen [20]. This may influence the damage behaviour of the tested materials, e.g. upon pore formation and the resulting hot spots in the materials' microstructure.

The aim of the current work is to present a step loading creep test setup at elevated temperature under uniaxial loading and vacuum for high-strength materials. To enable testing under tensile and compressive loads, a specimen geometry with a non-constant cross-section was used to avoid buckling under compressive loading. First exemplary results for a WC-Co hard metal under uniaxial tensile and compression loading for 500 seconds per stress level at 700 °C are shown. By this type of experiment, it is possible to analyze the creep behavior of materials under various levels of applied stress in a time-efficient single measurement.

## 2. Methodological approach

### 2.1 Experimental details

In order to investigate the creep behavior under isothermal conditions and a variation of stress, uniaxial step loading tests were performed. A specimen was loaded uniaxially under tensile load by a servo-hydraulic testing machine (Instron 8803). In addition to the tensile load test, another specimen was tested under compression load. The load was increased in steps of 50 MPa within a few seconds and was kept constant at each stress level for 500 s. The load change from one load level to the next was carried out in such a short time span, that the creep that occurs during the load change itself can be neglected. The test is completed when a certain load level has been reached or the specimen has failed. If the specimen did not fail during the test, it was unloaded after the last stress level, as shown in Figure 2.

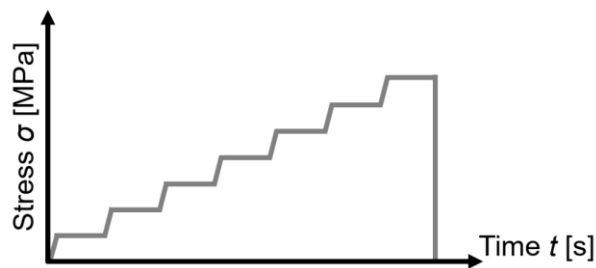


Figure 2: Schematic representation of the loading ramp in stepped loading creep tests performed in the same fashion under compression and tensile loads. In the stepped loading creep test, the load is increased in steps within a few seconds and kept constant for a certain time at each level. The test is completed when a certain predefined load level has been reached or the specimen has failed. If the specimen did not fail during the test, it was unloaded after the last stress level.

The test setup itself is flexible as specimens can be loaded at low or high temperatures up to high stress levels. A special specimen geometry was used to prevent hard metals from buckling under compressive loading. The specimen has an hourglass-shape with a minimum diameter in the axial center of 6 mm and a cylindrical shaft for clamping (maximum diameter of 20 mm), see Figure 3. The length of the specimens is 250 mm.

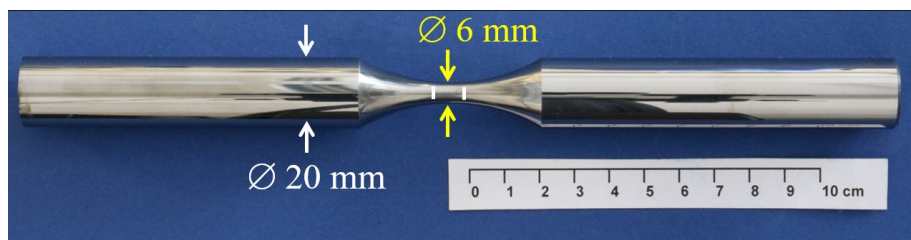


Figure 3: Hourglass-shaped specimens with a length of 250 mm. The minimum and maximum diameters are 6 mm and 20 mm, respectively.

Axial strain was measured contactless with a high precision laser extensometer (P-2S-50/400 Hz, Fiedler Optoelektronik GmbH, class of accuracy of 0.2) using measuring marks placed 4 mm to either side of the axial center of the specimen.

In order to avoid oxidation of the surface of certain specimens at elevated temperatures during the test, the standard Instron 8803 servo-hydraulic testing machine was equipped with an auxiliary vacuum chamber, see Figure 4(a.). The tests were performed with a base pressure of  $5 \cdot 10^{-6}$  mbar. During the experiment the specimen was inductively heated by eddy currents induced by an internally water-cooled copper coil. Thermal stability in the center of the measuring length of 8 mm was ensured during the measurement by constantly pulling on a non-soldered loop-shaped thermocouple wire, see Figure 4(b.4). If spot-welded thermocouples were used instead, they would cause stress concentrations under mechanical load which could influence the failure behavior of brittle materials such as hard metals. However, to ensure thermal uniformity within the gauge length with a non-soldered thermocouple, a calibration measurement was performed for each tested material grade and temperature level. During the calibration measurement, calibration specimens are equipped with three type K thermocouples placed at the gauge length's extreme ends and in its middle via spot-welding. Based on the calibration measurement, the required position within the induction coil was determined for each material grade and temperature, which ensured temperature stability during the measurements.

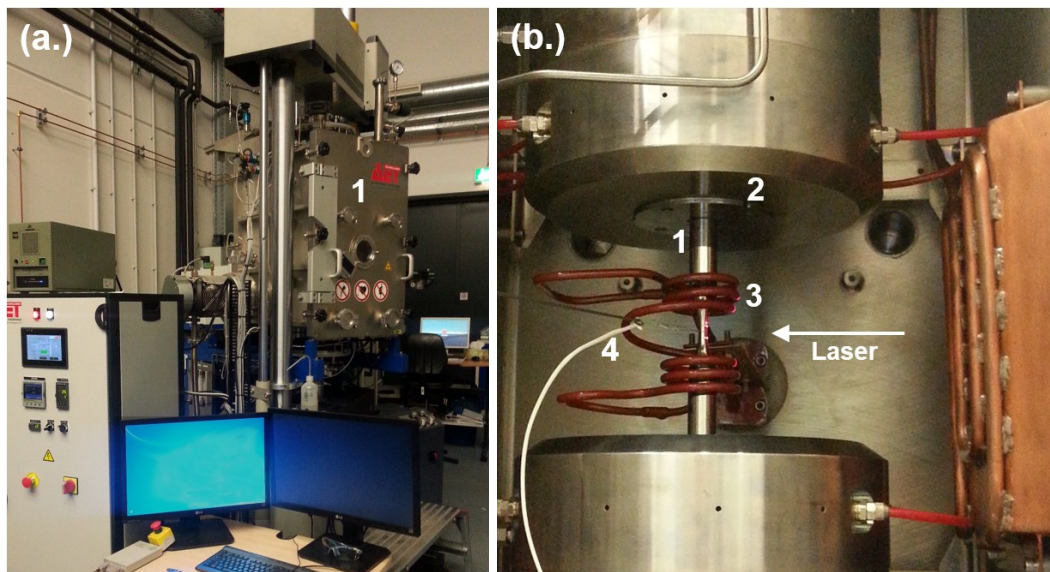


Figure 4: (a.) Servo-hydraulic testing machine with auxiliary vacuum chamber (a.1). (b.) Interior of the vacuum chamber with tested sample (b.1) hydraulically clamped in cylindrical clamping jaws (b.2). For testing at elevated temperatures, an induction coil (b.3) is used to heat the specimen by eddy current heating; a thermocouple (b.4) is used to control temperature. The strain measurement is carried out contactless via a laser extensometer.



## 2.2 Simulation details

As a result of the non-constant diameter of the specimens, the experimentally determined strain values are underestimated and must be strain-corrected. The correction is carried out via finite element simulations. The simulated material behavior is adapted iteratively in a mechanical 2D simulation in which the specimen's full 3D geometry is modelled exploiting the specimen's rotational symmetry. The simulated and experimentally measured displacements and forces are aligned for the whole test duration. The applied material model combines static plasticity with a simple creep model, the governing equation for the creep strain rate  $\underline{\dot{\epsilon}}^{cr}$  shown in Eq. (1).

$$\underline{\dot{\epsilon}}^{cr} = \left( A \cdot \tilde{q}^n \cdot [(m + 1) \cdot \underline{\epsilon}^{cr}]^m \right)^{\frac{1}{m+1}} \quad (1)$$

$A$ ,  $n$  and  $m$  are the model's parameters,  $\tilde{q}$  is the Mises equivalent stress.

The desired "corrected" strain values present at the lowest diameter of the hourglass-shaped specimen can then be obtained from the simulation's results database. The creep response of a fictitious specimen with a constant diameter equivalent to the minimum specimen diameter of 6 mm is also documented for visualization of the material creep behavior without any influence of the notch effect associated with the hourglass geometry. The material model adjusted in such a manner can then be implemented in a simulation model to describe the creep response of structures of arbitrary geometries.

## 3. Results for WC-Co hard metal

First exemplary step loading creep tests were performed under tension and compression at 700 °C. The used WC-Co hard metal specimen had an average WC grain size of 0.7  $\mu\text{m}$  and a Co binder content of 12 wt.%. In Figure 5 the experimentally determined step loading creep curve is shown for (a.) tension and (b.) compression load. The hard metal specimen fractured under tension load after a total time of 10,783 seconds at a stress level of 1,100 MPa and a total strain value of 0.8%. Under compression load, the specimen did not fracture during the test and was stopped at a stress level of -2,000 MPa and a total strain value of -3.00% after 19,876 s.

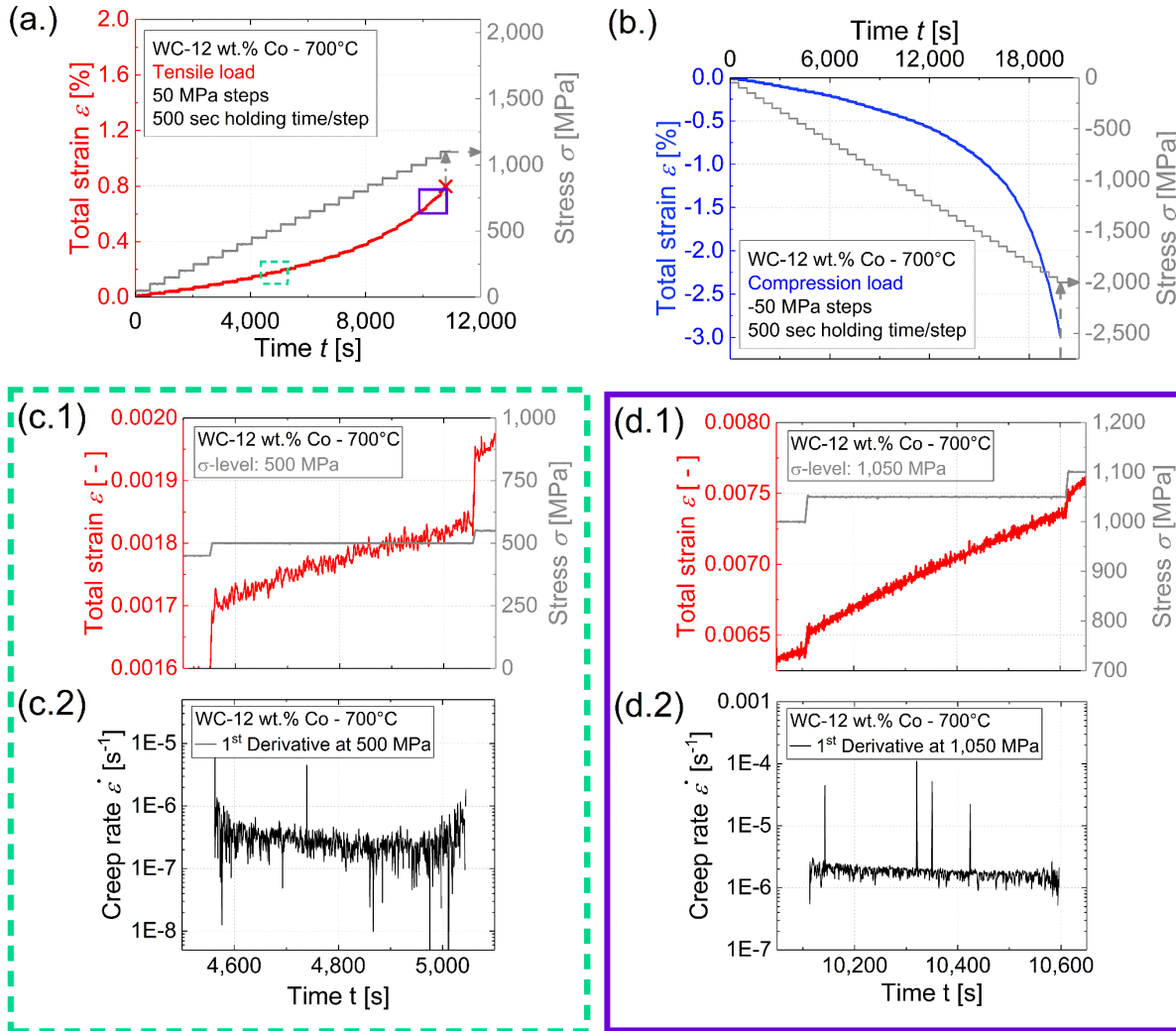


Figure 5: Step loading creep curves attained by the proposed uniaxial step loading creep test setup for a hard metal (WC-12 wt.% Co) at 700 °C under (a.) tensile load (red line) and (b.) compression (blue line) load. In addition to the creep curves, the corresponding applied stress levels (grey lines) are shown; grey dotted arrows indicate the final stress level. (c.) and (d.) are details of (a.), which are marked therein by a dashed green and a solid violet square, respectively. (c.1) and (d.1.) show the tensile step loading creep curve at the stress levels of 500 and 1,050 MPa. (c.2) and (d.2) show creep rate over time for the respective tensile stress levels.

In the tensile step loading creep curve, shown in Figure 5(a.), the 500 MPa and 1,050 MPa stress levels are marked with a dashed green and a solid violet square, respectively. Figure 5(c.1) and Figure 5(d.1) show the respective stress levels in more detail. In general, a graph of the tensile creep rate over time may provide information on the creep rate for all three creep phases [1]. In Figure 5(c.2.) and 5(d.2), the initial part of the curves with decreasing creep rate indicates that the material shows primary creep during this period of

time. If the creep rate stabilized or reached a distinct minimum value within the stress level, this value was interpreted to correspond to the secondary creep rate for the respective applied stress level. If the creep rate showed a distinct non-constant trend within the 500 second observation span, the associated stress level was interpreted to exhibit only primary creep. Note that no clear transition from secondary to tertiary creep was observed in the stress level measured before the specimen failed, see Figure 5(d). It is known from the literature that under certain conditions materials such as metals, cast alloys and ceramics such as silicon nitride do not exhibit all three regions of the creep curve. This can affect primary creep as well as tertiary creep [21,22]. From investigations using hard metal specimen geometries similar to the one used in the current work, it is known that a significant scatter of tensile strength occurs due to defects which are inherent to the material volume [23]. Consequently, it can be assumed that an inherent material defect can cause specimen failure before tertiary creep begins under the applied tensile load.

Under compressive loading, stabilization of the creep rates, i.e. minima of the creep rates were observed at and above a stress of -700 MPa. Higher stresses were observed in compression than under tension before the specimen failed at the end of the creep test. In the present tests, approximately twice as much stress was achieved under compressive load until a total strain value of -3.00%, -2,000 MPa, as under tensile load until a total strain value of 0.8%, 1,100 MPa. It should be noted, the compression test was stopped at a total strain of 3%. If the measurement had not been stopped, the sample would probably have endured much more stress. This is caused by the crack closing effect of compressive stresses present at the time of loading. However, cavities may open in between WC grains within the planes parallel to the loading direction as has been demonstrated for WC-Co hard metals under significantly higher temperature and lower mechanical load as applied in the current specimens [24].

#### **4. Strain corrected compression step loading creep curves**

In addition to the experimental step loading creep tests under tensile and compression stress, a strain correction for the compression step loading creep curve was carried out via finite element simulations. The results are representative also for the tensile step loading creep curve since smaller values of stresses and strains were reached in this case. Figure 6 shows the experimental compression step loading creep curve (blue line - square) and two strain corrected curves (green line - circle and red line - triangle). The green line represents the creep response of a fictitious specimen with a constant diameter equivalent to the minimum specimen diameter of 6 mm (“No-notch-effect”). The red line represents the “corrected” strain values of the hourglass-shaped specimen at its lowest specimen diameter (“Notch-effect”). The strains of the experimentally observed and the strain-corrected curves begin to show a difference at stress levels above -800 MPa, see gray dashed arrows in Fig. 6. The relevant differences in strain between the “Notch-effect”

curve and the experimental curve range between 0.02% at -1,000 MPa and 0.68% at the highest applied stress level at -2,000 MPa.

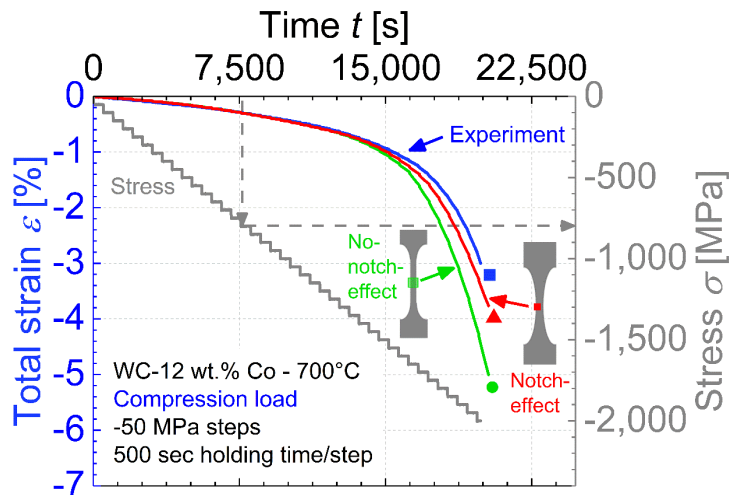


Figure 6: Experimentally observed compression step loading creep curve (blue line - square) with two strain corrected curves (green line - circle and red line - triangle). The green line represents the creep response of a fictitious specimen with a constant diameter of 6 mm (“No-notch-effect”). The red line represents the “corrected” strain values of the hourglass-shaped specimen at its lowest specimen diameter (“Notch-effect”).

## 5. Conclusions

- The current work presents a test setup for an uniaxial step loading creep test under isothermal conditions in vacuum. In contrast to established creep test setups, the currently used specimen geometry was designed to avoid buckling under compressive loading and was thus applicable for the determination of step loading creep curves in tension and compression.
- First exemplary results of the step loading creep test of a WC-Co hard metal grade under tensile load at 700 °C showed minima in the creep rate at and above 500 MPa during the holding time of 500 seconds at each applied stress level. The minimal creep rates were interpreted as the secondary creep rates for the respective stress levels.
- Results under compression loading at 700 °C shows that tests can be performed above -1000 MPa.
- As the used specimen’s cross section is non-constant, the experimentally observed strain values were corrected by means of finite element simulation.

### Acknowledgements

The authors gratefully acknowledge the financial support under the scope of the COMET program within the K2 Center “Integrated Computational Material, Process and Product Engineering (IC-MPPE)” (Project No 859480). This program is supported by the Austrian Federal Ministries for Climate Action, Environment, Energy, Mobility, Innovation and Technology (BMK) and for Digital and Economic Affairs (BMDW), represented by the Austrian research funding association (FFG), and the federal states of Styria, Upper Austria and Tyrol.

### References

- [1] J. Roesler, H. Harders, M. Baeker, *Mechanical Behaviour of Engineering Materials* 1st ed., Springer-Verlag Berlin Heidelberg, 2007, <https://doi.org/10.1007/978-3-542-73448-2>.
- [2] M.E. Kassner, *Fundamentals of Creep in Metals and Alloys*, 3rd ed., Elsevier Science, 2015, <https://books.google.at/books?id=OOp9BAAAQBAJ>.
- [3] J. Granacher, *Zur Übertragung von Hochtemperaturkennwerten auf Bauteile*, VDI-Berichte Nr. 852, VDI-Verlag, Düsseldorf, 1991.
- [4] J. Betten, *Creep Mechanics*, 3rd ed, Springer-Verlag, Berlin Heidelberg, 2008, <https://doi.org/10.1007/978-3-540-85051-9>.
- [5] G. Wirmark, G.L. Dunlop, C. Chatfield, Tensile creep of WC-co cemented carbides at 800 - 900 C, *Sci. Hard Mater. Proc. Int. Conf.* (1986) 153–157.
- [6] R. Useldinger, U. Schleinkofer, Creep behaviour of cemented carbides — influence of binder content, binder composition and WC grain size, *Int. J. Refract. Met. Hard Mater.* 62 (2017) 170–175, <https://doi.org/10.1016/j.ijrmhm.2016.06.013>.
- [7] J.T. Smith, J.D. Wood, Elevated temperature compressive creep behavior of tungsten carbide-cobalt alloys, *Acta Metall.* 16 (1968) 1219–1226, [https://doi.org/10.1016/0001-6160\(68\)90003-5](https://doi.org/10.1016/0001-6160(68)90003-5).
- [8] H.G. Schmid, D. Mari, W. Benoit, C. Bonjour, The mechanical behaviour of cemented carbides at high temperatures, *Mater. Sci. Eng.* 105–106 (1988) 343–351, [https://doi.org/10.1016/0025-5416\(88\)90716-1](https://doi.org/10.1016/0025-5416(88)90716-1).
- [9] J.C. Zunega, *High Temperature Indentation of WC/Co Hardmetals*, University of Southampton, 2013, <https://eprints.soton.ac.uk/id/eprint/352190>.
- [10] B. Roebuck, S. Moseley, Tensile and compressive asymmetry in creep and monotonic deformation of WC/Co hardmetals at high temperature, *Int. J. Refract. Met. Hard Mater.* 48 (2015) 126–133, <https://doi.org/10.1016/j.ijrmhm.2014.08.007>.

- [11] N.E. Dowling, *Mechanical Behavior of Materials: Engineering Methods for Deformation, Fracture, and Fatigue*, 4th ed., Pearson, Boston, MA, 2012 <http://cds.cern.ch/record/2064030>.
- [12] I.P. Giannopoulos, C.J. Burgoyne, Prediction of the long-term behaviour of high modulus fibres using the stepped isostress method (SSM), *J. Mater. Sci.* 46 (2011) 7660–7671, <https://doi.org/10.1007/s10853-011-5743-x>.
- [13] R.J. Miller, Design approaches for high temperature composite aeroengine components, *Compr. Compos. Mater.* (2000) 181–207, <https://doi.org/10.1016/B0-08-042993-9/00138-8>.
- [14] R. Goti, B. Viguier, F. Crabos, Effect of thermal cycling on high temperature creep of coated CMSX-4, *Superalloys 2012* (2012) 411–419, <https://doi.org/10.1002/9781118516430.ch45>.
- [15] W.-G. Kim, J.-Y. Park, I.M.W. Ekaputra, S.-J. Kim, J. Jang, Influence of hold time and stress ratio on cyclic creep properties under controlled tension loading cycles of grade 91 steel, *Nucl. Eng. Technol.* 49 (2017) 581–591, <https://doi.org/10.1016/J.NET.2016.11.007>.
- [16] D.H. Jack, Ceramic cutting tool materials, *Mater. Des.* 7 (1986) 267–273. [https://doi.org/10.1016/0261-3069\(86\)90053-1](https://doi.org/10.1016/0261-3069(86)90053-1).
- [17] T. Tepperneegg, T. Klünsner, C. Kremsner, C. Tritremmel, C. Czettl, S. Puchegger, S. Marsoner, R. Pippan, R. Ebner, High temperature mechanical properties of WC–Co hard metals, *Int. J. Refract. Met. Hard Mater.* 56 (2016) 139–144. <https://doi.org/10.1016/J.IJRMHM.2016.01.002>.
- [18] D. Mari, D.R. Gonseth, A new look at carbide tool life, *Wear.* 165 (1993) 9–17, [https://doi.org/10.1016/0043-1648\(93\)90366-T](https://doi.org/10.1016/0043-1648(93)90366-T).
- [19] S.N. Basu, V.K. Sarin, Oxidation behavior of WC-Co, *Mater. Sci. Eng. A.* 209 (1996) 206–212. [https://doi.org/10.1016/0921-5093\(95\)10145-4](https://doi.org/10.1016/0921-5093(95)10145-4).
- [20] K.P. Mingard, B. Roebuck, Private communication at EHMG Summerv 2016 - Examining High Temperature Deformed Structures in the SEM, (2016).
- [21] D.J. Wulpi, *Understanding How Components Fail*, 3rd ed., ASM International, 2013.
- [22] M.J. Hoffmann, G. Petzow, *Tailoring of Mechanical Properties of Si<sub>3</sub>N<sub>4</sub> Ceramics*, 1st ed., Springer Netherlands, 1994. <https://doi.org/10.1007/978-94-011-0992-5>.
- [23] M. Jonke, T. Klünsner, P. Supancic, W. Harrer, J. Glätzle, R. Barbist, R. Ebner, Strength of WC-Co hard metals as a function of the effectively loaded volume, *Int. J. Refract. Met. Hard Mater.* (2017). <https://doi.org/10.1016/j.ijrmhm.2016.11.003>.
- [24] M.A. Yousfi, J. Weidow, A. Nordgren, L.K.L. Falk, H.-O. André, Deformation mechanisms in a WC–Co based cemented carbide during creep, *Int. J. Refract. Met. Hard Mater.* 49 (2015) 81–87. <https://doi.org/10.1016/j.ijrmhm.2014.07.016>.

## **Publication II**

**A physical reason for asymmetric creep deformation  
behaviour of WC-Co hardmetal under tension and  
compression loading at 700 °C and 800 °C**

**Kathrin Maier, Thomas Klünsner, Werner Ecker, Philip Pichler,  
Stefan Marsoner, Christoph Czettl, Jonathan Schäfer, Reinhold Ebner**

**Published in**

**International Journal of Refractory Metals & Hard Materials,  
97 (2021) 105526**

## **A physical reason for asymmetric creep deformation behaviour of WC-Co hardmetal under tension and compression loading at 700 °C and 800 °C**

Kathrin Maier<sup>1\*</sup>, Thomas Klünsner<sup>1</sup>, Werner Ecker<sup>1</sup>, Philip Pichler<sup>1</sup>, Stefan Marsoner<sup>1</sup>,  
Christoph Czettel<sup>2</sup>, Jonathan Schäfer<sup>2</sup>, Reinhold Ebner<sup>1</sup>

<sup>1</sup> Materials Center Leoben Forschung GmbH, Roseggerstraße 12, 8700 Leoben, Austria

<sup>2</sup> CERATIZIT Austria GmbH, Metallwerk-Plansee Straße 71, 6600 Reutte, Austria

\*Corresponding author: kathrin.maier@mcl.at

**Keywords:** WC-Co hardmetal; Uniaxial step-loading creep test; Elevated temperature; Tension and compression strain asymmetry; Cavity formation; EBSD

### **Abstract**

WC-Co hardmetals are popular tool materials, which are used in applications such as metal milling or turning. In these applications, elevated temperatures occur in the tools during the machining process, although they are also cooled. This results in a complex interaction of thermal and mechanical loads in the tools. Within this current work, a strain asymmetry of a WC-10 wt.% Co hardmetal after tensile and compression uniaxial step-loading creep tests is described. Two types of tests were performed: Firstly, specimens were deformed to certain strain limits at 700 °C and 800 °C. Strain asymmetry was observed for tensile and compression stresses above 600 MPa at 700 °C and above 250 MPa at 800 °C. In the second type of test, the specimens were stepwise loaded up to a stress of 300 MPa under tensile and compressive load at 800 °C. The aim of test 2 was to identify the physical reason for the strain asymmetry from the first tests at 800 °C. The material's microstructure was analyzed for the specimens from test 2 by scanning electron microscopy (SEM) and electron backscatter diffraction (EBSD). The influence of the loading type was analyzed with regard to damage development and deformation behavior of the WC- and Co-phase. SEM images showed that the faster increase in strain over time under tensile than under compressive loading was caused by the formation of cavities at WC-WC interfaces and at WC-Co phase boundaries. Due to the larger number of observed microdefects under tension than under compression, it was assumed that this was the physical reason for the strain asymmetry. In addition, EBSD data showed that during the compression and tension creep tests, the fcc Co-phase was partially transformed into the hcp Co-phase.



## 1. Introduction

Applications of hardmetals are diverse and different types of loads and temperatures can occur [1]. By simulations, it is possible to represent the cutting process by the stresses and temperatures over time induced in the tool [2–4]. Depending on the load situation and temperature, damage such as cavity formation and subsequent cracking can occur. During milling using hardmetal tools temperatures can rise up to 800 °C [2]. As a result, thermal activation of creep processes plays a significant role for material damage evolution in addition to other phenomena that drive plasticity and associated fatigue.

Contributions of thermally activated processes, like diffusion or grain boundary diffusion, change the mechanisms of plastic deformation with temperature, and thus complicate the interpretation of force/displacement data [5]. In four-point bending test, it is possible to determine the maximum surface strain of tension and compression separately using strain gauges. However, often a large computational effort is required to attain separate strain values of tension and compression. Furthermore, due to the simultaneous occurrence of both types of loading in the same specimen, an influence on each other cannot be ruled out. Therefore, the separation between the tensile and compression strain values is not perfectly given, which leads to difficulties when interpreting strain data [6]. Uniaxial tests are preferable to facilitate a straight-forward interpretation of the data, since tests can be performed specifically under compression or tension. At elevated temperatures, hardmetals exhibit high strength [7], which has to be taken into account for tests under uniaxial loading conditions. Hence, there is a risk of specimens buckling under high uniaxial compressive loads. In order to prevent buckling of hardmetals, uniaxial tests are recommended to be performed using specimen geometries with non-constant diameters [8,9].

In order to investigate the influence of the type of load application in material testing set-ups on observed material behaviour, many researchers in the fields of ceramics, metal matrix composites and metals have tested and compared different load types [10–12]. Bending tests and also uniaxial tensile and compression tests have shown an asymmetric strain response of siliconized silicon carbide and hardmetals under tension and compression [6,11,13]. Roebuck et al. [11] performed alternately tension and compression electro-thermo-mechanical tests on WC-Co hardmetals at 1000 °C, recognizing an asymmetry of the stress-strain response. Also, the tensile creep rate was significantly higher at the same load than for compression. Roebuck et al. [11], undertook no microstructural investigations and did not identify which phenomena in the WC-Co microstructure are responsible for the strain asymmetry. Depending on the experimental set-up, different deformation mechanisms occur in the hardmetal specimens: elastic deformation or transgranular fracture of the cobalt (Co) or carbide (WC) phase, stress-assisted mass transport of the binder phase, cracking or sliding of interfaces between WC/Co or WC/WC, cavity formation at interfaces and within the Co-phase, and plasticity based on dislocation movement of one of the two phases [5,14,15]. In addition, the phase fractions of face-centered cubic (fcc) and hexagonally close-packed (hcp) structure in the Co-binder

have to be considered [16]. The diffusionless transformation of fcc Co into hcp Co influences the mechanical properties of the hardmetal during deformation [17–19]. The mechanical properties of the composite as a whole are influenced by the different deformation behaviour of both crystal phases, since they have a different number of slip systems [19].

In ceramics the formation of cavities or microcracks is an essential part of deformation. Tensile deformation is supported by preferred crack formation in the microstructure [20]. In contrast, compression loading inhibits plastic deformation by delaying the formation of microcracks. [21]. Hence, strain asymmetry in ceramics is attributed to the accelerated failure of specimens under tensile stress, which is based on increased cavity formation [10,20–23].

The current work investigated the strain asymmetry of a WC-10 wt.% Co hardmetal in uniaxial tensile and compression step-loading creep tests with subsequent scanning electron microscopy (SEM) and electron backscattering (EBSD) investigations. The effect of strain, phase transformation in the Co-phase and damage initiation under tensile and compression loading and their influence on the strain asymmetry are discussed.

## 2. Experimental details

The creep behavior of a hardmetal was analyzed as a function of tensile and compression loading at temperatures of 700 °C and 800 °C by an uniaxial step-loading creep test. The specimens were WC-Co hardmetals with an average WC grain size of 2.0 µm and a Co-content of 10 wt.%. Due to the elevated levels of mechanical property values of hardmetals at elevated temperatures [7], the specimens had an hourglass-shaped geometry, in order to prevent buckling during compression loading [8]. Note, that due to the non-constant specimen diameter within the strain gauge length, the measured strain values underestimated the actual strain values associated with the nominal stress in the specimen at its smallest diameter [8,24]. Although, strain correction is necessary to account for the hourglass shape of the specimen, according to Maier et al. [24] there is no significant deviation in strain between the experiment and the correction at low stress levels. Since the strain asymmetry occurs at low stresses, no strain correction was necessary.

The tensile and compression step-loading creep tests, as also described in detail in [24], were carried out by a servo-hydraulic testing machine (Instron 8803) including a vacuum chamber to avoid specimen oxidation. Each uniaxial creep test, tensile or compression loading, was performed using a new hourglass-shaped specimen. Hence, tensile and compression tests were analyzed separately without influence from previous compression/tensile loads. This was deemed necessary, since load history may affect the material deformation behavior at elevated temperature [11]. Contrary to standard creep experiments, the load was increased stepwise by 50 MPa and kept constant at each stress level for 500 s. The load increase was carried

out within 5 seconds, so that creep that occurs during the load change itself can be neglected. Tests were completed when a certain criteria had been reached, for example a stress level or strain value was surpassed, or the specimen had failed. If the specimen did not fail during the test, it was unloaded after the last applied stress level. To investigate the strain asymmetry, a test series referred to as “test 1” were carried out up to 2% strain under tension, and 3% strain under compression load, both at 700 °C and 800 °C. From the measured strain-time curves, it was possible to identify the start stress level of the strain asymmetry between tensile and compression loading, termed as onset-stress of strain asymmetry. In “test 2”, the same kind of tests performed for compressive and tensile load were carried out up to 300 MPa at 800 °C, which was 50 MPa above the onset-stress of strain asymmetry of test 1, to investigate the microstructure at (or close to) the start stress level of the strain asymmetry. Additionally, the minimal creep rates were determined for each investigated stress level and the associated time span, which was interpreted as the secondary creep rate for the corresponding stress level [24]. This allowed estimation of the initial stress level for secondary creep in the step-loading creep curves [24].

During the step-loading creep tests, axial strain was measured contactlessly with a high precision laser extensometer (P-2S-50/400 Hz, Fiedler Optoelektronik GmbH, class of accuracy of 0.2, ISO 9513) using measuring marks placed 4 mm on either side of the axial center of the hourglass-shaped specimen. The accuracy class 0.2, as defined in the international standard ISO 9513 [25] respectively in DIN EN 10002-4, describes the deviation of the measured strain from the correct strain. The value of 0.2 for the used laser extensometer means that the maximum deviation is  $\pm 0.2\%$  of the measured strain value or  $\pm 3$  times  $0.2 \mu\text{m}$  - whichever is greater. Error estimates based on information from the laser extensometer were performed to investigate differences in the presented strain values and to define a non-significant strain difference value of  $0.02\%$ . The specimens were inductively heated by eddy currents induced by an internally water-cooled copper coil. The thermal stability at the specimen center was controlled by thermocouples. To avoid oxidation of the surface at elevated temperatures, a vacuum chamber was used with a pressure of  $5 \cdot 10^{-6}$  mbar [24].

The specimens from test 2 were analyzed by scanning electron microscopy (SEM, GeminiSEM ® 450 / Carl Zeiss SMT) using secondary electron mode. Pieces of the hourglass-shaped specimens were taken from the center of the minimum diameter. Metallographic specimens were prepared with argon ion polishing as the final surface preparation step, which removed the deformed surface layers introduced during cutting and polishing [26]. The investigated cross-sectional plane was oriented perpendicular to the direction of loading in order to observe more effectively the crack initiation in compression. Under tensile loading, it was assumed that cracks were also clearly visible perpendicular to the direction of loading, albeit with a smaller number than parallel to the loading. The microstructure was investigated at three positions in the center of a cross section prepared at the minimum specimen diameter about  $500 \mu\text{m}$  away from each other,

within the argon polished area. To make a statistically sound comparison of the defect density in the microstructures, a counting of the number of microdefects was carried out manually for SEM micrographs of an individual size of  $11.3 \mu\text{m} \times 7.8 \mu\text{m}$  attained using secondary electron contrast mode using an InLens detector arrangement for a total area of  $3000 \mu\text{m}^2$  per investigated deformation state.

Phase transformations and plastic deformation in the WC- and Co-phases were analyzed by electron backscatter diffraction (EBSD) on the same tensile and compression loaded specimens investigated by SEM. The EBSD analysis (System: Symmetry / Oxford Instruments) was performed at 15 kV acceleration voltage and an applied step size of 50 nm to measure a total area of  $38.3 \mu\text{m} \times 28.8 \mu\text{m}$ . The specimen was tilted  $70^\circ$  in the direction of the EBSD camera and the working distance was 15 mm. A software-based evaluation of eleven Kikuchi bands with a Hough space resolution of 95 was performed. The software package “Orientation Imaging Microscopy” (OIM) version 7 from EDAX [27] was used to determine the kernel average misorientation (KAM) using the 1st nearest neighbor with a maximum misorientation angle of  $2^\circ$ . KAM maps can be used to show differences in dislocation density which gives additional information about lattice distortion and deformation localization [28]. Inverse pole figures (IPF) evaluations were performed with “MTEX Toolbox” version 5.3 [29] in Matlab Version R2019b for all phases to identify crystal orientation changes caused by plastic deformation and to determine the phase distributions. No grain dilation cleanup was applied to the generated EBSD data.

### 3. Results

#### 3.1. Step-loading creep curves

The tensile and compression step-loading creep curves at (a.)  $700^\circ\text{C}$  and (b.)  $800^\circ\text{C}$  for WC-10 wt.% Co are presented in Fig. 1. At  $700^\circ\text{C}$ , the tensile loaded specimen failed at a stress level of about 1000 MPa shortly before reaching the preset 2.0% strain limit. For compression, the specimen reached 3.0 % strain at about 1550 MPa. In the tests at  $800^\circ\text{C}$ , Fig. 1(b.), the tensile step-loading creep curve reached the preset strain limit value of 2.0% at about 600 MPa without fracture. Under compression, the step-loading creep test stopped at the strain limit of 3.0% at a stress level of about 1000 MPa.

It can be seen that for tensile loading, strain increased faster than under compression loading. Curve separation as a function of absolute values of stress with increasing time is termed strain asymmetry. At  $700^\circ\text{C}$ , the strain asymmetry was already present at very low stress levels. The tensile and compression step-loading creep curves exhibited a slight change in slope up to about 600 MPa. A comparison of the curves for individual equal stress levels revealed that the curves show a parallel shift of the curves attained under tensile load to greater absolute strain values compared to the ones attained under compressive load. The parallel shift of the step-loading creep curves was caused by the measuring accuracy class of the applied Laser extensometer of 0.2, which means that differences in strain values smaller than 0.02% could not be

regarded as significant. Hence, the strain data at 0.02% sometimes exhibited elongation instead of shortening, or vice versa. Furthermore, the whole step-loading creep curve shifted to smaller strain values for compression loading, see Fig. 1(a.). At 600 MPa, there was a significantly more pronounced curvature of the tensile step-loading creep curve than the compressive one, which was interpreted as the onset of the strain asymmetry. At 800 °C, the strain asymmetry was determined in the same manner, and started at a stress level about 250 MPa.

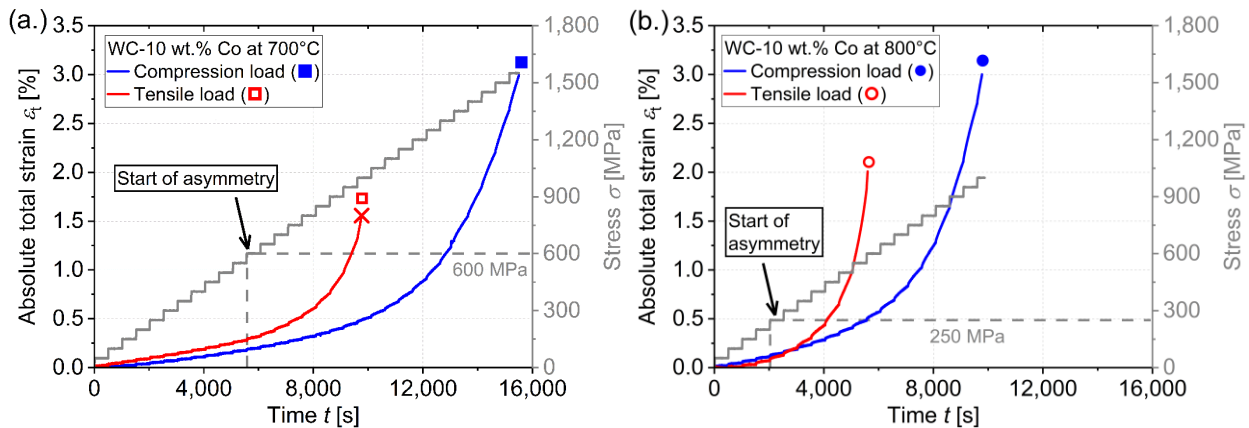


Fig. 1: Tensile (red - square / circle) and compression (blue - filled square / circle) step-loading creep curve at (a.) 700 °C and (b.) 800 °C of WC-10 wt.% Co. Above 600 MPa and 250 MPa (grey - dashed line), a difference in the step-loading creep curve shape between tensile and compression, or strain asymmetry, is seen. For the interpretation of colour, the reader is referred to the online-version of this article.

The strain asymmetry was analyzed in more precisely for test 2 at 800 °C and stress levels up to 300 MPa. Fig. 2 shows the tensile and compression step-loading creep curves from the test 2. In the first two loading levels for tension, a shortening of the specimen instead of an extension was observed, which was attributed to the measurement uncertainty of the laser extensometer used which was of the order of magnitude of the measured strain values. However, the tension and compression step-loading creep curves differed significantly above about 200 MPa, with a significantly faster strain accumulation for the tensile load than compression.

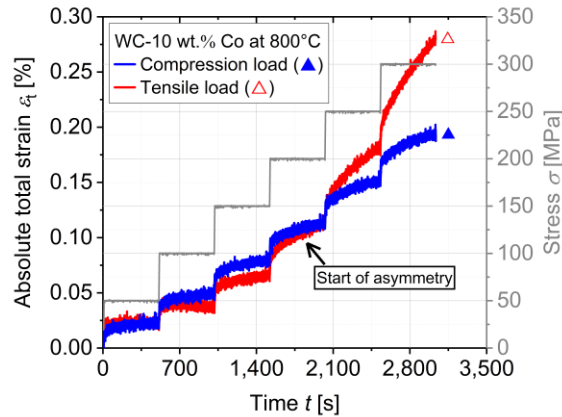


Fig. 2: Tensile (red - triangle) and compression (blue - filled triangle) step-loading creep curves from test 2 for WC-10 wt.% Co up to 300 MPa at 800 °C. Strain asymmetry starts at 200 MPa. For the interpretation of colour, the reader is referred to the online-version of this article.

The minimal creep rates,  $\dot{\epsilon}_{min}$ , determined at the end of each stress step at 800 °C are shown in Fig. 3. There were significant differences in the observed  $\dot{\epsilon}_{min}$  values for tension and compression above the respective stress values of 200 MPa in test 1, and above 150 MPa in test 2. The step-loading creep curve shapes of both tests were similar. The creep rate under tensile loading was higher than for compressive loading at the same stress level until the end of the test. This difference between tensile and compression load increased significantly with increasing stress. In test 1 at  $1.3 \cdot 10^{-4}$  1/s, the creep stress level under tension was 350 MPa, in contrast, under compression the same minimal creep rate value was reached at a creep stress level of 600 MPa. Additionally, twice as much tension was required under compressive load to achieve the tensile creep rate.

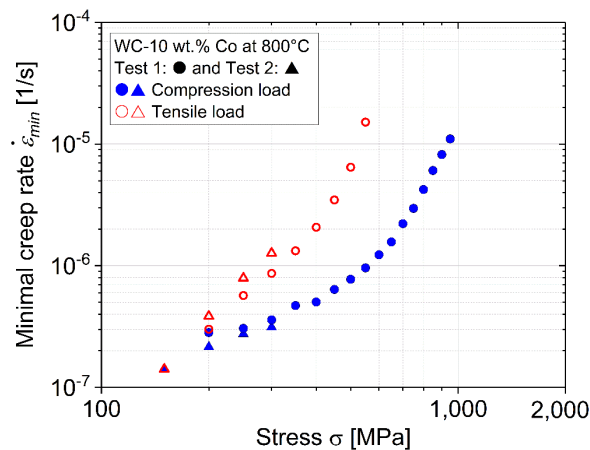


Fig. 3: Minimal creep rate  $\dot{\epsilon}_{min}$  for each individual stress level for all four specimens made of WC-10 wt.% Co tested under tensile (red) and compression (blue) loading conditions at 800 °C. Test 1, circles, shows the minimal creep rates for the stress levels from 200 MPa to 950 MPa under compression and from 200 MPa to 550 MPa under tension. Test 2, triangles, shows the rates from 150 MPa to 300 MPa for both loading conditions. For the interpretation of colour, the reader is referred to the online-version of this article.

### 3.2 Microstructure analysis

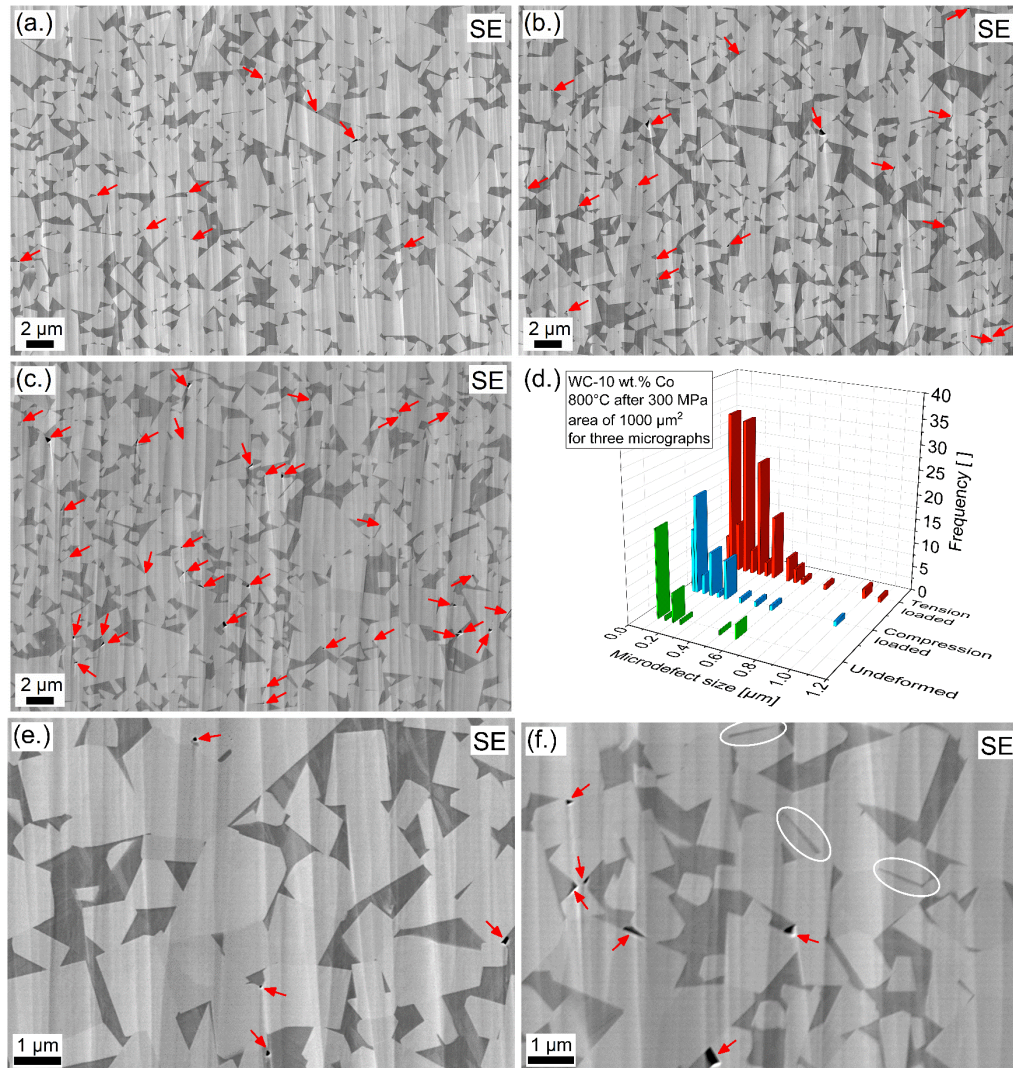


Fig. 4: SE micrographs of WC-10 wt.% Co: (a.) undeformed, after testing at 800 °C up to 300 MPa stress in test 2 under (b.) compression, and (c.) tension. The load direction point out of the image planes; red arrows mark microdefects. (d.) Microdefect size distribution over frequency for three micrographs as shown in (a.) to (c.) for an area of 1000 μm<sup>2</sup>. Enlarged representation of the deformed microstructure under compression (e.) and tension (f.). Microdefects are marked with red arrows and possible Co penetration with white ovals.

Fig. 4(a.) shows the microstructure of undeformed WC-10 wt.% Co. Fig. 4(b.) and 4(c.) show the microstructure after loading in test 2 up to 300 MPa at 800 °C for compression and tension tests, respectively. Comparing the undeformed and deformed microstructure, shows increased microdefects like nanopores and slightly larger cavities up to maximum dimension of about 1.0 μm and Co penetration, Fig. 4(e.) and 4(f.). The regions in which the observed microdefects were nucleated appeared slightly darker than the darker grey regions of the Co-binder, and are marked with red arrows in Fig. 4. Distinct cracks had not yet formed after reaching the stress level of 300 MPa in test type 2. Fewer and smaller microdefects

were detectable in the specimen loaded in compression, see Fig. 4(b.) and 4(e.), compared to that in tension, see Fig. 4(c.) and 4(f.). To make a statistically sound comparison of the defect density in the hardmetal microstructures, a counting of the number of microdefects was carried out for SEM micrographs such as shown in Fig. 4(e.) to Fig. 4(f.) for a total area of  $3000 \mu\text{m}^2$  per investigated deformation state. Next to the defect density, the defect size was also determined manually in the described way. The average microdefect number per image was 9, 17 and 39 for the undeformed, compression and tensile loaded specimens, respectively. In the investigated microstructures, more than twice as many microdefects formed under tension than under compression. Fig. 4(d.) shows the microdefects' size distribution over the frequency of their occurrence. The most frequent defect size, related to the total length, observed in the undeformed specimen was in the order of  $0.1 \mu\text{m}$  and only a few defects were larger. After loading up to 300 MPa, microdefects such as cavities or nanopores sizes were well below the hardmetal's average WC grain size of  $2.0 \mu\text{m}$ . The compression-loaded specimen as well as the tensile-loaded specimen showed a broader microdefect size distribution than the undeformed one, but the most frequent microdefect size is also about  $0.1 \mu\text{m}$ . Most of these microdefects had formed at sharp corners at triple phase boundaries, i.e. at WC/WC/Co interface junctions, at WC grain boundary triple points or in narrow Co ligaments between WC grains.

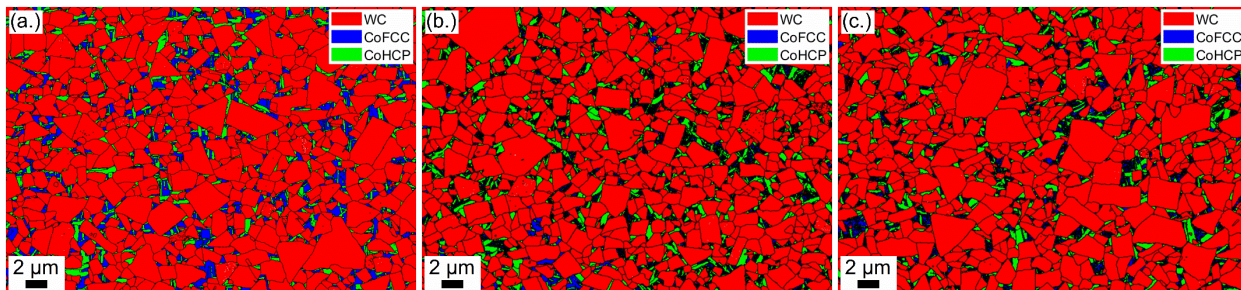


Fig. 5: EBSD phase images of WC-10 wt.% Co hardmetal specimens, showing WC (red), fcc Co (blue), hcp Co-phase (green) and grain boundaries: (a.) undeformed, (b.) compression loaded and (c.) tension loaded specimens. Loading conditions were testing in a step-loading creep test at  $800 \text{ }^\circ\text{C}$  up to 300 MPa, i.e. just after the onset of the strain asymmetry. The load direction points out of the image plane. For the interpretation of colour, the reader is referred to the online-version of this article.

Table 1: Phase fractions of WC, fcc Co and hcp Co in the undeformed specimen and the ones deformed in compression and tensile step-loading creep tests up to a stress level of 300 MPa at  $800 \text{ }^\circ\text{C}$ .

Phase	Area fraction of the hardmetal phases (%)		
	Undeformed	Compression loaded	Tensile loaded
<b>Not Indexed</b>	0.7	1.5	0.9
<b>WC</b>	82.0	82.0	83.0
<b>fcc Co</b>	8.3	4.5	5.1
<b>hcp Co</b>	9.0	12.0	11.0



EBSD data allowed the calculation of the phase distribution of WC grains, fcc Co and hcp Co-phase from an image section of  $38.3 \mu\text{m} \times 28.8 \mu\text{m}$ , Fig. 5. In the undeformed WC-10 wt. % Co, the Co-binder was present as both fcc and hcp, see Fig. 5(a). Table 1 lists the phase fractions of the different phases and deformation conditions. After compression or tensile step-loading creep tests, the fcc to hcp phase ratio decreased, see Fig. 5 and Table 1.

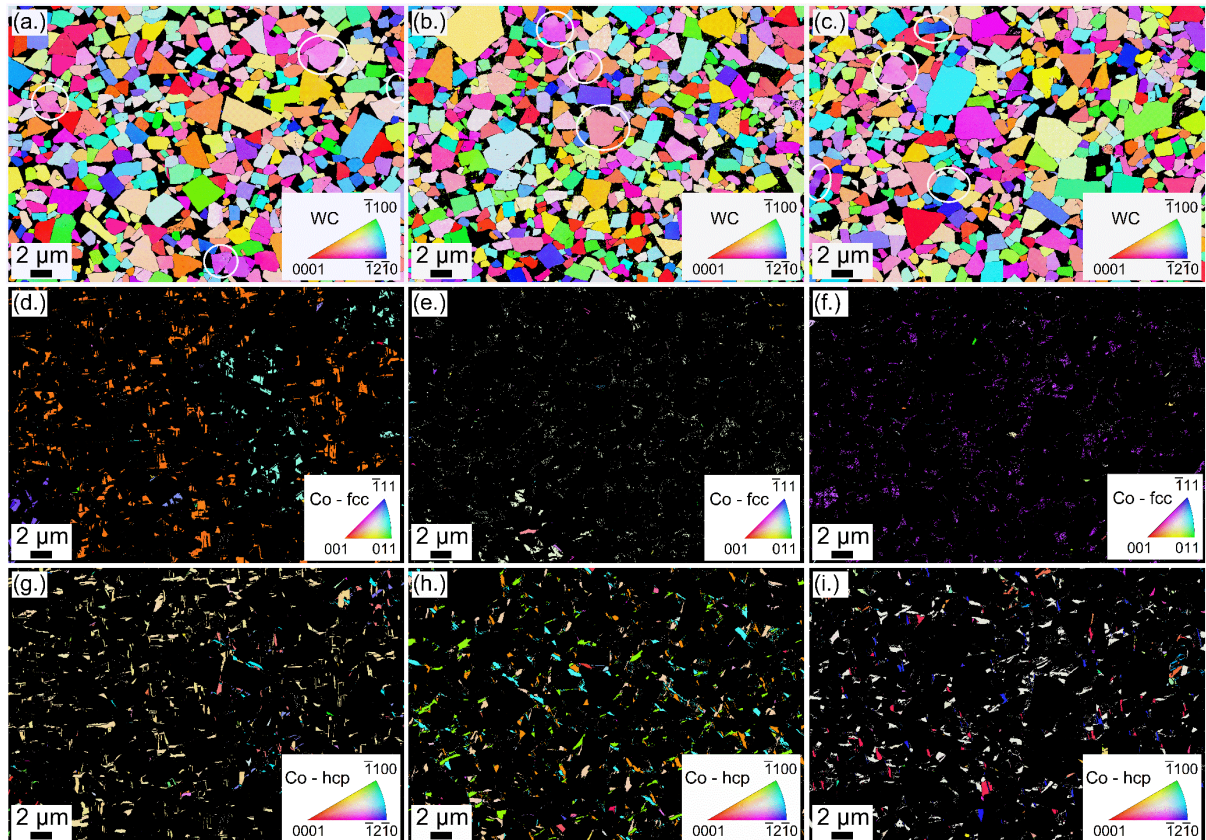


Fig. 6: EBSD inverse pole figure (IPF) maps of the investigated WC-10 wt.% Co hardmetal specimens are grouped according to the respective shown phases in horizontal rows: WC in (a.) to (c.); fcc Co in (d.) to (f.); and hcp Co in (g.) to (i.). The same deformation state is shown in the individual vertical columns: (a.), (d.), (g.) undeformed; (b.), (e.), (h.) compression creep deformed; and (c.), (f.), (i.) tensile creep deformed. Test conditions for deformed specimens: Uniaxial step-loading creep tests at  $800 \text{ }^\circ\text{C}$  up to 300 MPa. WC grains with crystal orientation change within the grain are marked with a white oval. The load directions point out of the image plane. For the interpretation of colour, the reader is referred to the online-version of this article.

In order to study the effect of straining in step-loading test on microstructural changes, inverse pole figure (IPF) calculations were carried out using EBSD data. In IPF, the individual grains are displayed in different colours according to their crystal orientation [30]. All phases were characterized in the undeformed as well as in loaded specimens at  $800 \text{ }^\circ\text{C}$  until a stress level of 300 MPa was reached in compression and tension, as shown in Fig. 6(a.) to 6(i.). Certain WC grains show a distinct crystal orientation change within a grain,

i.e. a change in the colour or a colour gradient, Fig. 6(a.) to 6(c.). The proportion of WC grains with such a distinct crystal orientation changes was the same in all three investigated specimens.

Fig. 6(d.) to 6(f.) show the IPF maps for the fcc Co-phase. The IPF maps for the hcp Co-phase is presented in Fig. 6(g.) to 6(i.). In the undeformed specimen, the Co-phase was observed to exhibit regions of same orientation, same colour, for both binder phases, hcp and fcc. Even after deformation, regions of same crystal orientations, were observed for fcc Co. In contrast, the size of hcp Co-regions of same crystal orientations decreased during deformation, compare Fig. 6(g.) with 6(h.) and 6(i.). Also, Mingard et al. [31] showed from 3D IPF maps that Co-regions with the same crystal orientation belong together and represent a large grain.

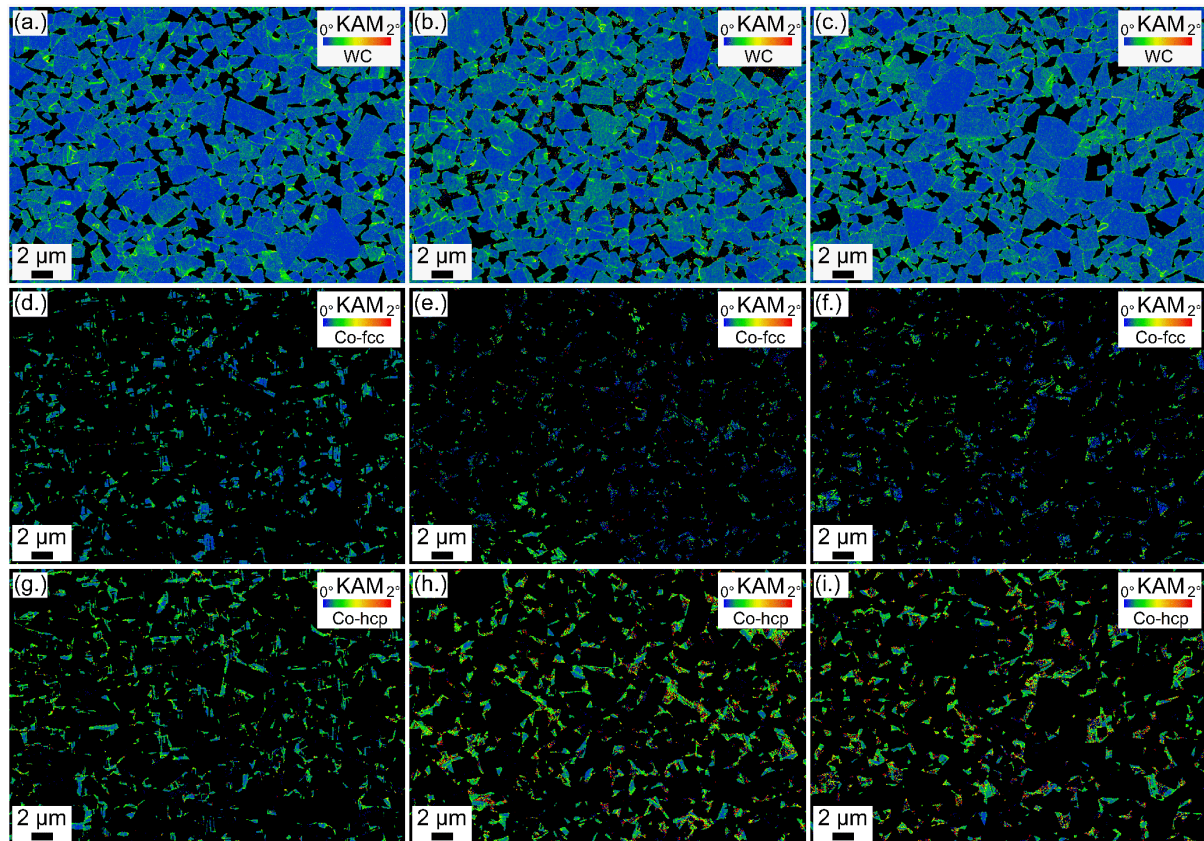


Fig. 7: EBSD kernel average misorientation (KAM) maps of the investigated WC-10 wt.% Co hardmetal specimens are grouped according to the respective shown phases in horizontal rows: WC in (a.) to (c.); fcc Co in (d.) to (f.); and hcp Co phase in (g.) to (i.). The same deformation state is shown in the individual vertical columns from left to right: (a.), (d.), (g.) undeformed; (b.), (e.), (h.) compression creep deformed; and (c.), (f.), (i.) tensile creep deformed specimens. The misorientation angle is shown from  $0^\circ$  to  $2^\circ$ . Test conditions for deformed specimens: Uniaxial step-loading creep at  $800^\circ\text{C}$  up to 300 MPa. The load direction points out of the image plane. For the interpretation of colour, the reader is referred to the online-version of this article.

Kernel average misorientation (KAM) calculations were performed to study local dislocation density differences and strain localizations. The color gradient from blue to red indicates misorientations

from  $0^\circ$  to  $2^\circ$  for the individual phases. In Fig. 7(a.) to 7(c.), the KAM maps for the WC phase are shown. Fig. 7(d.) to 7(f.) show the KAM maps for the fcc Co-phase, and Fig. 7(g.) to 7(i.), the KAM maps for hcp Co-phase. Additionally, the KAM maps in Fig. 7 are displayed in Fig. 8 as a distribution of the fraction of all indexed points in the entire EBSD image over the respective KAM values for each material phase. The comparison of the KAM charts indicates that no change in the KAM distribution in the WC grains were observed, Fig. 8(a.) and 8(d.). In contrast, a decrease in small misorientations, gray arrow, and a slight increase in higher misorientations, black arrow, occurred after creep tests in both Co-phases, see Fig. 8(b.) and 8(c.). This is also observed in the cumulative KAM charts, see Fig. 8(e.) and 8(f.).

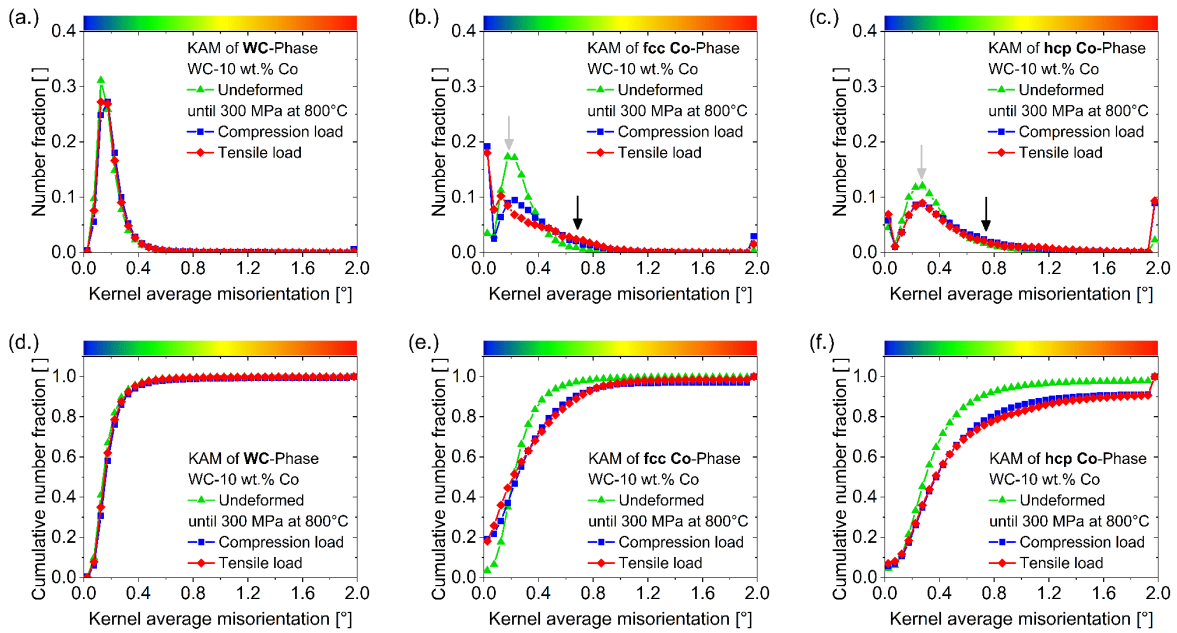


Fig. 8: Kernel average misorientation (KAM) charts ranging from  $0^\circ$  to  $2^\circ$  for (a.) the WC, (b.) the fcc Co and (c.) the hcp Co-phase with all three load cases compared: undeformed (green - triangle), compression deformed (blue - square) and tensile deformed (red - diamond) at  $800^\circ\text{C}$  up to 300 MPa. Cumulative KAM number fraction charts for (d.) WC, (e.) fcc Co and (f.) hcp Co-phase also for all three load cases. For the interpretation of colour, the reader is referred to the online-version of this article.

#### 4. Discussion

The results indicated that for low tensile and compressive stresses, creep behavior had similarities, at  $700^\circ\text{C}$  and at  $800^\circ\text{C}$ . As temperature increased, the onset-stress of strain asymmetry for tension and compression loading decreased, see Fig. 1. Furthermore, the strain under tension increased significantly with time after exceeding the onset-stress for the onset of strain asymmetry. Consequently, the strain increased faster at  $800^\circ\text{C}$  than at  $700^\circ\text{C}$  because of the greater difference from the onset-stress. Higher number densities of cavities were found after the onset-stress of strain asymmetry for tensile loaded specimen at  $800^\circ\text{C}$  than for compression loaded and undeformed specimens, see Fig. 4(a.) to 4(c.).

For minimal creep rate of test 1 and 2 at 800 °C, shown in Fig. 3, similar values were obtained for the compression and tensile deformed specimens at low stresses. The onset-stress of strain asymmetry differed by about 50 MPa between test 1 and 2, but the values of the creep rate were very similar for the tensile and compression loaded specimens, see Fig. 3. The difference in the onset-stress for strain asymmetry may be caused by: The slightly different WC grain size distribution and Co-binder ligament size distribution between WC grains in each hardmetal specimen in the region of maximum strain causing not exactly equal contributions to the total deformation by WC and Co, or by defects that are inherent in the material volume [9]. Jonke et al. [9] showed that these defects are present in the form of pores and individual larger WC grains. These are preferred starting points for stress gradients, especially pores act as notches under tensile load and accelerate the damage development in the microstructure. Roebuck et al. [11] performed creep experiments at 1000 °C with 150 MPa as lowest applied stress, whereby no symmetry contribution was observed comparing tensile and compression creep rates. In the current work, a decrease of the onset-stress of strain asymmetry was observed from 600 MPa to 250 MPa as temperature increased from 700 °C to 800 °C, shown in Fig. 1. As the creep curves, and the creep rates at low stresses were symmetrical, it was concluded that the creep mechanisms were identical in this range. To achieve the same creep rate under tensile and compressive loads, approximately twice the stress was required for the compression load at 800 °C. This agrees with values for ceramic materials [22,23], like glass-ceramics and silicon nitride, which lists a stress factor of two and above to achieve the same creep rate for compression and tension.

The microstructure of specimens from test 2 revealed that an increased number of microdefects was present above the onset-stress of strain asymmetry. These results agree with reports on siliconized silicon carbide [6,20] and glass-ceramics [22]: It was also observed that they underwent creep faster under tension than under compression loading. The investigation of the microstructure showed that for lithium zinc silicate glass-ceramics, cavity formation occurred within the glassy phase under both tensile and compression loads, with more cavities identified in the tensile-deformed specimen [22]. For Si/SiC composite materials, tensile creep is controlled by silicon deformation and cavity formation at Si/SiC interfaces, while compression creep is controlled by silicon carbide deformation but no cavity formation occurs [6,20]. In contrast to the current work, all reported ceramic specimens were kept at constant stresses and temperatures for several hours, which led to more than 5% larger strains than induced in the current work.

Since the number of microdefects that formed under the applied creep load was larger under tension than under compression, see Fig. 4(d.), this was assumed to be one of the physical reasons for the strain asymmetry, see Fig. 1 to 3. It is assumed in some point of loading, the fields of stress concentration associated with the cavities may have started to interact, which would foster the cavities' growth and consequently their contribution to the observed material failure. Hence, diffusion or dislocation slip or climb are interpreted to be no longer the only deformation mechanism. Instead, the formed cavities, or in later

loading stages also cracks, contributed significantly to the observed strain. Damage formation and fracture paths of WC-Co hardmetals at room temperature were analyzed in more detail by Sigl et al. [32,33] and Fischmeister [34]. Known fracture paths were transgranular fracture through the Co- or WC-phase and crack formation or sliding of interfaces at WC/Co or WC/WC interfaces [5,15,32]. Additionally, three crack zones have been observed in WC-Co hardmetals under monotonically increasing load [32]. In the first zone, both phases deform elastically and the microstructure is still completely coherent. The second zone is referred to as the multiligament zone, which describes crack formation between WC grains and pore formation triggered by plastic deformation within the Co-phase. In the third zone, both WC- and Co-phase fracture occurs [32]. The tensile creep deformed structure, shown in Fig. 4(c.) and 4(f.), shows that cavities formed at WC/Co and WC/WC boundaries but WC grains were not broken.

As described above, twice as many cavities formed under tension than under compression. In compression loading, the formation of cavities was delayed and thus the deformation under creep load was slower compared than in tension [21]. Frictional forces resulting from sliding of WC grains over each other are important in the deformation process, as observed for SiC material [20]. During deformation at elevated temperature, the interconnected network of WC grains distorts locally to allow WC grains to slide past one another [35]. In this process, compressive stresses oppose this distortion, because they increase friction forces between the WC grains. In contrast, tensile forces support the distortion and reduce friction between WC grains. Additionally, the resistance to creep under tension is reduced compared to compression. This causes a lower number of cavities in the compression than in the tensile deformed specimen, as seen in Fig. 4(b.) and 4(c.). Furthermore, these approaches are supported by the fact that in the KAM maps, see e.g. Fig. 7(b.) and 7(c.), it is possible to observe an increase in KAM, i.e. lattice distortion and thus deformation localizations at grain boundaries. In the past, creep tests and microstructure analysis for WC-Co hardmetals were performed at higher loads and higher temperatures than in test 2 in the current work. For example, Yousfi et al. [14] performed constant compressive load creep tests under 900 MPa at 1000 °C and 1100 °C. In the deformed microstructure shown by Yousfi et al. [14], intergranular cavities and WC/WC grain boundaries separated and were infiltrated by the Co-phase, “binder phase lamellae”, were observed. Additionally, number and size of the cavities were related to the observed degree of deformation. The constant compression load creep test at 1000 °C and up to 20% strain by Yousfi et al. [14] showed more and larger cavities than those deformed up to 10% strain at the same temperature. Consequently, with increasing strain during the step-loading creep tests performed in the current work, more and larger cavities than observed in Fig. 4(b.) and 4(e.), were expected to form. At the early deformation stages studied in the current work, less binder phase lamellae as documented in Yousfi et al. [14], were observed, see Fig. 4(b.). The reason for the difference could be the much higher compressive strain applied by Yousfi et al. [14] than in the current work at the 300 MPa stress level in the step-loading creep test, see Fig. 2. Furthermore,

Mingard et al. [36] performed uniaxial tensile step creep tests between 800 °C and 900 °C at 500 MPa to 700 MPa and less than 2% plastic strain. The tensile creep behaviour of WC-Co hardmetals with high to low carbon contents in 10 wt.% Co binder was investigated. Similar characteristic microstructural features were observed as in creep tests above 1000 °C [14,37] and in the current work, see red arrows and white ovals in Fig. 4(f.): Penetration of Co between WC-WC boundaries as well as cavity formation occur at WC-Co boundaries [36]. The Co penetration between WC grains were related to the boundary orientations of the two grains and an increase in cavities with increasing carbon content of the binder phase was observed [36]. Additionally, evidence of phase deformation in the Co-binder was observed and cavity formation and grain boundary sliding may also occur at 800 °C [36].

Pure Co is stable in the hcp crystal structure at room temperature up to 417 °C, and above 417 °C the fcc structure is stable [38]. However, both crystal phases can coexist in undeformed WC-Co hardmetals at room temperature [39–41], see Fig. 5(a.). Parts of the fcc Co-phase were transformed into hcp Co during the creep tests at 800 °C, see Fig. 5. Table 1 also shows that after the compression or tensile creep tests, the fcc to hcp phase fraction shifted and the amount of hcp phase increased. The fraction of hcp phase was similarly high under both load conditions, comparing Fig. 5(b.) and 5(c.). On the one hand, the observed phase transformation contributes to accommodate the strains necessary to inhibit the formation of cavities during deformation. On the other hand, if the hcp phase is present in the microstructure, it cannot compensate deformations as easily as the fcc Co-phase, because it has only three instead of 12 slip systems [42]. Hence, during creep tests, phase transformation from fcc to hcp has an inhibiting and a promoting effect on cavity formation and growth. In literature [17,43,44], phase transformation of the Co-phase in of WC-Co hardmetals has preferably been determined at room temperature near and in front of crack tips. Under fatigue conditions the phase transformation of cobalt was an important damage mechanism [43]. The Co phase transformation from fcc to hcp causes a volume change between the two crystal structures. It is unknown if the transformation from fcc to hcp leads to an increase or decrease in volume, because in the literature there are different opinions [16,44,45]. Additionally, the effect of volume change on cavity formation is not clear. In the case of pure cobalt the specific volume does not change noticeably [38]. However, in the case of WC-Co hardmetals, the Co-binder includes tungsten, carbon, and maybe other elements which can stabilize the fcc or hcp phase [46]. Additionally, these elements must also be rearranged during the phase transformation, which can influence the unit cell volume per atom [16]. Therefore, it is not excluded that certain elements have an influence on the volume change.

Since the KAM is related to dislocation density [28], the KAM maps in the specimens loaded up to 300 MPa at 800 °C suggest that under both loading conditions more dislocations were formed in both Co-phases than in the WC grains, see Fig. 7 and 8. This is consistent with the observed IPF for the WC phase, see Fig. 6(a.) to 6(c.), as the WC skeleton does not show significant orientation changes, i.e.

does not deform plastically to a significant degree for both loading directions. The extent of crystal orientation changes of the WC grains is approximately the same in the undeformed specimen as in both deformed specimens. Furthermore, the KAM chart in Fig. 8(a.) as well as the cumulative chart for the WC phase for all three cases in Fig. 8(d.) show that they lie on top of each other. Hence, loading up to 300 MPa does not affect the WC grain dislocation structure, although additional strains, caused by the Co-phase transformation, are present in the material. However, under certain conditions also some degree of plastic deformation was observed in WC grains, as like under compression loading at room temperature [47]. The KAM maps for the Co-phases shown in Fig. 7(d.) to 7(i.) suggests that both deformed specimens show larger areas of high misorientation (green and red) than the undeformed one. More details on the deformation behaviour of the binder phases is found by a closer look at the KAM charts derived from the data shown Fig. 7, shown in Fig. 8(b.) to 8(c.) and Fig. 8(e.) to 8(f.). Note that the KAM distributions exhibit two particularities: The high peaks of the KAM distributions located at small KAM values indicated by grey arrows in Fig. 8(b.) and 8(c.) are located at higher KAM values for the hcp Co- phase. Comparing the KAM distributions of the undeformed with the deformed material, the number fraction of misorientation decreases due to the deformation in a misorientation range of approximately  $0.2^\circ$  or  $0.3^\circ$ , Fig. 8. In this range, the specimens deformed by compression and tension loading show about the same level of the number fractions for fcc Co and hcp Co. Note, that the EBSD data were not subjected to a grain dilation clean-up. Hence, misorientation values of the deformed specimens were overestimated at the smallest and largest values of the plotted misorientation range, which means that an interpretation of these values should be omitted, see Fig. 8(b.) and 8(c.). The Co phase transformation resulted in a reduction of the size of the individual areas of the fcc Co and hcp Co- phase and led to an increase in noise in some areas of the KAM maps. This is visible for the orientations at or near  $0^\circ$  (dark blue) and at  $2^\circ$  (red) in the KAM maps showing only very localized and single-pixel-sized orientations, see Fig. 7(d.) to 7(i.). Furthermore, the areas of the distributions at around  $0.7^\circ$  KAM, marked by black arrows in Fig. 8(b.) and 8(c.), show higher values for both deformed binder phases compared to the undeformed ones. The cumulative plots in Fig. 8(e.) and 8(f.) also show that fcc Co and hcp Co in the case of the undeformed specimen exhibits low or no amount of misorientation above  $0.8^\circ$ . Also, Fig. 8(e.) and 8(f.) show that for tension and compression, the cumulative chart for fcc Co and hcp Co are similar but, as in the KAM maps in Fig. 8(b.) and 8(c.), there are slight differences in the misorientation trend. Note that for the fcc Co-phase, there was a more pronounced KAM rise in the region around  $0.7^\circ$  of the KAM distribution, whereas the hcp Co-phase KAM distribution shows higher values at the upper end of the investigated KAM interval. The increase in higher misorientations in deformed specimens indicates that the dislocation density increased in both Co-phases. The increase in the higher misorientation, see black arrows on Fig. 8, resulted in a decrease in the smaller misorientations in the deformed specimens. Simulations of indentation tests on surfaces of different crystallographic

orientations of fcc Co, hcp Co, WC and WC-Co composite at room temperature by Feng et al. [48], showed that the nucleation, expansion and interaction of dislocations in the Co-crystal strongly depended on the orientation of loading with respect to the orientation of the crystals. Additionally, it was documented that the type and the reaction of dislocations are different for fcc Co and hcp Co-crystals [48]. Comparing the lower left quarters of Fig. 7(e.), showing the KAM distribution, and Fig. 6(e.), showing the crystallite orientation distribution, a dependence of the observed amount of plastic strain, shown by a higher green fraction and associated higher KAM value in this area, on the crystal orientation was evident as explained by Feng et al. [48] at room temperature. The orientation of the crystallites may influence the observed traces of plastic deformation in the KAM, in the current work only a limited number of Co single crystal orientations are shown in the IPF, see Fig. 6(d.) to 6(i). The limited number of cobalt grains is caused by the fact that the Co-phase grains can be much larger than the WC grains and can have a dendritic morphology [39,49]. Co grains indicated by compact regions with a single lattice orientation (single coloured) were observed in the IPF maps of fcc Co and hcp Co in the undeformed specimen as well as in the compression and tensile deformed specimen for the fcc Co-phase, see Fig. 6(d.) to 6(g.). As phase transformation occurs during deformation, as verified by EBSD phase images, Fig. 5, a reduction in size of the regions with the same crystal orientation of cobalt occurred, compare Fig. 6(g.), 6(h.) and 6(i.). Within these Co-regions, hcp structures formed, indicated by the different colours in Fig. 6(h.) and Fig. 6(i.). This indicates that the transformation of the Co-binder from its fcc to its hcp modification occurs at various disperse locations within the microstructure.

## 5. Conclusions

- At 700 °C and 800 °C, an asymmetry in the strain evolution was observed between tension and compression step-loading creep curves determined for a WC-Co hardmetal with 10 wt. % Co binder and an average WC grain size of 2 µm. The strain asymmetry occurred at a stress level above 600 MPa at 700 °C, which was considered as onset-stress to cause creep asymmetry. At 800 °C, the strain asymmetry occurred at a stress level above an onset-stress of 250 MPa. This is due to the fact that at higher temperature, strain increased more rapidly with time under tension than under compression.
- Calculated minimal creep rates of tensile and compression loaded specimens at 800 °C show similar values, if the creep curve is symmetric in tension and compression, which is the case for stresses below the onset-stress. In case of strain asymmetry, the creep rate increases more rapidly for tensile load.
- The WC-10 wt.% Co hardmetal creeps - at stresses higher than the onset-stress - faster under tension than under compression. This was interpreted to be caused by the formation of microdefects, like



cavities, nanopores and to a lesser extent also of Co-phase lamellae between WC-WC grain boundaries, with a higher formation rate under tensile than compression creep loads. Since the number of microdefects under tension was larger compared to compression, this was assumed to be a physical reason for the strain asymmetry. This was confirmed by SEM-based microstructure analysis of two specimens that were tested under tension and compression just above the onset-stress of strain asymmetry. On basis of SEM images of tensile loaded creep specimen, it was possible to identify more than twice as many microdefects, like cavities and nanopores than in the compression loaded specimen for the same applied stress level.

- Tensile and compression step-loading creep deformation until 300 MPa at 800 °C resulted in an increase of the specimens' hcp Co-phase content. Additionally, it was shown that deformation was mostly carried by the Co-phases. The WC's dislocation structure as well as crystal orientation was constant.

### Acknowledgements

The authors gratefully acknowledge the financial support of the Frontrunner-Initiative of the project "Frontrunner: Integrated, data driven development for Cutting Tools" (Project No. 861280) and the scope of the COMET program within the K2 Center "Integrated Computational Material, Process and Product Engineering (IC-MPPE)" (Project No 859480). This program is supported by the Austrian Federal Ministries for Climate Action, Environment, Energy, Mobility, Innovation and Technology (BMK) and for Digital and Economic Affairs (BMDW), represented by the Austrian research funding association (FFG), and the federal states of Styria, Upper Austria and Tyrol.

### References

- [1] W. Schedler, Hartmetall für den Praktiker. Aufbau, Herstellung, Eigenschaften und industrielle Anwendung einer modernen Werkstoffgruppe, VDI (Verein Deutscher Elektriker) Verlag, Düsseldorf, 1988.
- [2] A.W. Nemetz, W. Daves, T. Klünsner, C. Praetzas, W. Liu, T. Tepperneegg, C. Czettel, F. Haas, C. Bölling, J. Schäfer, Experimentally validated calculation of the cutting edge temperature during dry milling of Ti6Al4V, *J. Mater. Process. Technol.* 278 (2020) 116544. doi:<https://doi.org/10.1016/j.jmatprotec.2019.116544>.
- [3] A.W. Nemetz, W. Daves, T. Klünsner, W. Ecker, J. Schäfer, C. Czettel, T. Antretter, Cyclic heat-up and damage-relevant substrate plastification of single- and bilayer coated milling inserts evaluated numerically, *Surf. Coatings Technol.* 360 (2019) 39–49. doi:<https://doi.org/10.1016/j.surfcoat.2019.01.008>.

- [4] I. Krajinović, W. Daves, M. Tkadletz, T. Tepperneegg, T. Klünsner, N. Schalk, C. Mitterer, C. Tritremmel, W. Ecker, C. Czettl, Finite element study of the influence of hard coatings on hard metal tool loading during milling, *Surf. Coatings Technol.* 304 (2016) 134–141. doi:10.1016/j.surfcoat.2016.06.041.
- [5] G. Östberg, K. Buss, M. Christensen, S. Norgren, H.-O. Andrén, D. Mari, G. Wahnström, I. Reineck, Mechanisms of plastic deformation of WC–Co and Ti(C, N)–WC–Co, *Int. J. Refract. Met. Hard Mater.* 24 (2006) 135–144. doi:https://doi.org/10.1016/j.ijrmhm.2005.04.009.
- [6] T. -J. Chuang, S.M. Wiederhorn, Damage-Enhanced Creep in a Siliconized Silicon Carbide: Mechanics of Deformation, *J. Am. Ceram. Soc.* 71 (1988) 595–601. doi:10.1111/j.1151-2916.1988.tb05925.x.
- [7] T. Tepperneegg, T. Klünsner, C. Kremsner, C. Tritremmel, C. Czettl, S. Puchegger, S. Marsoner, R. Pippan, R. Ebner, High temperature mechanical properties of WC-Co hard metals, *Int. J. Refract. Met. Hard Mater.* 56 (2016) 139–144. doi:10.1016/j.ijrmhm.2016.01.002.
- [8] T. Klünsner, S. Marsoner, R. Ebner, R. Pippan, J. Glätzle, A. Püschel, Effect of microstructure on fatigue properties of WC-Co hard metals, in: *Procedia Eng.*, 2010: pp. 2001–2010. doi:10.1016/j.proeng.2010.03.215.
- [9] M. Jonke, T. Klünsner, P. Supancic, W. Harrer, J. Glätzle, R. Barbist, R. Ebner, Strength of WC-Co hard metals as a function of the effectively loaded volume, *Int. J. Refract. Met. Hard Mater.* 64 (2017) 219–224. doi:10.1016/j.ijrmhm.2016.11.003.
- [10] M.J. Hoffmann, G. Petzow, *Tailoring of Mechanical Properties of Si<sub>3</sub>N<sub>4</sub> Ceramics*, 1st ed., Springer Netherlands, 1994. doi:10.1007/978-94-011-0992-5.
- [11] B. Roebuck, S. Moseley, Tensile and compressive asymmetry in creep and monotonic deformation of WC/Co hardmetals at high temperature, *Int. J. Refract. Met. Hard Mater.* 48 (2015) 126–133. doi:10.1016/j.ijrmhm.2014.08.007.
- [12] S. Xu, M.A. Gharghouri, M. Sahoo, Tensile-Compressive Creep Asymmetry of Recent Die Cast Magnesium Alloys, *Adv. Mater. Res.* 9 (2007) 807–812. doi:10.1002/adem.200700163.
- [13] S. Schachner, S. Jin, D. Gruber, H. Harmuth, Three stage creep behavior of MgO containing ordinary refractories in tension and compression, *Ceram. Int.* 45 (2019) 9483–9490. doi:10.1016/j.ceramint.2018.09.124.
- [14] M.A. Yousfi, J. Weidow, A. Nordgren, L.K.L. Falk, H.O. Andrén, Deformation mechanisms in a WC-Co based cemented carbide during creep, *Int. J. Refract. Met. Hard Mater.* 49 (2015) 81–87. doi:10.1016/j.ijrmhm.2014.07.016.
- [15] L.S. Sigl, H.E. Exner, Experimental study of the mechanics of fracture in WC-Co alloys, *Metall. Trans. A.* 18 (1987) 1299–1308. doi:10.1007/BF02647199.

- [16] B. Roebuck, E.A. Almond, A.M. Cottenden, The influence of composition, phase transformation and varying the relative F.C.C. and H.C.P. phase contents on the properties of dilute CoWC alloys, *Mater. Sci. Eng.* 66 (1984) 179–194. doi:10.1016/0025-5416(84)90179-4.
- [17] B. Roebuck, E.A. Almond, Deformation and fracture processes and the physical metallurgy of WC–Co hardmetals, *Int. Mater. Rev.* 33 (1988) 90–112. doi:10.1179/imr.1988.33.1.90.
- [18] S. Kursawe, P. Pott, H.G. Sockel, W. Heinrich, M. Wolf, On the influence of binder content and binder composition on the mechanical properties of hardmetals, *Int. J. Refract. Met. Hard Mater.* 19 (2001) 335–340. doi:10.1016/S0263-4368(01)00026-9.
- [19] V.K. Sarin, T. Johannesson, On the Deformation of WC–Co Cemented Carbides, *Met. Sci.* 9 (1975) 472–476. doi:10.1179/030634575790444531.
- [20] S.M. Wiederhorn, D.E. Roberts, T. -J. Chuang, L. Chuck, Damage-Enhanced Creep in a Siliconized Silicon Carbide: Phenomenology, *J. Am. Ceram. Soc.* 71 (1988) 602–608. doi:10.1111/j.1151-2916.1988.tb05926.x.
- [21] S.M. Wiederhorn, B.J. Hockey, High temperature degradation of structural composites, *Ceram. Int.* 17 (1991) 243–252. doi:10.1016/0272-8842(91)90018-U.
- [22] R. Morrell, K.H.G. Ashbee, High temperature creep of lithium zinc silicate glass-ceramics, *J Mater Sci.* 8 (1973) 1253–1270. doi:10.1007/BF00549340.
- [23] J.M. Birch, B. Wilshires, D.J. Godfrey, Deformation and fracture processes during creep of reaction bonded and pressed silicon nitride, *Proc. Brit. Ceram. Soc.* 26 (1978) 141–154.
- [24] K. Maier, T. Klünsner, M. Krobath, C. Tritremmel, S. Marsoner, C. Czettel, Uniaxial step loading test setup for determination of creep curves of oxidation-sensitive high strength materials in vacuum under tensile and compressive load, *Int. J. Refract. Met. Hard Mater.* 92 (2020) 105327. doi:10.1016/j.ijrmhm.2020.105327.
- [25] BS EN ISO 9513:2002 - Metallic materials - calibration of extensometers used in uniaxial testing, 2002.
- [26] B. Winiarski, A. Gholinia, K. Mingard, M. Gee, G.E. Thompson, P.J. Withers, Broad ion beam serial section tomography, *Ultramicroscopy.* 172 (2017) 52–64. doi:https://doi.org/10.1016/j.ultramic.2016.10.014.
- [27] EDAX Smart Insight, (n.d.). <https://www.edax.com/> (accessed September 20, 2020).
- [28] A.J. Schwartz, M. Kumar, B.L. Adams, D.P. Field, *Electron Backscatter Diffraction in Materials Science*, 2nd ed., Springer US, 2009. doi:10.1007/978-0-387-88136-2.
- [29] F. Bachmann, R. Hielscher, H. Schaeben, Texture analysis with MTEX- Free and open source software toolbox, in: *Solid State Phenom.*, Trans Tech Publications Ltd, 2010: pp. 63–68. doi:10.4028/www.scientific.net/SSP.160.63.

- [30] M. Gee, K. Mingard, B. Roebuck, Application of EBSD to the evaluation of plastic deformation in the mechanical testing of WC/Co hardmetal, *Int. J. Refract. Met. Hard Mater.* 27 (2009) 300–312. doi:10.1016/j.ijrmhm.2008.09.003.
- [31] K.P. Mingard, B. Roebuck, H.G. Jones, M. Stewart, D. Cox, M.G. Gee, Visualisation and measurement of hardmetal microstructures in 3D, *Int. J. Refract. Met. Hard Mater.* 71 (2018) 285–291. doi:10.1016/j.ijrmhm.2017.11.023.
- [32] L.S. Sigl, H.E. Exner, H.F. Fischmeister, Characterization of Fracture Processes and Fracture Relevant Parameters in WC-Co Hardmetals, in: *Institute of Physics Conference Series vol. 75*, Rhodos, Greece, 1984: pp. 631–644.
- [33] L.S. Sigl, H.F. Fischmeister, On the fracture toughness of cemented carbides, *Acta Metall.* 36 (1988) 887–897. doi:10.1016/0001-6160(88)90143-5.
- [34] H.F. Fischmeister, Conference Key Note Paper Development and Present Status of the Science and Technology of Hard Materials, in: R. Viswanadham (Ed.), *Sci. Hard Mater.*, 1st ed., Springer US, 1983: pp. 1–45. doi:10.1007/978-1-4684-4319-6.
- [35] D. Mari, S. Bolognini, G. Feusier, T. Viatte, W. Benoit, Experimental strategy to study the mechanical behaviour of hardmetals for cutting tools, *Int. J. Refract. Met. Hard Mater.* 17 (1999) 209–225. doi:10.1016/S0263-4368(98)00078-X.
- [36] K. Mingard, S. Moseley, S. Norgren, H. Zakaria, D. Jones, B. Roebuck, Microstructural observations of high temperature creep processes in hardmetals, *Powder Metall.* (2021) 1–11. doi:10.1080/00325899.2021.1877866.
- [37] S. Lay, J. Vicens, F. Osterstock, High temperature creep of WC-Co alloys, *J. Mater. Sci.* 22 (1987) 1310–1322. doi:10.1007/BF01233127.
- [38] A. Seeger, U. Dehlinger, *Kristallphysik II / Crystal Physics II*, 1st ed., Springer Berlin Heidelberg, Berlin, Heidelberg, 1958. doi:10.1007/978-3-642-45890-3.
- [39] K.P. Mingard, H.G. Jones, M.G. Gee, B. Roebuck, J.W. Nunn, In situ observation of crack growth in a WC-Co hardmetal and characterisation of crack growth morphologies by EBSD, *Int. J. Refract. Met. Hard Mater.* 36 (2013) 136–142. doi:10.1016/j.ijrmhm.2012.08.006.
- [40] J.M. Marshall, A. Kusoffsky, Binder phase structure in fine and coarse WC-Co hard metals with Cr and v carbide additions, in: *Int. J. Refract. Met. Hard Mater.*, 2013: pp. 27–35. doi:10.1016/j.ijrmhm.2013.04.001.
- [41] K.P. Mingard, B. Roebuck, J. Marshall, G. Sweetman, Some aspects of the structure of cobalt and nickel binder phases in hardmetals, *Acta Mater.* 59 (2011) 2277–2290. doi:10.1016/j.actamat.2010.12.004.

- [42] J. Roesler, H. Harders, M. Baeker, *Mechanical Behaviour of Engineering Materials*, 1st ed., Springer-Verlag Berlin Heidelberg, 2007. doi:10.1007/978-3-542-73448-2.
- [43] U. Schleinkofer, H.G. Sockel, K. Görting, W. Heinrich, Microstructural processes during subcritical crack growth in hard metals and cermets under cyclic loads, *Mater. Sci. Eng. A.* 209 (1996) 103–110. doi:10.1016/0921-5093(95)10098-9.
- [44] P. Kindermann, P. Schlund, H.G. Sockel, M. Herr, W. Heinrich, K. Görting, U. Schleinkofer, High-temperature fatigue of cemented carbides under cyclic loads, *Int. J. Refract. Met. Hard Mater.* 17 (1999) 55–68. doi:10.1016/S0263-4368(99)00014-1.
- [45] C.H. Vassel, A.D. Krawitz, E.F. Drake, E.A. Kenik, Binder deformation in WC-(Co, Ni) cemented carbide composites, *Metall. Trans. A.* 16 (1985) 2309–2317. doi:10.1007/BF02670431.
- [46] J.M. Marshall, M. Giraudel, The role of tungsten in the Co binder: Effects on WC grain size and hcp-fcc Co in the binder phase, *Int. J. Refract. Met. Hard Mater.* 49 (2015) 57–66. doi:10.1016/j.ijrmhm.2014.09.028.
- [47] L. Faksa, W. Daves, T. Klünsner, K. Maier, T. Antretter, C. Czettel, W. Ecker, Shot peening-induced plastic deformation of individual phases within a coated WC-Co hard metal composite material including stress-strain curves for WC as a function of temperature, *Surf. Coatings Technol.* 380 (2019) 125026. doi:10.1016/j.surfcoat.2019.125026.
- [48] Q. Feng, X. Song, H. Xie, H. Wang, X. Liu, F. Yin, Deformation and plastic coordination in WC-Co composite — Molecular dynamics simulation of nanoindentation, *Mater. Des.* 120 (2017) 193–203. doi:https://doi.org/10.1016/j.matdes.2017.02.010.
- [49] J. Weidow, H.-O. Andrén, Binder phase grain size in WC-Co-based cemented carbides, *Scr. Mater.* 63 (2010) 1165–1168. doi:https://doi.org/10.1016/j.scriptamat.2010.08.025.



## **Publication III**

**Creep behaviour of WC-12 wt.% Co hardmetals with different WC grain sizes tested in uniaxial tensile and compression step-loading tests at 700 °C and 800 °C**

**Kathrin Maier, Thomas Klünsner, Martin Krobath, Philip Pichler,  
Stefan Marsoner, Werner Ecker, Christoph Czettl,  
Jonathan Schäfer, Reinhold Ebner**

**Published in**

**International Journal of Refractory Metals & Hard Materials,**

**100 (2021) 105633**

## Creep behaviour of WC-12 wt.% Co hardmetals with different WC grain sizes tested in uniaxial tensile and compression step-loading tests at 700 °C and 800 °C

Kathrin Maier<sup>1\*</sup>, Thomas Klünsner<sup>1</sup>, Martin Krobath<sup>1</sup>, Philip Pichler<sup>1</sup>, Stefan Marsoner<sup>1</sup>,  
Werner Ecker<sup>1</sup>, Christoph Czettel<sup>2</sup>, Jonathan Schäfer<sup>2</sup>, Reinhold Ebner<sup>1</sup>

<sup>1</sup> Materials Center Leoben Forschung GmbH, Roseggerstraße 12, 8700 Leoben, Austria

<sup>2</sup> CERATIZIT Austria GmbH, Metallwerk-Plansee Straße 71, 6600 Reutte, Austria

\*Corresponding author: kathrin.maier@mcl.at

**Keywords:** WC-Co hardmetal, Uniaxial step-loading creep test; Elevated temperature; Creep behaviour, Damage behaviour

### Abstract

At elevated temperatures, the material behaviour of WC-Co hardmetals shows differences under similar loading conditions depending on WC grain size and Co-content. Variations in the chemical composition and microstructure in hardmetals cause different material properties such as strength or creep resistance. In the current work, the influence of WC grain size on creep mechanism and creep resistance was investigated for WC-12 wt. % Co hardmetals with 0.4  $\mu\text{m}$ , 0.7  $\mu\text{m}$  and 2.0  $\mu\text{m}$  average WC grain size. Specimens were tested in uniaxial tensile and compression step-loading creep tests at 700 °C and 800 °C under vacuum conditions. Time-dependent creep behaviour with steady-state secondary creep was observed for all hardmetal grades investigated, with specimens creeping faster under tensile than under compressive loading. At 700 °C, the medium-grained hardmetal grade exhibited the highest minimal creep rates  $\dot{\epsilon}_{\text{min}}$  compared to the submicron and ultrafine-grained grades. In contrast, the ultrafine-grained hardmetal grade showed higher  $\dot{\epsilon}_{\text{min}}$  at low stresses and 800 °C, because of the high amount of grain boundary area per unit volume, which is advantageous for vacancy diffusion at grain boundaries. Therefore, the  $\dot{\epsilon}_{\text{min}}$  of the medium-grained hardmetal grade was less affected by temperature than that of the finer-grained grade. Also two stress exponent  $n$ -ranges were observed at 700 °C and 800 °C: At low stress levels,  $n$  was in the range of about 1. Above a critical stress level,  $n$  reached values between about 4 and 6. Beside the influence of the WC grain size on the creep mechanism and creep resistance, damage evolution with increasing stress levels was analysed for the ultrafine-grained grade at 800 °C. The microstructures of three compression step-loading creep tested specimens were examined after maximum stress levels of -350 MPa, -950 MPa and -1350 MPa. Microstructural investigations performed via scanning electron microscopy showed that more and larger cavities had formed at WC/WC interfaces and WC/Co phase boundaries in the specimen tested up to -1350 MPa compared to the ones tested up to -350 MPa and -950 MPa.



## 1. Introduction

Hardmetal tools are mainly used for machining of metals by turning, milling and drilling but also for processing of wood and stone, where they are exposed to high temperatures [1]. Depending on the machined material, temperatures between 600 °C and 1000 °C are observed [2–4]. WC-Co hardmetals have high ductility and strength at room temperature, but at higher temperatures the strength decreases and creep deformations must be taken into account. Additionally, depending on WC grain size and Co-content, not all hardmetal grades are appropriate for specific practical applications because they fail earlier than others [5].

Several publications discuss mechanical and performance properties of WC-Co hardmetals at elevated temperatures [6–15]. Deformation mechanisms and microstructural changes at high temperatures have been studied, e.g. via creep [16,17], compression [13,18], tensile [19], bending [20,21] and turning tests [10] under different test conditions. Creep mechanism investigations in hardmetals were preferably performed at temperatures above 800 °C and under bending loads [14,21]. Experiments at lower temperatures and under uniaxial loading conditions were carried out only sporadically [12,17,22]. Uniaxial compression creep tests were performed with loads up to a maximum of 750 MPa [22] and up to 700 MPa under tension [12,17,23], both stress values are below typical operating stresses of metalworking tools which are reaching about 1000 MPa [2]. The mentioned lower loads are usually chosen to prevent premature damage under tension and specimens buckling under compression. To optimize the hardmetal tool material for its operating conditions, different hardmetal grades were examined with regard to creep [12,17,22–25]. Grades with WC grain sizes from submicron to coarse were investigated with Co-contents up to 10 wt.% [12,23,24]. Examinations of grades with more than 10 wt.% Co were predominantly carried out for coarser-grained grades [17,22].

There are different explanations in literature for creep mechanisms above 850 °C in WC-Co hardmetals. Models by Smith et al. are based on dislocation creep in dispersion strengthened materials [22]. Others [12,16,17,23,25–27] suggest vacancy diffusion and grain boundary sliding as possible creep mechanisms. Especially for small WC grain sizes, it is assumed that WC/WC boundary sliding is a creep rate determining factor [23]. Furthermore, it is observed that cavities form during tensile and compression creep tests at temperatures above 800 °C [12,16,17]. After application of a constant uniaxial tensile stress of 200 MPa for 50 hours, cavities were observed at WC/Co interfaces [12]. Cavities and the formation of Co-phase lamellae at WC/WC grain boundaries were also observed above 1000 °C under a constant uniaxial compressive stress of 900 MPa [16].

Depending on WC grain size and Co-content, hardmetals exhibit differences in creep resistance [13,14,22,28,29]. The creep rate is directly related to the amount of Co-phase [22,25,26], since Co creeps several orders of magnitude faster than WC [29]. WC grain size affects the creep rates depending on the temperature and the applied stress [14,22,30]. Creep rate increases with increasing WC grain size under

high stress conditions and temperatures below 900 °C [23,25,26]. Further, creep resistance is increased at high temperatures and low stresses for coarse WC grain sizes [23,25,26].

The above-mentioned creep tests were largely performed as standard creep tests, in which the specimens are tested over a long period of time under a constant load and temperature. Additionally, the creep behaviour of hardmetals has been investigated using step creep tests [17,31–33]. In these tests, the mechanical load is increased stepwise and the stress at each step is kept constant for a certain time. Hence, using step creep tests, it is possible to analyse the creep behaviour of materials under different applied stresses in a time-efficient single measurement. Mingard et al. [17], examined WC-Co hardmetals with different carbon content under this type of test at 800 °C and at tensile loads of 500 MPa to 700 MPa. Penetration of Co at WC/WC boundaries as well as cavity formation occur at WC/Co boundaries [17]. The Co penetration between WC grains was related to the relative boundary orientations of the two WC grains and an increase in cavities with increasing carbon content of the binder phase was observed [17]. Cavity formation and Co penetration between WC grains were also observed under uniaxial step creep tests at 800 °C at 300 MPa [33] and in standard creep tests above 1000 °C [12,16].

To investigate creep properties of high-strength materials, specific test setups are required, since these materials tend to oxidize at elevated temperatures [34] and exhibit high strength [35,36]. Note, that high uniaxial compressive loads may cause specimen buckling. In uniaxial compression tests, buckling is a limiting factor to the applicable load range [17,22,31]. Hence, a special specimen geometry with a non-constant cross-section is often used [16,32,37,38]. Because of the high tendency to oxidation of hardmetals above 600 °C [34], a special atmosphere is needed, such as vacuum [32,37], argon or an argon/5% hydrogen mixture [16,17,31].

However, despite various researches on creep of various hardmetals, little information is available on creep behaviour below 900 °C and loading conditions above 750 MPa. Also, investigations of hardmetal grades with 12 wt.% Co with WC grain size smaller than medium are lacking. Therefore, the current work discusses the influence of three average WC grain sizes (0.4 µm, 0.7 µm, and 2.0 µm) on creep mechanism and creep resistance of WC-12 wt.% Co hardmetals at 700 °C and 800 °C under uniaxial tensile and compression step-loading creep tests in vacuum. By performing step-loading creep tests at 700 °C and 800 °C, stresses from 50 MPa up to more than 1000 MPa are analysed by one creep test. The effect of the increasing stress on the damage development of the ultrafine-grained hardmetal grade is also discussed.

## 2. Methodological approach

Three different hardmetals were examined with the designation U12, S12 and M12 and their microstructures are shown in Fig. 1(a.) to Fig. 1(c.), respectively. The letters the specimen designation U, S and M refer to the average WC grain size of the grades: ultrafine, submicron and medium, respectively, according to the

ISO standard grain size classification scheme [39]. The number after the letter indicates the Co-content of 12 wt.%. Tab. 1 lists the average WC grain size and the Co-content as given by the material manufacturer Ceratizit Austria GmbH. Additionally, compression yield strength  $R_{p0.2}$  and Young's modulus  $E$  of the hardmetals as function of temperature are shown in Tab. 1. These two parameters were determined from strain-corrected [32] stress-strain curves of uniaxial compression tests performed with hourglass-shaped specimen. Tab. 1 also lists the materials' room temperature fracture toughness  $K_{IC}$  that was determined by Ceratizit Austria GmbH by SENB tests according to DIN EN ISO 12737.

Tab. 1: Composition of the three investigated hardmetal grades with their compression yield strength ( $R_{p0.2}$ ), Young's modulus ( $E$ ) as function of temperature, and room temperature fracture toughness ( $K_{IC}$ ) determined by SENB tests.

Grade	Average WC grain size [ $\mu\text{m}$ ]	Cobalt [wt.%]	Yield strength $R_{p0.2}$ [MPa]			Young's modulus $E$ [GPa]			$K_{IC}$ - SENB [MPa $\sqrt{\text{m}}$ ]
			25 °C	700 °C	800 °C	25 °C	700 °C	800 °C	25 °C
			U12	0.4	12	4890	2280	1140	530
S12	0.7	12	3810	1820	1125	520	500	420	9.7
M12	1.7	12	3175	1270	850	520	495	420	14.8

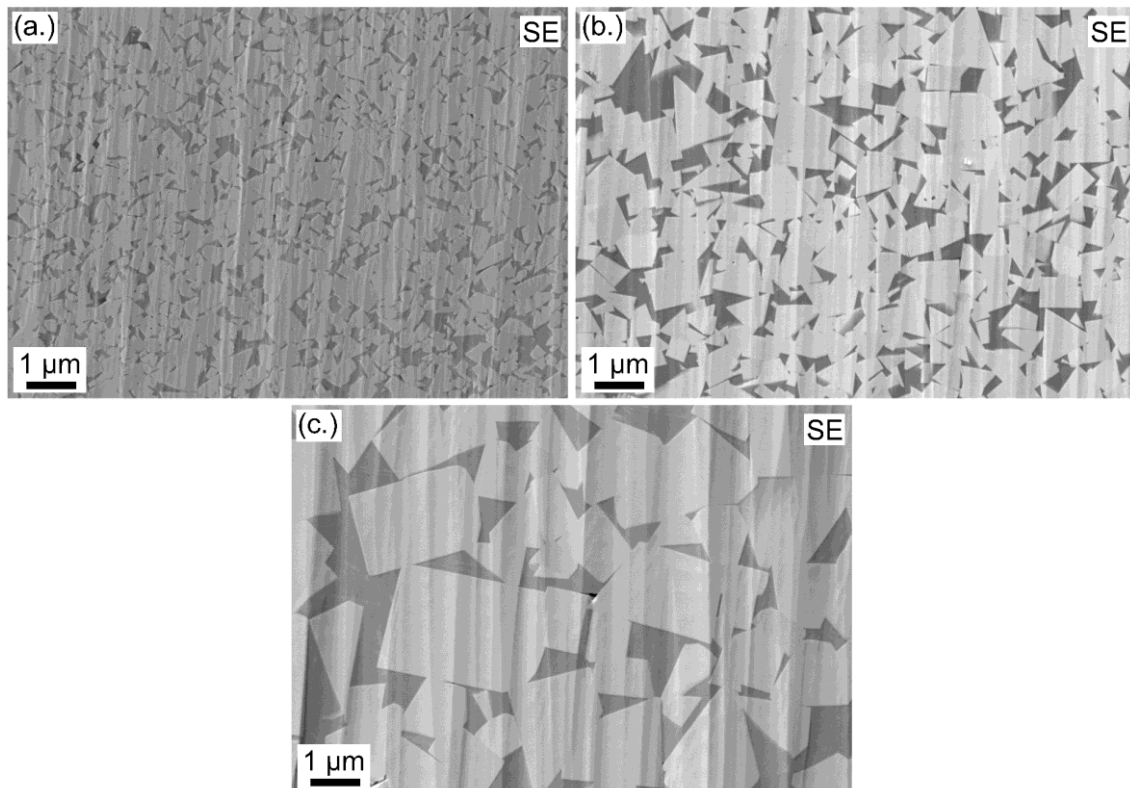


Fig. 1: Scanning electron microscopy (SEM) micrographs of the microstructure of the investigated hardmetal grades: (a.) U12 with an average WC grain size of 0.4  $\mu\text{m}$ , (b.) S12 with an average WC grain size of 0.7  $\mu\text{m}$  and (c.) M12 with an average WC grain size of 1.7  $\mu\text{m}$ . In the secondary electron images, the WC-phase is visible in light grey and the Co-phase in dark grey.

Step-loading creep tests were performed with a servo-hydraulic testing machine (Instron 8803) under uniaxial tensile or compression loading at 700 °C and 800 °C [32]. An hourglass-shaped specimen geometry was used to prevent buckling under uniaxial compression loading. The minimum diameter in the axial centre of the hourglass-shape was 6 mm and the maximum diameter at the cylindrical shaft for clamping was 20 mm. The total length of the specimens was 250 mm [32]. During the step-loading creep test, stress was increased in 50 MPa steps and kept constant at each stress level for 500 s. The load increase was carried out within 5 s, so the creep that occurred during the load level change itself can be neglected. Tests were completed when certain criteria had been met, for example a predefined stress level or strain value was surpassed, or the specimen had failed. If the specimen did not fail during the test, it was unloaded after the last stress level. Each step-loading creep test, whether under tensile or compression load, was performed with a new hourglass-shaped specimen, hence tensile and compression tests were analysed separately. This was deemed necessary, since load history may affect the material deformation behaviour at elevated temperature [31]. Under tensile load, the tests were carried out up to 2% observed strain or specimen failure. In contrast, compression tests were performed up to 3% observed strain. From step-loading creep tests, the minimal creep rates were determined by calculating the first derivative for each stress levels. If the creep rate stabilized or reached a distinct minimum value within the stress level, this value was interpreted to correspond to the secondary creep rate for the respective applied stress level. If the creep rate showed a distinct non-constant trend within the 500 s observation span, the associated stress level was interpreted to exhibit only primary creep [32]. Consequently, depending on the investigated hardmetal grades, minimal creep rates were observed at certain stress levels. The stress exponent  $n$  was determined from the slope of the minimal creep rate curve as function of the stress by a linear fit function.

A high-precision laser extensometer (P-2S-50/400 Hz, Fiedler Optoelektronik GmbH, accuracy class 0.2, ISO 9513) was used for non-contact measurement of axial strain with measurement markings placed 4 mm from either side of the axial centre of the hourglass-shaped specimen. The used non-constant specimen diameter lead to an underestimation of the measured strain data, therefore a strain correction was carried out via finite element simulations [32]. The simulated material behaviour was adapted iteratively in a mechanical 2D simulation in which the specimen's full 3D geometry was modelled exploiting the specimen's rotational symmetry. The simulated and experimentally measured displacements and forces were fitted to one another for the whole test duration. The applied material model combined static plasticity with a simple creep model [32], the governing equation for the creep strain rate  $\underline{\dot{\epsilon}}^{cr}$  is shown in Eq. (1).

$$\underline{\dot{\epsilon}}^{cr} = \left( A \cdot \tilde{q}^n \cdot [(m + 1) \cdot \underline{\epsilon}^{cr}]^m \right)^{\frac{1}{m+1}} \quad (1)$$

where  $A$ ,  $n$  and  $m$  are model parameters,  $\tilde{q}$  is the Mises equivalent stress. In the Appendix, the creep parameters used to calculate the creep strain rate according Eq. (1) are listed in Tab. A.1 for each material

state investigated in the current work. The desired information on the “corrected” strain values present at the lowest diameter of the hourglass-shaped specimen can then be obtained from the simulation's results database. The strain correction was carried out for compression and tensile step-loading creep tests at 700 °C and 800 °C for all three hardmetal grades. Fig. 2 shows a comparison of the strain values from the experiment and the corrected strain values gained from the FE simulation for different loading cases of the hardmetal grade M12 at 800 °C. The experimental step-loading creep curves under compression and tensile conditions are shown in blue in Fig. 2(a.) and 2(b.), respectively. The green dotted lines show the simulated strain fitted to the experimental strain over the whole step-loading creep test, referred to as “Aligned” in Fig. 2. The red dashed lines in Fig. 2 show the "corrected" strain values of the hourglass-shaped specimens at the minimum specimen diameter of 6 mm of the hardmetal grade M12, as demonstrated for the hardmetal grade S12 and the same specimen geometry in [32]. The strain values of the “Aligned” curve represents stress levels with primary and secondary creep precisely. Onsets of tertiary creep was also observed in addition to primary and secondary creep at very high strain values. Since the applied material model did not represent tertiary creep, deviations between the “Experiment” and “Aligned” curve were observed, see Fig. 2(c.) and 2(d.). Therefore, stress levels of all three hardmetal grades at both temperatures and loads which were not represented exactly by simulation due to tertiary creep were not considered in the determination of the minimal creep rates. At 700 °C and under compressive load, these were the last 8, 6 and 5 stress levels of U12, S12 and M12, respectively. At 800 °C, this was equivalent to the last 3 of U12 and the last 4 stress levels of S12 and M12. Under tensile loading, the last 2 of U12 and S12 and the last 3 stress levels of M12 at 700 °C were not considered for the determination of the minimal creep rate. In the case of 800 °C, the last 3 of U12 and M12 and the last 2 stress levels of S12 were not taken into account. However, care was taken to ensure that in these stress levels with tertiary creep, the last strain value of the respective stress level matches with the one of the experiments, see black circles in Fig. 2(d.). Hence, the last strain value before increasing the stress corresponds to the right corrected strain value. Note that because of the performed strain correction, the maximum creep strains shown in the following figures for compression and tensile step-loading creep tests are higher than the maximum 3% and 2% strain measured in the experiments, which was defined as stopping criterion for the tests. For determining the strain-corrected step-loading creep curves, the simulation curve fitted to the experiment was used, hence the noise signal of the strain- corrected curves was minimised and appeared smoother than the experimental step-loading creep curve. The specimens were inductively heated with thermal stability ensured by the use of thermocouples as described in [32]. To avoid specimen surface oxidation, a vacuum chamber was used that produced a testing atmosphere of a pressure of  $5 \cdot 10^{-6}$  mbar at the applied testing temperatures of 700 °C and 800 °C [32].

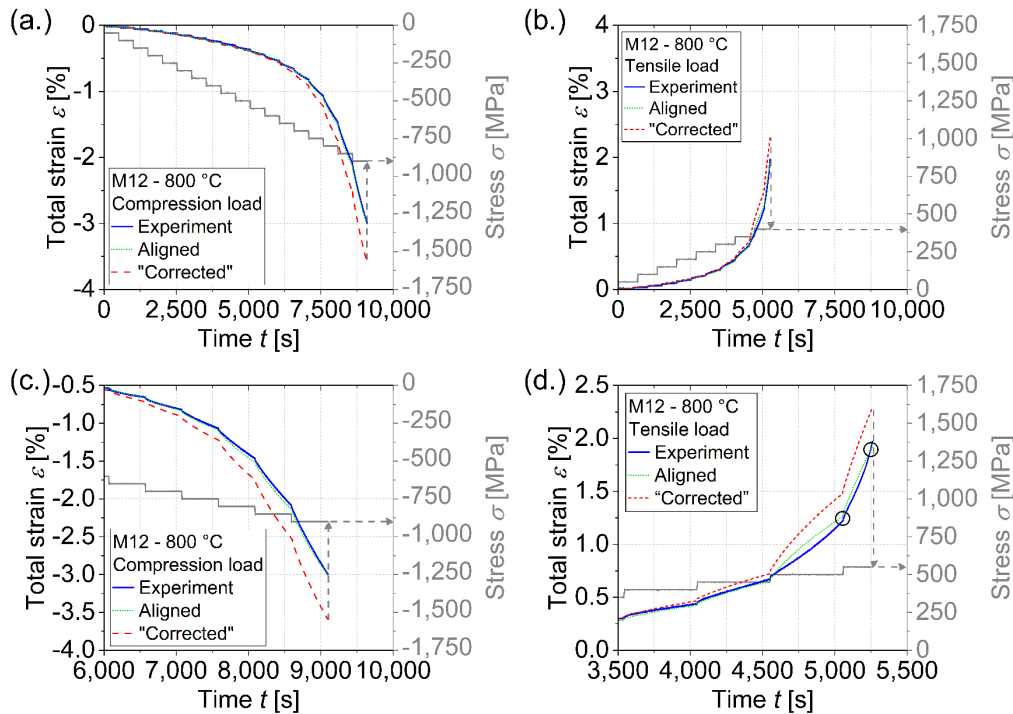


Fig. 2: Experimentally observed (a.) compression and (b.) tensile step loading creep curves (blue line - “Experiment”) of the hardmetal grade M12 at 800 °C with two simulation curves (green dotted line - “Aligned” and red dashed line - “Corrected”). The green dotted lines represent the strain fitted by simulation over the whole experimental step-loading creep test of a fictitious specimen with an hourglass-shaped geometry. The red dashed line represents the “corrected” strain values of the hourglass-shaped specimen at its lowest specimen diameter (“Corrected”). Enlarged representation of regions with high strain values in (a.) and (b.) are shown in (c.) for the compression and (d.) for the tensile step-loading creep curves. Black circles in (d.) mark the last strain value of the respective stress level with onset of tertiary creep. (For interpretation of the references to colour in this figure legend, the reader is referred to the web version of this article.)

In order to facilitate the investigation of damage at the microstructural level as a function of the applied compressive stress level at 800 °C, specimens made of grade U12 were tested in compression step-loading creep tests at this temperature up to -350 MPa and -950 MPa. The specimen from U12 from the compression step-loading creep test up to 3% at 800 °C, as described above, was also used with -1350 MPa as final stress level. These specimens were unloaded after reaching the above mentioned stress level in order to analyse their microstructure by scanning electron microscopy (SEM, GeminiSEM ® 450 / Carl Zeiss SMT) using the secondary electron contrast mode (SE). Test pieces were taken from the radial centre of the minimum diameter of the hourglass-shaped specimens. Metallographic specimens were prepared with argon ion polishing as the final surface preparation step, which removed the deformed surface layers introduced during cutting and polishing [40]. Argon ion polishing led to ridges on the specimen surface perpendicular to the ion beam direction, which were visible on SEM micrographs. The ridges were assumed not to affect the number or size of defects that form during mechanical testing. Nor did they affect the relative amount of fcc Co to hcp Co phase visible in the plane intersecting the material volume [40]. The investigated cross-

section planes were oriented perpendicular to the loading direction, i.e. when looking at the secondary electron images, the load direction points vertically along the image plane. The microstructure was examined at three positions in the centre of each cross-section at the minimum specimen diameter. One position roughly in the centre of the 6 mm specimen diameter and two at a distance of 500  $\mu\text{m}$  from this position away within the argon polished region. To determine the defect density and their size in the microstructure of U12, a manual evaluation of these was performed using multiple SEM micrographs with an individual area of around 80  $\mu\text{m}^2$  in secondary electron contrast mode with an InLens detector arrangement. A total area of 240  $\mu\text{m}^2$  was examined in such a manner covering approximately 2400 WC grains per applied compressive stress level. Additionally to the microstructure of the specimens made of grade U12, the initial porosity for all three hardmetal grades was determined as described above.

### 3. Results

#### 3.1 Compression and tensile step-loading creep curves at 700 °C and 800 °C

Creep behaviour of three WC-Co hardmetals, U12, S12 and M12, was investigated by step-loading creep tests under tensile and compression loading. The strain-corrected compression step-loading creep curves are shown for 700 °C in Fig. 3(a.) and for 800 °C in Fig. 3(b.). Each step in the strain-corrected step-loading creep curve corresponds to a stress level. Therefore, in Fig. 3 and Fig. 4, the stresses parallel to the step-loading creep curves were also shown in grey. Also, the grey dashed arrows for the respective last step of each hardmetal grade in the step-loading creep curve indicate the corresponding stress level. At 700 °C, the step-loading creep curve of M12 first significantly deviated from the step-loading creep curve of U12 at -400 MPa, Fig. 3(a.). Next to M12, first significant deviation of the step-loading creep curve of S12 from the step-loading creep curve of U12 was observed at -1300 MPa. At 700 °C, M12 reached a maximal corrected creep strain of -3.6% after 12,993 s at a stress level of -1300 MPa, see grey dashed arrows in Fig. 3(a.). S12 reached a maximal corrected creep strain of -3.4% at -2000 MPa after 19,876 s, and U12 reached a maximal corrected creep strain of -3.4% at -2350 MPa after 23,392 s.

Fig. 3(b.) shows the compression step-loading creep curves for all three hardmetal grades at 800 °C. The compression step-loading creep curve of U12 shifted more towards faster creep than the other grades, i.e. in between the step-loading creep curve of M12 and S12. Also, the step-loading creep curves were symmetric to each other until certain stress levels as at 700 °C. The step-loading creep curve of M12 deviated from the one of S12 already at a stress level of -100 MPa. Next to M12, U12 creeps faster than S12 starting at a stress level of -350 MPa, see Fig. 3(b.). At 800 °C, M12 reached a maximum corrected creep strain of -3.6% after 9,097 s and a stress level of -900 MPa, marked with grey dashed arrows in Fig. 3(b.). U12 reached a maximum corrected creep strain of -3.3% after 13,260 s at a stress level of -1350 MPa. For S12, a maximum corrected creep strain of -3.4% is obtained after 13,888 s at a stress level of -1400 MPa.

The step-loading creep curves for U12 and S12 in Fig. 3(b.) show that the compression step-loading creep curves separate at low stresses but converge to each other again at higher stresses.

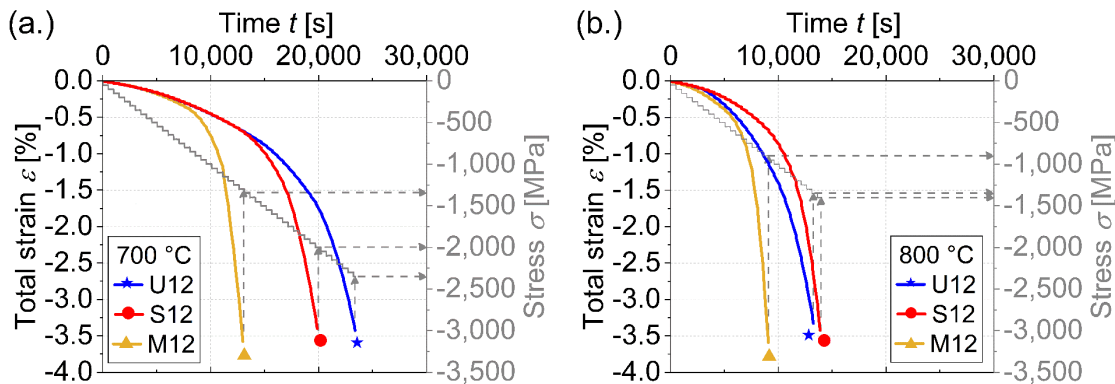


Fig. 3: Strain-corrected compression step-loading creep curves at (a.) 700 °C and (b.) 800 °C of three hardmetal grades: U12 (blue - star), S12 (red - circle) and M12 (dark yellow - triangle). In addition to the step-loading creep curves, the corresponding applied stress levels (grey lines) are shown; grey dotted arrows indicate the final stress level. (For interpretation of the references to colour in this figure legend, the reader is referred to the web version of this article.)

Additional to compression, tensile step-loading creep tests for U12, S12 and M12 were performed at elevated temperatures. The resulting strain-corrected step-loading creep curves are shown in Fig. 4 for 700 °C (a.) and 800 °C (b.). In Fig. 4, the moments of specimen failure were marked with a cross for 700 °C and 800 °C. U12 reached a maximal corrected creep strain of 1.2% after 12,210 s at a stress level of 1250 MPa, marked with grey dashed arrows in Fig. 4(a.). S12 failed at a maximum corrected creep strain of 0.8% after 10,785 s and a stress level of 1100 MPa and M12 failed at a maximum corrected creep strain of 1.9% after 8,282 s and a stress level of 850 MPa. Note that M12 creeps faster than the other two materials, which is shown in Fig. 4(a.) as the step-loading creep curve deviated significantly from U12 and S12 starting from 200 MPa. In contrast, S12 and U12 had a similar curve progression.

Fig. 4(b.) shows the tensile step-loading creep curves at 800 °C. Compared to the case for 700 °C, the creep curve of U12 shifted more towards faster creep than the other grades, i.e. in between M12 and S12, and shows the same step-loading creep curve progression as M12 at low stresses. However, starting from 350 MPa onward, M12 crept significantly faster than U12 and failed at 550 MPa at a maximum corrected creep strain of 2.3% after 5,260 s. S12 had lower creep rates than M12 and U12, see Fig. 5(d.), and the specimen failed at 650 MPa at a maximum corrected creep strain of 1.7% after 6,430 s. In contrast, U12 did not fail and reached a maximum corrected creep strain of 2.2% after 6,084 s at 650 MPa.



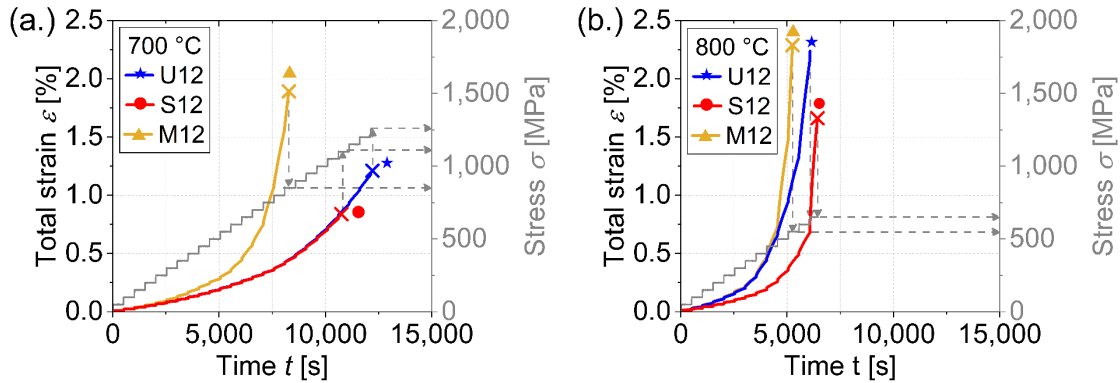


Fig. 4: Strain-corrected tensile step-loading creep curves at (a.) 700 °C and (b.) 800 °C of three hardmetal grades: U12 (blue - star), S12 (red - circle) and M12 (dark yellow - triangle). In addition to the step-loading creep curves, the corresponding applied stress levels (grey lines) are shown; grey dotted arrows indicate the final stress level. Failed specimens are marked with a cross at the final strain value. (For interpretation of the references to colour in this figure legend, the reader is referred to the web version of this article.)

### 3.2 Compression and tensile minimal creep rates at 700 °C and 800 °C

Based on strain-corrected compression and tensile step-loading creep curves, minimal creep rates were determined. Since tertiary creep was observed in addition to primary and secondary creep at very high strain values, as mentioned in Section 2, there were deviations between the experiment and the strain corrected curve, see Fig. 2. Therefore, stress levels which were not represented exactly by simulation were not considered in the determination of the minimal creep rates. Additionally, it is assumed that next to vacancy diffusion, grain boundary sliding and dislocation creep, also the formation of cavities [17,33] contributes significantly to the observed strain in all cases to be discussed. Fig. 5(a.) to Fig. 5(d.) show the minimal creep rates as function of the stress levels for both investigated temperatures and loading conditions on double-logarithmic scales. The slopes of the curves of the minimal creep rate as function of the stress were determined by linear regression, and are indicated by lines in Fig. 5, with their respective slopes representing the stress exponents  $n_i$  which were classified into two regimes  $n_I$  (1 to 2.5) and  $n_{II}$  ( $>2.5$ ). The  $n_i$  values rounded to integer values for the respective line are shown at the margin of each diagram in Fig. 5, the more exact values of  $n_i$  and the corresponding stress level range for all three hardmetal grades under compression and tensile loading are given in Tab. 2 and Tab. 3. The corresponding  $n$ -values are in the range of 0.9 to 5.9. Next to Tab. 2 and Tab. 3, Fig. 6(a.) and Fig. 6(b.) show graphically the stress exponent  $n_i$  as function of the stress level range  $\sigma_i$  for compression and tensile loading at 700 °C and 800 °C, respectively. The beginning and end of the stress level range is marked by symbols referring to the hardmetal grade.

As the step-loading creep curves of U12 at 800 °C in Fig. 3(b.) and Fig. 4(b.), also the minimal creep rate curves for tensile and compression loading of U12 shifted more towards faster creep, i.e. in between the other two hardmetal grades S12 and M12 compared to the cases at 700 °C, as shown in Fig. 5(c.) and 5(d.), respectively.

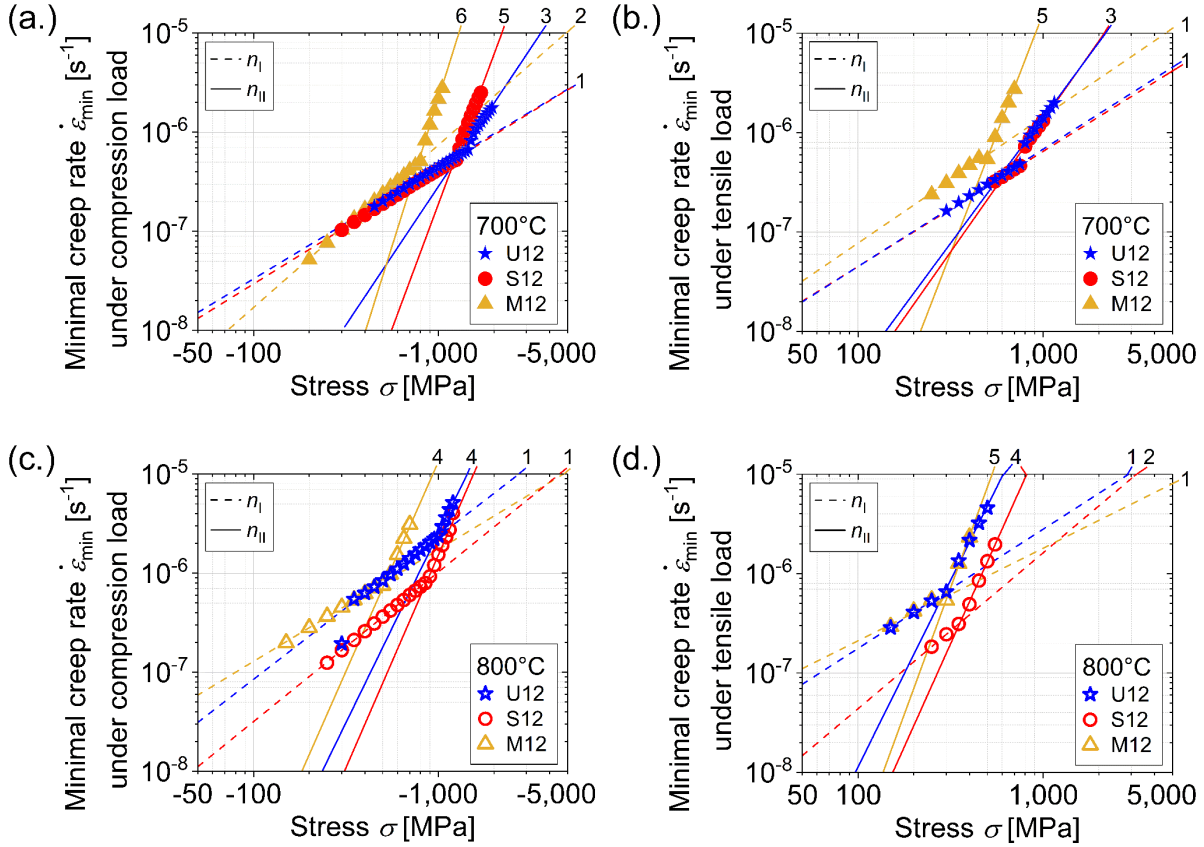


Fig. 5: Minimal creep rate  $\dot{\epsilon}_{\min}$  as function of stress in (a.), (c.) for compression and in (b.), (d.) for tensile load at 700 °C, filled symbols, and 800 °C, open symbols, of U12, blue stars, S12, red circles, and M12, dark yellow triangles. Rounded values of stress exponents classified into two regimes  $n_I$  (dotted lines) and  $n_{II}$  (full lines) are given at the margin of each diagram. (For interpretation of the references to colour in this figure legend, the reader is referred to the web version of this article.)

Tab. 2: Numerical values of the compression stress exponent  $n_I$  for 700 °C and 800 °C derived from the data in Fig. 5(a.) and 5(c.). The stress level range  $\sigma_I$  in which the respective stress exponent  $n_I$  was determined is pointed out. The creep behaviour at low and medium stresses is marked with index I, at higher stresses with index II.

Compression load				
Material	$n_I$	$\sigma_I$ [MPa]	$n_{II}$	$\sigma_{II}$ [MPa]
700 °C				
U12	1.1	-450 – -1450	2.8	-1500 – -1950
S12	1.1	-300 – -1250	5.0	-1300 – -1700
M12	1.6	-200 – -800	5.9	-850 – -1050
800 °C				
U12	1.4	-350 – -950	3.8	-1000 – -1200
S12	1.5	-250 – -850	4.3	-850 – -1200
M12	1.1	-150 – -500	4.2	-500 – -700

Tab. 3: Numerical values of the tensile stress exponent  $n_i$  for 700 °C and 800 °C derived from the data in Fig. 5(b.) and 5(d.). The stress level range  $\sigma_I$  in which the respective stress exponent  $n_i$  was determined is pointed out. The creep behaviour at low and medium stresses is marked with index I, at higher stresses with index II.

Tensile load				
Material	$n_I$	$\sigma_I$ [MPa]	$n_{II}$	$\sigma_{II}$ [MPa]
700 °C				
U12	1.2	300 – 750	2.5	800 – 1150
S12	1.2	550 - 750	2.6	800 – 1000
M12	1.3	250 – 500	4.8	500 – 700
800 °C				
U12	1.2	150 – 300	3.8	300 – 500
S12	1.6	250 - 350	4.1	350 – 550
M12	0.9	150 – 300	5.1	300 – 400

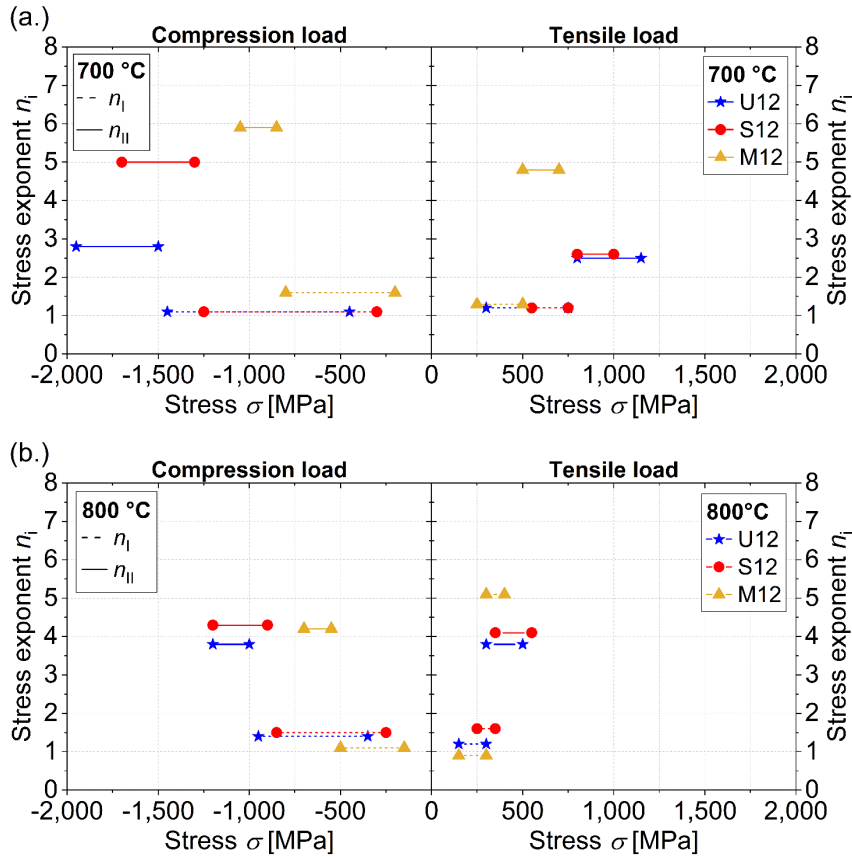


Fig. 6: Stress exponent  $n_i$  as function of stress  $\sigma$  for compression and tensile load at (a.) 700 °C and (b.) 800 °C, of U12, blue stars, S12, red circles, and M12, dark yellow triangles. The stress exponents were classified into two regimes  $n_I$  (dotted lines) and  $n_{II}$  (full lines). An overview of the corresponding numerical values for all three hardmetal grades under both loading conditions and temperatures is given in Tab. 2 and Tab. 3. (For interpretation of the references to colour in this figure legend, the reader is referred to the web version of this article.)

### 3.3 Microstructure analysis of compression step-loaded U12 at 800 °C

In Fig. 7(a.), three U12 strain-corrected compression step-loading creep curves at 800 °C are shown. The first specimen was tested up to -350 MPa, achieving -0.16% strain. The second specimen was tested up to -950 MPa, achieving -1.0% strain. The third specimen reached a strain of -3.3%, and a final stress level of -1350 MPa. The minimal creep rates were determined for all individual stress levels for all three tests, see Fig. 7(b.). A pronounced secondary creep behaviour, i.e. a minimal creep rate was observed for all specimens starting at -300 MPa. Even though the step-loading creep curves of the tests performed up to -950 MPa and -1350 MPa start to separate at -550 MPa, similar minimal creep rates were observed. The minimal creep rate curve exhibited two distinct regimes defined with  $n_I$  of about 1 and  $n_{II}$  of about 4, see also Tab. 4. For the specimen tested up to -350 MPa, far too less data points were available to determine  $n$ . For the specimen tested up to -950 MPa, it was possible to determine the stress exponent only in the range of  $n_I$ . In the case of the specimen tested up to -1350 MPa, two stress exponent ranges  $n_I$  and  $n_{II}$  were observed. Subsequently, to understand the creep processes better, the microstructure was analysed in detail by SEM for the three tested specimens.

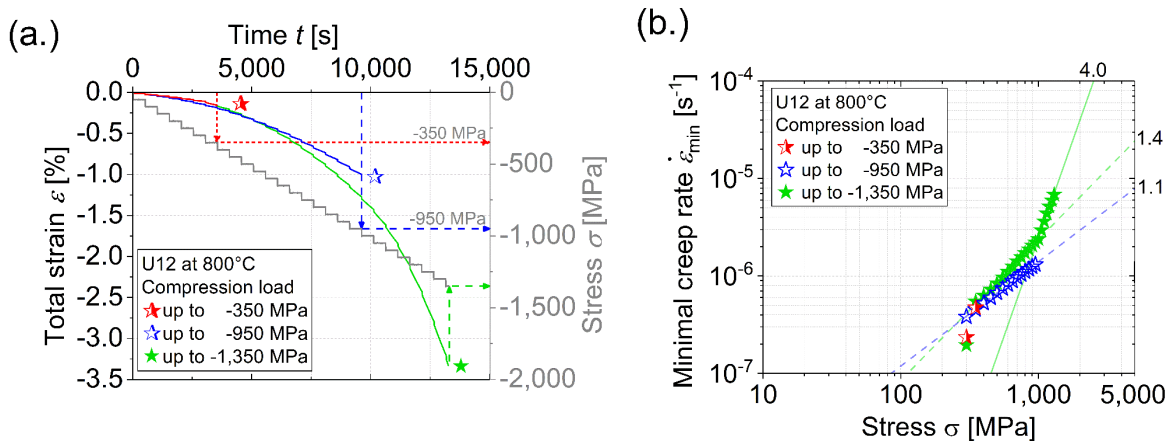


Fig. 7: (a.) Compression step-loading creep curves and (b.) minimal creep rates  $\dot{\epsilon}_{min}$  at 800 °C of the hardmetal grade U12. (a.) shows three compression step-loading creep curves until certain stress levels: -350 MPa (red; half-filled stars), -950 MPa (blue; open stars) and -1350 MPa (green; filled stars). (b.) shows the trend of the minimal creep rates  $\dot{\epsilon}_{min}$  over the stress  $\sigma$  for all three cases. (For interpretation of the references to colour in this figure legend, the reader is referred to the web version of this article.)

Tab. 4: Numerical values of the stress exponent  $n_i$  for compression loading at 800 °C in the given stress level intervals  $\sigma_i$  derived from the data in Fig. 6(b.). The displayed stress level range is indicated by index I for lower stress levels and an index II for higher stress levels.

U12 at 800 °C under compression loading				
Maximum test stress level [MPa]	$n_I$	$\sigma_I$ [MPa]	$n_{II}$	$\sigma_{II}$ [MPa]
-950	1.1	-300 – -950	/	/
-1350	1.4	-350 – -1000	4.0	-1000 – -1300

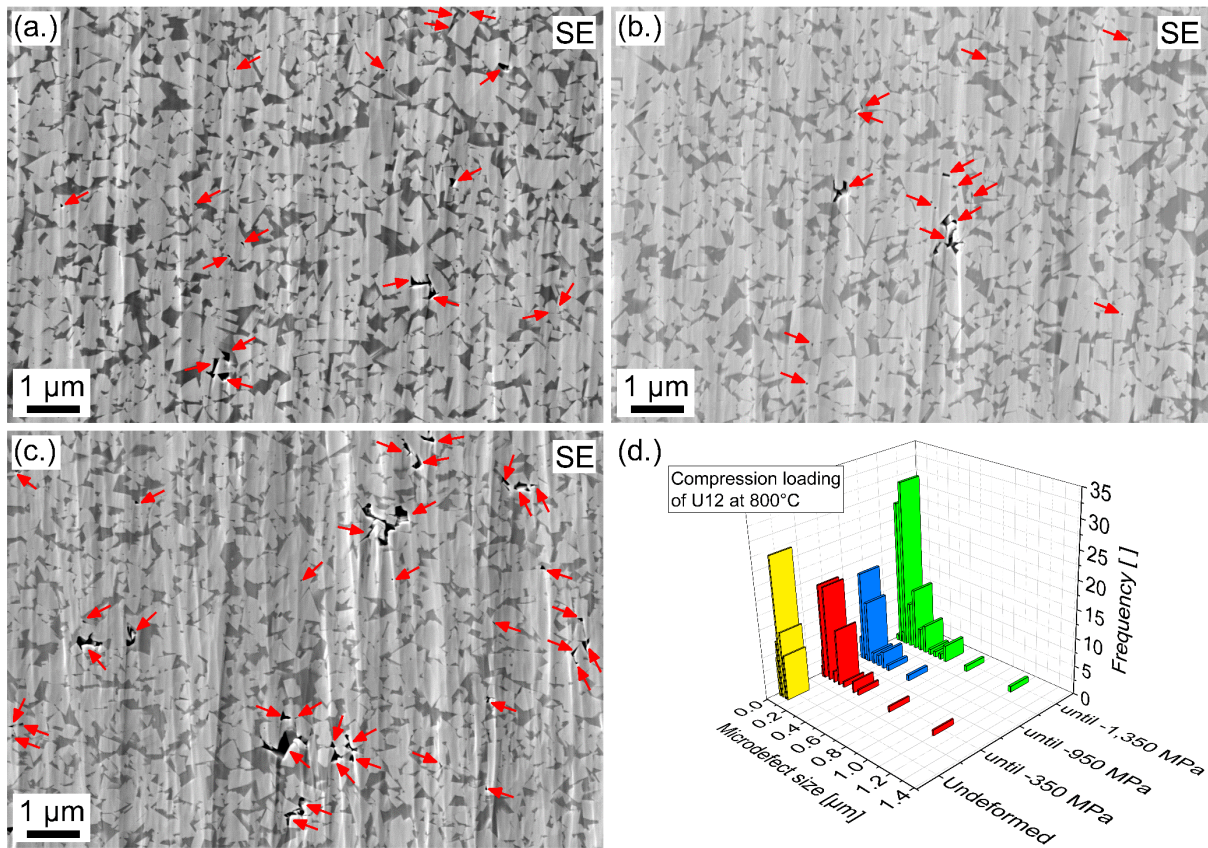


Fig. 8: SEM micrographs showing the microstructure of the hardmetal grade U12 in three compressive step-loading creep cases at 800 °C after maximum test stresses of: (a.) -350 MPa, (b.) -950 MPa, and (c.) -1350 MPa. The load direction points vertically along the image plane and red arrows mark microdefects. (d.) Microdefect size (equivalent diameter determined from the microdefect area) distribution over frequency for the undeformed specimen in yellow and for micrographs shown in (a.) with red bars, (b.) with blue bars and (c.) with green bars. (For interpretation of the references to colour in this figure legend, the reader is referred to the web version of this article.)

Fig. 8(a.) to Fig. 8(c.) show compression-deformed microstructures of U12 at 800 °C up to -350 MPa, -950 MPa and -1350 MPa of applied stress, respectively. The deformed microstructures showed microdefects such as cavities and nanopores. Microdefects are slightly darker than the Co-binder, dark grey, and marked with red arrows. No cracks had formed after -1350 MPa, but large microdefects are optically visible, see Fig. 8(c.). Additionally to optical assessment of an individual micrograph, counting of existing microdefects and their size were carried out using three SEM micrographs per compressive stress level, each with an area of 80  $\mu\text{m}^2$ , as exemplarily shown in Fig. 1(a.) and Fig. 8(a.) to Fig. 8(c.). The microdefect size was determined as the equivalent diameter determined from the microdefect area. The average microdefect number per micrograph was 15, 16, 14 and 30 on the investigated area of 80  $\mu\text{m}^2$  for the undeformed specimen, and the ones tested up to -350 MPa, -950 MPa and -1350 MPa, respectively. Fig. 8(d.) shows the size distribution of the microdefects. The undeformed specimen, see Fig. 1(a.) and yellow bars in Fig. 8(c.), show that the major part of its defect sizes are in the order of 0.1  $\mu\text{m}$  and only a

few defects were above 0.1  $\mu\text{m}$  in size. For the other two hardmetal grades M12 and S12, the initial microdefects were also determined on an investigated area of 80  $\mu\text{m}^2$ . The average microdefect number per micrograph was 1 and 3 for M12 and S12, respectively. The average defect sizes are also in the order of around 0.1  $\mu\text{m}$  for S12 as for U12, but for the hardmetal grade M12 the average defect sizes are larger and around 0.3  $\mu\text{m}$ . The compression loaded specimens of U12 tested up to -350 MPa, -950 MPa and -1350 MPa show a broader microdefect size distribution than the undeformed one of U12, but the majority of the microdefects is still of a size of about 0.1  $\mu\text{m}$ . From Fig. 8, it can be deduced that the microdefects form mainly at internal notches, i.e. sharp corners at WC/Co phase boundaries, narrow Co regions, or triple points of WC/WC/WC and WC/WC/Co.

#### 4. Discussion

##### 4.1 Influence of grain size on creep mechanism and creep resistance in WC-12 wt. % Co

Based on strain-corrected compression step-loading creep curves at 700 °C, see Fig. 3(a.), it was observed that the grade M12 with the largest investigated, i.e. medium, WC grain size had the highest creep rates. A similar behaviour was observed in specimens tested under tension, see Fig. 4(a.), although tests were not carried out up to similarly high stresses as under compression, as the specimens failed prematurely under tensile loads. Minimal creep rate curves from compression and tensile step-loading creep tests, see Fig. 5(a.) and Fig. 5(b.), showed that the medium-grained grade exhibits higher minimal creep rate values above -500 MPa under compression and above 250 MPa under tension than grades with smaller WC grains at the same stresses. Both the submicron-grained and ultrafine-grained grades showed a similar minimal creep rate progression up to -1250 MPa under compression at 700 °C, see Fig. 5(a.). Above the transition (when exceeding a critical stress level, i.e. the transition stress) between the regimes of  $n_I$  and  $n_{II}$  at -1250 MPa, the minimal creep rate of the submicron-grained grade showed a detectably faster increase with increasing stress in Fig. 5(a.) than the ultrafine-grained grade. Also, in the compression step-loading creep curves in Fig. 3(a.), it was observed that the two curves of the submicron-grained and ultrafine-grained grade separate at nearly -1250 MPa. The submicron-grained grade S12 exhibited a higher stress exponent than the ultrafine-grained grade U12 above the transition stress of -1250 MPa at 700 °C. Under tension and at 700 °C, the minimal creep rates of S12 and U12 did not differ and both materials showed comparable values of  $n_I = 1.2$  and  $n_{II} = 2.5$  up to the maximum stress level of 1000 MPa, see Fig. 5(b.).

Fig. 3(b.) and Fig. 4(b.) show step-loading creep curves of the three investigated materials for 800 °C. It was observed that the medium-grained grade exhibited the highest creep rate just as at 700 °C. In contrast to the case at 700 °C, however, an increase in creep rate was observed for the ultrafine-grained grade at 800 °C, as the step-loading creep curve had shifted more towards faster creep than the other two grades, i.e. its creep curve shifted between the medium and submicron-grained grades for both loading

conditions, see Fig. 3(b.) and Fig. 4(b.). At low compressive and tensile stresses, the ultrafine-grained grade showed the same behaviour as the medium-grained grade, and with increasing stresses, the step-loading creep curve converged the one of the submicron-grained grade. This behaviour was also observed for the minimal creep rate curves for 800 °C, shown in Fig. 5(c.) and Fig. 5(d.). The step-loading creep curves at 800 °C, also showed that all three grades creep significantly faster than at 700 °C. Comparing the step-loading creep curves with regard to temperature influence, it was observed that under compression, see Fig. 3, a strain of 3.4% is reached at about 1000 MPa, 600 MPa and 400 MPa lower stress at 800 °C than at 700 °C in the ultrafine, submicron and medium-grained grades, respectively. Temperature exerted the greatest influence on the creep behaviour of the grade with the finest WC grain size. Under tensile load, it was observed that specimens showed higher strain values in shorter time at 800 °C, see Fig. 4(b.). The creep behaviour of the medium-grained hardmetal grade was less affected by temperature than those of the ultrafine-grained grade. Additionally, the faster increase in strain over time under tensile than under compressive loading was known as strain asymmetry, as reported by [33]. The physical reason for the strain asymmetry was the faster formation of cavities at WC/WC interfaces and at WC/Co phase boundaries under tensile than under compressive loading [33].

The stress exponent  $n$  was used to estimate which rate-controlling creep mechanism is active in which stress level range and at what temperature. Based on step-loading creep tests,  $n$ -values between 1 and 6 at 700 °C, and 1 and 5 at 800 °C were determined in the current work, see Tab. 2 and Tab. 3. The same order of magnitude for  $n$  was also reported in [12,22,25] for test conditions under tension and compression, although not up to as high loads and for significantly higher temperatures compared to the ones investigated in the current work. In literature, maximal loads up to -750 MPa under compression [22] and up to 400 MPa under tensile load [12,25] were investigated between 800 °C and 1000 °C. Compared to the current work, hardmetal grades with lower Co-content [12,25] or larger average WC grain size [22,23] were investigated. The influence of increasing temperature on the progression of the stress exponent can only be estimated from two temperatures in the current work. Looking at  $n$ -values as function of the stress levels, see Fig. 6, the stress exponents generally changed from a lower to a higher value when exceeding the transition stress for all three hardmetal grades under compression and tensile loading. Under compression step-loading creep tests,  $n$ -values increased with increasing temperature between 950 MPa to 1200 MPa for U12 and S12 and between 500 MPa and 700 MPa for M12, see Fig. 6. Considering the  $n$ -values under tension, an increase was observed between 300 MPa to 500 MPa for all three hardmetal grades, compare Fig. 6(a.) with Fig. 6(b.). Additionally, with increasing temperature, the creep mechanism changed and the associated increase in  $n$  was observed to be shifted to lower stress levels. The shift of the mechanism change to lower stresses with increasing temperature was also evident in Ashby's deformation mechanism map for different

materials [41]. However, for more detailed statements on the effect of temperature on the stress exponent from step-loading creep tests of WC-Co hardmetals, more temperatures need to be investigated.

Additionally, Ueda et al. [12] and Doi et al. [23] observed an increase of  $n$  with decreasing WC grain size for WC-10 wt.% Co hardmetals. Thereby, they performed uniaxial tensile creep tests with loads up to a maximum of 300 MPa and temperatures between 750 °C and 900 °C. Furthermore, they observed that the stress exponent difference between WC grain sizes is smaller at 750 °C than at 900 °C. In the current work, no dependence of the stress exponent on WC grain sizes was observed at stresses up to -800 MPa and 500 MPa for compression and tensile loading, respectively, for 700 °C, see Fig. 6(a.), Fig. 5(a.) and Fig. 5(b.). Above these two stress values, the stress exponent of M12 was observed to increase while the values of U12 and S12 remained constant. Also, at 800 °C under compressive and tensile loads, the  $n$ -value of M12 increased above -500 MPa and 300 MPa, which the other two hardmetal grades had approximately similar orders of magnitude, see Fig. 6(b.). However, at stresses up to -500 MPa and 300 MPa at 800 °C, a lower stress exponent value for the medium-grained than for the submicron-grained grade was observed in the current work, see Fig. 6(b.), as for WC-10 wt.% Co hardmetals in literature [12,23]. Under -500 MPa and 300 MPa at 800 °C, the  $n$ -values were approximately similar as at 700 °C for all three hardmetal grades, see Fig. 6(b.), Fig. 5(b.) and Fig. 5(c.). A decrease in  $n$  with decreasing WC grain size was observed above certain stress levels at 700 °C and 800 °C for both loading cases. However, for compression creep tests for WC-12 wt. % Co and an average WC grain size between 2.2  $\mu\text{m}$  and 4.5  $\mu\text{m}$  [22], a decrease in the stress exponent value with decreasing WC grain size at 800 °C was also observed, as in the current work.

The influence of the WC grain size on the stress exponent observed in the current work differed from results documented in literature, but differences are also present in literature as mentioned above, which is caused by the different WC-Co composition and loading conditions. The stress exponents  $n_I$  observed in the current work for WC-12 wt.% Co hardmetals for low stresses were in the range of 1 to 2 and for  $n_{II}$  for high stresses in the range of 3 to 6 under compression and tension for 700 °C and 800 °C, see Tab. 2 and Tab. 3. In literature [12,23], stress exponents above 3.5 were observed in tensile creep tests up to a maximum stress of 300 MPa at 800 °C. Note that in [12,23] hardmetal grades with 10 wt.% Co and an average WC grain size between 0.6  $\mu\text{m}$  and 2.6  $\mu\text{m}$  were investigated. However, investigations on WC-10 wt.% Co hardmetals with an average WC grain size of 2.0  $\mu\text{m}$  were also carried out by Maier et al. [33] to investigate the tension-compression creep asymmetry up to 300 MPa at 800 °C. Thereby, a similar stress exponent of about 3 was observed in [33] under tension as in [12,23] for the hardmetal grade with similar WC grain size. Additionally, cavity formation was observed to occur faster under tension than under compression [33]. Therefore, it was assumed that different stress exponents and thus different creep mechanisms exist under tension and compression under the same stresses. The cavity formation is further assumed to contribute to the creep strain in addition to the previously attributed creep mechanisms such as



vacancy diffusion or dislocation creep [12,22,23,25]. Hence, in the current work up to 300 MPa, the influence of the WC grains was expected to be different, since a different creep mechanism is more pronounced than in the cases documented in literature, due to different stress exponents and Co-content. A similar stress exponent of about 1 for a stress interval up to 500 MPa as in the current work was observed for a WC-12 wt.% Co hardmetal with a WC grain size of 2.2  $\mu\text{m}$  in [22]. Although different stress exponents at different stresses have been noted in literature for different hardmetal grades, the same creep mechanisms have been identified for the same stress exponent values, as mentioned above.

Creep strain is the sum of dislocation creep, grain boundary sliding, diffusion creep and cavity formation [42]. Based on microstructural, stress exponent and activation energy investigations of different deformed WC-Co hardmetal specimens, potential creep mechanisms have been identified in loading ranges up to a maximum compressive load of -750 MPa [22] and up to 400 MPa under tension [12,23,25] between 750 °C to 1000 °C, which may be a combination of different deformation mechanisms depending on stress [12,14,22,23,25]: At low stresses, up to 400 MPa,  $n = 1$  was observed and associated with diffusion of Co in the bulk of the matrix around WC grains as the dominant creep mechanism [12,14,22]. When the stress is increased, above 400 MPa,  $n$ -values from 2 to 6 occur, which are associated with WC grain boundary sliding for values between 2 and 3 and dislocation creep with looping and climb of dislocations above 3 [12,14,22–25,42]. WC grain size had an influence on the creep mechanism, since it controlled the occurrence and kinetics of diffusion creep and grain boundary sliding [23,25,26,42]. Additionally, researchers observed that the influence of the WC grain size on the creep rate changed with the applied temperatures and stresses [22–25]. In the case of temperatures below 900 °C and stresses above 400 MPa, the creep rate increased with increasing WC grain sizes [22,23]. At temperatures above 900 °C and stresses up to 400 MPa, the creep rate decreased with increasing WC grain size [22,26]. Under these conditions, the dominant creep mechanism was vacancy diffusion in the Co binder [12,14,22]. Grades with coarse WC grains, associated with a comparatively large mean free path in Co, had lower creep rate if creep strain is controlled by vacancy diffusion in Co, because less grain boundary areas per unit volume are available for the faster grain boundary diffusion [22]. These conclusions were drawn from standard creep tests for WC-Co composition with different average WC grain size and Co-content at low stresses compared to the stresses applied in step-loading creep tests in the current work. Stress exponents in the current work were observed to be similar in magnitude to the above mentioned literature, albeit up to higher stress levels and lower temperatures. Based on the above mentioned creep mechanisms and the  $n$ -values from literature, it is assumed: The increasing creep rate with increasing application temperature under compression and tensile loading of the ultrafine-grained grade, with  $n$  equal to about 1, occurred due to diffusion processes at grain boundaries, see Fig. 5(c.), Tab. 2 and Tab. 3.

Step-loading creep results in Fig. 3(a.) and Fig. 4(a.) at 700 °C showed a typical creep behaviour at low temperatures: Materials with small grain sizes had the highest creep resistance up to certain temperatures [43]. The  $n_I$  values for all three specimens was between 1 and 2 at low stress levels, which indicates vacancy diffusion, as mentioned above. Additionally, the  $n_I$  value range at 700 °C was observed at low to medium stresses in the current work, see Tab. 2 and Tab. 3. At low stresses, the dislocation density is low and therefore the creep strain due to dislocation sliding is negligible and vacancy diffusion is dominant [42]. Considering the temperature influence, the following rule of thumb is valid for creep of ceramics and two-phase alloys: If the ratio of the applied temperature  $T$  with the melting temperature  $T_m$ , both in Kelvin, is greater than or equal to 0.5, creep processes are active [42,44]. In the case of WC-Co hardmetals, 500 °C (773.15 K) is a temperature limit with  $T/T_m = 0.5$ . This is attributed to the fact that most of the strain is carried by the Co-phase which contains tungsten and carbon, and the ternary eutectic of W-C-Co has a melting temperature of 1280 °C (1553,1 K) [1]. For an applied temperature of 700 °C (973.15 K), in the current work, the ratio  $T/T_m = 0.6$ . Hence, creep processes are activated in tests at 700 °C and 800 °C, but deformation due to the formation of thermally induced dislocation structures above the yield strength also contributes to the total strain, see  $R_{p0.2}$  values at 700 °C and 800 °C in Tab. 1. However, note that a direct comparison of total strain values in creep experiments with  $R_{p0.2}$  values is not permissible, as plastic strains are already present below the 0.2% yield strength, and therefore thermally induced dislocation movement already occurs at lower stress levels. In room temperature tests, hardmetal grades with finer WC grain size exhibited higher compressive yield strength than grades with coarser WC grain size with the same Co-content [38]. The yield strength in Tab. 1 shows the influence of temperature at 700 °C, which  $R_{p0.2}$  values above 1800 MPa for both finer grained materials. In compression, step-loading creep curves, see Fig. 3(a.), a comparable behaviour was observed: The observed total strain shows a pronounced rise with time in the stress exponent regime  $n_{II}$  at the stress levels which were in the range of the yield strength in Tab. 1 and Fig. 5(a.). Similar behaviour was also observed in the  $n_{II}$  regime under compressive loading at 800 °C but at stress levels below the  $R_{p0.2}$  value at that temperature.

When the temperature was increased to 800 °C, the creep resistance of the ultrafine-grained grade was reduced more pronouncedly than for the other investigated grades, indicated by the shift of the step-loading creep curve to shorter times in Fig. 3(b.) and Fig. 4(b.). The influence of WC grain size on creep resistance changed with increasing temperature, and the creep rate increased with decreasing WC grain size [12,23,24]. As mentioned above, the creep behaviour of the medium-grained grade were less affected by temperature than those of the other two grades. Since grades with coarse WC grains have a higher creep resistance when diffusion is the active creep mechanism, as they have fewer grain boundary areas per unit volume. Furthermore, it has to be taken into account that up to date, to the best knowledge of the authors, no investigations on creep of ultrafine-grained grades have been performed under conditions such as applied

in the current work. Step-loading creep tests were previously not reported up to very high stresses at 800 °C and 700 °C. Next to the shift in the minimal creep rate of the ultrafine-grained grade, the minimal creep rate of U12 was higher than that of S12 at low compressive stress levels, but both showed similar slopes of the minimal creep rate - stress curves, see Fig. 5(c.). Also in uniaxial compression creep tests performed up to 750 MPa from 800 °C to 1000 °C by Smith et al. [22], the strain rate increased at low stresses as the WC grain size decreased. This was observed for hardmetal specimens with a Co-content of 12 wt.% and 15 wt.% and a WC grain size between 2.2 µm and 4.5 µm. For the stress exponent in the range of 1, vacancy diffusion is considered to be the dominant creep mechanism [22]. Also, the compressive minimal creep rates of U12 and S12 were observed to become more similar at stresses above 1000 MPa at 800 °C, see Fig. 5(c.). Hence, in the ultrafine-grained grade above 1000 MPa, dislocation movement and WC grain boundary sliding are considered to be the dominant creep mechanism, as suggested for compression creep tests for hardmetal grades larger WC grain size in [22]. However, due to the rapidly increasing strain of 0.3% within 500 s above 1200 MPa, microdefect formation, as reported in [33] and shown in Fig. 8, is interpreted to play an important role on the strain rate in addition to dislocation motion and grain boundary sliding.

#### 4.2. Damage evolution during step-loading creep tests

A comparison of three step-loading creep curves of U12 at 800 °C, see Fig. 7(a.), shows almost equal strain values in the step-loading creep curves up to -500 MPa. Above -500 MPa, the slope of step-loading creep curve increased differently for the tests up to -950 MPa and -1350 MPa. In addition to the factors discussed above, the slope difference may be also affected by some differences in the formation kinetics of cavities that form during creep of WC-Co hard metals [17,33] that in turn may be influenced by factors such as slight variations in binder chemistry [17].

In specimens loaded up to -350 MPa and -950 MPa, a similar number of defects as in the undeformed specimen was observed, compare, Fig. 8(a.), Fig. 8(b.) and Fig. 1(a.). This and the observed small number of the initial defects of the grades investigated in the current work suggests that not their number or size but the cavity nucleation and growth behaviour during creep loading is most relevant when trying to understand creep-induced defect formation. The number of the smallest defects of a size in the order of 0.1 µm decreased in the specimens deformed up to -350 MPa and -950 MPa and larger ones appeared in both cases, which indicates that small defects had grown, see Fig. 8(d.). The hypothesis of defects growing during creep loading is supported also by the defect histogram entries for the specimen loaded up to -1350 MPa, see Fig. 8(d.). The fact that the number of the smallest cavities in this plot did not decrease for this specimen compared to the initial cavity content as in the other deformed states, may indicate that the nucleation rate of the smallest cavities rises at higher stress levels. This and the higher strains at equal stress levels, see Fig. 7(a.), and the steeper rise of the minimal creep rate with stress, see

Fig. 7(b.), for this specimen compared to the other two shown in Fig. 7, may be an indication of slight differences in the specimen-specific growth rates of the cavities that contribute to the total strain signal. For a well-founded assessment of the quantitative influence of the orientation, number and size of the initial and creep load-induced porosity on the quantitative contribution to the creep strain, in-situ investigations during creep loading are necessary. They could be coupled with digital image correlation techniques to assess possible rearrangement of the WC grains within the material during creep in future work that may aim to determine the contribution of cavity formation to the total creep strain signal. The defects formed at internal notches, i.e. sharp corners at WC/Co phase boundaries, narrow Co regions, or triple points of WC/WC/WC and WC/WC/Co, see Fig. 8(a.) and Fig. 8(b.). Because of the few minimal creep rate data points for the specimen loaded up to -350 MPa, no stress exponent was determined, see Fig. 7(b.). For the specimen loaded up to -950 MPa, the stress exponent  $n_I$  was about 1.1, see Tab. 4, and is interpreted to be associated with vacancy diffusion as active creep mechanism, as suggested in [12,22]. Since similar microdefect sizes and numbers were observed in the specimens loaded up to -350 MPa and -950 MPa, vacancy diffusion is also interpreted to be the dominant creep mechanism in the specimen loaded up to -350 MPa.

A stress exponent  $n_I$  of about 1.4 was observed in the specimen loaded up to -1350 MPa in the stress range between -350 MPa and -1000 MPa, see Tab. 4. The stress exponent was, as already mentioned above,  $n_I = 1.1$  for the specimen loaded up to -950 MPa. Since larger microdefects in the specimen loaded up to -950 MPa were observed than in the undeformed specimen, it is assumed that an increase in damaged occurred, and smaller defects grow at a stress exponent of  $n_I = 1.4$ . The attained SEM micrographs of U12 loaded up to -1350 MPa at 800 °C showed that after loading the specimen to this stress value, that is slightly higher than  $R_{p0.2} = 1140$  MPa at this temperature, cf. Tab. 1, damage in form of cavity formation seem to contribute to creep in addition to WC/WC grain boundary sliding and time-independent plastic deformation above the compressive yield strength as reported by Ashby deformation mechanism maps [41], see Fig. 8(c.). The stress exponent,  $n_{II} = 4$  was determined between -1000 MPa and -1300 MPa, see Fig. 7(b.) and Tab. 4. After loading up to -1350 MPa, twice as many microdefects and a broader defect size distribution were observed than in specimens loaded to -350 MPa and -950 MPa, see Fig. 8(d.). Additionally, the observed creep strain showed a significant increase, see Fig. 7(a.), which is interpreted to be fostered also by the formation of cavities. Below -1250 MPa, an increase in strain of maximum 0.1% within 500 s was observed, whereas above -1250 MPa an increase of 0.3% strain was observed. The types of defects were cavities at WC/WC interfaces and nanopores, see Fig. 8(a.) to Fig. 8(c.). Cavities are located at internal notches, i.e. sharp corners at WC/Co phase boundaries, narrow Co regions or triple points of WC/WC/WC and WC/WC/Co. Depending on temperature and applied stress, the above-mentioned mechanism of WC/WC grain boundary sliding between WC grains, at triple points of WC/WC/WC and WC/WC/Co, and dislocation creep may led to formation of cavities. When the load was increased, cavities broke up the

mentioned interfaces, but neither cracks nor broken WC grains were observed. These results agree with results from literature, which documented cavities to occur in the vicinity of WC grains that slide relative to each other, or WC grains to have shifted relative to one another during creep tests [16,17,22]. Additionally, nanopores are interpreted to have started to grow in size and to also have joined to form larger cavities in the material, whose size was in the order of magnitude of the WC grains and above, see Fig. 8(c.) and Fig. 8(d.).

The minimal creep rate increased discontinuously between stress levels of -300 MPa and -400 MPa in the tested specimens of the hardmetal grade U12 at 800 °C, see Fig. 5(c.) and Fig. 7(b.). The increase is interpreted to be associated with a change in the dominant deformation process [41]. At the stress level range of -350 MPa to -1000 MPa, the hardmetal grades U12 had a stress exponent  $n_I$  of 1.4, see Tab. 2 and Tab. 4. In this stress level range, vacancy diffusion occurred and grades with large WC grains had a higher creep resistance than ones with small grains, e.g. because less grain boundary area per unit volume is available for grain boundary diffusion that occurs faster than bulk diffusion [12,22]. In contrast, in the submicron grade, an increase in the creep rate and a related mechanism change occurs already at stresses exceeding -850 MPa. Compressive stresses higher -1000 MPa in the ultrafine grade and higher than -850 MPa in the submicron grade,  $n_{II} > 4$  was observed, and is associated with dislocation creep as the dominant creep mechanism [23,26]. Additionally, as shown in the microstructure analysis, see Fig. 8, cavities are formed at high stresses, that also contribute to the observed strain and stress exponent in the ultrafine-grained hardmetal grade. Same creep rates and stress exponents as in the ultrafine-grained hardmetal grade above -1000 MPa at 800 °C under compression were also observed for the submicron-grained hardmetal grades in the current work, see Fig. 5(c.). Also, the medium-grain hardmetal grade exhibited the same creep rates and stress exponents as the ultrafine-grain grade up to -550 MPa at 800 °C. Due to intervals of equal stress exponents as in the ultrafine grade, same creep mechanisms are assumed to be present in the medium- and submicron-grained grades.

The shift in the step-loading creep curve of the ultrafine-grained grade between the medium and submicron-grained grades at 800 °C, see Fig. 3(b.) and Fig. 4(b.), is attributed to the fact that with increasing temperature, minimal creep rate and diffusion increase at low stress levels. As mentioned above, diffusion processes are active in compression step-loading creep tests up to high stress levels for the ultrafine-grained grade, see Fig. 5(c.) as well as Tab. 2. Due to the change of the creep mechanism at higher stresses and the increase of the minimal creep rate at low stresses, the creep rates and the step-loading creep curves of the ultrafine-grained and submicron-grained grades approach each other above -1000 MPa, see Fig. 3(b.) and Fig. 5(c.). However, at 800 °C, the medium-grained grade still exhibits the highest creep rates. No statement was possible on the only basis of the microstructure investigation at which nanometer-sized cavities, next to vacancy diffusion and dislocation creep, contribute to the creep strain. For investigations of the influence

of cavities on the creep strain, SEM observations performed in-situ during creep loading are suggested for future work. Based on results of the current investigations, a contribution was made to available literature on creep behaviour of WC-Co hardmetals for the optimal selection of hardmetal grades for applications with intermediate thermal and high mechanical loads.

## 5. Conclusion

Uniaxial tensile and compression step-loading creep tests were performed for three WC-Co hardmetal grades with ultrafine, submicron and medium WC grain sizes. The step-loading creep tests at 700 °C and 800 °C were performed with 50 MPa stress steps, which were applied in 5 s followed by a hold time of 500 s at each stress steps. Stress steps were applied until a predefined number of steps or a predefined strain was reached. The results can be summarized as follows:

- All three hardmetals investigated exhibit time-dependent creep behaviour under tensile and compressive step-loading at 700 °C and 800 °C, with steady-state secondary creep achieved at stresses above about 150 MPa within 500 s after each loading step; with specimens creeping faster under tensile loading, because of the preferred formation of cavities.
- Two regions with different stress exponents were observed. At low stress levels, the stress exponent is in the range of about 1, and above a characteristic critical stress level (transition stress), the stress exponent increases and reaches values between about 4 and 6.
- Compression and tensile step-loading creep curves attained at 700 °C showed that the hardmetal grade with the medium WC grain sizes exhibits the highest minimal creep rates above stress levels of 300 MPa compared to the grades with submicron and ultrafine grain sizes. In contrast to that, the ultrafine-grained hardmetal grade showed higher minimal creep rates at 800 °C, because of the higher amount of grain boundary areas per unit volume, which is advantageous for vacancy diffusion at grain boundaries.
- Under compression step-loading at 700 °C, a strain of about -3.4% was achieved when the stress level reached a value of about -1300 MPa, -2000 MPa and -2350 MPa for the medium, submicron and ultrafine grades, respectively. In contrast to that, under tensile step-loading at 800 °C, it was observed that 3.4% strain was achieved at lower stresses of about 900 MPa, 1400 MPa and 1350 MPa for the medium, submicron and ultrafine grades, respectively.
- The creep rate of the medium-grained hardmetal grade is less affected by temperature than the finer-grained grade. As a cause, it is assumed that diffusion creep becomes more important with increasing temperature and grades with larger WC grains have higher creep resistance due to their smaller grain boundary areas per unit volume.

- Step-loading creep tests allow testing up to very high stresses and at low temperatures in reasonable testing times. At both temperatures of 700 °C and 800 °C, an increase of the stress exponent was observed, when the transition stress was exceeded. This is interpreted as a creep mechanism change from vacancy diffusion to grain boundary sliding and dislocation creep.
- At 700 °C and compressive loading, the transition stress is about -850 MPa, -1300 MPa and -1500 MPa for the medium-grained, the submicron-grained and the ultrafine-grained grade. At 800 °C and compressive loading, the transition stress is about -500 MPa, -850 MPa and -1000 MPa for the medium-grained, the submicron-grained and the ultrafine-grained grade, respectively. In the case of tensile loading, the transition stress was observed at lower stress levels than under compressive loading at 700 °C and 800 °C.
- Three WC-12 wt.% Co hardmetals with ultrafine WC grains were subjected to compression step-loading at 800 °C up to different maximum stress levels of -350 MPa, -950 MPa and -1350 MPa in order to investigate the resulting damage. Microstructure analysis revealed that testing up to a stress level of -950 MPa and -1350 MPa has caused damage in form of cavity formation with more and larger cavities at the stress level of -1350 MPa. In particular, microdefects such as nanopores that form at WC/WC interfaces and WC/Co phase boundaries have increased and promoted the formation of larger cavities when they grow together.

## 6. Acknowledgements

The authors gratefully acknowledge the financial support of the Frontrunner-Initiative of the project "Frontrunner: Integrated, data driven development for Cutting Tools" (Project No. 861280) and the scope of the COMET program within the K2 Center "Integrated Computational Material, Process and Product Engineering (IC-MPPE)" (Project No 859480). This program is supported by the Austrian Federal Ministries for Climate Action, Environment, Energy, Mobility, Innovation and Technology (BMK) and for Digital and Economic Affairs (BMDW), represented by the Austrian research funding association (FFG), and the federal states of Styria, Upper Austria and Tyrol.

## 7. Appendix

Tab. A.1 shows the elastic definitions of the materials and the sum of creep parameters following Eq. (1) to calculate the creep strain rates. Two sets of creep parameters were defined for each material state (i.e. A1, n1, m1 and A2, n2, m2). The material model switches between the two sets at the defined "von Mises" switching stress. This value correlates roughly with the stress range of the stress exponent change as shown in Fig. 5. The later stages of creep at very high strain values with tertiary creep characteristics were excluded from this table.

Tab. A.1: Material parameters for calculation of creep strain rates by finite element simulation.

Material	[-]	M12				S12				U12					
		Tension		Compression		Tension		Compression		Tension		Compression			
Loading direction	[-]														
Temperature	[°C]	700	800	700	800	700	800	700	800	700	800	700	800	700	800
Young's modulus	[GPa]	495	420	495	420	500	420	500	420	505	450	505	450	505	450
Poisson ratio	[-]	0.21	0.22	0.21	0.22	0.21	0.22	0.21	0.22	0.21	0.22	0.21	0.22	0.21	0.22
A1	$[N^{-n1}mm^{2-n1}s^{-1-m1}]$	3.3E-10	4.1E-9	3.5E-11	2.8E-9	6E-10	1.5E-10	4.0E-10	1.0E-10	6.3E-10	4.0E-9	4.3E-10	1.2E-10	4.3E-10	1.2E-10
n1	[-]	1.8	1.5	2.0	1.5	1.6	1.9	1.6	1.9	1.6	1.5	1.6	2.0	1.6	2.0
m1	[-]	-0.5	-0.5	-0.5	-0.5	-0.5	-0.5	-0.5	-0.5	-0.5	-0.5	-0.5	-0.5	-0.5	-0.5
Switching stress	[MPa]	475	275	775	475	775	375	1225	825	775	325	1475	975	775	325
A2	$[N^{-n1}mm^{2-n1}s^{-1-m1}]$	1.1E-16	8.0E-16	2.8E-21	1.3E-16	2.3E-13	2.0E-16	4.0E-19	1.8E-17	2.4E-13	5.0E-14	6.9E-14	1.3E-16	2.4E-13	5.0E-14
n2	[-]	4.2	4.2	5.5	4.2	2.8	4.2	4.5	4.2	2.8	3.5	2.8	4.0	2.8	3.5
m2	[-]	-0.5	-0.5	-0.5	-0.5	-0.5	-0.5	-0.5	-0.5	-0.5	-0.5	-0.5	-0.5	-0.5	-0.5



**References**

- [1] W. Schedler, *Hartmetall für den Praktiker. Aufbau, Herstellung, Eigenschaften und industrielle Anwendung einer modernen Werkstoffgruppe*, VDI (Verein Deutscher Elektriker) Verlag, Düsseldorf, 1988.
- [2] A.W. Nemetz, W. Daves, T. Klünsner, W. Ecker, J. Schäfer, C. Czettl, T. Antretter, Cyclic heat-up and damage-relevant substrate plastification of single- and bilayer coated milling inserts evaluated numerically, *Surf. Coatings Technol.* 360 (2019) 39–49. doi:<https://doi.org/10.1016/j.surfcoat.2019.01.008>.
- [3] A.W. Nemetz, W. Daves, T. Klünsner, C. Praetzas, W. Liu, T. Tepperneegg, C. Czettl, F. Haas, C. Bölling, J. Schäfer, Experimentally validated calculation of the cutting edge temperature during dry milling of Ti6Al4V, *J. Mater. Process. Technol.* 278 (2020) 116544. doi:<https://doi.org/10.1016/j.jmatprotec.2019.116544>.
- [4] T. Kagnaya, M. Lazard, L. Lambert, C. Boher, T. Cutard, Temperature evolution in a WC-6%Co cutting tool during turning machining: Experiment and finite element simulations, *WSEAS Trans. Heat Mass Transf.* 6 (2011) 71–80.
- [5] H.G. Schmid, The mechanisms of fracture of WC-11 wt% Co between 20° C and 1000° C, *Mater. Forum.* 10 (1987) 184–197.
- [6] X. Han, N. Sacks, Y. V. Milman, S. Luyckx, On plastic deformation mechanisms of WC-15 wt% Co alloys at 1000 °C, *Int. J. Refract. Met. Hard Mater.* 27 (2009) 274–281. doi:10.1016/j.ijrmhm.2008.09.021.
- [7] K. Buss, D. Mari, High temperature deformation mechanisms in cemented carbides and cermets studied by mechanical spectroscopy, *Mater. Sci. Eng. A.* 370 (2004) 163–167. doi:10.1016/j.msea.2002.12.004.
- [8] F. Ueda, H. Doi, F. Fujiwara, H. Masatomi, Bend Deformation And Fracture Of WC-Co Alloys At Elevated Temperatures, *Trans Jpn Inst Met.* 18 (1977) 247–256. doi:10.2320/matertrans1960.18.247.
- [9] T. Sakuma, High-Temperature Plastic Flow in Cemented Carbides and Cermets, *Key Eng. Mater.* 108–110 (1995) 435–448. doi:10.4028/www.scientific.net/KEM.108-110.435.
- [10] G. Östberg, K. Buss, M. Christensen, S. Norgren, H.-O. Andrén, D. Mari, G. Wahnström, I. Reineck, Mechanisms of plastic deformation of WC–Co and Ti(C, N)–WC–Co, *Int. J. Refract. Met. Hard Mater.* 24 (2006) 135–144. doi:<https://doi.org/10.1016/j.ijrmhm.2005.04.009>.
- [11] I.C. Lee, T. Sakuma, High-temperature tensile ductility in WC-Co cemented carbides, *Metall. Mater. Trans. A Phys. Metall. Mater. Sci.* 28A (1997) 1843–1847. doi:10.1007/s11661-997-0114-6.

- [12] F. Ueda, H. Doi, F. Fujiwara, H. Masatomi, Y. Oosawa, Tensile Creep of WC-10%Co and WC-10%TaC-10%Co Alloys at Elevated Temperatures, *Trans. Japan Inst. Met.* 16 (1975) 591–600. doi:10.2320/matertrans1960.16.591.
- [13] T. Sakuma, H. Hondo, Plastic flow in WC-13wt.%Co at high temperatures, *Mater. Sci. Eng. A.* A156 (1992) 125–130. doi:10.1016/0921-5093(92)90144-P.
- [14] S. Lay, J. Vicens, F. Osterstock, High temperature creep of WC-Co alloys, *J. Mater. Sci.* 22 (1987) 1310–1322. doi:10.1007/BF01233127.
- [15] R.J. Gottschall, W.S. Williams, I.D. Ward, I.D. Ward, Microstructural study of hot-deformed cemented carbides, *Philos. Mag. A Phys. Condens. Matter, Struct. Defects Mech. Prop.* 41 (1980) 1–7. doi:10.1080/01418618008241826.
- [16] M.A. Yousfi, J. Weidow, A. Nordgren, L.K.L. Falk, H.O. Andrén, Deformation mechanisms in a WC-Co based cemented carbide during creep, *Int. J. Refract. Met. Hard Mater.* 49 (2015) 81–87. doi:10.1016/j.ijrmhm.2014.07.016.
- [17] K. Mingard, S. Moseley, S. Norgren, H. Zakaria, D. Jones, B. Roebuck, Microstructural observations of high temperature creep processes in hardmetals, *Powder Metall.* (2021) 1–11. doi:10.1080/00325899.2021.1877866.
- [18] I. Lee, High-temperature plastic flow behaviour in the binder of WC-Co cemented carbides, *Met. Mater.* 2 (1996) 97–101. doi:10.1007/BF03025952.
- [19] M.J. Murray, D.C. Smith, Stress induced cavitation in cobalt bonded tungsten carbide, *J. Mater. Sci.* 8 (1973) 1706–1710. doi:10.1007/BF02403520.
- [20] W. Acchar, U.U. Gomes, W.A. Kaysser, J. Goring, Strength degradation of a tungsten carbide-cobalt composite at elevated temperatures, *Mater. Charact.* 43 (1999) 27–32. doi:10.1016/S1044-5803(98)00056-4.
- [21] H.G. Schmid, D. Mari, W. Benoit, C. Bonjour, The mechanical behaviour of cemented carbides at high temperatures, *Mater. Sci. Eng.* 105–106 (1988) 343–351. doi:10.1016/0025-5416(88)90716-1.
- [22] J.T. Smith, J.D. Wood, Elevated temperature compressive creep behavior of tungsten carbide-cobalt alloys, *Acta Metall.* 16 (1968) 1219–1226. doi:10.1016/0001-6160(68)90003-5.
- [23] H. Doi, F. Ueda, Y. Fujiwara, H. Masatomi, Influence of carbide grain size on elevated temperature tensile creep of WC-10%Co alloy, *Int. J. Refract. Hard Met.* 3 (1984) 146–148.
- [24] R. Useldinger, U. Schleinkofer, Creep behaviour of cemented carbides — Influence of binder content, binder composition and WC grain size, *Int. J. Refract. Met. Hard Mater.* 62 (2017) 170–175. doi:10.1016/j.ijrmhm.2016.06.013.

- [25] G. Wirmark, G.L. Dunlop, C. Chatfield, Tensile Creep of WC-Co Cemented Carbides at 800 - 900 C, *Int. J. Refract. Hard Met.* 5 (1986) 153–157.
- [26] F. Osterstock, HIGH TEMPERATURE CREEP OF SOME WC-Co ALLOYS., in: *Sci. Hard Mater.*, 1983: pp. 671–687. doi:10.1007/978-1-4684-4319-6\_36.
- [27] S.A. Humphry-Baker, L.J.M. Vandeperre, Creep deformation of WC hardmetals with Fe-based binders, *Int. J. Refract. Met. Hard Mater.* 95 (2021) 105462. doi:10.1016/j.ijrmhm.2020.105462.
- [28] I.C. Lee, A threshold stress for high-temperature plastic flow in WC-CO cemented carbides, *Met. Mater.* 1 (1995) 125–132. doi:10.1007/BF03025923.
- [29] S. Lay, F. Osterstock, HIGH TEMPERATURE CREEP OF PURE TUNGSTEN CARBIDE AND WC-Co ALLOYS WITH LOW COBALT VOLUMIC RATIOS., in: *Mater. Sci. Res.*, 1984: pp. 463–471. doi:10.1007/978-1-4615-6802-5\_31.
- [30] B. Roebuck, E.A. Almond, Deformation and fracture processes and the physical metallurgy of WC-Co hardmetals, *Int. Mater. Rev.* 33 (1988) 90–112. doi:10.1179/imr.1988.33.1.90.
- [31] B. Roebuck, S. Moseley, Tensile and compressive asymmetry in creep and monotonic deformation of WC/Co hardmetals at high temperature, *Int. J. Refract. Met. Hard Mater.* 48 (2015) 126–133. doi:10.1016/j.ijrmhm.2014.08.007.
- [32] K. Maier, T. Klünsner, M. Krobath, C. Tritremmel, S. Marsoner, C. Czettel, Uniaxial step loading test setup for determination of creep curves of oxidation-sensitive high strength materials in vacuum under tensile and compressive load, *Int. J. Refract. Met. Hard Mater.* 92 (2020) 105327. doi:10.1016/j.ijrmhm.2020.105327.
- [33] K. Maier, T. Klünsner, W. Ecker, P. Pichler, S. Marsoner, C. Czettel, J. Schäfer, R. Ebner, A physical reason for asymmetric creep deformation behaviour of WC-Co hardmetal under tension and compression loading at 700 °C and 800 °C, *Int. J. Refract. Met. Hard Mater.* 97 (2021) 105526. doi:https://doi.org/10.1016/j.ijrmhm.2021.105526.
- [34] S.N. Basu, V.K. Sarin, Oxidation behavior of WC-Co, *Mater. Sci. Eng. A.* 209 (1996) 206–212. doi:10.1016/0921-5093(95)10145-4.
- [35] M. Jonke, T. Klünsner, P. Supancic, W. Harrer, J. Glätzle, R. Barbist, R. Ebner, Strength of WC-Co hard metals as a function of the effectively loaded volume, *Int. J. Refract. Met. Hard Mater.* 64 (2017) 219–224. doi:10.1016/j.ijrmhm.2016.11.003.
- [36] T. Klünsner, S. Wurster, P. Supancic, R. Ebner, M. Jenko, J. Glätzle, A. Püschel, R. Pippan, Effect of specimen size on the tensile strength of WC-Co hard metal, *Acta Mater.* 59 (2011) 4244–4252. doi:10.1016/j.actamat.2011.03.049.

- [37] T. Tepperneegg, T. Klünsner, C. Kremsner, C. Tritremmel, C. Czettl, S. Puchegger, S. Marsoner, R. Pippan, R. Ebner, High temperature mechanical properties of WC-Co hard metals, *Int. J. Refract. Met. Hard Mater.* 56 (2016) 139–144. doi:10.1016/j.ijrmhm.2016.01.002.
- [38] T. Klünsner, S. Marsoner, R. Ebner, R. Pippan, J. Glätzle, A. Püschel, Effect of microstructure on fatigue properties of WC-Co hard metals, in: *Procedia Eng.*, 2010: pp. 2001–2010. doi:10.1016/j.proeng.2010.03.215.
- [39] ISO 4499-2, ISO 4499-2:2008 Hardmetals-Metallographic determination of microstructure-Part 2: Measurement of WC grain size, 2008.
- [40] B. Winiarski, A. Gholinia, K. Mingard, M. Gee, G.E. Thompson, P.J. Withers, Broad ion beam serial section tomography, *Ultramicroscopy.* 172 (2017) 52–64. doi:https://doi.org/10.1016/j.ultramic.2016.10.014.
- [41] J. Roesler, H. Harders, M. Baeker, *Mechanical Behaviour of Engineering Materials*, 1st ed., Springer-Verlag Berlin Heidelberg, 2007. doi:10.1007/978-3-542-73448-2.
- [42] R. Bürgel, H. Jürgen Maier, T. Niendorf, *Handbuch Hochtemperatur- Werkstofftechnik*, 2011. doi:10.1007/978-3-8348-9907-1.
- [43] F. Abe, T.-U. Kern, V. R., *Creep-Resistant Steels*, Woodhead Publishing, 2008.
- [44] O.D. Sherby, P.M. Burke, Mechanical behavior of crystalline solids at elevated temperature, *Prog. Mater. Sci.* 13 (1968) 325–390. doi:10.1016/0079-6425(68)90024-8.

# **Publication IV**

**Strain ratcheting limit stresses as a function of  
microstructure of WC-Co hardmetals under uniaxial cyclic  
loads under a stress ratio of  $R = -\infty$  at elevated temperatures**

**Kathrin Maier, Thomas Klünsner, Philip Pichler, Stefan Marsoner,  
Werner Ecker, Christoph Czettel, Jonathan Schäfer, Reinhold Ebner**

**Published in**

**Journal of Refractory Metals and Hard Materials,**

**102 (2021) 105699**

## Strain ratcheting limit stresses as a function of microstructure of WC-Co hardmetals under uniaxial cyclic loads under a stress ratio of $R = -\infty$ at elevated temperatures

Kathrin Maier<sup>1\*</sup>, Thomas Klünsner<sup>1</sup>, Philip Pichler<sup>1</sup>, Stefan Marsoner<sup>1</sup>, Werner Ecker<sup>1</sup>,  
Christoph Czettel<sup>2</sup>, Jonathan Schäfer<sup>2</sup>, Reinhold Ebner<sup>1</sup>

<sup>1</sup> Materials Center Leoben Forschung GmbH, Roseggerstraße 12, 8700 Leoben, Austria

<sup>2</sup> CERATIZIT Austria GmbH, Metallwerk-Plansee Straße 71, 6600 Reutte, Austria

\*Corresponding author: kathrin.maier@mcl.at

**Keywords:** WC-Co hardmetal; Cyclic stress-strain hysteresis; Elevated temperature; Strain ratcheting; Limit stresses; EBSD

### Abstract

The aim of the current work was the experimental determination of limit stresses in the uniaxial cyclic compression test that lead to advancing ratcheting in different WC-Co hardmetal grades at elevated temperature. At stresses below the limit stress the plastic strain per cycle reduces and plastic strain accumulation stops after a characteristic number of load cycles. Special attention was paid to the microstructural influence on the onset of advancing ratcheting and the associated damage development at the microstructure level. WC-Co hardmetals are used in various areas such as forming and forging tools, where they are exposed to high temperatures and pressure loads. Their good high-temperature properties allow them to be used under these conditions, but these properties are influenced by the microstructure. Investigations of the mechanical properties of hardmetals had been carried out under monotonously increasing loads and cyclic tests at room temperature and elevated temperatures. In these tests, the effect of different stress ratios  $R = \sigma_{\min}/\sigma_{\max}$  on the fatigue behaviour of hardmetals were studied, However, no studies are known for WC-Co hardmetals and their limit stresses in relation to strain ratcheting under cyclic compressive loading at elevated temperature. Hence, in the current work the influence of increasing stresses as a function of microstructure and their effect on the evolution of the strain of six different WC-Co hardmetal grades are discussed. For this purpose, the materials were investigated by uniaxial cyclic compression tests at a stress ratio of  $R = -\infty$  at 700 °C and 800 °C in vacuum. The investigated hardmetal grades differ on the one hand in their WC grain size, which varies between 0.4 µm and 2.0 µm, and on the other hand in their Co-content, which varies between 6 wt.% and 12 wt.%. The residual strain value  $\epsilon_{\text{res}}$  at zero applied stress was observed to stabilize with increasing number of load cycles at low applied stress ranges. Strain ratcheting occurred above a critical stress range, referred to as the limit stress for strain

ratcheting. Strain ratcheting is the accumulation of plastic strain with increasing number of load cycles in which no strain stabilization occurs. Further, for all investigated hardmetal grades, the limit stresses were observed to decrease with increasing temperature. In the following, the microstructure of one hardmetal grade was analysed after loading below and above the limit stress by scanning electron microscopy and electron backscatter diffraction (EBSD). The influence of strain stabilization and ratcheting was analysed with regard to damage development and deformation behaviour of the WC and Co-phases. Strain ratcheting was observed to result in the formation of cavities and nanopores at phase boundary triple points and WC/Co interfaces. Additionally, the EBSD data showed that the fcc Co-phase was transformed into hcp Co. Therefore, it is assumed that on the one hand, a certain strain value needs to be exceeded for strain ratcheting to occur and, on the other hand, that besides dislocation movement, microdefect formation and phase transformation significantly contribute to the increase in strain.

## 1. Introduction

Hardmetals are often the only materials with sufficient resistance to high pressure loads and elevated temperature. Hence, they are used in various applications where they are exposed to high pressure loads, such as in the field of metal machining tools [1], for example in forming and forging tools [2]. Investigations of the mechanical properties of hardmetals had been carried out with regard to their plastic flow and stress-strain curves under monotonously increasing loads at room temperature and elevated temperatures by mechanical spectroscopy [3], uniaxial [4–6] and bending loading experiments [3,7]. Additionally, cyclic tests had been performed at room temperature [4,8] and elevated temperatures under air [9] and also under vacuum [10]. In these tests, the effect of different stress ratios  $R = \sigma_{\min}/\sigma_{\max}$  on the fatigue behaviour of hardmetals were examined [4,9–12]. During application of hardmetal tools, temperatures up to 800 °C or even higher can be reached [1]. Therefore, room temperature data are of limited usefulness for simulations and for understanding the material behaviour of WC-Co hardmetals at application-relevant temperatures. But, mechanical property data of hardmetals at different elevated temperatures for different stress ratios are insufficiently available in literature.

Uniaxial cyclic mechanical tests under  $R = -\infty$  and room temperature of WC-Co hardmetals show a similar dependence of the cyclic strains on the microstructure as observed for monotonously increasing loads: At constant applied stress amplitudes, there is a decrease of strain with decreasing binder content and decreasing WC grain size [4]. In order to investigate the cyclic stress-strain behaviour of hardmetals, they used to be tested under bending because of the easier handling [9], to avoid specimen buckling as possible under uniaxial compressive load. Hence, uniaxial cyclic tests at elevated temperatures are rarely performed: Roebuck et al. [6] show a history-dependence of the stress-strain curves at  $R = -1$  for a single hardmetal grade for three load cycles at 1100 °C for only very small maximum applied tensile and compressive stresses

of 110 MPa. Similar stress-strain curves at 1100 °C as function of load cycles were only observed when the first loading direction was applied under compression, then tension [6]. Further, Tritremmel et al. [10] show stress-strain curves with strain ratcheting for a single hardmetal grade up to 5000 load cycles at 600 °C and 700 °C in vacuum for  $R = -\infty$  with stress ranges of 2900 MPa and 3500 MPa. Hence, changes of cyclic stress-strain hysteresis during testing over more than three cycles are only reported at room temperature in [4] and at elevated temperatures in [10], which studied strain ratcheting for different hardmetal grades and damage behaviour.

Ratcheting corresponds to an accumulation of plastic strain, cycle by cycle, due to plasticity effects during the unloading and reloading process [13,14]. The accumulated plastic strain increases with increasing number of cycles when ratcheting occurs and there is no stabilisation at a certain strain value as the number of cycles increases [15]. The occurrence of ratcheting is considered in the literature to be a major factor in material failure [16,17], which is associated with an early stage of fatigue damage and a reduction of the fatigue life of components [15,18]. Ratcheting can be associated with the formation of cavities in the microstructure until the total accumulated strain reaches a critical value and component failure occurs [19]. Hence, limits can be defined for the onset of advancing strain ratcheting and the associated early stages of fatigue, which may depend on the mean stress and stress amplitude [20,21], temperature [22] or loading rate [23,24]. However, to date no information has been provided on different hardmetal grades and their limit stresses in relation to strain ratcheting under cyclic compression at elevated temperatures.

The aim of the current work is to examine limit stresses for the onset of advancing strain ratcheting of different WC-Co hardmetal grades at a stress ratio of  $R = -\infty$  at 700 °C and 800 °C. Therefore, changes of cyclic stress-strain hysteresis with increasing uniaxial stress and temperature are discussed. Also, changes in the microstructure and the behaviour of the WC- and Co-phase below and above the limit stresses for advancing strain ratcheting were investigated at 700 °C for one WC-Co hardmetal grade and correlated with the progression of the strain. The investigated temperatures are below the range usually given in literature, but are typical for many fields of application.

## 2. Materials and experimental details

Six different WC-Co hardmetal grades were investigated, characterized by average WC grain size, Co-binder content, compressive yield strength  $R_{p0.2}$ , Young's modulus  $E$  and fracture toughness  $K_{IC}$  as a function of temperature, values are listed in Table 1. The average WC grain size and the Co-content are as given by the material manufacturer Ceratizit Austria GmbH. The letters in the grade abbreviations in the first column of Table 1 refer to the average WC grain size of the investigated grades: U for ultrafine, S for submicron and M for medium, according to the ISO standard grain size classification scheme [25]. The numbers after the letters indicate the Co-content of 6 wt. %, 10 wt. % and 12 wt. %. Compression yield strength  $R_{p0.2}$  and



Young's modulus  $E$  of the WC-Co hardmetal grades were determined from strain-corrected [26] stress-strain curves attained in uniaxial compression tests performed with hourglass-shaped specimen. The materials' room temperature fracture toughness  $K_{IC}$  was determined by Ceratizit Austria GmbH by SENB tests according to DIN EN ISO 12737.

Table 1: Composition of six WC-Co hardmetal grades with their compression yield strength  $R_{p0.2}$ ; Young's modulus  $E$  as function of temperature, and room temperature fracture toughness  $K_{IC}$  determined by SENB tests.

Grade	Average WC grain size [ $\mu\text{m}$ ]	Co [wt.%]	Yield strength $R_{p0.2}$ [MPa]			Young's modulus $E$ [GPa]			$K_{IC}$ - SENB [MPa $\sqrt{\text{m}}$ ]
			25 °C	700 °C	800 °C	25 °C	700 °C	800 °C	25 °C
U12	0.4	12	4890	2280	1140	530	500	450	7.5
S6	0.7	6	5530	2500	1630	620	580	570	9.0
S10	0.7	10	4470	1950	1360	570	530	520	9.9
S12	0.7	12	3810	1820	1130	520	500	420	9.7
M10	2.0	10	3530	1450	920	570	530	520	14.6
M12	2.0	12	3175	1270	850	520	500	420	14.8

For all WC-Co hardmetal grades, load-controlled uniaxial cyclic tests were performed with a servo-hydraulic testing machine (Instron 8803) at a stress ratio  $R = \sigma_{\min}/\sigma_{\max} = -\infty$  at 700 °C and 800 °C [26]. An hourglass-shaped specimen geometry was used to prevent buckling under uniaxial compression loading. The minimum diameter in the axial centre of the hourglass-shaped specimen was 6 mm and the maximum diameter at its cylindrical shaft for clamping was 20 mm. The total length of the specimens was 250 mm [26]. During the tests, the length change from the initial gauge length was measured contactlessly with a high-precision laser extensometer (P-2S-50/400 Hz, Fiedler Optoelektronik GmbH, accuracy class 0.2, ISO 9513). Measuring marks were placed  $\pm 4$  mm from the minimum diameter of the hourglass-shaped specimen. The used non-constant specimen diameter leads to an underestimation of the strain measurement values in the smallest cross section, therefore a strain correction should be carried out when analysing the strain values [26]. Please note, that the strain values given in this current work were not corrected for the non-constant specimen diameter within the strain gauge length, as would be necessary when quantitative strain values are of interest. As the main focus of the current work was to determine the limit stresses, no quantitative strain values were required as the limit stress determination procedure remained unaffected by the absolute values of the strain.

The specimen temperature was inductively induced by eddy currents and temperature stability in the gauge length was ensured by the use of thermocouples, providing a constant temperature of  $\pm 10$  °C [26]. In addition, a vacuum chamber with a pressure of  $5 \cdot 10^{-6}$  mbar was used to avoid oxidation at the surface at elevated temperatures. All cyclic tests were carried out with a sinusoidal load curve and a test frequency of

0.25 Hz and stopped after  $N = 2000$  load cycles ( $\sim 2.2$  h). The specimens were loaded under zero-to-compression loading up to different stress ranges  $\Delta\sigma = \sigma_{\max} - \sigma_{\min}$ : 500 MPa, 750 MPa, 1000 MPa, 1500 MPa, 2000 MPa and 2500 MPa. For each  $\Delta\sigma$ , the residual strain  $\varepsilon_{\text{res}}$  at the maximum stress  $\sigma_{\max} = 0$  MPa was determined with regard to strain stabilization or ratcheting during the applied 2000 load cycles. In the current work, strain stabilisation is meant to be the stabilisation of the  $\varepsilon_{\text{res}}$  to a certain strain value at a certain load cycle. Strain ratcheting meant that the  $\varepsilon_{\text{res}}$  increased up to 2000 load cycles and no strain stabilisation had occurred. When strain ratcheting was observed for certain materials, no further tests were performed at higher compressive stresses. Based on the observed strain development, limits were determined for each of the six WC-Co hardmetal grades, defined as limit stresses. The stress range at which strain stabilized was set as the lower limit stress and the stress range at which strain ratcheting was first visible was denoted as the upper limit stress. The true limit stress, where strain ratcheting starts, is between these two values, since stress steps of 250 MPa below 1000 MPa and stress steps of 500 MPa above 1000 MPa are used.

In order to examine the difference between the lower and the upper limit in terms of damage development, the microstructure of the WC-Co hardmetal grade M10 was analysed after loading to 2000 load cycles at  $\Delta\sigma = 1000$  MPa and  $\Delta\sigma = 1500$  MPa at 700 °C. Additionally, an unloaded specimen of the same grade was analysed as reference specimen. The microstructure of the specimens was analysed by scanning electron microscopy (SEM, GeminiSEM ® 450 / Carl Zeiss SMT) in secondary electron (SE) contrast mode. The investigated cross-sections of the hourglass-shaped specimens were taken from their axial centres, i.e. at the minimum diameter of the hourglass-shaped specimens. Metallographic specimens were prepared with argon ion polishing as the final surface preparation step, which removes the deformed surface layers introduced during cutting and polishing [27]. The ridges that form on the specimen surface in this procedure were assumed not to affect the number or size of defects that were formed during mechanical testing. Nor did they affect the relative amount of fcc Co to hcp Co-phase visible in the plane intersecting the material volume [27]. The investigated cross-section planes were oriented perpendicular to the loading direction, i.e. when looking at the secondary electron images, the load direction points out of the image plane. The microstructure was investigated at three positions in the centre of the cross sections prepared at the minimum specimen diameter for each investigated deformation state. The three positions were about 500  $\mu\text{m}$  away from each other within the argon polished area. A counting of the number of microdefects was carried out manually for SEM micrographs of an individual size of 11.3  $\mu\text{m} \times 7.8 \mu\text{m}$  attained using secondary electron contrast mode using an InLens detector arrangement for a total area of 3000  $\mu\text{m}^2$  per investigated deformation state, covering approximately 2400 WC grains. The number of microdefects within these three areas was in the same order of magnitude for an individual specimen.

Phase transformations and plastic deformation in WC- and Co-phases were analysed by electron backscatter diffraction (EBSD) on the same three specimens investigated via SEM. The EBSD analysis (System: Symmetry / Oxford Instruments) was performed at 15 kV acceleration voltage and an applied step size of 50 nm for a zone of 38.3  $\mu\text{m}$  x 28.8  $\mu\text{m}$ . The specimen was tilted by 70° in the direction of the EBSD camera and the working distance was set to 15 mm. A software-based evaluation of eleven Kikuchi bands with a Hough space resolution of 95 was performed. The software package “Orientation Imaging Microscopy” (OIM) version 7 from EDAX [28] was used to determine the kernel average misorientation (KAM) using the 1<sup>st</sup> nearest neighbour with a maximum misorientation angle of 2°. KAM maps can be used to show differences in dislocation density which give additional information about lattice distortion and strain localization [29]. Inverse pole figure (IPF) evaluations were performed with “MTEX Toolbox” version 5.3 [30] in Matlab Version R2019b for all phases to identify crystal orientation changes, caused by plastic strain and to determine the phase distributions. No grain dilation clean-up was applied to the generated EBSD data.

### 3. Results and Discussion

#### 3.1. Cyclic stress-strain behaviour of six WC-Co hardmetal grades at 700 °C and 800 °C

Fig. 1(a.) and Fig. 1(b.) show cyclic stress-strain hysteresis curves of the WC-Co hardmetal grade S12 for 700 °C and 800 °C up to a stress range  $\Delta\sigma = 1000$  MPa at  $R = -\infty$ . This means that the specimens were cyclically loaded between 0 and -1000 MPa. The tests were stopped after  $N = 2000$  cycles without specimen fracture. The largest plastic deformation increment occurred in the first load cycle and subsequent hysteresis loops' width became narrower with increasing number of load cycles, up to a point where it remained constant and larger than zero, see Fig. 1(a.) and Fig. 1(b.). On the one hand, at 700 °C the strain stabilized within 970 load cycles and reached an uncorrected residual strain  $\varepsilon_{\text{res}}$  at zero stress of -0.12%. On the other hand, at 800 °C the strain did not stabilize, instead strain ratcheting occurred with continuous strain increase. The test reached an uncorrected  $\varepsilon_{\text{res}}$  at zero stress of -0.34%. The  $\varepsilon_{\text{res}}$ -development as a function of the number of load cycles for both cases is shown in Fig. 1(c.). Please note that the strain values given in this current work were not corrected for the non-constant specimen diameter within the strain gauge length [26] as would be necessary when quantitative strain values are of interest. At  $\Delta\sigma = 1000$  MPa and for 700 °C and 800 °C, strain stabilization and ratcheting were observed, respectively. Strain ratcheting was attributed on the one hand to the yield strength decrease with increasing temperature [5], see Table 1, and on the other hand to the creep at elevated temperature that plays a significant role in addition to the time-independent cyclic plastic strain accumulation [31–33]. Hence, dislocation movement is fostered by increasing temperature and the onset of advancing strain ratcheting shifts to lower stresses than at lower temperatures.

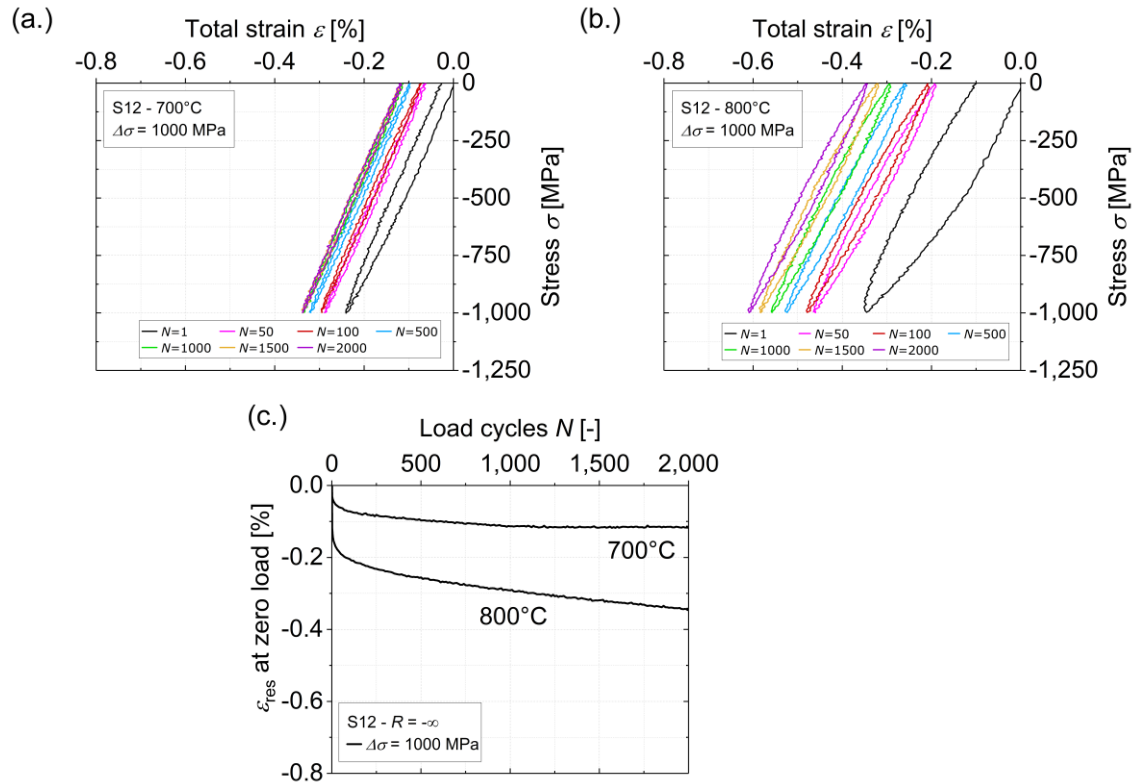


Fig. 1: Cyclic stress-strain hysteresis loops of WC-Co hardmetal grade S12 under a stress ratio of  $R = -\infty$  loaded up to a stress range  $\Delta\sigma = 1000$  MPa at (a.) 700 °C and (b.) 800 °C up to 2000 load cycles  $N$ . For better visualization,  $N = 1$ st (black), 50th (magenta), 100th (red), 500th (blue), 1000th (green), 1500th (orange) and 2000th (purple) load cycles are shown. (c.) Uncorrected residual strains  $\varepsilon_{res}$  for S12 at zero stress as function of the load cycles  $N$  for both temperatures. (For interpretation of the references to colour in the figure legends, the reader is referred to the web version of this article.)

The uncorrected  $\varepsilon_{res}$  at zero stress as function of load cycles for all six investigated WC-Co hardmetal grades is shown in Fig. 2 for 700 °C and 800 °C. In the Appendix, the response of the six WC-Co hardmetal grades to cyclic compressive loading is shown in individual diagrams for all tested stress ranges  $\Delta\sigma$  at 700 °C and 800 °C, see Fig. A.1 and Fig. A.2. Fig. 2(a.) shows the uncorrected strain development for  $\Delta\sigma = 750$  MPa, 1000 MPa, 1500 MPa and 2000 MPa at 700 °C. Fig. 2(b.) shows the same for  $\Delta\sigma = 500$  MPa, 750 MPa and 1000 MPa at 800 °C. At 800 °C, strain ratcheting was observed at lower stress ranges than at 700 °C, compare Fig. 2(a.) and Fig. 2(b.).

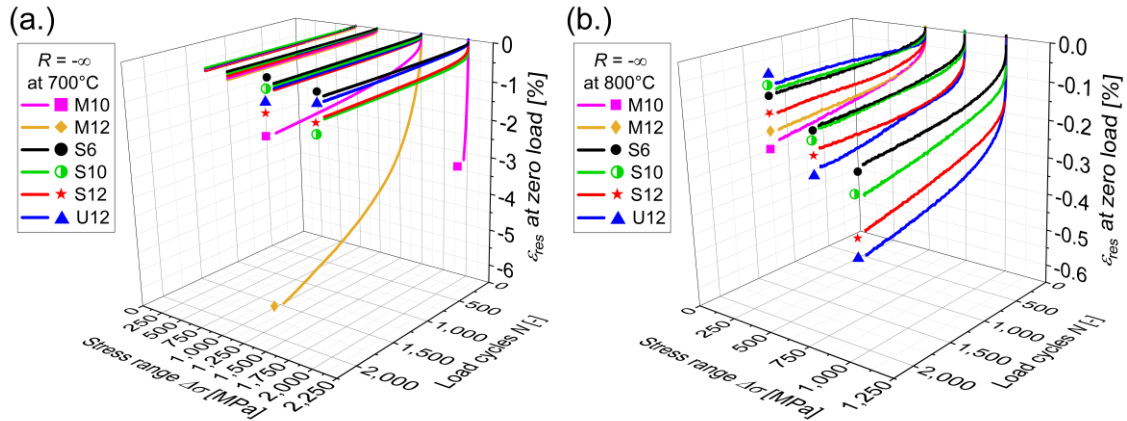


Fig. 2: Uncorrected residual strain  $\varepsilon_{res}$  at zero stress under stress ratio of  $R = -\infty$  for six WC-Co hardmetal grades at (a.) 700 °C and (b.) 800 °C as function of load cycles  $N$ . The specimens were loaded at stress ranges  $\Delta\sigma = 750$  MPa, 1000 MPa, 1500 MPa and 2000 MPa at 700 °C and at  $\Delta\sigma = 500$  MPa, 750 MPa, 1000 MPa at 800 °C. (For interpretation of the references to colour in the figure legends, the reader is referred to the web version of this article.)

Additionally to the temperature influence, the onset of advancing strain ratcheting was observed at different stress ranges. For example, looking at the grade M12 at  $\Delta\sigma = 1500$  MPa at 700 °C, strain ratcheting was observed, but for grade S6 the strain still stabilized under these conditions, see Fig. 2(a.). In the case of M10, which was loaded up to  $\Delta\sigma = 2000$  MPa at 700 °C, the maximum number of load cycles of 2000 was not reached because of thermocouple failure after 60 load cycles. Since strain ratcheting already occurred for M10 at  $\Delta\sigma = 1500$  MPa and accumulation of plastic strain increased faster at  $\Delta\sigma = 2000$  MPa than at the lower load, it is assumed that the strain would not have stabilized for M10. At 800 °C, strain ratcheting was observed at lower stress ranges than at 700 °C, as mentioned above. Note that when strain ratcheting was observed during testing of one WC-Co hardmetal grade, no further tests were performed at higher compressive stress ranges. This is the case, for example, for grades M10 and M12 at 800 °C, where at  $\Delta\sigma = 500$  MPa no strain stabilization was observed and no further test were performed, see Fig. 2(b.). For both temperatures it was observed that the grades with an average WC grain size of 2  $\mu\text{m}$  show an onset of advancing strain ratcheting at low stress ranges, see Fig. 2. This behaviour is attributed to the fact that these grades have large Co mean free paths between their WC grains [34,35] and therefore dislocations can move more easily compared to the other investigated grades. Additionally, the creep behaviour of these grades under such loads is pronounced at these temperatures, as shown by Maier et al. [33] and Mingard et al. [32]. Furthermore, creep tests have shown that at low temperatures fine-grained hardmetals have a higher creep resistance than coarse-grained grades [33,36,37]. This behaviour is reversed with increasing temperature, and coarser-grained grades are more creep-resistant at high temperatures [33,36,37]. This is assumed to be the case at 800 °C, for the grade U12 with very fine microstructure but rich in Co which showed higher  $\varepsilon_{res}$  at  $\Delta\sigma = 1000$  MPa than the other WC-Co hardmetal grades and also earlier start of strain ratcheting than at

700 °C. In contrast, the grade with the lowest Co-content S6, shows very low  $\epsilon_{res}$ , see Fig. 2(b.). Further, Fig. 2 shows that with increasing temperature and above 500 MPa at 800 °C, U12 shows faster strain ratcheting than S12. Therefore, in addition to time-independent plastic strain, creep strain is also expected to be responsible for not inhibiting dislocation movement in Co-rich materials.

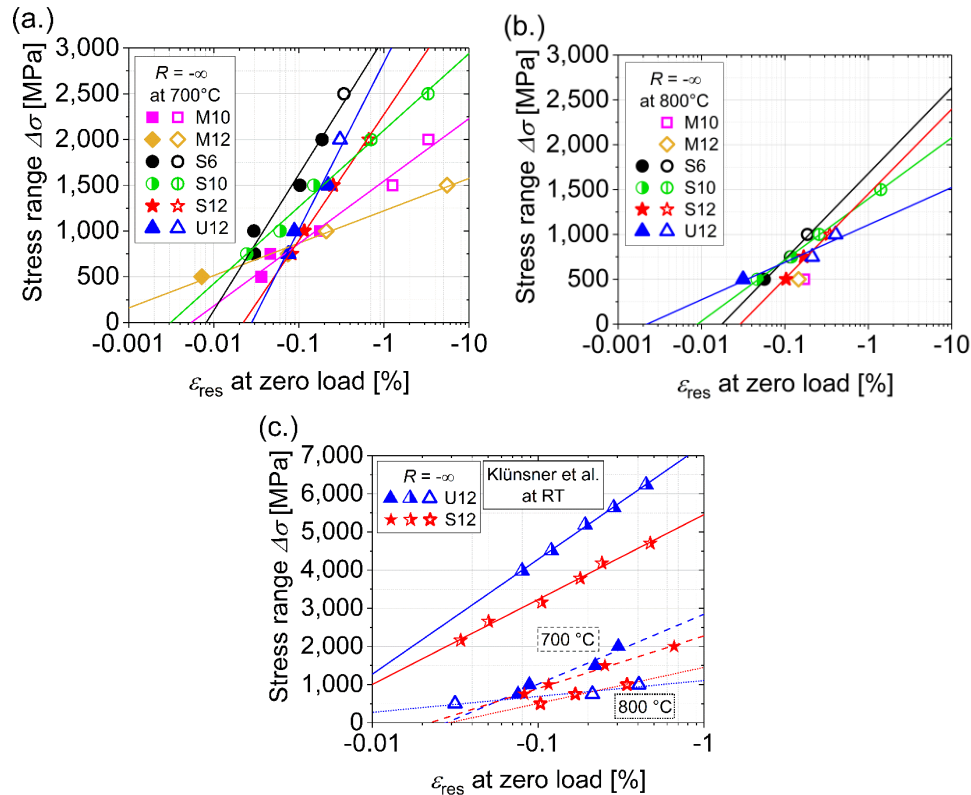


Fig. 3: Relationship between stress range  $\Delta\sigma$  and uncorrected residual strain  $\epsilon_{res}$  at zero stress for six WC-Co hardmetal grades under  $R = -\infty$  at (a.) 700 °C and (b.) 800 °C after  $N = 2000$ . A distinction is made between stabilized (full and half full symbols) and not stabilized strain values (non-filled symbols) data. (c.) Comparison of residual strain  $\epsilon_{res}$  data from cyclic tests under  $R = -\infty$  for ultrafine- and submicron-grained hardmetal grades with 12 wt.% Co for room temperature tests from [4] with results from (a.) and (b.). Full, dashed and dotted lines indicate linear regression fits of  $\Delta\sigma$  vs.  $\epsilon_{res}$  for room temperature, 700 °C and 800 °C, respectively. (For interpretation of the references to colour in this figure, the reader is referred to the web version of this article.)

Fig. 3(a.) and Fig. 3(b.) show the relationship between stress range  $\Delta\sigma$  and uncorrected  $\epsilon_{res}$  at zero stress after the last load cycles for all grades under  $R = -\infty$  at 700 °C and 800 °C, respectively.  $\epsilon_{res}$  at zero stress increased with increasing  $\Delta\sigma$ . It was also observed that uncorrected  $\epsilon_{res}$  at zero stress was the lowest for a given applied stress range above 750 MPa for grade S6 for both temperatures, see Fig. 3. A comparison of grades with 12 wt.% Co as U12, S12 and M12 at 700 °C, shows that U12 has almost the same uncorrected  $\epsilon_{res}$  values as M12 at a  $\Delta\sigma$  of 750 MPa and as S12 at 750 MPa to 1500 MPa, Fig. 3(a.). This trend of similar uncorrected  $\epsilon_{res}$  values is also observed for S6 and S10 at  $\Delta\sigma = 500$  MPa to 1000 MPa at 800 °C, see Fig. 3(b.). From the slope of the linear regression fits of  $\Delta\sigma$  vs.  $\epsilon_{res}$  at 700 °C, it was observed that the slope

of the coarse-grained hardmetal grades was lower than that of the submicron and ultrafine-grained grades, see Fig. 3(a.). This is due to the larger Co mean free path between WC grains in coarse-grained grades than in the other two grades, which fosters plastic deformation of the hardmetals [34,35]. At 800 °C, the slopes for all WC-Co hardmetal grades were lower than at 700 °C, and the ultrafine grade exhibited a smaller slope than the submicron grades, see Fig. 3(b.). Investigations of the strain ratcheting behaviour of hardmetal grades U12 and S12 under  $R = -\infty$  at room temperature have been carried out by [4]. As in the current work, it was shown that the uncorrected  $\varepsilon_{\text{res}}$  at zero stress increases with increasing stress range  $\Delta\sigma$ , but at elevated temperature the slope of  $\Delta\sigma$  vs.  $\varepsilon_{\text{res}}$  decreases with increasing temperature, see Fig. 3(c.). With increasing temperature, the compressive yield strength  $R_{p0.2}$  decreases with increasing temperature, compare Table 1 and [5]. At room temperature, plastic deformation occurs due to dislocation gliding and at elevated temperatures, next to dislocation gliding, creep processes also occur in the Co-binder, such as thermal activated dislocation climbing and diffusion processes, as suggested by [33,38]. Due to the reduction of the compressive yield strength  $R_{p0.2}$  and the easier deformability at elevated temperatures than at room temperature, similar uncorrected  $\varepsilon_{\text{res}}$  values at zero stress were observed as at room temperature but at lower stress ranges.

The occurrence of strain stabilization and ratcheting was investigated as a function of the stress range  $\Delta\sigma$ , hardmetal grade and temperature. Hence, limit stresses were defined for each temperature and material, based on the cyclic stress-strain behaviour of each WC-Co hardmetal grade, see Fig. 4. On the one hand, the lower limit stress was defined by the highest  $\Delta\sigma$  at which strain stabilization was observed. On the other hand, the upper limit was defined by the lowest  $\Delta\sigma$  for which strain ratcheting was documented. By comparing the limit stresses of all six investigated hardmetal grades, it was observed that under  $R = -\infty$  at 700 °C, the grade with the lowest Co-content and the smallest, i.e. submicron-sized, WC grains, S6, had the highest limit stress of 2500 MPa, which drops to 1000 MPa at 800 °C. At 800 °C and the chosen step size of  $\Delta\sigma$ , S6 shows the same limit stress as the other investigated submicron-grades S10 and S12. The grade with the lowest limit stress at 700 °C and 800 °C is the grade with an average WC grain size of 2  $\mu\text{m}$  and the highest Co-content, M12. The upper limit stress at 700 °C for the grade S10 was observed at an applied  $\Delta\sigma$  of 2000 MPa, see green open triangle facing upwards in Fig. 4. An uncorrected  $\varepsilon_{\text{res}}$  value at zero stress after  $N = 2000$  of 0.70% was observed, see Fig. 3(a.). Strain ratcheting was also observed by Tritremmel et al. [10] in an uniaxial cyclic test setup under  $R = -\infty$  at 700 °C with a stress range of 2900 MPa for S10. In this test, an uncorrected total strain of 10 % was reached after 171 load cycles without strain stabilization and failure of the specimen. Additionally, the applied stress range of 2900 MPa by Tritremmel et al. [10] is above the upper limit stress at which strain ratcheting was observed in the current work, see Fig. 4. Also, strain ratcheting was observed in uniaxial cyclic tests under  $R = -\infty$  at room

temperature for fine and submicron-grained WC-12 wt.% Co hardmetals at the highest applied stresses [4]. For the fine and submicron-grained WC-12 wt.% Co hardmetal [4], strain ratcheting was observed at  $\Delta\sigma = 4390$  MPa with uncorrected  $\varepsilon_{\text{res}} = 0.45\%$  and at  $\Delta\sigma = 4710$  MPa with uncorrected  $\varepsilon_{\text{res}} = 0.48\%$  after 2000 load cycles, respectively. Next to the fine and submicron-grained, also an ultrafine-grained WC-12 wt.% Co hardmetal was investigated up to  $\Delta\sigma = 6230$  MPa by [4], but for this grade no unstabilized strain ratcheting was observed. Stress ranges with unstabilized strain ratcheting were determined for U12 and S12, as described in [4] and in the current work by the upper limit stresses. Comparing the room temperature with the high temperature results, a decrease of the upper limit stresses was observed with increasing temperature, see Fig. 3 and Fig. 4. Additionally, the upper limit stresses determined in the current work were near and below the compressive yield strength  $R_{p0.2}$  at 700 °C and 800 °C, respectively, see Fig. 4(b.). Due to the occurrence of strain ratcheting below the compressive yield strength  $R_{p0.2}$  at elevated temperatures, the limit stresses represent important parameters to be considered in the design process of components and tools made of hardmetal.

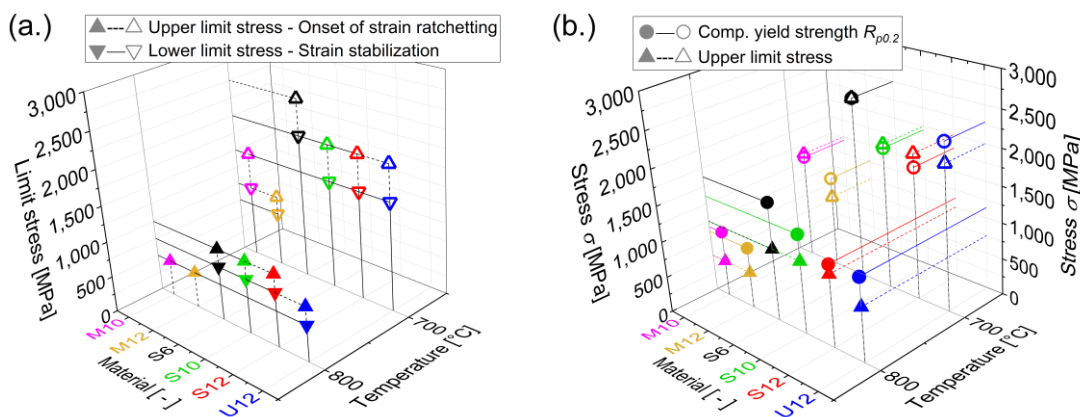


Fig. 4: (a.) Limit stresses for six WC-Co hardmetal grades tested under a stress ratio of  $R = -\infty$  at test temperatures of 700 °C and 800 °C. The lower limit stress (triangle facing downwards) and upper limit stress (triangle facing upwards) for a certain loading situation are defined by the maximum and minimum stress range values at which strain stabilization or start of strain ratcheting were observed, respectively. (b.) Comparison of the upper limit stresses and the compressive yield strength  $R_{p0.2}$  for each investigated WC-Co hardmetal grade in the current work at 700 °C and 800 °C. (For interpretation of the individual grades' symbol colours that are constant throughout this paper's figures, the reader is referred to the web version of this article.)

### 3.2. Microstructure analysis of M10 at 700 °C in the range of the limit stress

Fig. 5 shows the residual strain  $\varepsilon_{\text{res}}$  at zero stress of M10 for  $\Delta\sigma = 1000$  MPa and  $\Delta\sigma = 1500$  MPa of applied stress range over the number of load cycles at 700 °C. For the selected stress ranges, a compressive stress range of 1000 MPa corresponds to the lower limit stress with strain stabilization and 1500 MPa to the upper limit stress with the first observation of strain ratcheting, see the magenta open triangles in Fig. 4. Both specimens were investigated by SEM and EBSD methods with regard to structural changes. Additionally to the two loaded specimens, an unloaded specimen was investigated as reference.



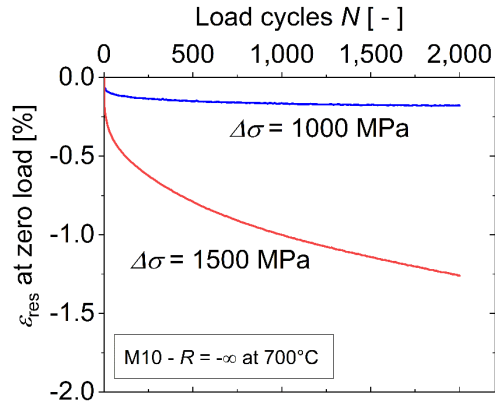


Fig. 5: Residual strain  $\varepsilon_{res}$  at zero stress as a function of load cycles  $N$  for the WC-Co hardmetal grade M10 under a stress ratio of  $R = -\infty$  at  $700\text{ }^{\circ}\text{C}$ . Comparison of stress ranges  $\Delta\sigma = 1000\text{ MPa}$  and  $\Delta\sigma = 1500\text{ MPa}$  until  $N = 2000$ .

Fig. 6(a.) to Fig. 6(c.) show the microstructure of the unloaded, and both specimens loaded with  $\Delta\sigma = 1000\text{ MPa}$  and  $\Delta\sigma = 1500\text{ MPa}$  after  $N = 2000$  without fracture of the specimens, respectively. Additionally, Fig. 6(d.) shows a detail from the specimen loaded with  $\Delta\sigma = 1500\text{ MPa}$ . In the SEM micrographs, WC grains appear in light grey, the Co-phase in dark grey and microdefects such as cavities or nanopores in black.

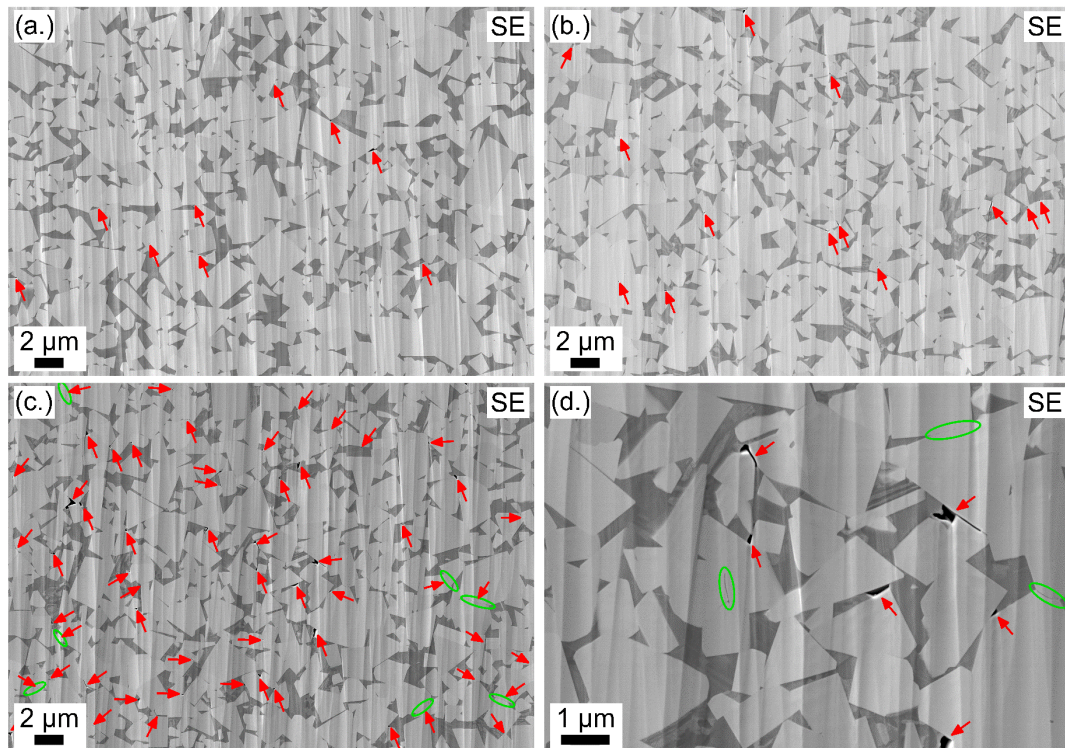


Fig. 6: SEM micrographs for the WC-Co hardmetal grade M10 for three different uniaxial cyclic load cases: (a.) unloaded; (b.)  $\Delta\sigma = 1000\text{ MPa}$  and (c.)  $\Delta\sigma = 1500\text{ MPa}$  under a stress ratio of  $R = -\infty$  at  $700\text{ }^{\circ}\text{C}$ . (d.) shows a detail from (c.). The load directions point out of the image planes and microdefects are marked with red arrows and nanopore chains with green ovals.

Microdefects are marked with red arrows and nanopore chains with green ovals in Fig. 6. In the considered area of  $1000 \mu\text{m}^2$ , a significant increase in the frequency of these microdefects was observed after exceeding the lower limit stress, see Fig. 6(c.). When comparing the number of defects in the microstructures for a total area of  $3000 \mu\text{m}^2$  per investigated loading state, a number of 31, 38 and 181 was observed in the unloaded specimen and after loading with  $\Delta\sigma = 1000 \text{ MPa}$  and  $\Delta\sigma = 1500 \text{ MPa}$ , respectively, as shown for  $1000 \mu\text{m}^2$  in Fig. 6(a.) to Fig. 6(c.). Up to the lower limit stress, the observed cyclic strains are assumed to be mainly due to dislocation movement, as the number of visible defects is similar to the ones in the unloaded specimen, compare Fig. 6(a.) and Fig. 6(b.). The frequency of microdefects is about six times greater in the specimen with strain ratcheting than in the unloaded specimen, see Fig. 6(a.) and Fig. 6(c.). Based on the number of microdefects, the continuous increase in strain during strain ratcheting is expected to result from dislocation movement and the formation of microdefects at WC/WC boundaries, WC/Co interfaces and phase triple points. Additionally, nanopore chains between WC/WC carbides were observed in the specimen loaded up to 1500 MPa, see green ovals in Fig. 6(c.) and Fig. 6(d.). The deformation and fracture behaviour of high-energy WC/WC boundaries, WC/Co interfaces and WC grains in hardmetal were investigated by microcantilever bending tests [39]. Csanádi et al. [39] observed that the fracture strength of high-energy WC/WC boundaries is lower than that of WC grains at room temperature. Probably due to this fracture strength difference, microdefects at WC/WC boundaries and WC/Co interfaces and no fractured WC grains were observed in the current work. Cavities, or the formation of cavities, have also been observed by other research groups after cyclic tests at room temperature [8,40,41] and elevated temperatures [10]. Tritremmel et al. demonstrated that a pronounced formation of cavities occurs after application of a stress range of  $\Delta\sigma = 2900 \text{ MPa}$  under  $R = -\infty$  at  $700 \text{ }^\circ\text{C}$  to a hardmetal grade S10, as investigated in the current work [10]. Cavities and nanopores at WC/WC boundaries and WC/Co interfaces are also observed in WC-Co hardmetals after creep tests at temperatures of  $800 \text{ }^\circ\text{C}$  and above [31–33,42]. Analysis of the creep asymmetry at  $800 \text{ }^\circ\text{C}$  by [42] revealed a not very pronounced formation in microdefects at WC/WC interfaces and WC/Co phase boundaries under compressive load. The microstructure of the hardmetal grade M10, which is the same as the one used in the current work, was investigated in uniaxial step-loading creep tests at  $800 \text{ }^\circ\text{C}$  after 3000 s and reaching  $-300 \text{ MPa}$  at around  $-0.2\%$  plastic strain. No microstructure analysis was reported for  $700 \text{ }^\circ\text{C}$ , but by stepwise increasing of the compressive stress up to  $-800 \text{ MPa}$  within 8000 s, a creep strain value of  $-0.3\%$  was reached at  $700 \text{ }^\circ\text{C}$  [42]. 8000 s correspond approximately to the time required for 2000 load cycles in the current work. Also, a similar step-loading creep curve slope at  $700 \text{ }^\circ\text{C}$  after 8000 s and at  $800 \text{ }^\circ\text{C}$  after 3000 s was observed [42]. Based on observed microdefects at  $800 \text{ }^\circ\text{C}$  and similar step-loading creep curve slopes between  $700 \text{ }^\circ\text{C}$  and  $800 \text{ }^\circ\text{C}$  by [42], the formation of cavities in the current work can be attributed to a combination of creep strain and cyclic plastic strain. Additionally, these microdefects, next to defects that are inherent in the material volume [43], are to be

regarded as sites of stress concentration that cause changes to the stress fields in the material. The inhomogeneous stress field accelerates the growth of the microdefects and the associated failure of the specimen with further loading.

The microstructures shown in Fig. 6(a.) to Fig. 6(c.) were also investigated by EBSD measurements. Fig. 7(a.) to Fig. 7(c.) show the phase distributions of the WC-, fcc Co- and hcp Co-phase of the unloaded and both loaded specimens at  $\Delta\sigma = 1000$  MPa and  $\Delta\sigma = 1500$  MPa, respectively. In the unloaded specimen made of M10, see Fig. 6(a.) and Fig. 7(a.), equal fractions of fcc Co- and hcp Co-phases were observed, see Table 2. Both crystal phases can coexist in unloaded specimens at room temperature, as reported by [44–46], due to the presence of dissolved tungsten, carbon or other elements in Co [45,47–50], the WC grain size [45], and the thermal expansion stress [51] in the WC/Co phases. The phase distribution observed in the specimen after cyclic loading at 1000 MPa showed no significant change in the amount of hcp compared to the unloaded specimen, see Fig. 7(a.), Fig. 7(b.) and Table 2. In contrast, the specimen loaded up to 1500 MPa showed an occurrence of strain ratcheting, and the fcc to hcp ratio had shifted: After 2000 load cycles, more hcp Co-phase than fcc Co-phase was observed in the microstructure compare Fig. 7(a.), Fig. 7(c.) and Table 2. Comparing the  $\epsilon_{\text{res}}$  at zero stress in Fig. 5 for the relevant applied stress ranges, the strain for the specimen loaded at 1500 MPa is 7 times larger than at 1000 MPa. Due to the increasing phase transformation from fcc Co to hcp Co, the binder phase is less ductile with each loading cycle, because the number of possible glide systems is reduced from 12 for fcc Co to 3 for hcp Co [52]. Phase transformation is a stress- and/or strain-controlled process and takes place when the strain in the Co-binder increases [53].

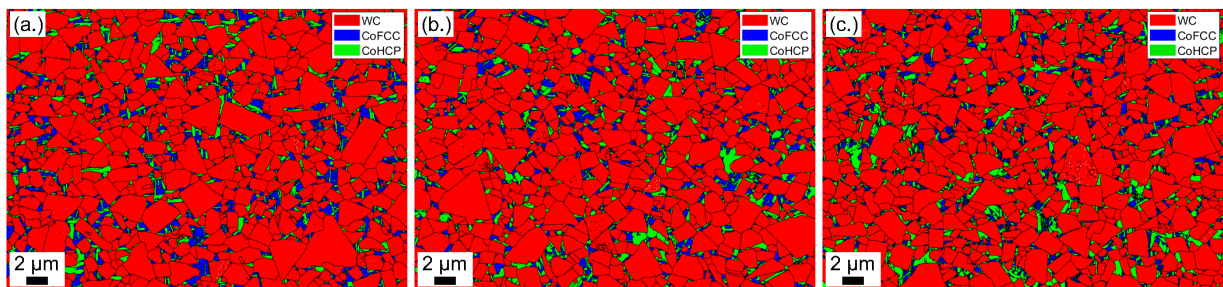


Fig. 7: EBSD phase distribution maps for WC-Co hardmetal grade M10 for three different cases: (a.) unloaded, and for both uniaxial cyclically specimens loaded under a stress ratio of  $R = -\infty$  at 700 °C at (b.)  $\Delta\sigma = 1000$  MPa and (c.)  $\Delta\sigma = 1500$  MPa. Figures (a.) to (c.) show the same image sections of the microstructure as present in Fig. 6(a.) to Fig. 6(c.). The load directions point out of the image planes. (For the interpretation of colour, the reader is referred to the online version of this article.)

Table 2: Area phase fractions of WC, fcc Co and hcp Co in the unloaded specimen and the ones loaded at  $\Delta\sigma = 1000$  MPa and  $\Delta\sigma = 1500$  MPa under a stress ratio of  $R = -\infty$  at 700 °C until 2000 load cycles.

Phase	Area fraction of the hardmetal phases [%]		
	Unloaded	$\Delta\sigma = 1000$ MPa	$\Delta\sigma = 1500$ MPa
<b>Not Indexed</b>	0.7	0.8	1.3
<b>WC</b>	82.0	83.0	81.4
<b>fcc Co</b>	8.3	7.0	6.3
<b>hcp Co</b>	9.0	9.2	11.0

The described observation is supported by room temperature experiments performed under monotonous and cyclic loading that result in the phase transformation from fcc to hcp [8,9,54,55]. Based on observations of Co phase transformation that takes place with increasing strain, it is assumed that no Co phase transformation has occurred due to strain stabilisation at loading with  $\Delta\sigma = 1000$  MPa, see Fig. 5 and Fig. 7(b.). However, an increase of the hcp Co-phase at loading with  $\Delta\sigma = 1500$  MPa is likely to occur due to the occurrence of strain ratcheting, see Fig. 5 and Fig. 7(c.). Additionally, influences on the mechanical properties, like decrease of fatigue strength [47], fracture toughness [8] or increase of magnetic coercive force [55,56], caused by phase transformation have been observed by different research groups. The phase transformation also causes an increase in microdefect formation, as discussed by [8,54]. When comparing Fig. 6(c.) with Fig. 7(c.), it becomes apparent that the hcp Co-phase can be also observed in areas without microdefects. On the one hand, this is due to the fact that the M10 hardmetal grade has hcp Co-phase fractions in areas without microdefects already in the unloaded state. On the other hand, 2D microstructure micrographs were investigated in the current work, and therefore no statements about the presence of microdefects in areas below the investigated image plane with hcp Co-phases are possible.

Additionally to phase fraction determinations, EBSD was used to determine inverse pole figures (IPFs), see Fig. 8, and kernel average misorientations (KAMs), see Fig. 9 and Fig. 10. The WC, fcc Co- and hcp Co-phase were analysed after loading with  $\Delta\sigma = 1000$  MPa and  $\Delta\sigma = 1500$  MPa at 700 °C and compared to the unloaded specimen. In IPFs, the individual grains are displayed in different colours according to their crystal orientation and orientation changes in individual grains that show plastic deformation can be detected [57]. Fig. 8(a.) to Fig. 8(c.) show the IPF for the WC phase of the unloaded specimen and both specimens loaded with  $\Delta\sigma = 1000$  MPa and 1500 MPa, respectively. It was observed that the frequency of deformed WC grains with crystal orientation changes, marked by white ovals, is approximately the same in all three specimens. This is an indication that during cyclic compression loading the deformation is mainly carried by the Co-phase. It was observed that the Co grains are many times larger than the WC grain size, as large areas of the same binder crystal orientation were observed, see Fig. 8(d.) to Fig. 8(f.). That the Co-binder grains are larger than those of WC was also reported in [58] and [59]. Hence, only few grains of the fcc Co-phase IPF were visible, in the unloaded as well as in the two loaded specimens in the current work. In the

unloaded specimen, the hcp Co-phase also showed large areas of the same crystal orientation, see Fig. 8(g.), this has also been observed by Marshall et al. [48] for WC-Co hardmetal grades with coarse grain size. In contrast, both loaded specimens showed areas of equal crystal orientation, but they were smaller than in the unloaded specimen, compare Fig. 8(g.) with Fig. 8(h.) and Fig. 8(i.). The areas of the hcp Co-phase in both loaded specimens indicated scattered formation of hcp Co-phases in the fcc Co-phase, since different crystal orientation were observed side by side, Fig. 8(h.) and Fig. 8(i.). Additionally, the IPF of the fcc- and hcp Co-phase of the specimen loaded up to 1500 MPa, Fig. 8(f.) and Fig. 8(h.), shows that the area fraction of the fcc Co-phase is lower than for the hcp Co-phase. This may be attributed to the increase in the hcp Co-phase during cyclic loading at  $\Delta\sigma = 1500$  MPa, see Table 2.

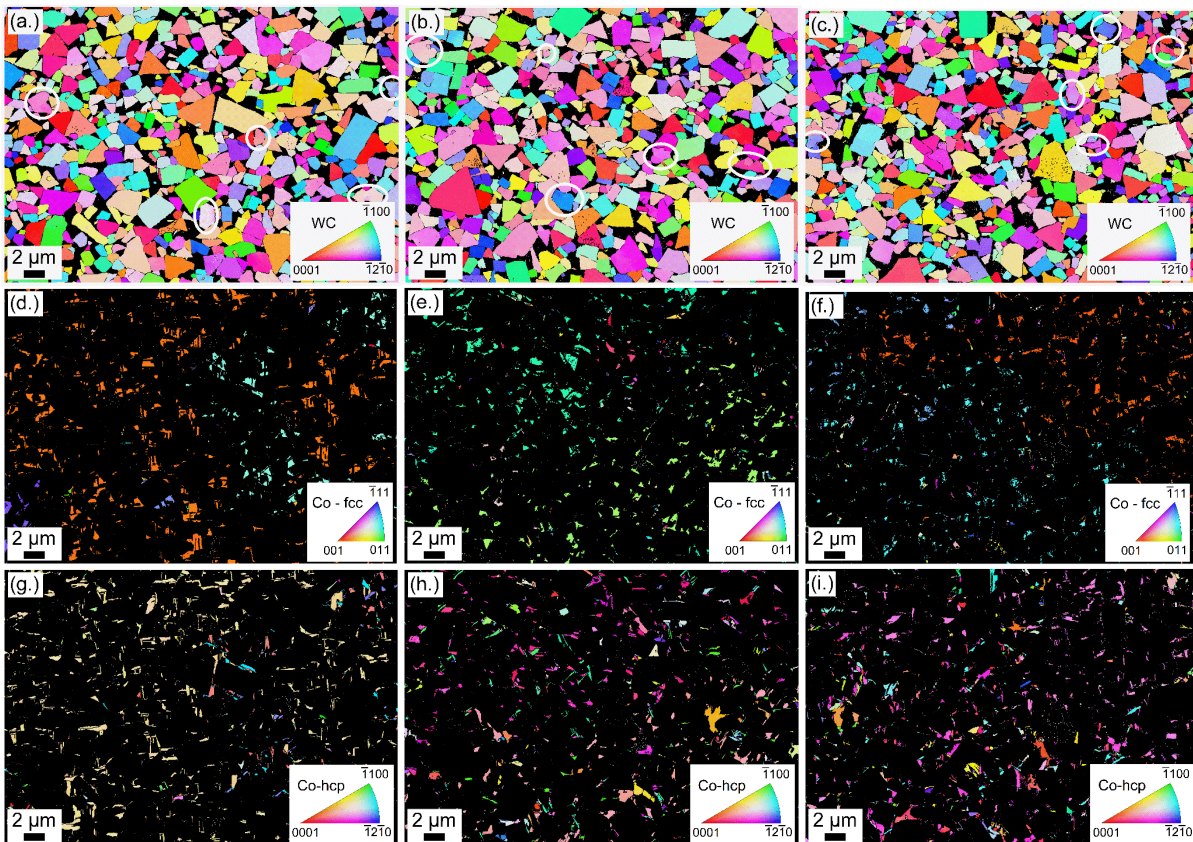


Fig. 8: EBSD inverse pole figure (IPF) maps for the WC-Co hardmetal grade M10: (a.), (d.) and (g.) show the unloaded specimen. Specimens cyclically loaded under a stress ratio of  $R = -\infty$  after  $N = 2000$  at  $700$  °C are shown for  $\Delta\sigma = 1000$  MPa in (b.), (e.) and (h.) and for  $\Delta\sigma = 1500$  MPa in (c.), (f.) and (i.). The IPFs are shown in: (a.) to (c.) for the WC-phase, in (d.) to (f.) for the fcc Co, and in (g.) to (i.) for the hcp Co-phase. The load directions point out of the image planes. (For the interpretation of colour, the reader is referred to the online version of this article.)

Fig. 9(a.) to Fig. 9(c.) show kernel average misorientation (KAM) maps for the WC phase of the unloaded specimen and both loaded ones at 1000 MPa and 1500 MPa, respectively. The colours in the KAM maps plot the misorientations between  $0^\circ$  (blue) and  $2^\circ$  (red). Additionally to the KAM maps, KAM number

fraction distributions for all three specimens for the WC phase are shown in Fig. 10(a.) using the colour scaling from the KAM maps as a reference to the respective misorientation values shown on the abscissa. The same EBSD data were the basis of the KAM distribution in Fig. 10 as for the visualization of the KAM maps in Fig. 9. The KAM maps show, that the misorientations in the WC grains have a high blue and green fraction, see Fig. 9(a.) to Fig. 9(c.). Dislocation structures and subgrains within WC grains in unloaded WC-Co hardmetal grades have been documented, caused by the accumulation of stresses in sintered materials [60]. Based on this observation [60], the green portion in form of lines in WC grains or at WC/Co interfaces in this work, marked with white arrows in Fig. 9(a.) to Fig. 9(c.), can be interpreted as dislocation structures. These grains had also shown a change in crystal orientation in the IPF in Fig. 8(a.) to Fig. 8(c.). Comparing the unloaded with the loaded specimens optically, a similar behaviour was observed. The KAM distribution for the WC-phase in Fig. 10(a.) confirms this impression and shows that at a KAM value of  $0.13^\circ$  the highest number of the same misorientation can be found in all three compared specimens. The cumulative KAM map for WC, see Fig. 10(d.), also shows that no changes exist between the unloaded specimen to the two loaded ones. It is therefore assumed that the WC grains deform mainly elastically under the investigated cyclic loads, as it was also indicated by the IPF map. Fig. 9(d.) to Fig. 9(f.) show the KAM maps for the fcc Co-phase of the unloaded specimen and both loaded ones at  $\Delta\sigma = 1000$  MPa and  $\Delta\sigma = 1500$  MPa, respectively. In the unloaded specimen, a high fraction of small misorientations was observed, which indicates, that a small amount of dislocations was present in the ductile binder phase, as mentioned above for the WC-phase. Comparing the unloaded with the two loaded specimens, see Fig. 9(d.) to Fig. 9(f.), an increase in binder misorientation was observed in both loaded cases. In the specimen loaded up to  $\Delta\sigma = 1500$  MPa, see Fig. 9(f.), a binder crystal orientation dependence with respect to deformation was observed. In the upper right-hand section of the image, the Co grain located there shows a higher misorientation than the grains in the rest of the image. This area represents a single Co grain, see IPF in Fig. 8(f.). This dependence was also observed in the specimen loaded with  $\Delta\sigma = 1000$  MPa, but to a smaller extent. In contrast, such a dependence is not found in the unloaded specimen, where the misorientation is homogeneously distributed over the image. The dependence of the deformability of different crystal orientations of the Co-phase was also reported by Feng et al. based on room temperature indentation simulations of indentation experiments [61]. The increase in dislocation density after loading of the specimens for the fcc Co-phase is also represented in the KAM distribution, see Fig. 10(b.) and Fig. 10(e.). Firstly, at a misorientation of  $0.20^\circ$  there was a distinct peak for all three specimens, marked with a grey arrow in Fig. 10(b.), with the highest number fraction for this misorientation for the unloaded specimen. In the case of the two loaded specimens, the number fraction at  $0.20^\circ$  decreased with increasing load. Secondly, the peak for the specimen loaded with  $\Delta\sigma = 1500$  MPa showed a lower slope to higher misorientation values than the specimen loaded with  $\Delta\sigma = 1000$  MPa, this is marked with a black arrow in Fig. 10(b.). The

cumulative KAM diagram for the fcc Co phase, see Fig. 10(e.), also shows that the curves of the unloaded specimen differ only minimally from the specimen loaded with  $\Delta\sigma = 1000$  MPa and that no pronounced high misorientations are visible for both cases. Hence, the KAM distribution confirms the optically determined increase to higher misorientation in the loaded specimens in Fig. 9(d.) to Fig. 9(f.). Thirdly, a peak was observed at the extreme ends of the investigated misorientation value spectrum at zero and two degrees for the loaded specimens. These increases are due to the fact that raw EBSD data were used for the analysis and individual pixels show such misorientations. Hence, these data should be treated with caution and should not be further interpreted.

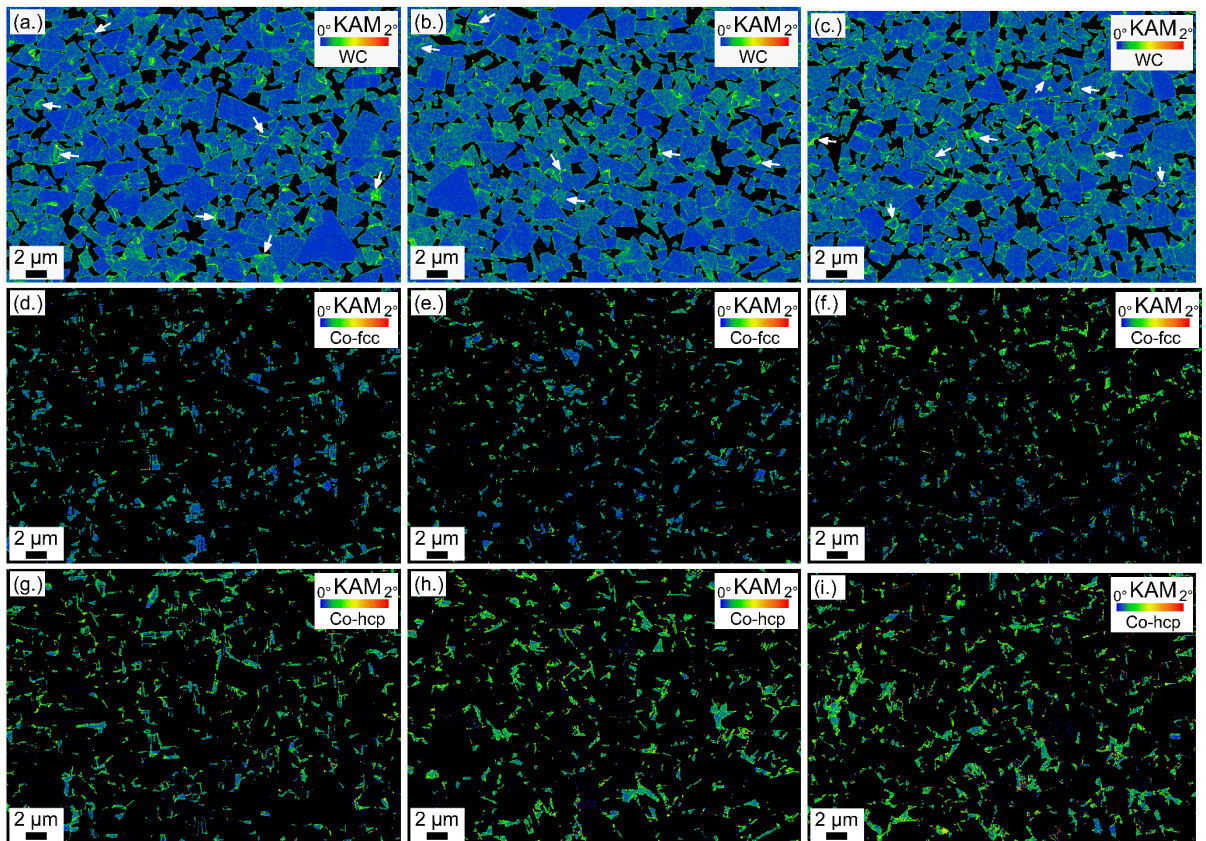


Fig. 9: Kernel average misorientation (KAM) maps for the WC-Co hardmetal grade M10 for specimens in (a.), (d.), (g) an unloaded state, (b.), (e.), (h.) a cyclically loaded state with an applied stress range  $\Delta\sigma = 1000$  MPa, and (c.), (f.), (i.) a cyclically loaded specimen with  $\Delta\sigma = 1500$  MPa under a stress ratio  $R = -\infty$  at  $700$  °C after a number of load cycles  $N = 2000$ . The misorientation ranges from  $0^\circ$  (blue) to  $2^\circ$  (red). The KAM is shown in: (a.) to (c.) for the WC-phase, in (d.) to (f.) for the fcc Co, and in (g.) to (i.) for the hcp Co-phase. The load directions point out of the image planes. (For the interpretation of colour, the reader is referred to the online version of this article.)

Fig. 9(g.) to Fig. 9(i.) show the KAM maps, Fig. 10(c.) the KAM distribution and Fig. 10(f.) the cumulative KAM distribution for the hcp Co-phase of the unloaded specimen, and the ones loaded at 1000 MPa and 1500 MPa, respectively. In the unloaded specimen, a higher misorientation in the hcp Co ( $0.25^\circ$ ) than in the fcc Co-phase ( $0.20^\circ$ ) was observed, i.e. a higher green than blue fraction, compare Fig. 9(d.) with Fig. 9(g.)

and grey arrows in Fig. 10(b.) and Fig. 10(c.). With increasing amount of the hcp Co phase, the ability of the Co-binder to deform under full shape compatibility with its surroundings decreases and the binder embrittles, as reported in [54,62]. This is attributed to the fact that the dislocation movement is limited to fewer slip systems in hcp-Co than in fcc-Co [52] and during phase transformation, the mean free path of dislocation decreases and leads to strengthening of the Co-phase, as suggested in [63]. Therefore, the misorientation that corresponds to the density of stored dislocations is higher in the hcp Co than in the fcc Co-phase. Comparing the unloaded and both loaded specimens, an increase in misorientation was observed in both loaded specimens, see Fig. 9(g.) to Fig. 9(i.). In the case of the KAM distribution, a distinct peak was observed for the hcp Co-phase, marked with a grey arrow in Fig. 10(c.). Note that the peak for the unloaded specimen was found at a lower misorientation of  $0.25^\circ$  than for the two loaded specimens at  $0.30^\circ$ . Further, compared to the unloaded specimen, the cyclically loaded specimens exhibit a slight increase in the region of higher KAMs, which is marked with a black arrow in Fig. 10(c.). The fraction of hcp Co-phase with high misorientation is equally pronounced in both loaded specimens compared to the unloaded one, indicating a saturation of the dislocation density already at 1000 MPa stress amplitude which was not observed for the fcc Co-phase, cf. Fig. 10(e.) and Fig. 10(f.).

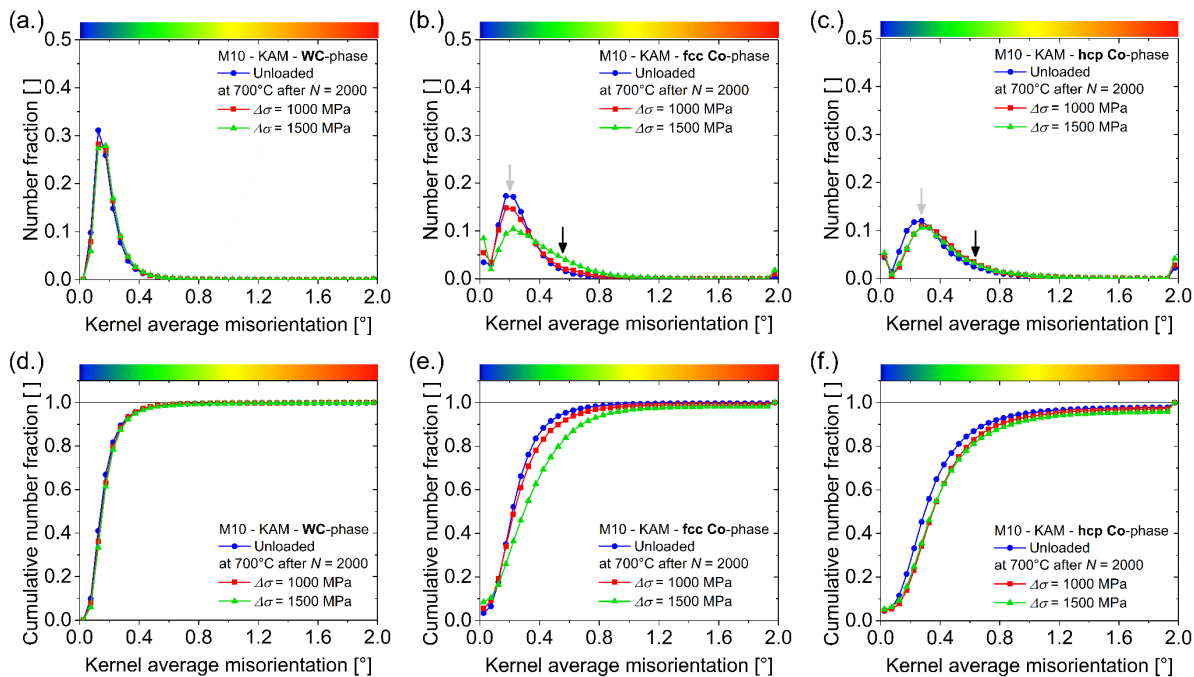


Fig. 10: Kernel average misorientation (KAM) distributions for the WC-Co hardmetal grade M10 based on the EBSD data shown in Fig. 9: for (a.) the WC, (b.) the fcc Co and (c.) the hcp Co-phase with all three load cases compared: unloaded (blue - circle),  $\Delta\sigma = 1000$  MPa (red - square) and  $\Delta\sigma = 1500$  MPa (green - triangle) under a stress ratio  $R = -\infty$  at  $700^\circ\text{C}$  loaded up to  $N = 2000$  load cycles. Cumulative KAM charts for (d.) WC, (e.) fcc Co and (f.) hcp Co-phase also for the three load cases in the before mentioned order. (For interpretation of the references to colour in this figure legend, the reader is referred to the web version of this article.)



Based on microstructural analysis in the current work on M10 after deformation at the lower and upper limit stresses at 700 °C, see Fig. 5 and Fig. 4, an increase in microdefects was observed at the upper limit stress when strain ratcheting occurs, see Fig. 6(c.). Similar results were observed in uniaxial cyclic  $R = -\infty$  tests at 700 °C for the hardmetal grade S10 [10], at a stress above the upper limit stress established in the current work. With increasing temperature and stress range, creep processes occur more pronouncedly in hardmetals and dislocation movement and microdefect formation at WC/WC interfaces and WC/Co phase boundaries are enhanced, as reported in [33]. As a result, strain ratcheting occurred at lower stress ranges with increasing temperature. The occurrence of strain ratcheting is considered in the literature to be a major factor in material failure [16,17], associated with an early stage of fatigue crack growth and a reduction in fatigue life of components [15,18]. Based on results of the current work and by [10], an increase of microdefect density in the microstructure is expected for all investigated WC-Co hardmetal grades above the upper limit stress determined in the current work, see Fig. 4. Therefore, statements about early failure are assumed to be possible based on compressive stress-strain data and the course of the residual strain  $\epsilon_{\text{res}}$  with increasing number of cycles. The determined limit stresses are therefore considered to represent limits for fail-safe application of tools and components.

#### 4. Conclusions

Load-controlled uniaxial cyclic tests were performed for six WC-Co hardmetal grades that differ on the one hand in their average WC grain size and on the other hand in their Co-content. The uniaxial cyclic tests were carried out under a stress ratio  $R = \sigma_{\text{min}}/\sigma_{\text{max}} = -\infty$  up to different stress ranges  $\Delta\sigma$  at 700 °C and 800 °C in vacuum. The main findings of the current work are the following:

- Based on the residual strain  $\epsilon_{\text{res}}$  development as function of the number of load cycles, lower and upper cut-of values of the limit stresses were determined for all investigated WC-Co hardmetal grades. Taking the chosen cyclic stress levels into account, the lower limit stresses defined the highest stress range at which strain stabilization was observed, and the upper values for the limit stress defined the lowest stress range at which advancing strain ratcheting occurred. Strain ratcheting describes the continuous advancing accumulation of the strain of a specimen at zero stress, cycle by cycle during the test.
- At the same applied compressive stress range  $\Delta\sigma$ , continuous advancing strain ratcheting occurred earlier at 800 °C than at 700 °C, due to reduction of the compressive yield strength  $R_{p0.2}$  with increasing temperatures and the simultaneous occurrence of elastic, plastic and creep strain.
- At 700 °C, the grade with the lowest investigated Co-content and smallest investigated submicron-sized WC grains has the highest limit stress which reaches  $\Delta\sigma = 2500$  MPa, whereas at 800 °C this limit stress drops to about  $\Delta\sigma = 1000$  MPa. At 800 °C, for all investigated submicron-grained hardmetals with different Co-contents, the limit stress was observed in the range of about

$\Delta\sigma = 1000$  MPa in the current work. The true limit stress at which strain ratcheting starts is around the determined limit stresses, since stress steps of 250 MPa below 1000 MPa and stress steps of 500 MPa above 1000 MPa were used.

- With increasing temperature, a continuous advancing strain ratcheting was observed at smaller stress ranges for the ultrafine-grained hardmetal grade than for the submicron-grained hardmetal grade. Comparable behaviour was observed for the same WC-Co hardmetal grades with increasing temperature for the creep rate in step-loading creep tests by Maier et al. [33].
- The grade with the lowest limit stress at 700 °C and 800 °C is the one with the highest Co-content and the largest grain size investigated, i.e. the medium-grained hardmetal grade.
- The determined upper limit stresses were below but near to the compressive yield strength  $R_{p0.2}$  at 700 °C and 800 °C.
- From microstructure analyses in the lower and upper limit stress range at the same temperature for a medium-grained hardmetal grade with 10 wt.% Co-content the following conclusions can be drawn: The specimens loaded at stress ranges at or above the upper limit stress contained a significantly higher number of defects than the specimen loaded at stress ranges at or below the lower limit stress. No distinct cracks were observed in the microstructure. Instead, microdefects were found at WC/WC boundaries, WC/Co interfaces and phase triple points.
- An increase in dislocation density occurs in the Co-phase, but the WC grains do not exhibit plastic deformation after application of a stress range above the upper limit stress. Further, it was demonstrated that an increase in applied stress range leads to an increase in the phase fraction of the hcp Co-phase in the Binder.
- Based on the results of this work for cyclic loading at stress ratios  $R = -\infty$ , it is possible to deduce from stress-strain curves whether microdefects are formed in the material that can lead to failure of the material/component under further loading.

## 5. Acknowledgements

We thank Bernhard Sartory and his team for their exceptional work on SEM and EBSD. Additionally, the authors gratefully acknowledge the financial support of the Frontrunner-Initiative of the project "Frontrunner: Integrated, data driven development for Cutting Tools" (Project No. 861280). Additionally, the financial support under the scope of the COMET program within the K2 Center "Integrated Computational Material, Process and Product Engineering (IC-MPPE)" (Project No 859480). This program is supported by the Austrian Federal Ministries for Climate Action, Environment, Energy, Mobility, Innovation and Technology (BMK) and for Digital and Economic Affairs (BMDW), represented by the Austrian research funding association (FFG), and the federal states of Styria, Upper Austria and Tyrol.

6. Appendix

In addition to the three-dimensional representations in Fig. 2, Fig. A.1 and Fig. A.2 show the uncorrected residual strain  $\epsilon_{res}$  at zero applied stress as a function of the number of load cycles in two-dimensional diagrams for each of the investigated hard metal grades individually. Fig. A.1 shows the development of the uncorrected residual strain for maximum five stress ranges  $\Delta\sigma$ : 750 MPa, 1000 MPa, 1500 MPa, 2000 MPa and 2500 MPa at 700 °C. Fig. A.2 shows the uncorrected strain development for maximum four stress ranges  $\Delta\sigma$ : 500 MPa, 750 MPa, 1000 MPa and 1500 MPa at 800 °C.

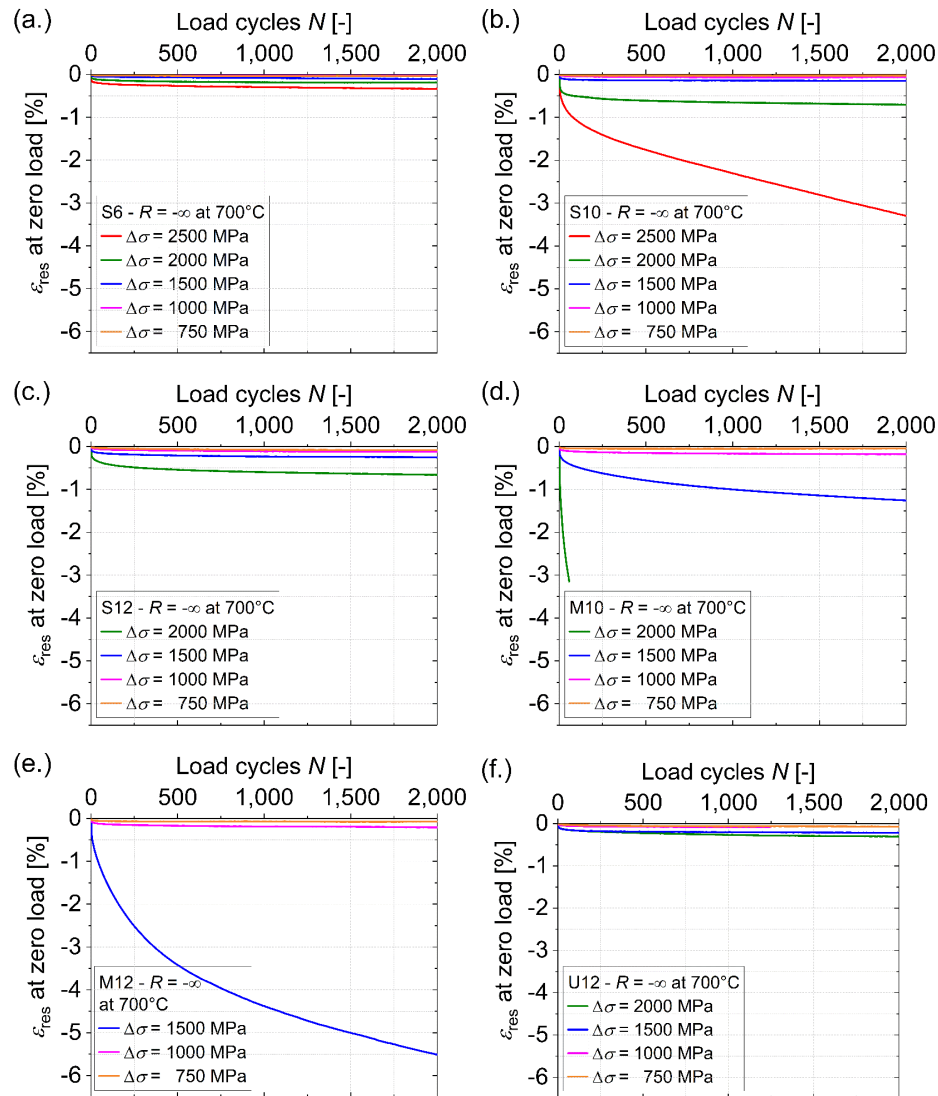


Fig. A.1: Uncorrected residual strain  $\epsilon_{res}$  at zero stress after cyclic loading at a stress ratio of  $R = -\infty$  for six WC-Co hardmetal grades at 700 °C as a function of the number of load cycles  $N$  to the applied stress ranges  $\Delta\sigma$ : 750 MPa, 1000 MPa, 1500 MPa, 2000 MPa and 2500 MPa. No further tests were performed at higher compressive stress ranges once strain ratcheting occurred at a given cyclic stress range. The respective shown materials are: (a.) S6, (b.) S10, (c.) S12, (d.) M10, (e.) M12, and (f.) U12.

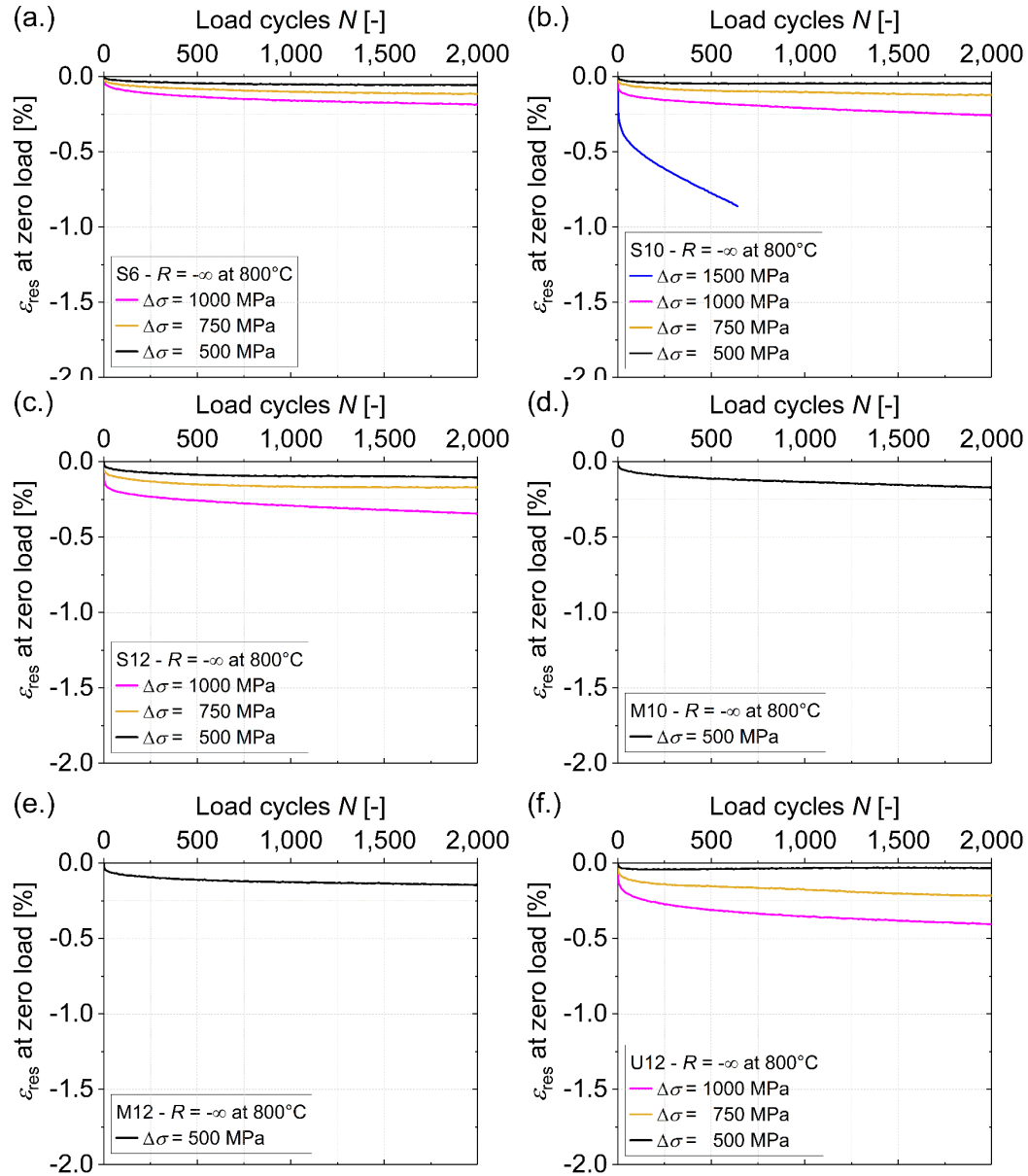


Fig. A.2: Uncorrected residual strain  $\epsilon_{res}$  at zero stress after cyclic loading at a stress ratio of  $R = -\infty$  for six WC-Co hardmetal grades at 800 °C as a function of load cycles  $N$  to the applied stress ranges  $\Delta\sigma$ : 500 MPa, 750 MPa, 1000 MPa, 1500 MPa. No further tests were performed at higher compressive stress ranges once strain ratcheting occurred at a given cyclic stress range. The respective shown materials are: (a.) S6, (b.) S10, (c.) S12, (d.) M10, (e.) M12, and (f.) U12.

**References**

- [1] G.-J. Liu, Z.-C. Zhou, X. Qian, W.-H. Pang, G.-H. Li, G.-Y. Tan, Wear Mechanism of Cemented Carbide Tool in High Speed Milling of Stainless Steel, *Chinese J. Mech. Eng.* 31 (2018) 1–10. doi:10.1186/s10033-018-0298-2.
- [2] Ceratizit Group, Hot forming technology, (2020). <https://www.ceratizit.com/en/products/wear-protection/list/detail/product-detail/hot-forming-technology/> (accessed November 23, 2020).
- [3] D. Mari, S. Bolognini, G. Feusier, T. Viatte, W. Benoit, Experimental strategy to study the mechanical behaviour of hardmetals for cutting tools, *Int. J. Refract. Met. Hard Mater.* 17 (1999) 209–225. doi:10.1016/S0263-4368(98)00078-X.
- [4] T. Klünsner, S. Marsoner, R. Ebner, R. Pippan, J. Glätzle, A. Püschel, Effect of microstructure on fatigue properties of WC-Co hard metals, in: *Procedia Eng.*, 2010: pp. 2001–2010. doi:10.1016/j.proeng.2010.03.215.
- [5] T. Teppernegg, T. Klünsner, C. Kremsner, C. Tritremmel, C. Czettel, S. Puchegger, S. Marsoner, R. Pippan, R. Ebner, High temperature mechanical properties of WC-Co hard metals, *Int. J. Refract. Met. Hard Mater.* 56 (2016) 139–144. doi:10.1016/j.ijrmhm.2016.01.002.
- [6] B. Roebuck, S. Moseley, Tensile and compressive asymmetry in creep and monotonic deformation of WC/Co hardmetals at high temperature, *Int. J. Refract. Met. Hard Mater.* 48 (2015) 126–133. doi:10.1016/j.ijrmhm.2014.08.007.
- [7] G. Östberg, K. Buss, M. Christensen, S. Norgren, H.-O. Andrén, D. Mari, G. Wahnström, I. Reineck, Mechanisms of plastic deformation of WC–Co and Ti(C, N)–WC–Co, *Int. J. Refract. Met. Hard Mater.* 24 (2006) 135–144. doi:https://doi.org/10.1016/j.ijrmhm.2005.04.009.
- [8] U. Schleinkofer, H.G. Sockel, K. Görting, W. Heinrich, Microstructural processes during subcritical crack growth in hard metals and cermets under cyclic loads, *Mater. Sci. Eng. A.* 209 (1996) 103–110. doi:10.1016/0921-5093(95)10098-9.
- [9] P. Kindermann, P. Schlund, H.G. Sockel, M. Herr, W. Heinrich, K. Görting, U. Schleinkofer, High-temperature fatigue of cemented carbides under cyclic loads, *Int. J. Refract. Met. Hard Mater.* 17 (1999) 55–68. doi:10.1016/S0263-4368(99)00014-1.
- [10] C. Tritremmel, T. Klünsner, B. Sartory, C. Czettel, S. Marsoner, Cyclic plastic deformation behaviour of WC-Co hard metals at elevated temperatures, in: *19th Plansee Semin. - Int. Conf. Refract. Met. Hard Mater.*, Plansee Group, Reutte/Austria, 2017: pp. 1–9.
- [11] Y. Torres, M. Anglada, L. Llanes, Fatigue mechanics of WC-Co cemented carbides, in: *Int. J. Refract. Met. Hard Mater.*, 2001: pp. 341–348. doi:10.1016/S0263-4368(01)00032-4.
- [12] U. Schleinkofer, H.G. Sockel, K. Görting, W. Heinrich, Fatigue of hard metals and cermets, *Mater. Sci. Eng. A.* 209 (1996) 313–317. doi:10.1016/0921-5093(95)10106-3.

- [13] J.L. Chaboche, D. Nouailhas, A unified constitutive model for cyclic viscoplasticity and its applications to various stainless steels, *J. Eng. Mater. Technol. Trans. ASME*. 111 (1989) 424–430. doi:10.1115/1.3226490.
- [14] T.H. Lin, Y.M. Ito, Mechanics of a fatigue crack nucleation mechanism, *J. Mech. Phys. Solids*. 17 (1969) 511–523. doi:10.1016/0022-5096(69)90006-4.
- [15] E. Weiß, B. Postberg, T. Nicak, J. Rudolph, Simulation of ratcheting and low cycle fatigue, *Int. J. Press. Vessel. Pip.* 81 (2004) 235–242. doi:10.1016/j.ijpvp.2004.01.002.
- [16] J.L. Chaboche, A review of some plasticity and viscoplasticity constitutive theories, *Int. J. Plast.* 24 (2008) 1642–1693. doi:10.1016/j.ijplas.2008.03.009.
- [17] G. Kang, Y. Liu, Z. Li, Experimental study on ratchetting-fatigue interaction of SS304 stainless steel in uniaxial cyclic stressing, *Mater. Sci. Eng. A*. 435–436 (2006) 396–404. doi:10.1016/j.msea.2006.07.006.
- [18] R.J. Rider, S.J. Harvey, H.D. Chandler, Fatigue and ratcheting interactions, *Int. J. Fatigue*. 17 (1995) 507–511. doi:10.1016/0142-1123(95)00046-V.
- [19] A. Kapoor, A RE-EVALUATION OF THE LIFE TO RUPTURE OF DUCTILE METALS BY CYCLIC PLASTIC STRAIN, *Fatigue Fract. Eng. Mater. Struct.* 17 (1994) 201–219. doi:10.1111/j.1460-2695.1994.tb00801.x.
- [20] J.L. Chaboche, On some modifications of kinematic hardening to improve the description of ratchetting effects, *Int. J. Plast.* 7 (1991) 661–678. doi:10.1016/0749-6419(91)90050-9.
- [21] T. Hassan, S. Kyriakides, Ratcheting in cyclic plasticity, part I: Uniaxial behavior, *Int. J. Plast.* 8 (1992) 91–116. doi:10.1016/0749-6419(92)90040-J.
- [22] G. Kang, Y. Li, Q. Gao, Non-proportionally multiaxial ratcheting of cyclic hardening materials at elevated temperatures: Experiments and simulations, *Mech. Mater.* 37 (2005) 1101–1118. doi:10.1016/j.mechmat.2005.01.006.
- [23] C.J. Lissenden, D. Doraiswamy, S.M. Arnold, Experimental investigation of cyclic and time-dependent deformation of titanium alloy at elevated temperature, *Int. J. Plast.* 23 (2007) 1–24. doi:10.1016/j.ijplas.2006.01.006.
- [24] G. Kang, Q. Kan, J. Zhang, Y. Sun, Time-dependent ratchetting experiments of SS304 stainless steel, *Int. J. Plast.* 22 (2006) 858–894. doi:10.1016/j.ijplas.2005.05.006.
- [25] ISO 4499-2, ISO 4499-2:2008 Hardmetals-Metallographic determination of microstructure-Part 2: Measurement of WC grain size, 2008.
- [26] K. Maier, T. Klünsner, M. Krobath, C. Tritremmel, S. Marsoner, C. Czettl, Uniaxial step loading test setup for determination of creep curves of oxidation-sensitive high strength materials in vacuum under tensile and compressive load, *Int. J. Refract. Met. Hard Mater.* 92 (2020) 105327.

- doi:10.1016/j.ijrmhm.2020.105327.
- [27] B. Winiarski, A. Gholinia, K. Mingard, M. Gee, G.E. Thompson, P.J. Withers, Broad ion beam serial section tomography, *Ultramicroscopy*. 172 (2017) 52–64.  
doi:<https://doi.org/10.1016/j.ultramic.2016.10.014>.
- [28] EDAX Smart Insight, (n.d.). <https://www.edax.com/> (accessed September 20, 2020).
- [29] A.J. Schwartz, M. Kumar, B.L. Adams, D.P. Field, *Electron Backscatter Diffraction in Materials Science*, 2nd ed., Springer US, 2009. doi:10.1007/978-0-387-88136-2.
- [30] F. Bachmann, R. Hielscher, H. Schaeben, Texture analysis with MTEX- Free and open source software toolbox, in: *Solid State Phenom.*, Trans Tech Publications Ltd, 2010: pp. 63–68.  
doi:10.4028/www.scientific.net/SSP.160.63.
- [31] M.A. Yousfi, J. Weidow, A. Nordgren, L.K.L. Falk, H.O. Andrén, Deformation mechanisms in a WC-Co based cemented carbide during creep, *Int. J. Refract. Met. Hard Mater.* 49 (2015) 81–87.  
doi:10.1016/j.ijrmhm.2014.07.016.
- [32] K. Mingard, S. Moseley, S. Norgren, H. Zakaria, D. Jones, B. Roebuck, Microstructural observations of high temperature creep processes in hardmetals, *Powder Metall.* (2021) 1–11.  
doi:10.1080/00325899.2021.1877866.
- [33] K. Maier, T. Klünsner, M. Krobath, P. Pichler, S. Marsoner, W. Ecker, C. Czettel, J. Schäfer, R. Ebner, Creep behaviour of WC-12 wt% Co hardmetals with different WC grain sizes tested in uniaxial tensile and compression step-loading tests at 700 °C and 800 °C, *Int. J. Refract. Met. Hard Mater.* 100 (2021) 105633. doi:10.1016/j.ijrmhm.2021.105633.
- [34] L. Makhele-Lekala, S. Luyckx, F.R.N. Nabarro, Semi-empirical relationship between the hardness, grain size and mean free path of WC–Co, *Int. J. Refract. Met. Hard Mater.* 19 (2001) 245–249.  
doi:[https://doi.org/10.1016/S0263-4368\(01\)00022-1](https://doi.org/10.1016/S0263-4368(01)00022-1).
- [35] S. Luyckx, A.D. Love, Empirical quantitative relationships among grain size, mean free path, contiguity and cobalt content in WC-Co hardmetal, *Trans. R. Soc. South Africa.* 58 (2003) 145–148. doi:10.1080/00359190309520469.
- [36] N. V. Novikov, V.P. Bondarenko, V.T. Golovchan, High-temperature mechanical properties of WC-Co hard metals (Review), *J. Superhard Mater.* 29 (2007) 261–280.  
doi:10.3103/s1063457607050012.
- [37] B. Roebuck, E.A. Almond, Deformation and fracture processes and the physical metallurgy of WC–Co hardmetals, *Int. Mater. Rev.* 33 (1988) 90–112. doi:10.1179/imr.1988.33.1.90.
- [38] J.T. Smith, J.D. Wood, Elevated temperature compressive creep behavior of tungsten carbide-cobalt alloys, *Acta Metall.* 16 (1968) 1219–1226. doi:10.1016/0001-6160(68)90003-5.
- [39] T. Csanádi, M. Vojtko, J. Dusza, Deformation and fracture of WC grains and grain boundaries in a

- WC-Co hardmetal during microcantilever bending tests, *Int. J. Refract. Met. Hard Mater.* 87 (2020) 105163. doi:10.1016/j.ijrmhm.2019.105163.
- [40] L. Llanes, Y. Torres, M. Anglada, On the fatigue crack growth behavior of WC-Co cemented carbides: Kinetics description, microstructural effects and fatigue sensitivity, in: *Acta Mater.*, 2002: pp. 2381–2393. doi:10.1016/S1359-6454(02)00071-X.
- [41] T. Sailer, M. Herr, H.G. Sockel, R. Schulte, H. Feld, L.J. Prakash, Microstructure and mechanical properties of ultrafine-grained hardmetals, in: *Int. J. Refract. Met. Hard Mater.*, 2001: pp. 553–559. doi:10.1016/S0263-4368(01)00041-5.
- [42] K. Maier, T. Klünsner, W. Ecker, P. Pichler, S. Marsoner, C. Czettel, J. Schäfer, R. Ebner, A physical reason for asymmetric creep deformation behaviour of WC-Co hardmetal under tension and compression loading at 700 °C and 800 °C, *Int. J. Refract. Met. Hard Mater.* 97 (2021) 105526. doi:10.1016/j.ijrmhm.2021.105526.
- [43] M. Jonke, T. Klünsner, P. Supancic, W. Harrer, J. Glätzle, R. Barbist, R. Ebner, Strength of WC-Co hard metals as a function of the effectively loaded volume, *Int. J. Refract. Met. Hard Mater.* 64 (2017) 219–224. doi:10.1016/j.ijrmhm.2016.11.003.
- [44] K.P. Mingard, H.G. Jones, M.G. Gee, B. Roebuck, J.W. Nunn, In situ observation of crack growth in a WC-Co hardmetal and characterisation of crack growth morphologies by EBSD, *Int. J. Refract. Met. Hard Mater.* 36 (2013) 136–142. doi:10.1016/j.ijrmhm.2012.08.006.
- [45] J.M. Marshall, A. Kusoffsky, Binder phase structure in fine and coarse WC-Co hard metals with Cr and v carbide additions, in: *Int. J. Refract. Met. Hard Mater.*, 2013: pp. 27–35. doi:10.1016/j.ijrmhm.2013.04.001.
- [46] K.P. Mingard, B. Roebuck, J. Marshall, G. Sweetman, Some aspects of the structure of cobalt and nickel binder phases in hardmetals, *Acta Mater.* 59 (2011) 2277–2290. doi:10.1016/j.actamat.2010.12.004.
- [47] B. Roebuck, E.A. Almond, A.M. Cottenden, The influence of composition, phase transformation and varying the relative F.C.C. and H.C.P. phase contents on the properties of dilute CoWC alloys, *Mater. Sci. Eng.* 66 (1984) 179–194. doi:10.1016/0025-5416(84)90179-4.
- [48] J.M. Marshall, M. Giraudel, The role of tungsten in the Co binder: Effects on WC grain size and hcp-fcc Co in the binder phase, *Int. J. Refract. Met. Hard Mater.* 49 (2015) 57–66. doi:10.1016/j.ijrmhm.2014.09.028.
- [49] J. Weidow, S. Norgren, H.O. Andrén, Effect of V, Cr and Mn additions on the microstructure of WC-Co, *Int. J. Refract. Met. Hard Mater.* 27 (2009) 817–822. doi:10.1016/j.ijrmhm.2009.02.002.
- [50] M. Eizadjou, H. Chen, C. Czettel, J. Pachthofer, S. Primig, S.P. Ringer, An observation of the binder microstructure in WC-(Co+Ru) cemented carbides using transmission Kikuchi diffraction,



- Scr. Mater. 183 (2020) 55–60. doi:10.1016/j.scriptamat.2020.03.010.
- [51] S. Adjam, D. Mari, T. LaGrange, Strain glass transition of cobalt phase in a cemented carbide, *Int. J. Refract. Met. Hard Mater.* 87 (2020) 105161. doi:10.1016/j.ijrmhm.2019.105161.
- [52] A.G. Jackson, Slip Systems, in: *Handb. Crystallogr.*, Springer, New York, NY, 1991: pp. 83–88. doi:[https://doi.org/10.1007/978-1-4612-3052-6\\_7](https://doi.org/10.1007/978-1-4612-3052-6_7).
- [53] E.A. Almond, B. Roebuck, Fatigue-crack growth in WC–Co hardmetals, *Met. Technol.* 7 (1980) 83–85. doi:10.1179/030716980803287080.
- [54] V.K. Sarin, T. Johannesson, On the deformation of WC–Co cemented carbides, *Met. Sci.* 9 (1975) 472–476. doi:10.1179/030634575790444531.
- [55] A. Hara, T. Ikeda, BEHAVIOR OF COMPRESSIVE DEFORMATION OF WC-Co CEMENTED CARBIDE., *Trans Jap Inst Met.* 13 (1972) 128–133. doi:10.2320/matertrans1960.13.128.
- [56] U. Beste, H. Engqvist, S. Jacobson, Pressure cycling induced modification of a cemented carbide, in: *15th Int. Plansee Semin.*, Reutte/Austria, 2001: pp. 685–697.
- [57] M. Gee, K. Mingard, B. Roebuck, Application of EBSD to the evaluation of plastic deformation in the mechanical testing of WC/Co hardmetal, *Int. J. Refract. Met. Hard Mater.* 27 (2009) 300–312. doi:10.1016/j.ijrmhm.2008.09.003.
- [58] J. Weidow, H.-O. Andrén, Binder phase grain size in WC–Co-based cemented carbides, *Scr. Mater.* 63 (2010) 1165–1168. doi:<https://doi.org/10.1016/j.scriptamat.2010.08.025>.
- [59] K.P. Mingard, B. Roebuck, H.G. Jones, M. Stewart, D. Cox, M.G. Gee, Visualisation and measurement of hardmetal microstructures in 3D, *Int. J. Refract. Met. Hard Mater.* 71 (2018) 285–291. doi:10.1016/j.ijrmhm.2017.11.023.
- [60] B.M. Jablon, K. Mingard, A. Winkelmann, G. Naresh-Kumar, B. Hourahine, C. Trager-Cowan, Subgrain structure and dislocations in WC–Co hard metals revealed by electron channelling contrast imaging, *Int. J. Refract. Met. Hard Mater.* 87 (2020) 1–7. doi:10.1016/j.ijrmhm.2019.105159.
- [61] Q. Feng, X. Song, H. Xie, H. Wang, X. Liu, F. Yin, Deformation and plastic coordination in WC–Co composite — molecular dynamics simulation of nanoindentation, *Mater. Des.* 120 (2017) 193–203. doi:<https://doi.org/10.1016/j.matdes.2017.02.010>.
- [62] P.R. Fry, G.G. Garrett, Fatigue crack growth behaviour of tungsten carbide-cobalt hardmetals, *J. Mater. Sci.* 23 (1988) 2325–2338. doi:10.1007/BF01111884.
- [63] M. Padmakumar, J. Guruprasath, P. Achuthan, D. Dinakaran, Investigation of phase structure of cobalt and its effect in WC–Co cemented carbides before and after deep cryogenic treatment, *Int. J. Refract. Met. Hard Mater.* 74 (2018) 87–92. doi:10.1016/j.ijrmhm.2018.03.010.



# **Publication V**

**Damage indicators for early fatigue damage assessment of WC-Co hardmetals under uniaxial cyclic loads at a stress ratio of  $R = -1$  at elevated temperatures**

**Kathrin Maier, Thomas Klünsner, Philip Pichler, Stefan Marsoner, Werner Ecker, Christoph Czettel, Jonathan Schäfer, Reinhold Ebner**

**Submitted**

**Manuscript number: IJRMHM-D-21-00682**

**Journal of Refractory Metals and Hard Materials,**

**XX (2021) XX**

## Damage indicators for early fatigue damage assessment of WC-Co hardmetals under uniaxial cyclic loads at a stress ratio of $R = -1$ at elevated temperatures

Kathrin Maier<sup>1</sup>, Thomas Klünsner<sup>1</sup>, Philip Pichler<sup>1</sup>, Stefan Marsoner<sup>1</sup>, Werner Ecker<sup>1</sup>,  
Christoph Czettl<sup>2</sup>, Jonathan Schäfer<sup>2</sup>, Reinhold Ebner<sup>1</sup>

<sup>1</sup> Materials Center Leoben Forschung GmbH, Roseggerstraße 12, 8700 Leoben, Austria

<sup>2</sup> CERATIZIT Austria GmbH, Metallwerk-Plansee Straße 71, 6600 Reutte, Austria

**Keywords:** WC-Co hardmetal; Uniaxial cyclic test; Stress-strain-hysteresis loop; Elevated temperature; Damage indicator; Electron microscopy

### Abstract

The aim of the current work was the experimental determination of stress-strain-hysteresis loops for the investigation of damage indicators in uniaxial symmetric cyclic tests for WC-Co hardmetals. Certain stress-strain-hysteresis loop parameters increased with increasing stress amplitudes, temperature and number of load cycles. Special attention was paid to microstructural changes with increasing number of load cycles in correlation with stress-strain-hysteresis loop parameters and the resulting damage development at the microstructure scale.

WC-Co hardmetals are utilized as tool materials in metal cutting applications in which they are exposed to high mechanical cyclic loads and elevated temperatures. A better understanding of the failure mechanisms of WC-Co hardmetals under these application conditions and the ability to diagnose the damage evolution state are key factors to understand the limits of endurable cyclic load at a certain temperature.

Hence in the current work, two WC-Co hardmetals were loaded in uniaxial cyclic tests at three stress amplitudes of 750 MPa, 1000 MPa and 1500 MPa at a stress ratio  $R = \sigma_{\min}/\sigma_{\max} = -1$  at 700 °C and 800 °C in vacuum. The two investigated WC-Co hardmetal grades had a Co-content of 10 wt.% and an average WC grain size of 0.7 µm and 2.0 µm.

Stress-strain-hysteresis loops showed reversible plastic straining at low stress amplitudes at 700 °C. Also, an increase in the stress-strain-hysteresis loop area and tension-compression-strain asymmetry were recorded with increasing number of load cycles at 800 °C with earlier failure than at 700 °C. Besides the increase in hysteresis-loop area and strain asymmetry, cyclic creep was also clearly observed at 800 °C. Additionally, the microstructure for one WC-Co hardmetal grade was analyzed by scanning electron microscopy and electron backscatter diffraction after cyclic testing up to defined numbers of load cycles at a stress amplitude of 1000 MPa at 800 °C. The relationship between the stress-strain-hysteresis loop parameters and damage evolution state at microstructure level as well as the deformation behavior of

WC- and Co-phases with increasing number of load cycles, were analyzed. It was observed that the area of the hysteresis loop area and strain asymmetry increase with the formation and enlargement of nanopores at the WC/WC interfaces and the WC/Co phase boundaries, as well as the formation of cavities with increasing number of load cycles. Additionally, electron backscatter diffraction data showed that the fcc Co-phase partially transformed into hcp Co under cyclic loading. All specimens in which an increase in the stress-strain hysteresis loop or strain asymmetry was observed also ultimately failed at a sufficiently high number of load cycles. Therefore, the found results indicate that these parameters are reliable indicators for bulk material damage.

## 1. Introduction

Hardmetals are composite materials used in various applications in which they are exposed to high loads and temperatures, such as in the field of metal cutting tools [1]. For this reason, numerous investigations have already been carried out on monotonic increasing stress-strain and fatigue behavior of hardmetals [2-7]. Cyclic fatigue tests of hardmetals have been performed at room temperature [6,8,9] and elevated temperatures [7,10]. In these tests, the fatigue behavior of hardmetals was examined under different stress ratios  $R = \sigma_{\min}/\sigma_{\max}$  [4,6,7,9,10]. At room temperature, WC-Co hardmetals were examined e.g. by bending under  $R = -1$  [4,7] as well as under  $R = 0.1, 0.4, 0.7$  [9], or by uniaxial loading under  $R = -\infty$  [6]. Tests at elevated temperature were performed e.g. by bending under  $R = -1$  up to 900 °C [7] or uniaxial loading under  $R = -\infty$  at 600 °C and 700 °C [11]. During application of hardmetal tools, temperatures up to 800 °C or higher can be reached at the cutting edge [1,12]. Furthermore, local plastification causes mean stress in cutting edges to tend towards  $R = -1$  and about 1000 MPa load amplitude [13]. Therefore, room temperature data are of limited usefulness for simulations and for understanding the material behavior of WC-Co hardmetals at application-relevant temperatures. Also, mechanical property data of hardmetals at different elevated temperatures for different stress ratios are insufficiently available in literature.

In order to investigate the fatigue behavior of hardmetals, bending tests were used because of reduced experimental efforts and the fact that specimens can buckle under uniaxial compressive load. Hence, uniaxial cyclic tests at elevated temperatures are rarely performed: Roebuck et al. [14] show stress-strain curves at  $R = -1$  for a single WC-Co hardmetal grade for three load cycles at 1100 °C for only very small maximum applied tensile and compressive stresses of 110 MPa. Additionally, Tritremmel et al. [11] show stress-strain curves for a single WC-Co hardmetal grade at 600 °C and 700 °C under  $R = -\infty$  with stress ranges of 2900 MPa and 3500 MPa. Next to uniaxial, also cyclic bending loading tests are performed at high temperatures to analyze the fatigue behavior of hardmetals on the basis of Wöhler curves [7]. The cyclic stress-strain-hysteresis loop characteristics up to specimen failure, like loop area, plastic strain amplitude or strain asymmetry, were not investigated in detail for WC-Co hardmetals in the performed

fatigue tests. Changes of cyclic stress-strain-hysteresis loops during testing are only reported under  $R = -\infty$  in [6,11,15].

New industrial manufacturing trends are pushing tooling materials to the limits of their properties. In application, sudden failure of the tool can occur, long before the expected service life. An understanding of the microstructural damage mechanisms that occur during cyclic high-temperature loading with increasing number of load cycles is necessary for systematic further improvement of cutting tool materials. To evaluate early damage during application, parameters are necessary which make it possible to evaluate the fatigue behavior of a material or a construction. In literature, the stiffness, hysteresis loop area and plastic strain range over the duration of the cyclic loads are used as damage indicator for different metallic materials [16-19]. As these parameters indicate fatigue damage by an increase as the number of cycles increases. However, far less information is available on WC-Co hardmetals and the stress-strain-hysteresis loop characteristics in terms of parameters used as damage indicators under cyclic loading at elevated temperatures. In uniaxial cyclic tests for different WC-Co hardmetal grades under  $R = -\infty$  at 700 °C and 800 °C, an observed damage indicator was strain ratcheting, also known as cyclic creep, with increasing number of load cycles, which occurs above a critical stress range [15]. Above this critical stress range, in addition to strain ratcheting, the formation of cavities and nanopores was observed, which may trigger premature fracture [15].

The aim of the current work is to examine stress-strain-hysteresis loops for the determination of bulk material damage indicators for two WC-Co hardmetal grades at a stress ratio of  $R = -1$  at 700 °C and 800 °C. To this end, changes of the stress-strain-hysteresis loop characteristic with increasing uniaxial stress amplitude, temperature and number of load cycles were investigated and are discussed in this paper. Also, changes in the microstructure and the behavior of the WC- and Co-phase with increasing number of load cycles were investigated at 800 °C for one WC-Co hardmetal grade and correlated with the stress-strain-hysteresis loop evolution.

## 2. Methodological approach

Two hardmetal grades were examined with the designation S10 and M10, with their microstructures shown in Fig. 1(a.) and Fig. 1(b.). In the scanning electron microscopy (SEM) micrographs, WC grains appear in light grey and the Co-phase in dark grey. The letters in the specimen designation S and M refer to the average WC grain size of the grades: submicron and medium, according to the ISO standard grain size classification scheme [20]. The number after the letter indicates the Co-content in wt.%. Tab. 1 lists the average WC grain size and the Co-content as given by the material manufacturer Ceratizit Austria GmbH. Additionally, compression yield strength  $R_{p0.2}$  and Young's modulus  $E$  of the hardmetals as function of temperature are shown in Tab. 1. These two parameters were determined from strain-corrected [21] stress-strain curves of

uniaxial compression tests performed with hourglass-shaped specimens. Tab. 1 also lists the materials' room temperature fracture toughness  $K_{IC}$  that was determined by Ceratizit Austria GmbH by SENB tests according to DIN EN ISO 12737.

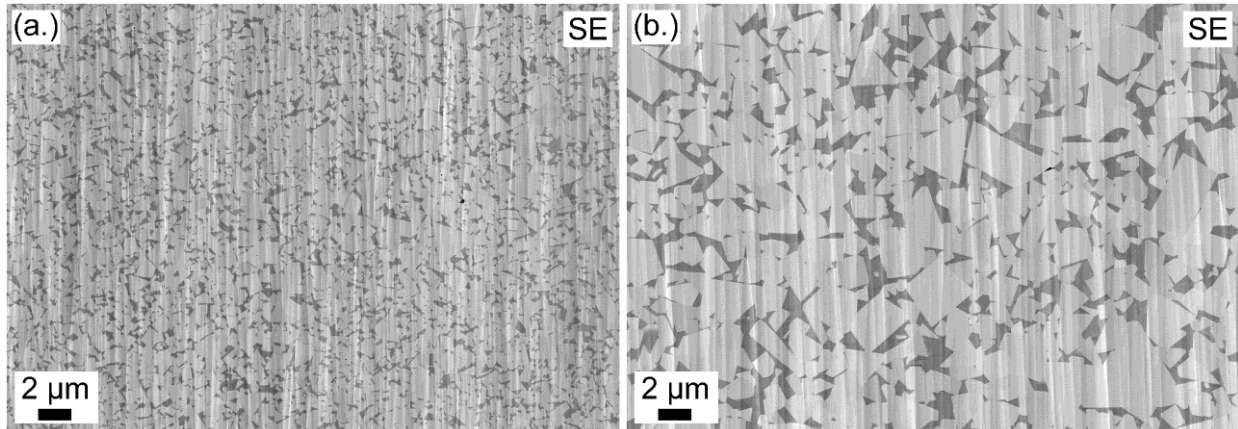


Fig. 1: Scanning electron microscopy (SEM) micrographs of the microstructure of the investigated WC-Co hardmetal grades: (a.) S10 with an average WC grain size of  $0.7 \mu\text{m}$  and (b.) M10 with an average WC grain size of  $2.0 \mu\text{m}$ . In the secondary electron images, the WC-phase is visible in light grey and the Co-phase in dark grey.

Tab. 1: Composition of the two investigated WC-Co hardmetal grades with their compression yield strength ( $R_{p0.2}$ ), Young's modulus ( $E$ ) as function of temperature, and room temperature fracture toughness ( $K_{IC}$ ) determined by SENB tests.

Grade	Average WC grain size [ $\mu\text{m}$ ]	Cobalt [wt.%]	Yield strength $R_{p0.2}$ [MPa]			Young's modulus $E$ [GPa]			$K_{IC}$ – SENB [MPa $\sqrt{\text{m}}$ ]
			25 °C	700 °C	800 °C	25 °C	700 °C	800 °C	25 °C
S10	0.7	10	4470	1950	1360	570	530	520	9.9
M10	2.0	10	3530	1450	920	570	530	520	14.6

For both WC-Co hardmetal grades, load-controlled uniaxial cyclic tests were performed with a servo-hydraulic testing machine (Instron 8803) [21] at a stress ratio  $R = \sigma_{\text{min}}/\sigma_{\text{max}} = -1$  under isothermal conditions at 700 °C and 800 °C. An hourglass-shaped specimen geometry was used to prevent buckling under uniaxial compression loading. The minimum diameter in the axial center of the hourglass-shaped specimen was 6 mm and the maximum diameter at its cylindrical shaft for clamping was 20 mm. The total length of the specimens was 250 mm [21]. During the tests, the length change from the initial gauge length was measured contactlessly with a high-precision laser extensometer (P-2S-50/400 Hz, Fiedler Optoelektronik GmbH, accuracy class 0.2, ISO 9513). Measuring marks were placed  $\pm 4$  mm from the minimum diameter of the hourglass-shaped specimen. The used non-constant specimen diameter lead to an underestimation of the measured strain data, therefore a strain correction is necessary [21]. Please note, that the strain values given

in the current work were not corrected for the non-constant specimen diameter within the strain gauge length, as would be necessary when quantitative strain values are of interest. As the main focus of the current work was on investigating the changes of the stress-strain-hysteresis loops with increasing number of load cycles, no quantitative strain values were required, since statements on the stress-strain-hysteresis loop shape were unaffected by the absolute values of strain. The specimen temperature was inductively induced by eddy currents and thermal stability in the gauge length was ensured by the use of thermocouples, providing a constant temperature of  $\pm 10$  °C [21]. In addition, a vacuum chamber was used with a pressure of  $5 \cdot 10^{-6}$  mbar to avoid oxidation at the surface above 600 °C [22]. All cyclic tests were performed at a test frequency of 0.25 Hz and stopped after  $N = 2500$  load cycles ( $\sim 2.8$  h) or specimen failure. The specimens were cyclically loaded with a mean stress  $\sigma_{\text{mean}} = 0$  (corresponding to  $R = -1$ ) up to different stress amplitudes  $\sigma_a = |\sigma_{\text{max}} - \sigma_{\text{min}}|/2$ : 750 MPa, 1000 MPa and 1500 MPa at 700 °C and 800 °C. For each stress amplitude and temperature state, the first load direction was under compression and stress-strain-hysteresis loops were logged up to  $N = 2500$  load cycles. The choice of the first loading direction was based on results by Roebuck et al. [14] on the history-dependence of the stress-strain curve: In cyclic tests at 1000 °C, similar stress-strain curves with increasing number of load cycles were observed only when the first loading direction was applied under compression, then tension. Due to the load history-dependence of the stress-strain response, a new hardmetal specimen was used for each cyclic test. The results of repetition tests on three M10 specimens from the same production batch, tested under the same conditions at  $\sigma_a = 1000$  MPa and 800 °C and not presented in detail in this paper, showed identical stress-strain-hysteresis loop curves. Therefore, it can be assumed that the cyclic test results shown in the current work are highly reproducible.

During cyclic loading, energy is dissipated in the tested material by micro-mechanisms like movement of dislocations and diffusion of point defects. The amount of energy dissipated in a unit volume of material per cycle is proportional to the area within the stress-strain-hysteresis loop [23]. Determinations of the stress-strain-hysteresis loop areas for each number of load cycles was performed with Origin 2017G [24], by using the tool "Polygon Area" to determine the absolute area. Due to directionality of the inelastic strain and the resulting accumulation, the mean strain of the hysteresis loop increases with increasing number of load cycles. This phenomenon is called cyclic creep or ratcheting, and is indicated by the shift of the stress-strain-hysteresis loop with increasing number of load cycles. At elevated temperatures, creep processes occur in hard metals during cyclic testing next to time-independent processes [15], and promote cyclic creep. Further, a tension-compression-strain asymmetry can occur, which is defined as a faster increase of strain under tension than under compression as reported for step-loading creep tests in [25]. The asymmetry is explained by the fact that microcracks open in tension and close in compression [26], and therefore the mechanical stiffness is lower in tension than in compression [27]. Due to the fast increase in strain and different mechanical stiffness under tension, a pronounced tilting of the stress-strain-hysteresis



loop occurs under tensile loading, see section 3.1. In the current work, the tension-compression-strain asymmetry value achieved at certain number of load cycles loading of the test was determined by Eq. (1).

$$\varepsilon_{asym}(N_x) = (\varepsilon_{max}(N_x) - \varepsilon_{max}(N_1)) - (\varepsilon_{min}(N_x) - \varepsilon_{min}(N_1)) \quad (1)$$

where  $\varepsilon_{max}$  is the strain in tension and  $\varepsilon_{min}$  is the strain in compression at the point of inflection of the stress-strain-hysteresis loop,  $N_x$  is a certain number of load cycle after the first one, and  $N_1$  is the first load cycle.

In order to examine the damage development with increasing number of load cycles at 800 °C, the microstructure of M10 was analyzed at  $\sigma_a = 1000$  MPa after  $N = 20$  and 80 load cycles without specimen fracture prior to cross-sectioning for the investigation. To this end, the specimens were immediately loaded monotonically up to +1000 MPa with a strain rate of 0.2 %/s after the end of cyclic testing and a subsequent cooldown phase to room temperature. The specimens were reloaded in this manner to resemble loading conditions present close to the cutting edges of milling tools after milling application as it was observed that the applied amplitude of tensile residual stress was still present in milling tools at room temperature [13,28]. Further, defects that could have closed after a last cyclic loading in compression should be reopened and facilitate their identification by SEM. Additionally, virgin specimens of the same grades were analyzed as reference specimens. The microstructure of the specimens was analyzed by scanning electron microscopy (SEM, GeminiSEM ® 450 / Carl Zeiss SMT) in secondary electron (SE) and backscattered electron (BSE) contrast mode. The investigated cross-sections of the hourglass-shaped specimens were taken from their axial centers, i.e. at the minimum diameter of the hourglass-shaped specimens. Metallographic specimens were prepared with argon ion polishing as the final surface preparation step, which removes the deformed surface layers introduced during cutting and polishing [29]. The ridges that form on the specimen surface in this procedure were assumed not to affect the number or size of defects that form during mechanical testing. Nor did they affect the relative amount of fcc Co- to hcp Co-phase visible in the plane intersecting the material volume [29]. The cross-section planes investigated were oriented parallel to the loading direction, i.e. when looking at the secondary electron images, the load direction points perpendicular to the image plane. The microstructure was examined at three positions in the center of each cross-section at the minimum specimen diameter. One position roughly was chosen in the center of the 6 mm specimen diameter and two at a distance of 500  $\mu\text{m}$  away from this position within the argon polished region. Counting of the number of microdefects was carried out manually for SEM micrographs of an individual size of 11.3  $\mu\text{m} \times 7.8 \mu\text{m}$  attained using secondary electron contrast mode using an InLens detector arrangement for a total area of 3000  $\mu\text{m}^2$  per investigated loading condition, covering approximately 2100 WC grains. The number of microdefects within these three areas was in the same order of magnitude for an individual specimen of a certain grade and loading condition.

Phase transformations and traces of plastic strain in WC- and Co-phases were analyzed by electron backscatter diffraction (EBSD) on the same three specimens investigated via SEM. The EBSD analysis

(System: Symmetry / Oxford Instruments) was performed at 15 kV acceleration voltage and an applied step size of 50 nm for a zone of 38.3  $\mu\text{m}$  x 28.8  $\mu\text{m}$ . The specimen was tilted by 70° in the direction of the EBSD camera and the working distance was set to 15 mm. A software-based evaluation of eleven Kikuchi bands with a Hough space resolution of 95 was performed. The software package “Orientation Imaging Microscopy” (OIM) version 7 from EDAX [30] was used to determine the kernel average misorientation (KAM) for the WC-, fcc and hcp Co-phase using the 1<sup>st</sup> nearest neighbor with a maximum misorientation angle of 2°. KAM maps can be used to show differences in dislocation density which give additional information about lattice distortion and strain localization [31]. Additionally, grain average misorientations (GAM) of each single grain for the WC-phase were also determined by OIM with a maximum misorientation angle of 2°. Inverse pole figure (IPF) evaluations were performed with “MTEX Toolbox” version 5.3 [32] in Matlab Version R2019b for all phases to identify crystal orientation changes, caused by plastic strain and to determine the phase distributions. No grain dilation clean-up was applied to the generated EBSD data.

### 3. Results

#### 3.1. Cyclic stress-strain behavior of two WC-Co hardmetal grades at 700 °C and 800 °C

Fig. 2 shows the uncorrected stress-strain-hysteresis loops of the respective number of load cycles  $N = 1, 50, 100, 210, 1230$  and 2500 of the WC-Co hardmetal grades S10 and M10 at 700 °C and 800 °C. Cyclic tests were carried out up to a maximum number of load cycle  $N = 2500$ . Fig. 2(a.) to Fig. 2(c.) show the stress-strain-hysteresis loops of the grade S10 at 700 °C for stress amplitudes of 750 MPa, 1000 MPa and 1500 MPa, respectively. At stress amplitudes of 750 MPa and 1000 MPa,  $N = 2500$  was reached, but at 1500 MPa the specimen failed after  $N_f = 212$  load cycles. Narrow and symmetric stress-strain-hysteresis loops were observed at 750 MPa and 1000 MPa, see Fig. 2(a.) and Fig. 2(b.). An enlarged stress-strain-hysteresis loop with increased number of load cycles was noticed especially at 1500 MPa, see Fig. 2(c.). Changes in the stress-strain-hysteresis loop area as a function of the number of load cycles for the three stress amplitudes are shown in Fig. 3(a.). The loop area at 750 MPa and 1000 MPa did not change significantly up to the maximum reached number of load cycle. Also, a higher stress-strain-hysteresis loop area was determined at 1000 MPa than at 750 MPa, see Fig. 3(a.). Additionally, at 1500 MPa, an increase of the stress-strain-hysteresis loop area was observed with increasing number of load cycles until specimen failure, see Fig. 3(a.). Furthermore, cyclic creep was not noticed at the three investigated stress amplitudes at 700 °C, see Fig. 2(a.) to Fig. 2(c.). However, at 1500 MPa, a very small tension-compression-strain asymmetry  $\varepsilon_{\text{asym}}$  was observed, see the inflection points at 1500 MPa marked with black arrows in Fig. 2(c.). Based on the asymmetry values calculated with Eq. (1) using the uncorrected stress-strain-hysteresis loops,

it was observed that the strain asymmetry value stabilized at 750 MPa and 1000 MPa and increased continuously at 1500 MPa with increasing number of load cycles, see Fig. 3(b.).

The WC-Co hardmetal grade S10 was also investigated at 800 °C at the same stress amplitudes as at 700 °C. Fig. 2(d.) to Fig. 2(f.) show the stress-strain-hysteresis loops for 750 MPa, 1000 MPa and 1500 MPa, respectively. At 800 °C, a widening of the hysteresis loops, see Fig. 2(d.) to Fig. 2(f.), and larger loop areas were observed at lower stress amplitudes than at 700 °C, compare Fig. 3(a.) - Fig. 3(c.). Also, at a stress amplitude of 1000 MPa an increase in the stress-strain-hysteresis loop area was observed with increasing number of load cycles, see Fig. 3(c.). Besides an increase in loop area, the plastic strain amplitude width of the hysteresis loop at  $\sigma = 0$  increased with increasing number of load cycles, compare Fig. 2(d.) - Fig. 2(e.). When the temperature increased, specimen failure was noticed earlier than at 700 °C, compare Fig. 2(a.) - Fig. 2(f.). Besides the widening of the stress-strain-hysteresis loops at 800 °C, cyclic creep was noticed, as the stress-strain-hysteresis loop shifted to higher positive strain values, see Fig. 2(d.) and Fig. 2(e.). The extent of cyclic creep increased with increasing stress amplitude. Investigations at 800 °C and a stress amplitude of 1000 MPa exhibited a tension-compression-strain asymmetry  $\varepsilon_{\text{asym}}$  which increased continuously with increasing number of load cycles until specimen failure, see Fig. 3(d.). At 750 MPa, a very small  $\varepsilon_{\text{asym}}$  was observed, which remained constant within the measurement accuracy over the investigated number of load cycles. Fig. 2(f.) shows the stress-strain-hysteresis loop at 1500 MPa and 800 °C of the grade S10, which failed during the first loading cycle under tension. Due to too few data points, no statement can be made about the stress-strain-hysteresis loop areas and  $\varepsilon_{\text{asym}}$  at 1500 MPa.

Fig. 2(g.) to Fig. 2(i.) show stress-strain-hysteresis loops of the WC-Co hardmetal grade M10 at the same stress amplitudes of 750 MPa, 1000 MPa and 1500 MPa as in the 700 °C tests, respectively. At 750 MPa and 1000 MPa, the hysteresis loops were found to be narrow and symmetrical, see Fig. 2(g.) and Fig. 2(h.). The calculated hysteresis loop areas as a function of number of load cycle at 750 MPa and 1000 MPa show a decrease up to  $N = 400$  load cycles and an almost constant value up to  $N = 2500$  load cycles, see Fig. 3(e.). The low decrease is assumed to be due to measurement errors. At  $\sigma_a = 1500$  MPa, the specimen failed at  $N_f = 9$  load cycles and exhibited a widening of the stress-strain-hysteresis loop, see Fig. 2(i.), and an increase in stress-strain-hysteresis loop area with increasing number of load cycles, see Fig. 3(e.). Similar to the WC-Co hardmetal grade S10, cyclic creep was not observed at the three stress amplitudes for the WC-Co hardmetal grade M10 at 700 °C. Furthermore, a minimal increase in the tension-compression-strain asymmetry  $\varepsilon_{\text{asym}}$  was determined at 750 MPa, 1000 MPa and 1500 MPa, see Fig. 3(f.). The  $\varepsilon_{\text{asym}}$  at 750 MPa and 1000 MPa increased at the beginning of the cyclic test and stabilized with increasing number of load cycles, see Fig. 3(f.).

Fig. 2(j.) to Fig. 2(l.) show stress-strain-hysteresis loops of the WC-Co hardmetal grade M10 at 800 °C for the same stress amplitudes as in the 700 °C tests. At 800 °C, a widening of the hysteresis loops,

see Fig. 2(j.) to Fig. 2(l.), and larger loop areas, see Fig. 3(g.), were observed at lower stress amplitudes than at 700 °C. As for S10 at 800 °C, the plastic strain amplitude width at  $\sigma=0$  increased with increasing number of load cycles, see Fig. 2(k.). When increasing the temperature, specimen failure was detected earlier than at 700 °C, compare Fig. 2(g.) - Fig. 2(l.). Besides the widening of the stress-strain-hysteresis loops at 800 °C, pronounced cyclic creep was observed, see Fig. 2(j.) and Fig. 2(k.). Investigations at stress amplitudes of 750 MPa and 1000 MPa exhibited a  $\varepsilon_{\text{asym}}$  which increased continuously with increasing number of load cycles until specimen failure, see Fig. 3(h.). At 750 MPa only a very small increase in  $\varepsilon_{\text{asym}}$  was observed, in contrast to the case of 1000 MPa, at which a great increase was determined at low number of load cycles. Fig. 2(l.) shows the stress-strain-hysteresis loop at 1500 MPa and 800 °C of the grade M10, which failed during the first loading cycle under tension. Due to too few data points, no statement can be made about the stress-strain-hysteresis loop areas and  $\varepsilon_{\text{asym}}$  at 1500 MPa.

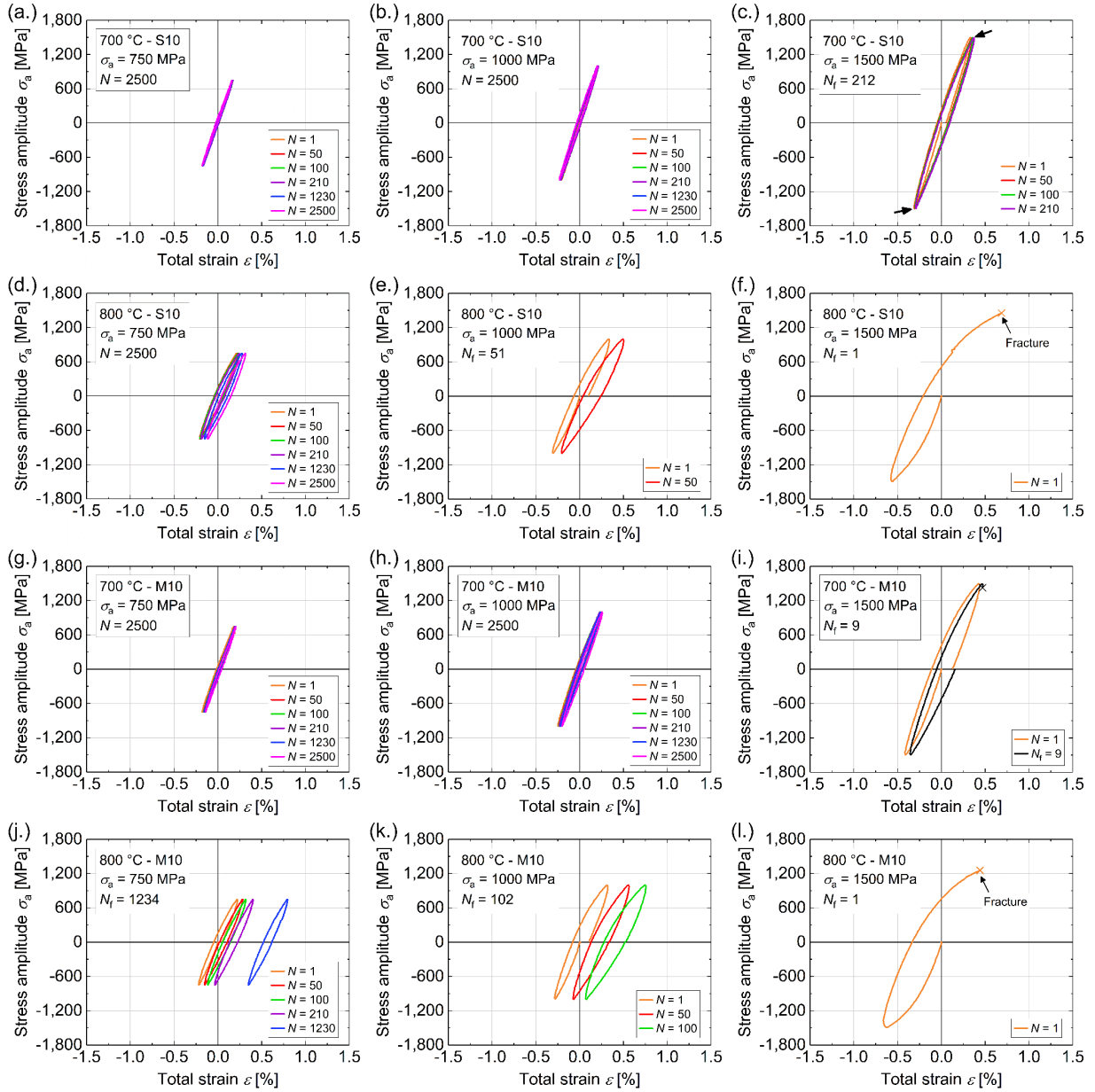


Fig. 2: Cyclic stress-strain-hysteresis loops of WC-Co hardmetal grades S10 in (a.) to (f.) and M10 in (g.) to (l.) under a stress ratio of  $R = -1$  loaded up to stress amplitudes  $\sigma_a = 750$  MPa, 1000 MPa and 1500 MPa at 700 °C and 800 °C up to  $N = 2500$  load cycles or specimen failure  $N_f$ . For better visualization, the same colors are used for loops of equal number of load cycle  $N = 1^{\text{st}}$  (orange),  $50^{\text{th}}$  (red),  $100^{\text{th}}$  (green),  $210^{\text{th}}$  (violet),  $1230^{\text{th}}$  (blue) and  $2500^{\text{th}}$  (magenta). (For interpretation of the references to color in the figure legends, the reader is referred to the web version of this article.)

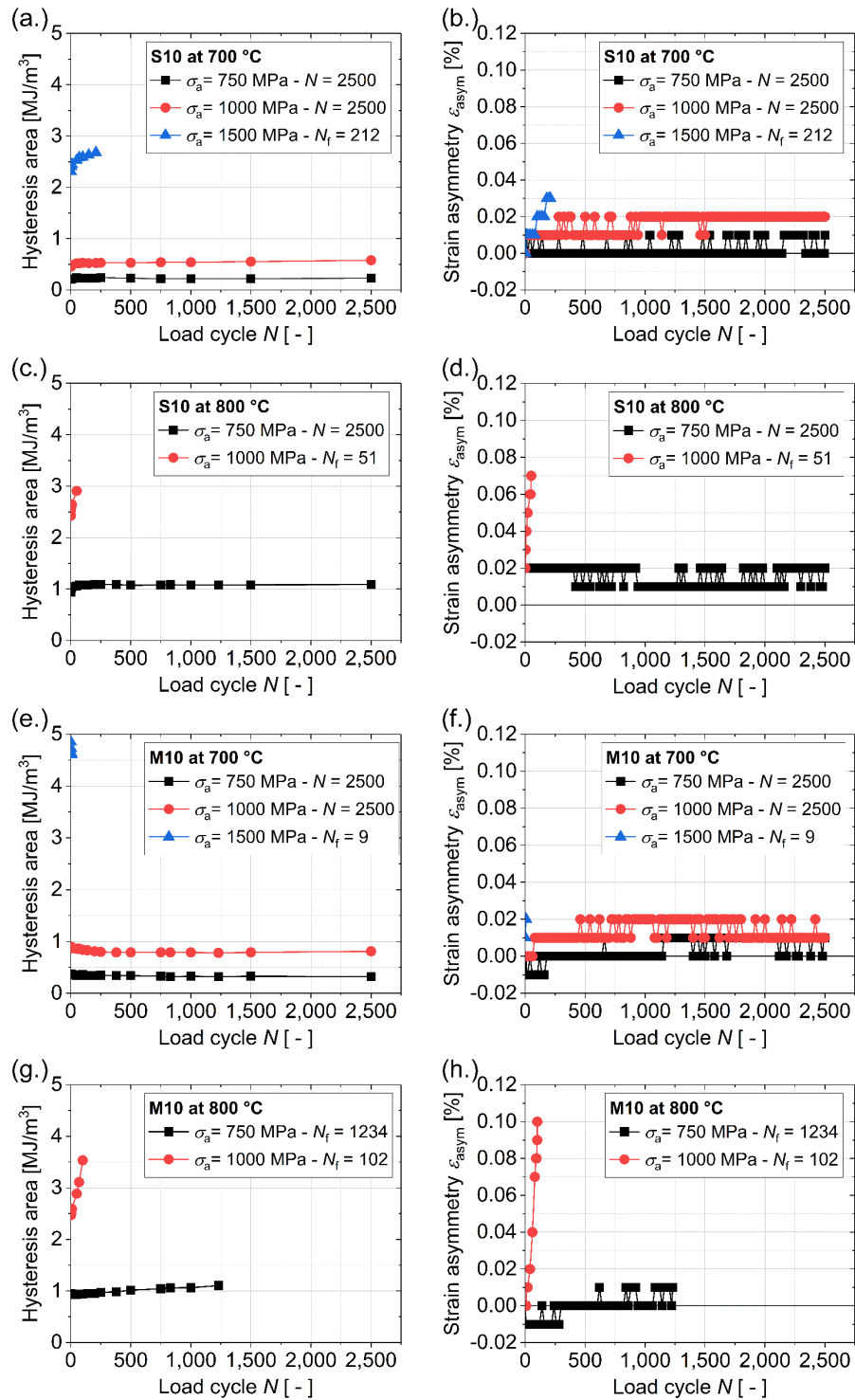


Fig. 3: Stress-strain-hysteresis loop area and tension-compression-strain asymmetry  $\epsilon_{asym}$  as a function of the number of load cycles  $N$  of WC-Co hardmetal grades S10 in (a.) to (d.) and M10 in (e.) to (h.) under a stress ratio of  $R = -1$  loaded up to stress amplitudes  $\sigma_a = 750$  MPa (black - square), 1000 MPa (red - circle) and 1500 MPa (blue - triangle) at 700 °C and 800 °C up to  $N = 2500$  load cycles or specimen failure  $N_f$ . (For interpretation of the references to color in the figure legends, the reader is referred to the web version of this article.)

### 3.2 Development of microdefects during increasing number of load cycles at 800 °C

Next to investigations of changes of the stress-strain-hysteresis loops with increasing number of load cycles, the microstructure of two hardmetal specimens made of M10 was analyzed after cyclic testing up to respective  $N = 20$  and 80 load cycles without specimen fracture during testing. The specimens were tested at a stress amplitude of 1000 MPa at 800 °C. Fig. 4(a.) and Fig. 4(b.) show the stress-strain-hysteresis loops for defined number of load cycles up to  $N = 20$  and 80. As with the specimens made of the WC-Co hardmetal grades S10 and M10 tested at 800 °C described previously, cyclic creep was observed with increasing number of load cycles, compare Fig. 2(d.) - Fig. 2(f.), Fig. 2(j.) - Fig. 2(l.) with Fig. 4(a.) and Fig. 4(b.). Also, the stress-strain-hysteresis loop area and tension-compression-strain asymmetry  $\varepsilon_{\text{asym}}$  with increasing number of load cycles were investigated, see Fig. 4(c.) and Fig. 4(d.). The arrow in Fig. 4(c.) indicates the onset of strain asymmetry.

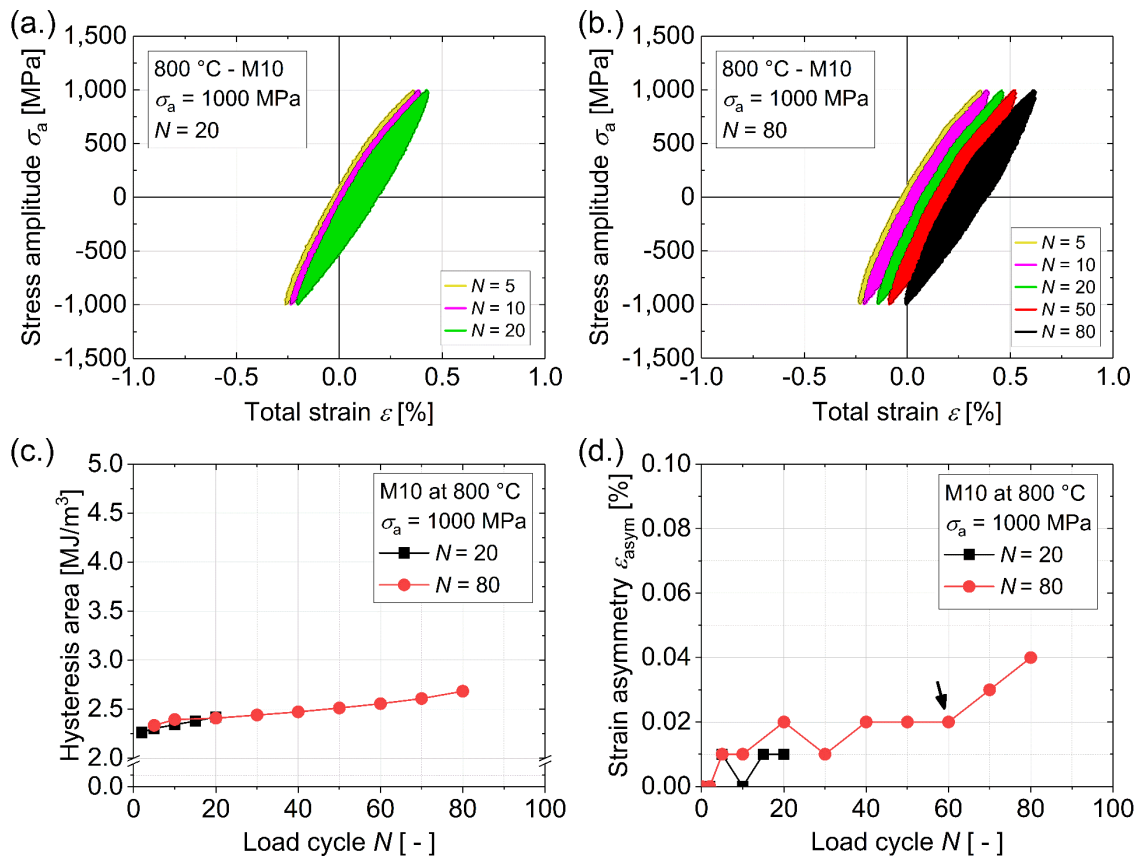


Fig. 4: Cyclic stress-strain-hysteresis loops of WC-Co hardmetal grade M10 at a stress ratio of  $R = -1$  loaded at a stress amplitude  $\sigma_a = 1000$  MPa at 800 °C up to (a.)  $N = 20$  and (b.) 80 load cycles without specimen failure. For better visualization, the same colors are used for loops of equal number of load cycle  $N = 5^{\text{th}}$  (yellow),  $10^{\text{th}}$  (magenta),  $20^{\text{th}}$  (green),  $50^{\text{th}}$  (red) and  $80^{\text{th}}$  (black). (c.) Stress-strain-hysteresis loop area and (d.) tension-compression-strain asymmetry  $\varepsilon_{\text{asym}}$  as a function of the load cycles  $N$  for the specimen investigated up to  $N = 20$  and 80 load cycles. The black arrow in (c.) indicates the onset of strain asymmetry. (For interpretation of the references to color in the figure legends, the reader is referred to the web version of this article.)

Fig. 5(a.) shows the microstructure of the virgin M10 hardmetal grade. Fig. 5(b.) and Fig. 5(c.) show the microstructure for the specimens tested up to  $N = 20$  and 80 load cycles at 1000 MPa and 800 °C, respectively. Additionally, Fig. 6 shows details for each investigated loading condition shown in Fig. 5. The regions where the observed microdefects occurred appeared slightly darker than the dark grey regions of the Co-binder, and are marked with red arrows in Fig. 5. A small number of defects was also found in the virgin specimen, which are assumed to have arisen during processing, e.g. due to different expansion coefficients of the phases involved. Distinct cracks had not yet formed after  $N = 20$  and 80 load cycles. Fewer and smaller microdefects were detectable in the specimen after  $N = 20$  load cycles, see Fig. 5(b.), compared to that after reaching  $N = 80$  load cycles, see Fig. 5(c.). A counting of the number of microdefects was carried out for SEM micrographs such as shown in Fig. 6(a.) to Fig. 6(c.) for a total area of 3000  $\mu\text{m}^2$  per investigated deformation state. The average microdefect number per deformation state was 10, 43 and 90 for the virgin, and the loaded specimens after  $N = 20$  and 80 load cycles, respectively.

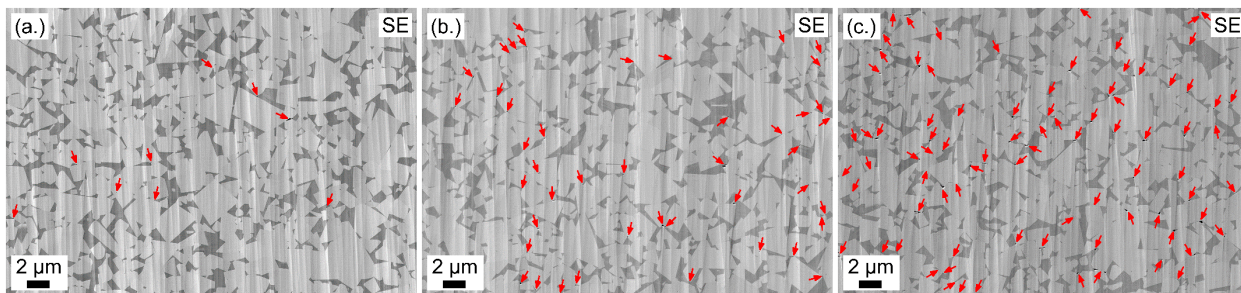


Fig. 5: SEM micrographs showing the microstructure at room temperature of the WC-Co hardmetal grade M10 in secondary electron (SE) contrast mode: (a.) virgin, and after cyclic tests under a stress ratio of  $R = -1$  loaded up to a stress amplitude  $\sigma_a = 1000$  MPa at 800 °C up to (b.)  $N = 20$  and (c.) 80 load cycles without specimen failure. The load direction is oriented perpendicular to the image plane and the red arrows mark microdefects.

Most of these microdefects had formed at sharp corners at triple phase boundaries, i.e. at WC/WC/Co interface junctions, at WC grain boundary triple points or in narrow Co ligaments between WC grains. Fig. 6(a.) to Fig. 6(c.) show SEM micrographs in secondary electron (SE) and Fig. 6(d.) to Fig. 6(f.) show the same micrographs in backscattered electron (BSE) contrast mode of the virgin and both loaded specimen at  $N = 20$  and 80 load cycles, respectively. Microdefects (red arrows) as well as twins in the Co-binder (green triangles) were observed in SE micrographs, see Fig. 6(a.) to Fig. 6(c.). Twins in the Co-binder were detected in the virgin and in both cyclically tested specimens. BSE micrographs also revealed nanopore chains at WC/WC grain boundaries, see white ovals in Fig. 6(e.) and Fig. 6(f.).



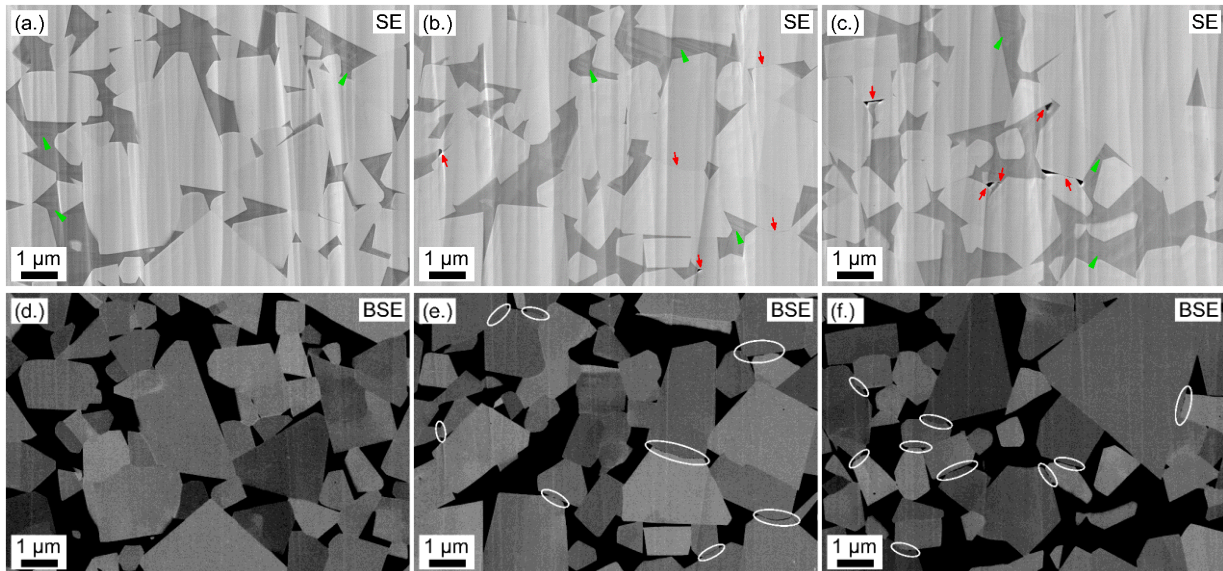


Fig. 6: SEM micrographs showing details of the microstructures from Fig. 5 at room temperature of the WC-Co hardmetal grade M10 (a.) to (c.) in secondary electron (SE) and (d.) to (f.) in backscattered electron (BSE) contrast mode. (a.) and (d.) show details from the virgin specimen. (b.), (e.) and (c.), (f.) show micrographs after cyclic tests under a stress ratio of  $R = -1$  loaded up to a stress amplitude  $\sigma_a = 1000$  MPa at  $800$  °C up to  $N = 20$  and  $80$  load cycles without specimen failure, respectively. The load direction is oriented perpendicular to the image plane. Microdefects, Co-binder twins and nanopore chains are marked by red arrows, green triangles and white ovals, respectively. (For interpretation of the color in the figure, the reader is referred to the web version of this article.)

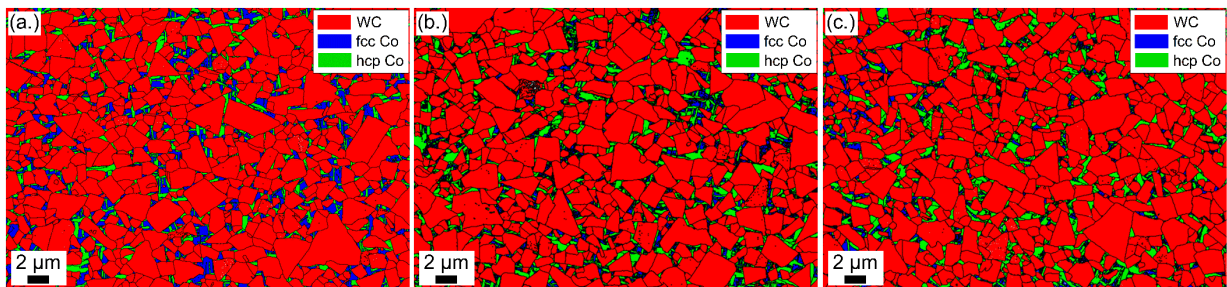


Fig. 7: EBSD phase distribution maps for WC-Co hardmetal grade M10, showing WC (red), fcc Co-phase (blue), hcp Co-phase (green) and grain boundaries, for three different cases: (a.) virgin, and after uniaxial cyclic loading under a stress ratio of  $R = -1$  loaded up to a stress amplitude  $\sigma_a = 1000$  MPa at  $800$  °C up to (b.)  $N = 20$  and (c.)  $N = 80$  load cycles without specimen failure. (a.) to (c.) show the same image section of the microstructure as present in Fig. 5(a.) to Fig. 5(c.). The load directions is oriented perpendicular to the image planes. (For the interpretation of color, the reader is referred to the online version of this article.)

EBSD data allowed the calculation of the phase distribution of WC grains, fcc Co-phase and hcp Co-phase. Fig. 7 shows the phase distribution of all three phases for the three investigated deformation states. For the three specimens, the same image sections were investigated as in Fig. 5(a.) to Fig. 5(c.). In the virgin as well as in the loaded states, the Co-binder was observed in both fcc and hcp crystal structures, see Fig. 7(a.) to Fig. 7(c.). Tab. 2 lists the area phase fractions of the different phases and deformation conditions. The results indicate that the area fraction of the fcc Co-phase decreases while that of the hcp Co-phase increases with the number of load cycles.

Tab. 2: Area phase fractions of WC, fcc Co and hcp Co in the virgin specimen made of M10 and the ones loaded at  $R = -1$  and  $\sigma_a = 1000$  MPa for 800 °C up to  $N = 20$  and 80 load cycles without specimen fracture.

Phase	Area fraction of the hardmetal phases [%]		
	Virgin	$N = 20$	$N = 80$
Not Indexed	0.7	1.1	1.4
WC	82.0	80.3	81.2
fcc Co	8.3	5.0	4.2
hcp Co	9.0	13.6	13.2

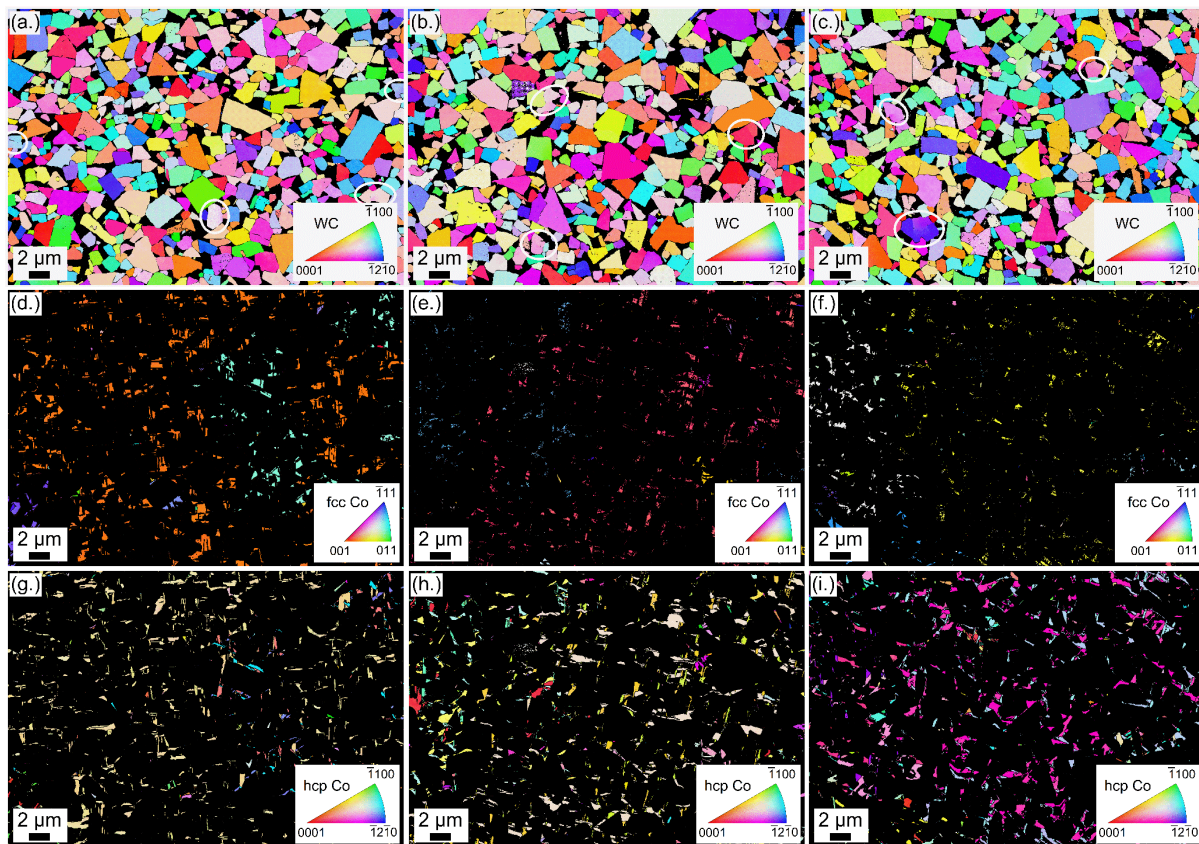


Fig. 8: EBSD inverse pole figure (IPF) maps show the same image location as present in Fig. 5(a.) to Fig. 5(c.) for the WC-Co hardmetal grade M10: (a.), (d.) and (g.) show the virgin specimen. Specimens cyclically loaded under a stress ratio of  $R = -1$  at 1000 MPa and at 800 °C are shown up to  $N = 20$  in (b.), (e.) and (h.) and up to  $N = 80$  load cycles in (c.), (f.) and (i.). The IPFs are shown in: (a.) to (c.) for the WC-phase, (d.) to (f.) for the fcc Co-phase, and (g.) to (i.) for the hcp Co-phase. WC grains with crystal orientation change within the grain, indicated by a color gradient, are marked with white ovals. The load directions point vertically along the image planes. (For the interpretation of color, the reader is referred to the online version of this article.)

In order to study the effect of straining on microstructural changes with increasing number of load cycles in uniaxial cyclic tests, inverse pole figure (IPF) calculations were carried out using EBSD data. In IPFs, individual phase regions are displayed in different colors according to their crystal orientation [33]. All phases were investigated in the virgin as well as in both specimens tested cyclically at  $\sigma_a = 1000$  MPa and

800 °C up to  $N = 20$  and 80 load cycles, as shown in Fig. 8(a.) to Fig. 8(i.). For the three loading conditions investigated, images were taken from the same locations as in Fig. 5(a.) to Fig. 5(c.). Certain WC grains showed a distinct crystal orientation change within a grain, i.e., a color gradient, see white ovals in Fig. 8(a.) to Fig. 8(c.). The proportion of WC grains with such a distinct crystal orientation change was the same in all three investigated specimens. Fig. 8(d.) to Fig. 8(f.) show the IPF maps for the fcc Co-phase. The IPF maps for the hcp Co-phase are presented in Fig. 8(g.) to Fig. 8(i.). In the virgin specimen, the Co-phase was observed to exhibit regions of same orientation, i.e. same color, for both binder phases, hcp Co- and fcc Co-phase. Also after loading, regions of the same crystal orientations were observed for fcc Co- and hcp Co-phase. Mingard et al. [34] showed from 3D IPF maps that adjacent Co-regions with the same crystal orientation belong together and represent a large grain. Note that the hcp Co-regions in the loaded specimens include different crystal orientations side by side, see Fig. 8(h.) and Fig. 8(i.), which may be attributed to the increase in hcp Co-phase during cyclic loading from the fcc Co-phase.

Grain average misorientation (GAM) calculations were performed to study the average misorientation in WC grains between neighboring points in interiors of grains [31]. In Fig. 9(a.) to Fig. 9(c.), the GAM maps for the WC-phase are shown for all three loading conditions: virgin,  $N = 20$  and 80 load cycles. Additionally, the GAM map data from Fig. 9(a.) to Fig. 9(c.) is displayed in Fig. 9(d.) as a distribution of the fraction of all indexed points in the entire EBSD image over the respective GAM values for the WC grains. The comparison of the GAM charts indicates that no change in the GAM distribution in the WC grains was observed as a result of the selected loading conditions, Fig. 9(d.). Additionally, kernel average misorientation (KAM) calculations were performed to study local dislocation density differences and strain localizations in the WC-phase. Fig. 10(a.) and Fig. 10(b.) show the KAM maps for the WC-phase of the virgin specimens and the specimen loaded up to  $N = 20$  load cycles. The color variation from blue to red therein indicates misorientations from  $0^\circ$  to  $2^\circ$  as in the GAM maps. The KAM map data from Fig. 10(a.) and Fig. 10(b.) is displayed in Fig. 10(c.) as a distribution of the fraction of all indexed points in the entire EBSD image over the respective KAM values for the WC-phase. KAM data for the loaded specimens up to  $N = 80$  load cycles were not evaluated because the behavior of the GAM data suggested that they can be assumed to show no different behavior than for 20 load cycles. The KAM maps show, that the misorientations in the WC grains have a high blue and green fraction, see Fig. 10(a.) and Fig. 10(b.). Dislocation structures and subgrains within WC grains in unloaded WC- Co hardmetal grades have been documented, caused by the accumulation of stresses in sintered materials [35]. Based on this observation [35], the green portion in form of lines in WC grains or at WC/Co interfaces in this work, see Fig. 10(a.) and Fig. 10(b.), can be interpreted as dislocation structures.

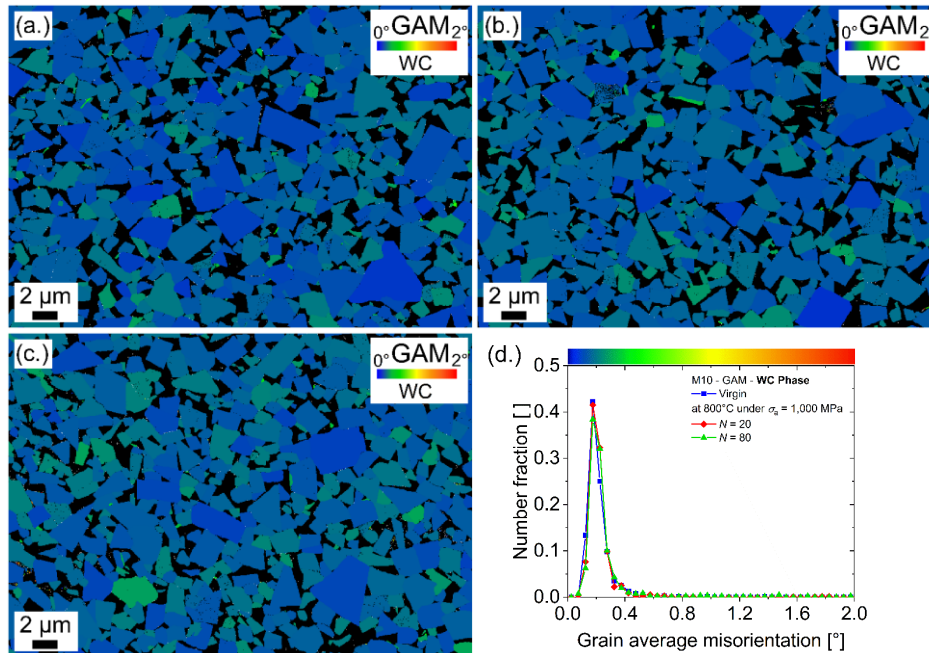


Fig. 9: EBSD grain average misorientation (GAM) maps for the WC-phase show the same image location as present in Fig. 5(a) to Fig. 5(c) for the WC-Co hardmetal grade M10 for specimens in (a.) virgin state and cyclically loaded state under a stress ratio of  $R = -1$  at 1000 MPa and at 800 °C up to (b.)  $N = 20$  and (c.)  $N = 80$  load cycles. The displayed misorientation ranges from 0° (blue) to 2° (red). The load directions point vertically along the image planes. (d.) GAM distributions of the EBSD data shown in (a.) to (c.) for the WC-phase with all three load cases compared: virgin (blue - square),  $N = 20$  (red - diamond) and  $N = 80$  (green - triangle). (For the interpretation of color, the reader is referred to the online version of this article.)

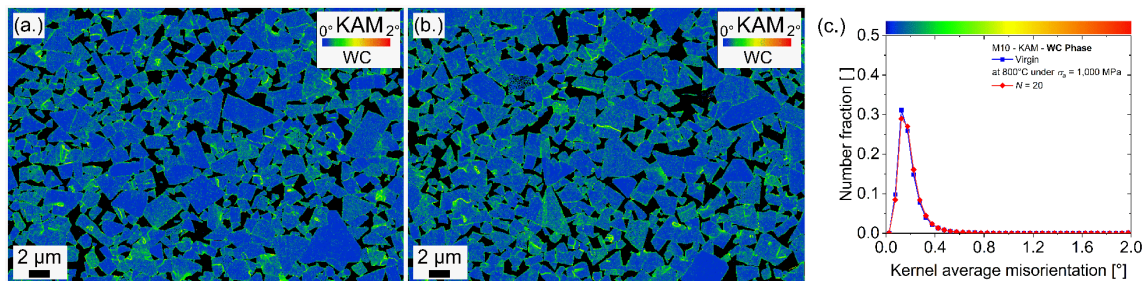


Fig. 10: EBSD kernel average misorientation (KAM) maps for the WC-phase show the same image location as present in Fig. 5(a.) and Fig. 5(b.) for the WC-Co hardmetal grade M10 for specimens in (a.) virgin state and cyclically loaded state under a stress ratio of  $R = -1$  at 1000 MPa and at 800 °C up to (a.)  $N = 20$  load cycles. The displayed misorientation ranges from 0° (blue) to 2° (red). The load directions point vertically along the image planes. (c.) KAM distributions of the EBSD data shown in (a.) and (b.) for the WC-phase: virgin (blue - square) and  $N = 20$  (red - diamond). (For the interpretation of color, the reader is referred to the online version of this article.)

Fig. 11(a.) to Fig. 11(c.) show the KAM maps for the fcc Co-phase and Fig. 11(e.) to Fig. 11(g.) for hcp Co-phase. Additionally, the KAM data from the fcc Co- and hcp Co-phase are displayed in Fig. 11(d.) and Fig. 11(h.) as a distribution of the fraction of all indexed points in the entire individual EBSD images over the respective KAM values for both Co-phases. A decrease in small misorientations, gray arrow, and a slight

increase in higher misorientations, black arrow, occurred after uniaxial cyclic tests in both Co-phases, see Fig. 11(d.) and Fig. 11(h.).

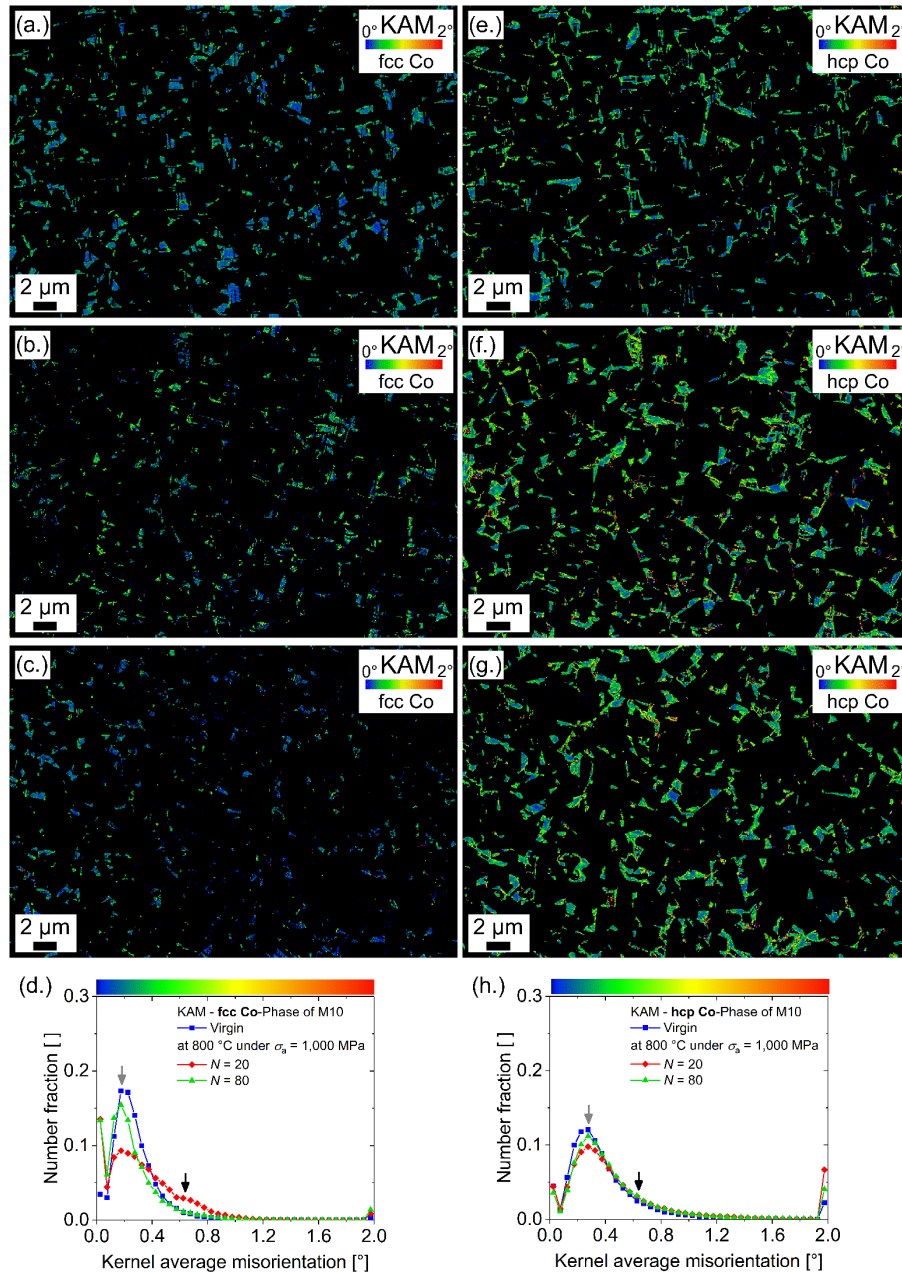


Fig. 11: Kernel average misorientation (KAM) maps for the fcc and hcp Co-phase show the same image section as present in Fig. 5(a.) to Fig. 5(c.) for the WC-Co hardmetal grade M10 for (a.), (e.) a virgin state, and for cyclically loaded specimens under a stress ratio  $R = -1$  at an applied stress amplitude  $\sigma_a = 1000$  MPa at  $800$  °C after (b.), (f.)  $N = 20$ , and (c.), (g.)  $N = 80$  load cycles. The displayed misorientation ranges from  $0^\circ$  (blue) to  $2^\circ$  (red). The KAM is shown in: (a.) to (c.) for the fcc Co and in (e.) to (g.) for the hcp Co-phase. The load directions point vertically along the image planes. (d.) and (h.) show the respective KAM distributions derived from the EBSD data shown in (a.) to (c.) and (e.) to (g.) with all three load cases compared: virgin (blue - square),  $N = 20$  (red - diamond) and  $N = 80$  (green - triangle). (For the interpretation of color, the reader is referred to the online version of this article.)

## 4. Discussion

### 4.1. Characterization of stress-strain-hysteresis loop shape at 700 °C and 800 °C

The stress-strain-hysteresis loops of the WC-Co hardmetal grades S10 and M10 at 700 °C and 800 °C suggest a dependence of the cyclic stress-strain-hysteresis loop behavior on temperature and stress amplitude, see Fig. 2. At 700 °C, narrow stress-strain-hysteresis loops were observed at 750 MPa and 1000 MPa for the WC-Co hardmetal grade S10, see Fig. 2(a.) and Fig. 2(b.). This was also the case at 750 MPa and 1000 MPa for the grade M10, but the stress-strain-hysteresis loops were slightly wider for the grade M10, see Fig. 2(g.) and Fig. 2(h.). Narrow stress-strain-hysteresis loops indicate reversible strain without plastic deformation [36]. Fig. 3(a.) and Fig. 3(e.) show the stress-strain-hysteresis loop area of both WC-Co hardmetal grades for all three investigated stress amplitudes 750 MPa, 1000 MPa and 1500 MPa at 700 °C. At 750 MPa, both grades show similar values for the stress-strain-hysteresis loop area, with a constant progression up to the maximum number of load cycles  $N = 2500$  without specimen failure. With increasing applied stress amplitude, the stress-strain-hysteresis loop area of both WC-Co hardmetal grades increased, see Fig. 2(a.) to Fig. 2(c.) and Fig. 2(g.) to Fig. 2(f.). At 1000 MPa, as at 1500 MPa, a larger hysteresis loop area was observed for the WC-Co hardmetal grade M10 compared to that of the grade S10 at 700 °C. As at 750 MPa, a constant progression of the hysteresis loop area was observed at 1000 MPa for both WC-Co hardmetal grades with increasing number of load cycles. An increase in the hysteresis loop area until failure of the specimen was observed at 1500 MPa in both WC-Co hardmetal grades, see Fig. 3(a.) and Fig. 3(e.). The stress-strain-hysteresis loop area corresponds to an energy dissipation or the specific deformation work in the material during a load cycle [37]. Microscopically, energy dissipation occurs due to movement of dislocations and diffusion of point defects in the material [38]. The increase in the hysteresis loop area indicates an increased movement of lattice defects [23]. Besides an increase in the hysteresis loop area, the plastic strain amplitude also increased, see Fig. 2(e.) and Fig. 2(k.), which can be interpreted as softening of the material, see e.g. [23,39,40]. Due to the larger WC grains in the medium-grained grade, a broader Co-binder mean free path is present than in the submicron-grained grade [41]. Since the Co binder phase is more ductile than the WC grains, the deformation occurs mainly in the binder. Due to the broader regions and higher ductility of the Co binder phase, the movement of lattice defects and phase transformation is more likely in the WC-Co hardmetal grade M10 than in the grade S10 for the same stress amplitude. In addition to the increase in stress-strain-hysteresis loop area, the value of tension-compression-strain asymmetry  $\varepsilon_{\text{asym}}$  at 700 °C was observed to be non-zero at 1000 MPa and 1500 MPa in both WC-Co hardmetal grades, Fig. 3(b.) und Fig. 3(f.). At 750 MPa and 1000 MPa, the  $\varepsilon_{\text{asym}}$  stabilizes and increases continuously at 1500 MPa with increasing number of load cycles until specimen failure for both WC-Co hardmetal grades.

At 800 °C, the same stress amplitudes as at 700 °C were investigated for the two WC-Co hardmetal grades S10 and M10. At 750 MPa and 1000 MPa a widening of the stress-strain-hysteresis loops with increasing number of load cycles was observed for both WC-Co hardmetal grades, see Fig. 2(d.) to Fig. 2(f.) and Fig. 2(j.) to Fig. 2(l.). Also, larger increase of the stress-strain-hysteresis loop area was observed with increasing number of load cycles than at 700 °C, see Fig. 3(c.) and Fig. 3(g.). The stress-strain-hysteresis loop areas were slightly higher for M10 but in the same order of magnitude for both hardmetals at 750 MPa and 1000 MPa. In the case of the WC-Co hardmetal grade M10 the hysteresis loop area did not stabilize with increasing number of load cycles before specimen failure for both stress amplitudes of 750 MPa and 1000 MPa and failed at  $N_f = 1234$  and 102 respectively, see Fig. 3(g.). With increasing temperature, specimen failure was observed at lower stress amplitudes than at 700 °C, compare Fig. 2(a.) - Fig. 2(f.) and Fig. 2(g.) - Fig. 2(l.), as also observed for thermo-mechanical fatigue tests under  $R = -1$  performed up to  $\sigma_a = 520$  MPa at 700 °C and 800 °C for different WC-Co hardmetals in [10]. A direct comparison of the number of load cycles until fracture is not permissible, because hardmetals contain internal defects, such as pores or WC grains larger than average, which are statistically distributed in the material and influence the number of cycles to failure [42]. Additionally, the stress and/or strain for specimen failure may be reduced due to internal defects, and the observed number of cycles to failure may show large scatter, as also reported from fatigue tests for WC-Co hardmetal at room temperature [43,44]. Therefore, no direct comparisons were made in the current work with respect to cycles to failure between materials and temperatures. A large number of further tests would have to be carried out in order to be able to make valid statements about which material has a higher resistance to failure under the loading conditions investigated in the current work. It should be noted, however, that the specimens of the WC-Co hardmetal grade M10, in contrast to S10, already failed at a stress amplitude of 750 MPa at 800 °C, see Fig. 2. An increase in the durability of the hardmetals under cyclic loading with decreasing Co mean free path, i.e. Co content at constant WC grain size, was also observed in thermomechanical fatigue tests performed with hardmetals with different average WC grain size, cobalt content and carbon content [10].

At 700 °C, no cyclic creep was observed at 750 MPa, 1000 MPa and 1500 MPa for both WC-Co hardmetal grades S10 and M10, see Fig. 2(a.) to Fig. 2(c.) and Fig. 2(g.) to Fig. 2(i.). However, at 800 °C cyclic creep was noticed for both grades, see Fig. 2(d.), Fig. 2(e.), Fig. 2(j.) and Fig. 2(k.). The extent of cyclic creep increased with increasing stress amplitude. Cyclic creep is associated with dislocation movement in the cobalt binder due to time-independent deformation and creep at elevated temperatures. Creep is relevant here as strain continues to increase even after load reversal at maximum load, Fig. 2. This assumption is supported by observations of cyclically loaded aluminum single crystals [45], for which also an increase in strain immediately after unloading was observed and associated with creep strain. By stopping and holding at the maximum load, it was confirmed that the increased strain corresponds to creep strain

[45]. Also for WC-Co hardmetals, the increase in strain has been observed to be greater under tension than under compression, which can be attributed to the faster creep under tension than under compression at 800 °C [14,25]. WC-Co hardmetal grades of equal average WC grains size of 2.0 µm and 0.7 µm to the ones investigated in the current work but a higher Co content of 12 wt.% Co were investigated in tensile and compression step-loading creep tests with respect to their creep behavior at 700 °C and 800 °C [46]. With increasing temperature and under loading conditions similar to this current work, decreasing creep resistance has been observed [46]. Also, it was reported by Maier et al. [46] that at the relevant stress levels, the investigated medium-grained grade creeps faster at 800 °C than the submicron-grained grade under tensile and compression step-loading creep and failed at lower stresses. From these findings, one can deduce that in addition to time-independent plastic strains, creep strains also occur under cyclic loading at elevated temperature and foster cyclic creep and accelerated failure of the specimens. When comparing the stress-strain-hysteresis loops with increasing number of load cycles of S10 and M10 at 800 °C it appears that under the same loading conditions, cyclic creep is more pronounced in the WC-Co hardmetal grade M10 than in S10, compare Fig. 2(d.) with Fig. 2(j.) and Fig. 2(e.) with Fig. 2(k.). The dependence of  $R_{p0.2}$  on temperature is greater for the case of the ductile medium-grained hardmetal grade than for the submicron one, see Tab. 1. For a given stress level, this promotes the movement of lattice defects in the Co-binder, creep and damage formation in the specimen.

As at 700 °C, tension-compression-strain asymmetry  $\varepsilon_{\text{asym}}$  was also observed at 800 °C which occurred at lower stress amplitudes for 800 °C than at 700 °C. Already at 750 MPa, a minimal  $\varepsilon_{\text{asym}}$  was observed for the WC-Co hardmetal grade S10, which remained constant with increasing number of load cycles, Fig. 3(d.). At 1000 MPa, the  $\varepsilon_{\text{asym}}$  increased continuously with increasing number of load cycles until specimen failure for S10, see Fig. 3(d.). For the WC-Co hardmetal grade M10, at stress amplitudes of 750 MPa and 1000 MPa the  $\varepsilon_{\text{asym}}$  increased continuously with increasing number of load cycles until specimen failure, see Fig. 3(h.). At 750 MPa only a minimal increase in  $\varepsilon_{\text{asym}}$  was observed, instead at 1000 MPa a large increase was determined at low number of load cycles. As for the stress-strain-hysteresis loop area values, both WC-Co hardmetal grades showed similar orders of magnitude for the tension-compression-strain asymmetry values at 800 °C, see Fig. 3(d.) and Fig. 3(h.). If the uncorrected  $\varepsilon_{\text{asym}}$  increased continuously with increasing number of load cycles, the specimens failed under cyclic loading within the investigated number of load cycles. Tension-compression-strain asymmetry was also documented by step-loading creep tests for the WC-Co hardmetal grade M10 at 700 °C and 800 °C [25]. The faster increase in strain under tension was observed to be due to a faster growth of cavities at WC-WC interfaces and at WC-Co phase boundaries than under compression. Tension-compression-strain asymmetry in hardmetals was also noted in creep tests via a thermomechanical tests at 1000 °C [14]. In both of the aforementioned cases the onset stress of the strain asymmetry decreased with increasing temperature



[14,25]. Earlier occurrence of tension-compression-strain asymmetry with increasing temperature under cyclic loading was also observed in the current work. When  $\varepsilon_{\text{asym}}$  occurred and increased with increasing number of load cycles, specimen failure occurred in the tensile half of the loading cycle. Therefore, tension was assumed to promote the formation of microdefects and specimen failure under cyclic loading. In-situ scanning electron microscopy observations in cyclic loading experiments for austenitic steel show crack opening and closure behavior under low-cycle fatigue loading under stress ratios of minus one [26]. Cracks were observed to close near the minimum stress and to reopen just before the transition from compression to tension. That cracks may be open during the compressive half-cycle has been attributed to creep, crack tip shielding effects and residual stress buildup, as reported in [26]. Based on the results in [26] and in the current work, it was assumed that creep plays a significant role in the damage evolution during cyclic loading of WC-Co hardmetals at elevated temperatures.

At  $\sigma_a = 1500$  MPa the specimen failed at  $N_f$  values significantly smaller than 2500 number of load cycles at 700 °C and 800 °C, with a decrease in cycles to failure with increasing temperature, see Fig. 2. A decrease in the cycles to failure  $N_f$  was also observed for a WC-9.5 wt.% Co hardmetal with an average WC grain size of 5  $\mu\text{m}$  under cyclic bending load at  $\sigma_a = 1400$  MPa under  $R = -1$  in air at room temperature up to 700 °C [7]. Thereby, a difference of five orders of magnitudes in fatigue life under cyclic loading at 700 °C compared to room temperature was observed [7].

Loading conditions present close to cutting edges, such as the load case of  $R = -1$  with a stress amplitude of 1000 MPa investigated in the current work, were also observed for milling inserts [13,28]. Stress-strain-hysteresis loop area and tension-compression-strain asymmetries from the current work showed that both WC-Co hardmetal grades exhibit similar cyclic deformation behavior at  $R = -1$  at 700 °C and 800 °C. Due to the larger Co areas, lattice defects can move more easily in the WC-Co hardmetal grade M10 than in S10, which favors both time-independent strain and creep strain, causing the material M10 to fail earlier than the grade S10. Also, for both WC-Co hardmetal grades it was observed that they failed within the observed 2500 load cycles when the stress-strain-hysteresis loop area and/or the strain asymmetry did not stabilize with increasing number of load cycles, Fig. 3, and cyclic creep occurred, Fig. 2. Based on results of the stress-strain-hysteresis loop area and strain asymmetry, both parameters could be used as damage indicators to predict early damage under cyclic loading.

#### 4.2 Damage indicators and microdefect evolution with increasing number of load cycles

A comparison of the stress-strain-hysteresis loops of specimens tested up to  $N = 20$  and 80 load cycles of M10 at  $\sigma_a = 1000$  MPa at 800 °C without specimen failure, see Fig. 4(a.) and Fig. 4(b.), showed increasing stress-strain-hysteresis loop area and strain asymmetry values with increasing number of load cycle, see Fig. 4(c.) and Fig. 4(d.). For the specimen loaded up to  $N = 20$ , only the loop area increased, see Fig. 4(c.),

but for the specimen loaded up to  $N = 80$ , next to the loop area also the strain asymmetry increased significantly, see arrow in Fig. 4(d.). In the cyclic tests up to  $N = 2500$  load cycles, see Fig. 2 and Fig. 3, those specimens failed that also showed an increase in loop area and strain asymmetry. Next to increasing strain-hysteresis loop area and strain asymmetry values, also cyclic creep was observed in those specimens.

The specimens tested up to  $N = 20$  and  $80$  load cycles were investigated by SEM and EBSD with regard to microstructural changes. Additionally to the two loaded specimens, a virgin specimen was investigated as a reference. In specimens loaded up to  $N = 20$  and  $80$  without specimen failure, an increased number of defects as compared to the virgin specimen was observed, compare Fig. 5(a.) - Fig. 5(c.). The types of defects found were cavities, see Fig. 6(b.) and Fig. 6(c.), nanopores and nanopore chains, see Fig. 6(e.) and Fig. 6(f.). Cavities appear to be located at internal notches, i.e. sharp corners at WC/Co phase boundaries, narrow Co regions or triple points of WC/WC/WC and WC/WC/Co, see Fig. 6. The behavior of WC/WC boundaries, WC/Co interfaces and WC grains in hardmetals during plastic straining and fracture was investigated by microcantilever bending tests under monotonously increasing load at room temperature [47]. Csanádi et al. [47] observed that the fracture strength of WC/WC boundaries is lower than that of WC grains at room temperature. Most likely, due to this fracture strength difference, microdefects at WC/WC boundaries and WC/Co interfaces were also observed in the present work under cyclic loading at  $R = -1$ , and no fractured WC grains were observed. In the specimen loaded up to  $N = 20$  load cycles, few microdefects, Fig. 6(b.), were present, but an increased number of nanopore chains between WC/WC carbides was detected, Fig. 6(e.). Since twice as many microdefects in the specimen loaded up to  $N = 80$  load cycles were observed than in the specimen loaded up to  $N = 20$ . The increase in damage is most likely due to the accumulation and merging of nanopores into larger defects during the load cycles, leading to the formation of larger and more numerous defects, Fig. 5(c.). In the present work, microdefects were only observed in the Co-phase as Co also segregated at WC/WC grain boundaries in submonolayer fractions, as reported in [48,49]. Also, in fatigue tests at room temperature [7,8,43,50] and elevated temperatures [7], as well as in creep tests [25,46,51], mainly intercrystalline fracture occurred in the Co-phase, although cleavage fracture of the WC grains was also observed. Further increase in number of load cycles above  $N = 80$  in the current work, is assumed to result in a size increase and merging of microdefects, until failure of the specimen occurs. Internal defects were observed in [6,43] as the origin of a fatigue cracks, which propagated to a critical size and resulted in fracture of the specimen. Additionally, the mechanism of fatigue crack growth in WC-Co hardmetals around notch tips was studied at room temperature in [50]: Microdefects such as observed in the current work were suggested to develop ahead of the crack tip. Furthermore, examination of fracture surfaces after cyclic loading often revealed less smooth surface than the fracture surface after monotonic loading [44]. Such less smooth fracture surfaces were attributed to multiple fracture origins and crack bifurcation of crack propagation paths due to microdefects developed under cyclic loading [44]. The

average fracture surface roughness from SENB specimens made out of WC-Co hardmetals with more than 8 wt.% Co were investigated in [52] and an increase of the fracture surface roughness with a rise of the fracture toughness at 800 °C was observed. A suggested explanation was that the increase of the fracture surface roughness is favored by inhomogeneities in the hardmetal in front of the crack tip [52]. Due to the elevated temperature, the yield strength is lowered and the plastic zone in front of the crack tip is enlarged compared to room temperature, resulting in a more likely interaction of the crack tip's stress field and the assumingly present inhomogeneities, which therefore may become part of the crack path. Based on the reports from literature, the microdefects observed in the current work are assumed to be the cause of the reported fracture surfaces peculiarities under cyclic [43] and monotonously increasing load. Microdefects may be one of the physical reasons for the jump-like increase in fracture toughness observed for hardmetals at 800 °C, as they occur in this temperature regime. These nanodefects, which can merge to form microdefects, can act as potential weak points in the microstructure that can become fracture origins in addition to material-inherent internal inhomogeneities or defects in the form of larger than average WC grains or pores [42].

From observations in the current work, correlations emerge between microdefect formation and the characteristics of the stress-strain-hysteresis loop: As the number of load cycles increases, the number of microdefects increases, Fig. 5, as well as the hysteresis loop area and the tension-compression-strain asymmetry, Fig. 4. Also, both parameters increased in the same order of magnitude for the specimen made of M10, which failed after  $N_f = 102$  load cycles at 1000 MPa at 800 °C, Fig. 2(k.). Therefore, stress-strain-hysteresis loop area and strain asymmetry are assumed to be damage indicators for early detection of damage under cyclic loading. Additionally, cyclic creep was observed, which increased with increasing number of load cycles, Fig. 4. Cyclic creep is attributed to the accumulation of plastic strain which is accelerated by thermally activated processes in the cobalt binder in addition to mechanical processes at elevated temperatures, as described above.

Pure Co is stable in the hcp crystal structure at room temperature up to 417 °C, and above this temperature the fcc structure is stable [53]. However, both crystal phases can coexist in WC-Co hardmetals, e.g. in twins at room temperature [54], see green triangles in Fig. 6 and EBSD area phase fraction maps in Fig. 7(a.). The coexistence of both phases can be attributed to the presence of dissolved tungsten, carbon or other elements in Co [55–58], the WC grain size [56], and the stresses caused by differences in the thermal expansion coefficient in the WC and Co-phases [59]. Parts of the fcc Co-phase were transformed into hcp Co during the cyclic test at 800 °C, see Fig. 7. Table 2 also shows that after  $N = 20$  and 80 load cycles, the fcc to hcp Co-phase fraction shifted and the amount of hcp phase increased. The fraction of hcp Co-phase was similarly high under both number of load cycles, comparing Fig. 7(b.) and Fig. 7(c.). The fcc to hcp transformation of the Co-phase is assumed to contribute to the accommodation of strains, which may also

retard the formation of cavities during straining. Also, the hcp Co-phase is less ductile with each loading cycle as the fcc Co-phase, because it has only three instead of 12 slip systems [60]. Hence, the Co-phase transformation can have an inhibiting and a promoting effect on cavity formation and growth. Phase transformation is a stress- and/or strain-controlled process and takes place when the strain in the Co-binder increases [61]. The described observation is supported by room temperature experiments performed under monotonously increasing [3,7,8,62] and cyclic loading [7,8,63,64] that result in the phase transformation from fcc to hcp Co-phase, near and in front of crack tips. Additionally, influences on the mechanical properties, like decrease of fatigue strength [55], fracture toughness [8] or increase of magnetic coercive force [65], caused by the fcc to hcp Co-phase transformation have been observed by different research groups. Under fatigue conditions, the phase transformation of cobalt is also an important damage mechanism [8,62,64] and the hcp Co-phase fraction was also observed to increase with increasing number of load cycles [63]. An increase of the hcp Co-phase fraction between  $N=20$  and 80 was not observed in the current work, this may be due to the too small difference between the numbers of load cycles or by the fact that the transformation occurs and is completed within a few load cycles. When comparing Fig. 6(b.) and Fig. 6(c.) with Fig. 7(b.) and Fig. 7(c.), it becomes apparent that the hcp Co-phase can be also observed in areas without microdefects. On the one hand, this may be due to the fact that the WC-Co hardmetal grade M10 has hcp Co-phase fractions in areas without subsequent microdefect formation compared to the virgin condition. On the other hand, only 2D microstructure micrographs were investigated in the current work, and therefore no statements about the presence of microdefects in areas below the investigated image plane within hcp Co-phase-rich regions are possible. Additionally, the Co-phase transformation from fcc to hcp Co-phase may cause a volume change between the two crystal structures. For the currently investigated material it is unknown whether the transformation from fcc to hcp Co-phase leads to an increase or a decrease in volume. In the literature there are contradicting findings reporting negative as well as positive volume changes [7,55,66] that may be associated with details of binder chemistry, local residual stress state and even magnetism. The effect of local chemistry on cavity formation may be important since the Co-binder includes tungsten, carbon, and maybe other elements which can stabilize the fcc or hcp Co-phase [56]. Additionally, these elements must also be rearranged during the phase transformation, which can influence the unit cell volume per atom [55]. Therefore, it is not excluded that certain alloying elements have an influence on the volume change.

Additionally to phase fraction determinations, EBSD was used to determine inverse pole figures (IPFs), see Fig. 8, grain average misorientations (GAMs) for the WC-phase, see Fig. 9, and kernel average misorientations (KAMs) for the WC-phase, Fig. 10, and the fcc and hcp Co-phase, see Fig. 11. It was observed that the frequency of deformed WC grains, i.e. such ones with crystal orientation changes within a grain, marked by white ovals, is approximately the same in all three specimens, Fig. 8(a.) to Fig. 8(c.).

The KAM maps for the WC-phase shown in Fig. 10 indicate a concentration of plastic deformation at the very edges of the WC grains that must have originated during the material manufacture process because it is basically the same in the virgin and cyclically loaded specimen, as shown in Fig. 10. This indicates that during cyclic loading under a stress ratio of  $R = -1$  at 800 °C the deformation is mainly carried by the Co-phase. The fcc and hcp Co-phase grains are many times larger than the WC grain size, as large areas of the same binder crystal orientation were observed in the virgin specimen, see Fig. 8(d.) to Fig. 8(g.). This was also the case for the fcc Co-phase in the two loaded specimens in the current work, see Fig. 8(e.) and Fig. 8(f.). The fcc Co-binder grains to be larger than the ones of WC was also reported for coarse-grained WC-Co hardmetals with mainly fcc Co-binder [34] and WC-Co hardmetals with fcc and hcp Co-phase [56]. Also, both loaded specimens showed areas of equal crystal orientation for the fcc and hcp Co-phase, see Fig. 8(h.) and Fig. 8(i.). The spatial distribution of the hcp Co-phase in both loaded specimens indicates a rather uniform distribution of the sites for formation of the hcp Co-phase in the fcc Co-phase.

The kernel average misorientations (KAM) is related to dislocation density [31] and can link to the grain average misorientation. The KAM and GAM maps for the specimens loaded up to  $N = 20$  and 80 load cycles at 800 °C suggest that under both number of loading cycles more dislocations were formed in both Co-phases than in the WC grains, see Fig. 9, Fig. 10 and Fig. 11. This is consistent with the observed inverse pole figures for the WC-phase, see Fig. 8(b.) and Fig. 8(c.), as the WC skeleton does not show significant orientation changes, i.e. does not deform plastically to a significant degree for both number of load cycles at  $R = -1$  at 800 °C compared to the virgin specimen. The extent of crystal orientation variation due to cyclic loading of the WC grains is approximately the same in the virgin specimen as in both loaded specimens. Furthermore, the GAM chart in Fig. 9(d.) and the KAM chart in Fig. 10(c.) shows that the WC-phase does not change significantly due to the imposed cyclic loading. Hence, cyclic loading up to  $N = 80$  load cycles does not affect the WC grains' deformation state. However, under certain conditions, some degree of plastic deformation was also observed in WC grains, e.g., at sufficiently high pure compression loading at room temperature [67]. The plastic deformation in the WC grains indicated by the green margins of the WC grains in Fig. 10 that corresponds to about 1° misorientation may have emerged during or after liquid-phase sintering, when the WC skeleton consolidates and/or differences in the thermal expansion coefficients as well as lattice distortion between WC and the Co-phase cause stresses and strains. However, the plastic deformation in the WC grains did not increase under increasing number of load cycles as shown in Fig. 9. For the current cyclic loading case at 800 °C, the IPF maps in Fig. 8(b.) and Fig. 8(c.) and the KAM distributions in Fig. 10(c.) clearly indicate that the WC grains deform mainly elastically under the applied cyclic load amplitude of 1000 MPa that is just lower than the estimated flow stress of WC at 800 °C [67]. The KAM maps for the hcp Co-phases shown in Fig. 11(e.) to Fig. 11(g.) suggests that both loaded specimens show larger areas of high misorientation (green) than the virgin one. More details on the behavior

of the binder phases during cyclic loading at 700 °C and 800 °C can be deduced by taking a closer look at the KAM charts shown in Fig. 11(d.) and Fig. 11(h.), derived from the data shown Fig. 11(a.) to Fig. 11(c.), and Fig. 11(e.) to Fig. 11(g.). Note that the KAM distributions exhibit two particularities: The high peaks of the KAM distributions located at small KAM values indicated by grey arrows in Fig. 11(d.) and Fig. 11(h.), are located at higher KAM values for the hcp Co-phase. With increasing amount of the hcp Co-phase, the ability of the Co-binder to deform under full shape compatibility with its surroundings decreases and the binder embrittles, as reported in [50,62]. This is attributed to the fact that the dislocation movement is limited by the fewer available slip systems in hcp Co-phase than in fcc Co-phase [60] and during phase transformation, the mean free path of dislocation decreases due to the rise in twin boundary density and leads to strengthening of the Co-phase, as suggested in [68]. Therefore, the misorientation that corresponds to the density of stored dislocations is higher in the hcp Co-phase than in the fcc Co-phase see Fig. 11. Comparing the KAM distributions of the virgin with the loaded specimens, it becomes apparent that the height of the number fraction peak at low misorientations at around 0.2° and 0.3° decreases due to the cyclic deformation, see gray arrows in Fig. 11(d.) and Fig. 11(h.). In this range, the specimen loaded up to  $N = 20$  load cycles shows lower number fractions for fcc Co-phase and hcp Co-phase than the virgin and the specimen loaded up to  $N = 80$  load cycles. Note, that the EBSD data were not subjected to a grain dilation clean-up. Hence, peaks were observed at the extreme ends of the investigated misorientation value spectrum at zero and two degrees for the investigated specimens, see Fig. 11(d.) and Fig. 11(h.). These increases are due to the fact that raw EBSD data were used for the analysis and individual pixels show such misorientations. Hence, these data should be treated with caution and should not be further interpreted. Furthermore, the areas of the KAM distributions at around 0.7° and 0.8° KAM, marked by black arrows in Fig. 11(d.) and Fig. 11(h.), show higher values for both loaded binder phases compared to the virgin ones. The observed increase in the higher misorientation, see black arrows on Fig. 11(d.) and Fig. 11(h.), was coupled with a decrease in the smaller misorientations in the loaded specimens. This indicates that the increase in higher misorientations in loaded specimens indicates that the dislocation density increased in the Co-phases.

Note that the fcc Co-phase in the specimen loaded up to  $N = 20$  load cycles shows a higher number fraction than the specimen loaded up to a higher number of load cycles. Additionally, different crystal orientations for the fcc Co-phase were observed in the virgin and both loaded specimens up to  $N = 20$  and 80 load cycles, see different colors in Fig. 8(g.) to Fig. 8(f). The different crystal orientations may also influence the stress-strain behavior of the WC-Co hardmetals, since the KAM misorientation is inhomogeneously distributed over the image in Fig. 11(b.) and Fig. 11(c.). In contrast, such a dependence is not found in the virgin specimen, with a homogeneous distributed over the image. Additionally, in the current work only a limited number of Co single crystal orientations are shown in the IPF, see Fig. 8. The

limited number of cobalt grains with different crystal orientation is caused by the fact that the fcc Co-phase grains can be much larger than the WC grains [54].

Simulations of indentation tests on surfaces of different crystallographic orientations of fcc Co, hcp Co, WC in WC-Co composite at room temperature by Feng et al. [69], showed that the nucleation, expansion and interaction of dislocations in the Co-crystal strongly depended on the orientation of loading with respect to the orientation of the crystals. Moreover, it was documented that the type and the interaction of dislocations are different for fcc and hcp Co-crystals [69]. Therefore, the orientation of the crystallites has a strong influence on the observed traces of plastic deformation in the KAM, and different number fractions of certain KAM values were observed for the fcc Co-phase of both loaded specimens, see Fig. 11(d.). To understand the dependence of the KAM distributions on the crystal orientation of the fcc and hcp Co-phases in more detail, large-scale in-situ high-temperature EBSD observations during cyclic loading are desirable.

Based on the gained results on the stress-strain-hysteresis loop and microstructure, two damage indicators were established: (i) Stress-strain-hysteresis loop area. and (ii) tension-compression-strain asymmetry. There was evidence from the experimental observations that when the loop area or/and the strain asymmetry increased with increasing number of load cycles, microdefects appeared in form of cavities and nanopores at WC/WC boundaries and WC/Co interfaces. Additionally, cyclic creep fosters microdefect formation. Using the aforementioned parameters, stress-strain-hysteresis loops can be used to infer whether or not microdefects, which can lead to failure of the material/component under further loading, are formed in the material under specific loading conditions.

## 5. Conclusions

Load-controlled uniaxial cyclic tests were performed on two WC-10 wt.% Co hardmetal grades, which differed in their average WC grain size of 0.7  $\mu\text{m}$  and 2.0  $\mu\text{m}$ . The uniaxial cyclic tests were carried out with a stress ratio  $R = \sigma_{\min}/\sigma_{\max} = -1$  at stress amplitudes of  $\sigma_a = 750$  MPa, 1000 MPa and 1500 MPa at 700 °C and 800 °C in vacuum. The main findings of the current work are the following:

- Different cyclic stress-strain-hysteresis loop behaviors were observed in the performed uniaxial cyclic tests with a mean stress  $\sigma_{\text{mean}} = 0$  with increasing number of load cycles: reversible stress-strain behavior, increase of stress-strain-hysteresis loop area associated with softening of the material, cyclic creep and strain asymmetry with more specimen compliance in tension than in compression.
- The both investigated hardmetal grades showed for all stress amplitudes reversible cyclic behavior at 700 °C with constant small stress-strain-hysteresis loop areas with increasing number of load cycles. At 800 °C and with increasing number of load cycles, the WC-Co hardmetal specimens showed an increase in stress-strain-hysteresis loop area, the occurrence of tension-compression-strain asymmetry, cyclic creep, and earlier failure than at 700 °C for all stress amplitudes.

- At 700 °C and small stress amplitudes, the two investigated WC-10 wt.% Co hardmetal grades showed narrow and symmetrical hysteresis loops and similar hysteresis loop area values. At the highest stress amplitude investigated, both specimens show a tension-compression-strain asymmetry.
- The onset of cyclic creep in the both WC-Co hardmetal grades was observed at the same stress amplitudes at 800 °C, with the medium-grained grade exhibiting increased cyclic creep compared to the submicron-grained WC-Co hardmetal grade. The specimens made of the medium-grained grade also failed at lower stress amplitudes than the ones made of the submicron-grained WC-Co hardmetal grade. Furthermore, at 800 °C both WC-Co hardmetal grades exhibited similar values for the stress-strain-hysteresis loop area and tension-compression-strain asymmetry.
- The WC-10 wt.% Co hardmetal grade with an average WC grains size of 2.0 μm were subjected to uniaxial cyclic loads at a stress amplitude of  $\sigma_a = 1000$  MPa at 800 °C up to  $N = 20$  and 80 load cycles in order to investigate the resulting damage evolution at microstructure level. Microstructure analysis revealed that testing up to  $N = 20$  load cycles had caused damage mainly in the form of nanopores at WC/WC interfaces and WC/Co phase boundaries and in a smaller number also in the form of cavities. The number of nanopores increased while promoting the formation of larger cavities with increasing number of loading cycles.
- Two damage indicators can be derived from the development of stress-strain hysteresis loops in conjunction with the development of damage at the microstructure scale: (i) The stress-strain-hysteresis loop area, and (ii) the tension-compression-strain asymmetry. As far as one of the two parameters did not stabilize with increasing number of load cycles, early failure of WC-Co hardmetal specimens was observed under uniaxial cyclic loading under  $R = -1$ .
- In the Co-phase, there is an increase in dislocation density, whereas the WC grains show no plastic deformation after cyclic loading at 800 °C. Further, it was demonstrated that uniaxial cyclic loading leads to an increase in the phase fraction of the hcp Co-phase in the Co-binder.

### Acknowledgements

We thank Bernhard Sartory and his team for their exceptional work on SEM and EBSD. Additionally, the authors gratefully acknowledge the financial support of the Frontrunner-Initiative of the project "Frontrunner: Integrated, data driven development for Cutting Tools" (Project No. 861280). Additionally, the financial support under the scope of the COMET program within the K2 Center "Integrated Computational Material, Process and Product Engineering (IC-MPPE)" (Project No 859480). This program is supported by the Austrian Federal Ministries for Climate Action, Environment, Energy, Mobility, Innovation and Technology (BMK) and for Digital and Economic Affairs (BMDW), represented by the Austrian research funding association (FFG), and the federal states of Styria, Upper Austria and Tyrol.



**References**

- [1] G.J. Liu, Z.C. Zhou, X. Qian, W.H. Pang, G.H. Li, G.Y. Tan, Wear Mechanism of Cemented Carbide Tool in High Speed Milling of Stainless Steel, *Chinese J. Mech. Eng. (English Ed.* 31 (2018) 1–10. doi:10.1186/s10033-018-0298-2.
- [2] M.G. Gee, A.J. Gant, B. Roebuck, K.P. Mingard, Wear of Hardmetals, in: *Compr. Hard Mater.*, 2014: pp. 363–383. doi:10.1016/B978-0-08-096527-7.00012-X.
- [3] B. Roebuck, E.A. Almond, Deformation and fracture processes and the physical metallurgy of WC Co hardmetals, *Int. Mater. Rev.* 33 (1988) 90–112. doi:10.1179/imr.1988.33.1.90.
- [4] U. Schleinkofer, H.G. Sockel, K. Görting, W. Heinrich, Fatigue of hard metals and cermets, *Mater. Sci. Eng. A.* 209 (1996) 313–317. doi:10.1016/0921-5093(95)10106-3.
- [5] L. Llanes, M. Anglada, Y. Torres, Fatigue of Cemented Carbides, in: *Compr. Hard Mater.*, Elsevier Ltd., 2014: pp. 345–362. doi:10.1016/B978-0-08-096527-7.00011-8.
- [6] T. Klünsner, S. Marsoner, R. Ebner, R. Pippan, J. Glätzle, A. Püschel, Effect of microstructure on fatigue properties of WC-Co hard metals, in: *Procedia Eng.*, 2010: pp. 2001–2010. doi:10.1016/j.proeng.2010.03.215.
- [7] P. Kindermann, P. Schlund, H.G. Sockel, M. Herr, W. Heinrich, K. Görting, U. Schleinkofer, High temperature fatigue of cemented carbides under cyclic loads, *Int. J. Refract. Met. Hard Mater.* 17 (1999) 55–68. doi:10.1016/S0263-4368(99)00014-1.
- [8] U. Schleinkofer, H.G. Sockel, K. Görting, W. Heinrich, Microstructural processes during subcritical crack growth in hard metals and cermets under cyclic loads, *Mater. Sci. Eng. A.* 209 (1996) 103–110. doi:10.1016/0921-5093(95)10098-9.
- [9] Y. Torres, M. Anglada, L. Llanes, Fatigue mechanics of WC-Co cemented carbides, in: *Int. J. Refract. Met. Hard Mater.*, 2001: pp. 341–348. doi:10.1016/S0263-4368(01)00032-4.
- [10] F.C. Dary, B. Roebuck, M.G. Gee, Effects of microstructure on the thermo-mechanical fatigue response of hardmetals using a new miniaturized testing rig, *Int. J. Refract. Met. Hard Mater.* 17 (1999) 45–53. doi:10.1016/S0263-4368(98)00070-5.
- [11] C. Tritremmel, T. Klünsner, B. Sartory, C. Czettel, S. Marsoner, Cyclic plastic deformation behaviour of WC-Co hard metals at elevated temperatures, in: *19th Plansee Semin. - Int. Conf. Refract. Met. Hard Mater.*, Plansee Group, Reutte/Austria, 2017: pp. 1–9.
- [12] A.W. Nemetz, W. Daves, T. Klünsner, C. Praetzas, W. Liu, T. Teppernegg, C. Czettel, F. Haas, C. Bölling, J. Schäfer, Experimentally validated calculation of the cutting edge temperature during dry milling of Ti6Al4V, *J. Mater. Process. Technol.* 278 (2020) 116544. doi:https://doi.org/10.1016/j.jmatprotec.2019.116544.

- [13] A.W. Nemetz, W. Daves, T. Klünsner, W. Ecker, J. Schäfer, C. Czettl, T. Antretter, Cyclic heat-up and damage-relevant substrate plastification of single- and bilayer coated milling inserts evaluated numerically, *Surf. Coatings Technol.* 360 (2019) 39–49. doi:<https://doi.org/10.1016/j.surfcoat.2019.01.008>.
- [14] B. Roebuck, S. Moseley, Tensile and compressive asymmetry in creep and monotonic deformation of WC/Co hardmetals at high temperature, *Int. J. Refract. Met. Hard Mater.* 48 (2015) 126–133. doi:10.1016/j.ijrmhm.2014.08.007.
- [15] K. Maier, T. Klünsner, P. Pichler, S. Marsoner, W. Ecker, C. Czettl, J. Schäfer, R. Ebner, Submitted - Strain ratcheting limit stresses as a function of microstructure of WC-Co hardmetals under uniaxial cyclic loads under a stress ratio of  $R = -\infty$  at elevated temperatures, *Int. J. Refract. Met. Hard Mater.* (2021).
- [16] M.M. Chowdhury, M.A. Hoque, N. Fu, J.C. Suhling, S. Hamasha, P. Lall, Characterization of Material Damage and Microstructural Evolution Occurring in Lead Free Solders Subjected to Cyclic Loading, in: *Proc. - Electron. Components Technol. Conf.*, 2018: pp. 865–874. doi:10.1109/ECTC.2018.00134.
- [17] F. Orth, L. Hoffmann, H. Zilch-Bremer, G.W. Ehrenstein, Evaluation of composites under dynamic load, *Compos. Struct.* 24 (1993) 265–272. doi:10.1016/0263-8223(93)90220-K.
- [18] T.F. Tan, C.K.H. Dharan, Cyclic hysteresis evolution as a damage parameter for notched composite laminates, *J. Compos. Mater.* 44 (2010) 1977–1990. doi:10.1177/0021998309360942.
- [19] J. Lemaitre, How to use damage mechanics, *Nucl. Eng. Des.* 80 (1984) 233–245. doi:10.1016/0029-5493(84)90169-9.
- [20] ISO 4499-2, ISO 4499-2:2008 Hardmetals-Metallographic determination of microstructure-Part 2: Measurement of WC grain size, 2008.
- [21] K. Maier, T. Klünsner, M. Krobath, C. Tritremmel, S. Marsoner, C. Czettl, Uniaxial step loading test setup for determination of creep curves of oxidation-sensitive high strength materials in vacuum under tensile and compressive load, *Int. J. Refract. Met. Hard Mater.* 92 (2020) 105327. doi:10.1016/j.ijrmhm.2020.105327.
- [22] S.N. Basu, V.K. Sarin, Oxidation behavior of WC-Co, *Mater. Sci. Eng. A.* 209 (1996) 206–212. doi:10.1016/0921-5093(95)10145-4.
- [23] D.R. Fancher, Stress-strain hysteresis loops and rheological epicycles Item Type text; Thesis-Reproduction (electronic), The University of Arizona., 1968. <http://hdl.handle.net/10150/318730> (accessed June 10, 2021).
- [24] OriginLab Corporation, OriginLab - Polygon Area, (2021). <https://www.originlab.com/doc/Origin-Help/Math-PolygonArea> (accessed May 18, 2021).

- [25] K. Maier, T. Klünsner, W. Ecker, P. Pichler, S. Marsoner, C. Czettel, J. Schäfer, R. Ebner, A physical reason for asymmetric creep deformation behaviour of WC-Co hardmetal under tension and compression loading at 700 °C and 800 °C, *Int. J. Refract. Met. Hard Mater.* 97 (2021) 105526. doi:10.1016/j.ijrmhm.2021.105526.
- [26] R. Pippan, A. Hohenwarther, Fatigue crack closure: a review of the physical phenomena, *Fatigue Fract. Eng. Mater. Struct.* 40 (2017) 471–495. doi:10.1111/ffe.12578.
- [27] J. Lemaitre, R. Desmorat, *Engineering damage mechanics: Ductile, creep, fatigue and brittle failures*, 2005. doi:10.1007/b138882.
- [28] T. Tepperneegg, T. Klünsner, P. Angerer, C. Tritremmel, C. Czettel, J. Keckes, R. Ebner, R. Pippan, Evolution of residual stress and damage in coated hard metal milling inserts over the complete tool life, *Int. J. Refract. Met. Hard Mater.* 47 (2014) 80–85. doi:10.1016/j.ijrmhm.2014.07.005.
- [29] B. Winiarski, A. Gholinia, K. Mingard, M. Gee, G.E. Thompson, P.J. Withers, Broad ion beam serial section tomography, *Ultramicroscopy.* 172 (2017) 52–64. doi:https://doi.org/10.1016/j.ultramic.2016.10.014.
- [30] EDAX Smart Insight, (n.d.). <https://www.edax.com/> (accessed September 20, 2020).
- [31] A.J. Schwartz, M. Kumar, B.L. Adams, D.P. Field, *Electron Backscatter Diffraction in Materials Science*, 2nd ed., Springer US, 2009. doi:10.1007/978-0-387-88136-2.
- [32] F. Bachmann, R. Hielscher, H. Schaeben, Texture analysis with MTEX- Free and open source software toolbox, in: *Solid State Phenom.*, Trans Tech Publications Ltd, 2010: pp. 63–68. doi:10.4028/www.scientific.net/SSP.160.63.
- [33] M. Gee, K. Mingard, B. Roebuck, Application of EBSD to the evaluation of plastic deformation in the mechanical testing of WC/Co hardmetal, *Int. J. Refract. Met. Hard Mater.* 27 (2009) 300–312. doi:10.1016/j.ijrmhm.2008.09.003.
- [34] K.P. Mingard, B. Roebuck, H.G. Jones, M. Stewart, D. Cox, M.G. Gee, Visualisation and measurement of hardmetal microstructures in 3D, *Int. J. Refract. Met. Hard Mater.* 71 (2018) 285–291. doi:10.1016/j.ijrmhm.2017.11.023.
- [35] B.M. Jablon, K. Mingard, A. Winkelmann, G. Naresh-Kumar, B. Hourahine, C. Trager-Cowan, Subgrain structure and dislocations in WC-Co hard metals revealed by electron channelling contrast imaging, *Int. J. Refract. Met. Hard Mater.* 87 (2020) 1–7. doi:10.1016/j.ijrmhm.2019.105159.
- [36] B.I. Sandor, *Fundamentals of Cyclic Stress and Strain*, University of Wisconsin Press, 1972.
- [37] V. Kliman, M. Bílý, Hysteresis energy of cyclic loading, *Mater. Sci. Eng.* 68 (1984) 11–18. doi:10.1016/0025-5416(84)90239-8.
- [38] J. Roesler, H. Harders, M. Baeker, *Mechanical Behaviour of Engineering Materials*, 1st ed., Springer-Verlag Berlin Heidelberg, 2007. doi:10.1007/978-3-542-73448-2.

- [39] W. Reik, P. Mayr, E. Macherauch, • Vergleich Der Woehler-Kurven Aus Spannungsgesteuerten, Gesamtdehnungsgesteuerten Und Plastischdehnungsgesteuerten Versuchen., Arch. Fur Das Eisenhüttenwes. 50 (1979) 407–411. doi:10.1002/srin.197904765.
- [40] A. Schmiedt-Kalenborn, Mikrostrukturbasierte Charakterisierung des Ermüdungs- und Korrosionsermüdungsverhaltens von Lötverbindungen des Austenits X2CrNi18-9 mit Nickel- und Goldbasislot, 1st ed., Springer Vieweg, Wiesbaden, 2020. doi:10.1007/978-3-658-30105-7.
- [41] L. Makhele-Lekala, S. Luyckx, F.R.N. Nabarro, Semi-empirical relationship between the hardness, grain size and mean free path of WC–Co, Int. J. Refract. Met. Hard Mater. 19 (2001) 245–249. doi:https://doi.org/10.1016/S0263-4368(01)00022-1.
- [42] M. Jonke, T. Klünsner, P. Supancic, W. Harrer, J. Glätzle, R. Barbist, R. Ebner, Strength of WC-Co hard metals as a function of the effectively loaded volume, Int. J. Refract. Met. Hard Mater. 64 (2017) 219–224. doi:10.1016/j.ijrmhm.2016.11.003.
- [43] K. Obrtlík, J. Polák, M. Hájek, J. Vrbka, Low Cycle Fatigue in WC-Co Cemented Carbides, in: Low Cycle Fatigue Elasto-Plastic Behav. Mater., 1992: pp. 43–48. doi:10.1007/978-94-011-2860-5\_8.
- [44] A. Li, J. Zhao, D. Wang, X. Gao, H. Tang, Three-point bending fatigue behavior of WC-Co cemented carbides, Mater. Des. 45 (2013) 271–278. doi:10.1016/j.matdes.2012.08.075.
- [45] N. Thompson, C.K. Coogan, J.G. Rider, Experiments on aluminum crystals subjected to slowly alternating stresses, Inst. Met. -- J. 84 (1955) 73–80.
- [46] K. Maier, T. Klünsner, M. Krobath, P. Pichler, S. Marsoner, W. Ecker, C. Czettel, J. Schäfer, R. Ebner, Creep behaviour of WC-12 wt% Co hardmetals with different WC grain sizes tested in uniaxial tensile and compression step-loading tests at 700 °C and 800 °C, Int. J. Refract. Met. Hard Mater. 100 (2021) 105633. doi:10.1016/j.ijrmhm.2021.105633.
- [47] T. Csanádi, M. Vojtko, J. Dusza, Deformation and fracture of WC grains and grain boundaries in a WC-Co hardmetal during microcantilever bending tests, Int. J. Refract. Met. Hard Mater. 87 (2020) 105163. doi:10.1016/j.ijrmhm.2019.105163.
- [48] M. Christensen, G. Wahnström, Effects of cobalt intergranular segregation on interface energetics in WC-Co, Acta Mater. 52 (2004) 2199–2207. doi:10.1016/j.actamat.2004.01.013.
- [49] A. Henjered, M. Hellsing, H.D. Andrén, H. Nordén, Quantitative microanalysis of carbide/carbide interfaces in WC–Co-base cemented carbides, Mater. Sci. Technol. (United Kingdom). 2 (1986) 847–855. doi:10.1179/mst.1986.2.8.847.
- [50] P.R. Fry, G.G. Garrett, Fatigue crack growth behaviour of tungsten carbide-cobalt hardmetals, J. Mater. Sci. 23 (1988) 2325–2338. doi:10.1007/BF01111884.

- [51] K. Mingard, S. Moseley, S. Norgren, H. Zakaria, D. Jones, B. Roebuck, Microstructural observations of high temperature creep processes in hardmetals, *Powder Metall.* (2021) 1–11. doi:10.1080/00325899.2021.1877866.
- [52] T. Tepperneegg, T. Klünsner, C. Kremsner, C. Tritremmel, C. Czettl, S. Puchegger, S. Marsoner, R. Pippan, R. Ebner, High temperature mechanical properties of WC-Co hard metals, *Int. J. Refract. Met. Hard Mater.* 56 (2016) 139–144. doi:10.1016/j.ijrmhm.2016.01.002.
- [53] A. Seeger, U. Dehlinger, *Kristallphysik II / Crystal Physics II*, 1st ed., Springer Berlin Heidelberg, Berlin, Heidelberg, 1958. doi:10.1007/978-3-642-45890-3.
- [54] K.P. Mingard, H.G. Jones, M.G. Gee, B. Roebuck, J.W. Nunn, In situ observation of crack growth in a WC-Co hardmetal and characterisation of crack growth morphologies by EBSD, *Int. J. Refract. Met. Hard Mater.* 36 (2013) 136–142. doi:10.1016/j.ijrmhm.2012.08.006.
- [55] B. Roebuck, E.A. Almond, A.M. Cottenden, The influence of composition, phase transformation and varying the relative F.C.C. and H.C.P. phase contents on the properties of dilute CoWC alloys, *Mater. Sci. Eng.* 66 (1984) 179–194. doi:10.1016/0025-5416(84)90179-4.
- [56] J.M. Marshall, M. Giraudel, The role of tungsten in the Co binder: Effects on WC grain size and hcp-fcc Co in the binder phase, *Int. J. Refract. Met. Hard Mater.* 49 (2015) 57–66. doi:10.1016/j.ijrmhm.2014.09.028.
- [57] J. Weidow, S. Norgren, H.O. Andrén, Effect of V, Cr and Mn additions on the microstructure of WC-Co, *Int. J. Refract. Met. Hard Mater.* 27 (2009) 817–822. doi:10.1016/j.ijrmhm.2009.02.002.
- [58] M. Eizadjou, H. Chen, C. Czettl, J. Pachlhofer, S. Primig, S.P. Ringer, An observation of the binder microstructure in WC-(Co+Ru) cemented carbides using transmission Kikuchi diffraction, *Scr. Mater.* 183 (2020) 55–60. doi:10.1016/j.scriptamat.2020.03.010.
- [59] S. Adjam, D. Mari, T. LaGrange, Strain glass transition of cobalt phase in a cemented carbide, *Int. J. Refract. Met. Hard Mater.* 87 (2020) 105161. doi:10.1016/j.ijrmhm.2019.105161.
- [60] A.G. Jackson, Slip Systems, in: *Handb. Crystallogr.*, Springer, New York, NY, 1991: pp. 83–88. doi:https://doi.org/10.1007/978-1-4612-3052-6\_7.
- [61] E.A. Almond, B. Roebuck, Fatigue-crack growth in WC-Co hardmetals, *Met. Technol.* 7 (1980) 83–85. doi:10.1179/030716980803287080.
- [62] V.K. Sarin, T. Johannesson, On the deformation of WC-Co cemented carbides, *Met. Sci.* 9 (1975) 472–476. doi:10.1179/030634575790444531.
- [63] K. Miyake, Y. Fujiwara, K. Nishigaki, On the Fatigue of WC-Co Alloys, *J. Japan Inst. Met.* 32 (1968) 1128–1131. doi:10.2320/jinstmet1952.32.11\_1128.

- [64] A. OTSUKA, K. TOHGO, H. SUGAWARA, F. UEDA, H. HOHJO, Fatigue of WC–Co Hardmetals Under Tension-compression Loading — the Effects of Co Content and WC Grain Size, in: Proc. 7th Int. Conf. Fract., 1989: pp. 1289–1296. doi:10.1016/b978-0-08-034341-9.50143-1.
- [65] U. Beste, H. Engqvist, S. Jacobson, Pressure cycling induced modification of a cemented carbide, in: 15th Int. Plansee Semin., Reutte/Austria, 2001: pp. 685–697.
- [66] C.H. Vassel, A.D. Krawitz, E.F. Drake, E.A. Kenik, Binder deformation in WC-(Co, Ni) cemented carbide composites, Metall. Trans. A. 16 (1985) 2309–2317. doi:10.1007/BF02670431.
- [67] L. Faksa, W. Daves, T. Klünsner, K. Maier, T. Antretter, C. Czettel, W. Ecker, Shot peening-induced plastic deformation of individual phases within a coated WC-Co hard metal composite material including stress-strain curves for WC as a function of temperature, Surf. Coatings Technol. 380 (2019) 125026. doi:10.1016/j.surfcoat.2019.125026.
- [68] M. Padmakumar, J. Guruprasath, P. Achuthan, D. Dinakaran, Investigation of phase structure of cobalt and its effect in WC–Co cemented carbides before and after deep cryogenic treatment, Int. J. Refract. Met. Hard Mater. 74 (2018) 87–92. doi:10.1016/j.ijrmhm.2018.03.010.
- [69] Q. Feng, X. Song, H. Xie, H. Wang, X. Liu, F. Yin, Deformation and plastic coordination in WC-Co composite — molecular dynamics simulation of nanoindentation, Mater. Des. 120 (2017) 193–203. doi:https://doi.org/10.1016/j.matdes.2017.02.010.

